TRANSIENT AND FAULT-RIDE-THROUGH CONTROL SOLUTIONS FOR ENHANCING SYSTEM PROTECTION AND DYNAMICS VIA GRID-FORMING CONVERTERS

CHEN XINQUAN

PhD

The Hong Kong Polytechnic University

2025

The Hong Kong Polytechnic University

Department of Electrical and Electronic Engineering

Transient and Fault-Ride-Through Control Solutions for Enhancing System Protection and Dynamics via Grid-Forming Converters

CHEN Xinquan

A thesis submitted in partial fulfilment of the requirements for the degree of Doctor of Philosophy

February 2025

CERTIFICATE OF ORIGINALITY

I hereby declare that this thesis is my own work and that, to the best of my knowledge and belief, it reproduces no material previously published or written, nor material that has been accepted for the award of any other degree or diploma, except where due acknowledgement has been made in the text.

_____ (Signed)

___CHEN Xinquan_____ (Name of student)

Abstract

With the increasingly ambitious objectives of reaching carbon neutrality, a substantial amount of renewable energy sources, such as wind and solar, are connected to the power system. These resources are typically connected to the grid through power-electronic inverters; hence collectively known as Inverter-Based Resources (IBRs). As an advanced IBR control approach, grid-forming (GFM) converter technology has gained significant attention in recent years, and it is expected to play an important role in future power systems. Being a voltage-source converter (VSC), the behavior of a GFM-IBR is mainly controlled by its embedded controller, which typically includes outer-loop and inner-loop control blocks and current limiters. Therefore, it is critical to investigate how the integration of GFM and its various control strategies affect the operation of the power system.

During unbalanced grid conditions, GFM controls alter the magnitude and angle of the negative sequence current contributed by IBRs, differing from grid-following (GFL) controls and synchronous generators. This behavior may violate fault ride-through (FRT) requirements and cause maloperation of certain protection elements. First, this thesis clarifies the fundamentals and impacting factors of GFM inverters in the negative sequence system using dynamic and static analytical models. From the perspective of system dynamics, a decoupled-sequence dynamic model for GFM-IBR is proposed to study the internal oscillatory modes in negative sequence systems, providing crucial insights into the behavior of 2ω negative-sequence components within the GFM BPSC system under unbalanced perturbations. For the perspective of steady-state fault conditions, the equivalent negative-sequence impedance of GFM-IBR is estimated, considering balanced positive sequence control (BPSC) and positive and negative sequence control (PNSC) strategies. Comparative studies using the IEEE PSRC D29 system reveal that the magnitude and angle of negative sequence impedance are primarily determined by the inner voltage control parameters under the GFM BPSC strategy. Hence, the GFM inverter may provide sufficient negative sequence reactive current injection. When the inverter's current capacity is insufficient due to fault proximity, IBRs should rely on PNSC strategies to regulate the negative sequence system response appropriately.

GFM control behavior during unbalanced grid faults can impact system stability and protection. Per IEEE 2800 standard, IBR should be capable of FRT capability. There is a need for the regulation of positive and negative sequence currents to comply with recent grid codes when unbalanced faults occur. For full converter-based GFM-IBRs, a PNSC structure for GFM-IBRs is proposed to regulate sequence components independently, with flexibility in utilizing different power synchronization loops and current limiters. To prevent overcurrent, an enhanced current saturation-based (CS-based) current limiting method (CLM) is developed for IEEE 2800 compliance, including reactive current injection and full utilization of current capacity during unbalanced faults. Another solution is the virtual impedance-based (VI-based) CLM, which updates the positive sequence internal voltage vectors to retain inner voltage dynamics. To improve the grid synchronization and voltage support capability, this thesis proposes a three-mode switching GFM control solution for Type-IV wind turbine generators (WTGs). Once the FRT start-up triggers, WTGs operate in the restricted mode. A sequence-domain $\alpha\beta$ voltage synchronization loop (VSL) is activated to enhance frequency stability and maintain synchronism, while the CS-based

CLM is used to inject optimal reactive currents for low-voltage ride-through. After fault clearance, the VI-based CLM is employed to eliminate transient components for WTG restoration in the transition mode. For doubly fed induction generator-based (DFIG-based) WTGs, this thesis proposes asymmetrical FRT controls for the GFM-DFIG based on the mechanism for forming the grid voltage. Firstly, internal voltage vectors are designed for the assessment of asymmetrical FRT capabilities. Then a PNSC is proposed to support the sequence components of internal voltage vectors for the GFM-DFIG. On this basis, an asymmetrical FRT control structure is proposed, incorporating negative-sequence reactive current injection and two types of positive-sequence control schemes: the current saturation-based method and the virtual impedance-based method. Additionally, a simplified calculation method for transient voltages is utilized to eliminate the impacts of transient flux leakage. All the proposed FRT control solutions are validated by using the EPRI benchmark system.

To facilitate rapid and accurate short-circuit fault analysis of the system with IBR, a comprehensive and efficient solver incorporating phasor domain short-circuit models of GFM- and GFL-IBRs is proposed for steady-state fault calculations considering various CLMs. The proposed approach is validated by comparing it with detailed EMT modeling and simulations using a modified IEEE 39 bus system with multi-IBRs. The proposed solver platform enables system operators to perform rapid and accurate short-circuit computations and protective relay studies in power systems with high penetration of IBRs, facilitating the assessment of FRT strategies and compliance with grid codes.

To evaluate the performance of AC protective relays in a system with GFM-IBRs, the impacts of GFM-IBR on the apparent impedance measured by distance relays are elaborated analytically during unbalanced faults in a two-bus system. The analysis provides the first explanation for why GFM-IBR may alter the trajectory of the apparent impedance, potentially causing maloperation of distance protection. EMT simulations using the EPRI benchmark system are conducted to validate the analytical findings and provide in-depth investigations. In a modified IEEE PSRC D29 system with IBRs, the performance of distance protection is investigated under varying impact factors, including K factors, fault proximity, and fault resistance. In addition, the performance of the negative sequence components-based protective relays, i.e., the instantaneous negative sequence overcurrent (50Q), directional negative sequence overcurrent (67Q), and fault-identification (FID) elements, are tested in a modified IEEE PSRC D29 system with IBRs with various FRT solutions, to identify potential maloperation issues.

The conclusions of the thesis shed light on the merits and drawbacks of GFM-IBRs under unbalanced grid conditions. The suggestions and prospects for future IBR accommodation are inspired.

List of Publications

[1] **Xinquan Chen**, Siqi Bu, Ilhan Kocar, Grid-Forming IBRs under Unbalanced Grid Conditions: Challenges, Solutions, and Prospects, *in IEEE Transactions on Sustainable Energy*, doi: 10.1109/TSTE.2025.3577568. (Early access, 2025)

[2] **Xinquan Chen**, Aboutaleb Haddadi, Evangelos Farantatos, Ilhan Kocar, Siqi Bu, Power Swing in Systems with Varying Penetration of Grid-Forming IBRs: Protection and Dynamics, *Protection and Control of Modern Power System*, vol. 10, no. 4, pp. 116-129, July 2025, doi: 10.23919/PCMP.2024.000355.

[3] **Xinquan Chen**, Tao Xue, Ilhan Kocar, Siqi Bu, Maxime Berger, Sustained Oscillations of Grid-forming lBRs under Unbalanced Perturbation: Modal Analysis and EMT Studies, *Electric Power Systems Research*. (Accepted, 2025)

[4] **Xinquan Chen**, Ilhan Kocar, Siqi Bu, Evangelos Farantatos, Aboutaleb Haddadi, "Comparative Analysis of Negative Sequence Behavior in Grid-Following and Grid-Forming Inverters: Modeling, Control, and Protection," *IEEE Transactions on Power Delivery*, vol. 40, no. 3, pp. 1730-1742, June 2025, doi: 10.1109/TPWRD.2025.3559001

[5] **Xinquan Chen**, Aboutaleb Haddadi, Zhe Yang, Evangelos Farantatos, Ilhan Kocar, "Efficient, Robust, and Comprehensive Fault Calculation of IBR-Rich Systems Considering Diverse Controls," *IEEE Open Access Journal of Power and Energy*, vol. 12, pp. 378-390, 2025, doi: 10.1109/OAJPE.2025.3572769.

[6] **Xinquan Chen**, Yuanzhu Chang, Ilhan Kocar, Grid-Forming Control of DFIG-based Wind Turbine Generator by Using Internal Voltage Vectors for Asymmetrical Fault Ride-Through, *IEEE Transactions on Energy Conversion*, doi: 10.1109/TEC.2024.3470588. (Early access, 2024)

[7] Aboutaleb Haddadi, **Xinquan Chen**, Evangelos Farantatos, Ilhan Kocar, "A Robust Solver for Phasor-Domain Short-Circuit Analysis with Inverter-Based Resources," in *IEEE Transactions on Power Delivery*, doi: 10.1109/TPWRD.2025.3573231. (Early access, 2025)

[8] **Xinquan Chen**, Siqi Bu, Aboutaleb Haddadi, Ilhan Kocar, "Performance of distance protection under inverter-based resources with IEEE 2800 current injection requirements," *18th International Conference on Developments in Power System Protection (DPSP APAC 2025)*, Hong Kong, China, 2025, pp. 577-582, doi: 10.1049/icp.2025.0585.

[9] **Xinquan Chen**, Tao Xue, Ilhan Kocar, "Impacts of Grid-Forming Converters on Distance Protection During Unbalanced Faults," *2024 8th International Conference on Power Energy Systems and Applications (ICoPESA)*, Hong Kong, 2024, pp. 281-287, doi: 10.1109/ICOPESA61191.2024.10743721.

[10] **Xinquan Chen**, Ilhan Kocar, Aboutaleb Haddadi, Evangelos Farantatos, Comparative Analysis of Virtual Impedance and Current Saturation Methods for IBR Fault Current Limiting Against IEEE 2800 Requirements, *CIGRE 2025 International Symposium*, Montreal, 2025. (Accepted, 2025)

Acknowledgments

I would like to express my heartfelt gratitude to my chief supervisor, Dr. Siqi Bu, and my co-supervisor, Prof. Ilhan Kocar, for their unwavering support, trust, and invaluable guidance throughout my research and Ph.D. studies. Their knowledge and approachable nature have always inspired me during our meetings. Dr. Siqi Bu has been particularly supportive, enabling me to continue my studies. I feel incredibly fortunate and honored to be a Ph.D. student in the EEE department at HK PolyU. I am also deeply appreciative of being awarded the PolyU Presidential PhD Fellowship Scheme (PPPFS). This fellowship is invaluable to me as it alleviates my financial burden, allowing me to fully dedicate myself to my research, coursework, and other meaningful pursuits.

I am also very grateful to my co-supervisor, Prof. Ilhan Kocar, a renowned researcher worldwide and a full professor at Polytechnique Montreal. His groundbreaking contributions to professional simulation tools and the development of industrial-grade solutions for the large-scale integration of inverter-based resources (IBRs) into electric grids are truly remarkable. Without his guidance and patience, I would not have been able to quickly grasp grid-forming IBRs and electromagnetic transient modeling at the start of my Ph.D. studies. I would also like to extend my special and sincere thanks to Dr. Yuanzhu Chang for his invaluable guidance and patience in my research. He has always been generous with his help, providing me with professional feedback and constructive advice on finding research directions and writing academic papers. He has kindly guided me in using PowerFactory and understanding the control design of wind turbines.

During my Ph.D. studies, I received tremendous support from experts at the Electric Power Research Institute (EPRI), Dr. Evangelos Farantatos and Dr. Aboutaleb Haddadi, who guided me in studying fault current limiting methods and power swing studies. I am also deeply grateful for the generous help and support from many individuals at HK PolyU. Special thanks go to Dr. Zhe Yang, Dr. Tao Xue, and Mr. Yang Zhu for their invaluable assistance with short circuit calculations, protective relays, and power system dynamics. Additionally, I am very thankful to all the staff and technicians in the department for their support, which has been instrumental in my pursuit of a Ph.D. degree. I truly appreciate the valuable feedback from my paper reviewers and thesis examiners, which has significantly improved my research.

Finally, I would like to express my deepest and most heartfelt gratitude to my family for their unwavering support, love, and encouragement during the challenging times in both my life and studies. Their constant spiritual support has been a cornerstone throughout my research journey.

Table of Contents

1 Introduction

1.1 Research Background

To reach the increasingly ambitious objective of carbon neutrality, there is a global rise in the proportion of renewable energy sources (RESs), such as wind and solar, in the generation fleet of power grids [1], as depicted in Fig. 1.1 [2]. These resources are typically connected to the grid through power-electronic inverters; hence collectively known as Inverter-Based Resources (IBRs) [3], such as wind turbine generators (WTGs), photovoltaic (PV) inverters, and battery energy storage systems (BESSs).

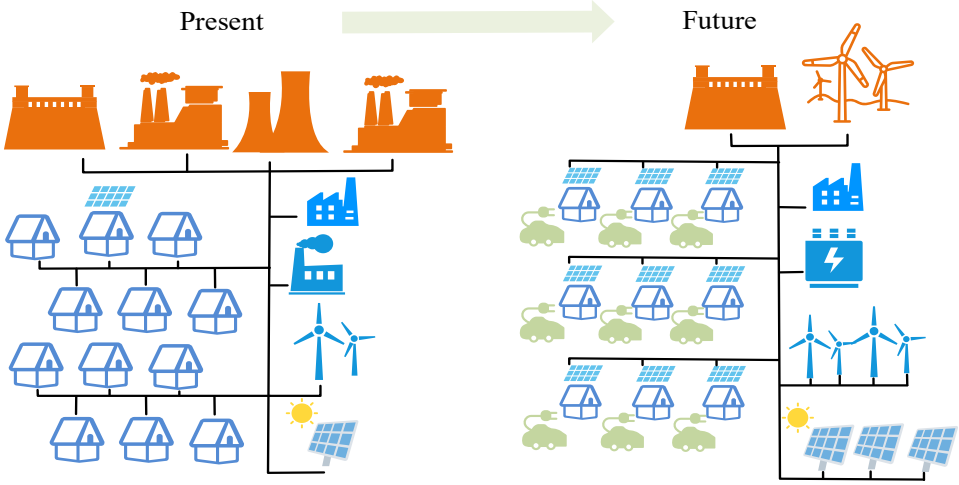

Fig. 1.1 Comparison between present and future power grids [2]

From the perspective of control nature, the control schemes employed by IBRs can be broadly categorized into two types: grid-following (GFL) controls and grid-forming (GFM) controls [4], [5]. GFL controls rely on the phasor-lock loop (PLL) to latch onto and follow the grid voltage and frequency and inject active and reactive power at the inverter terminals. Consequently, they are limited in supporting system restoration. To accommodate larger shares of renewables and enhance the stability of IBR-rich power systems, GFM controls are developed to emulate the characteristics of synchronous generators (SGs) [6], thus autonomously establishing frequency and maintaining a constant or near-constant internal voltage phasor in the sub-transient to transient time frame [7], [2]. This makes them ideal for providing black-start capability and facilitating system restoration following a blackout [8]. As a result, In the future IBR-dominated power system, a significant number of IBRs will transfer from the GFL type to the GFM type, promoting the capabilities and performances of IBRs, including forming system voltage, supporting system frequency [9], and improving stability [10].

For a clear understanding, typical topologies of GFM control-based IBR (GFM-IBR) units are shown in Fig. 1.2 [11]. The full-scale converter-based IBRs, e.g., Type-IV WTGs, employ full-scale converters (FSCs) for energy conversion, with a GFM control used in the grid-side converter (GSC). The doubly fed induction generator-based WTG (DFIG-based WTG), also known as Type-III WTG, facilitates the use of a generator at varying speeds and requires a smaller power converter relative to full converter-based IBRs. The GFM control is applied to the rotor-side converter (RSC). The embedded GFM controller typically includes the inner controllers, power synchronization loop (PSL), reactive

power droop (Q-droop) control, and current limiting method (CLM), as illustrated in Fig. 1.3. The prevalent primary control strategies include droop control, virtual synchronous machine (VSM) control, and dispatchable virtual oscillator control (dVOC) [12].

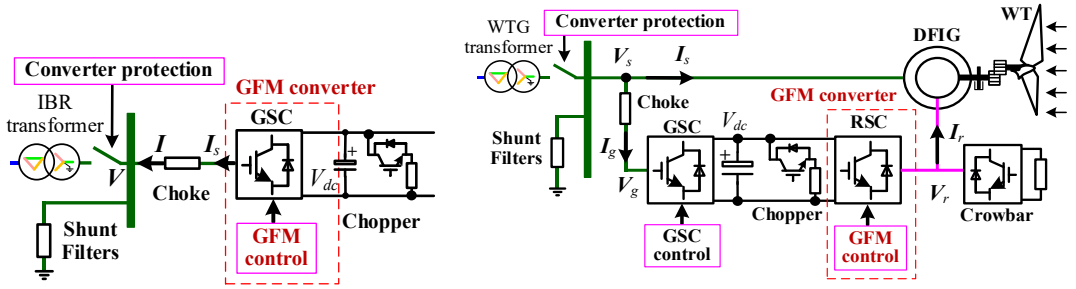

(a) Full converter-based IBR (b) Type-III WTGs

Fig. 1.2 Topology of GFM-IBR unit

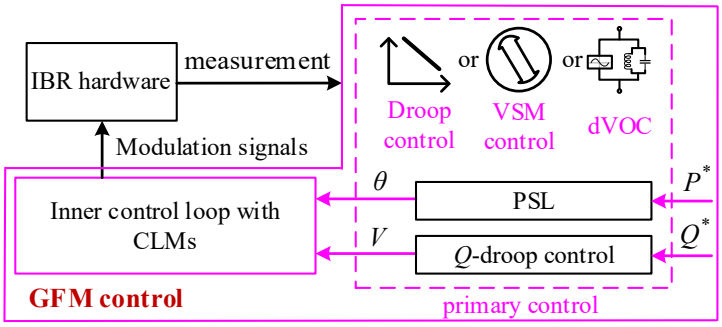

Fig. 1.3 Closed-loop structure for IBR with its embedded GFM controller

Although GFM-IBR can imitate the behavior of SGs, they may not retain GFM operation during faults due to the limited current capacity. Regarding this, IEEE 2800 standard indicates that there are two operation modes for GFM controls [13]:

- Actual GFM mode (when energy capacity is sufficient).
- Restricted mode (when the current limit is reached).

In normal operation, GFM-IBR can operate in the actual GFM mode. Upon reaching the current limit, the current limiting method is triggered to safeguard the converters against overcurrent. Consequently, the operation of GFM-IBR transitions to a restricted mode. When operating in this mode, the inner voltage control may be out of service since current references are regulated through a CLM instead of inner voltage control. Consequently, this can result in the inability to keep terminal voltages stable.

Owing to the dispersed nature of RESs, large-scale IBRs are usually situated in remote locations. Unbalanced grid faults occur frequently on the transmission line. During unbalanced grid conditions, the current and voltage of each phase are inconsistent in magnitude and phase angle, generating positive sequence components ($\boldsymbol{X}^{+}$) and negative sequence components ($\boldsymbol{X}^{-}$), as illustrated in Fig. 1.4 [14]. Specific controllers and protective relays can further process these components to maintain system stable operation. On the shortest sub-transient timescales (i.e., 0–5 cycles) after a fault, GFM-IBRs aim at maintaining a desired voltage magnitude and phase angle and prioritizing the support of voltage magnitude and frequency at its terminals, producing sequence components that differ from those of GFL control-based IBRs (GFL-IBRs). To be replaced with SGs in future power systems, GFM-IBRs should

also be designed to ideally reproduce the negative-sequence behavior of SGs under unbalanced gird conditions [5], e.g., by providing a path for the flow of negative sequence current (I2). Based on existing studies, the negative-sequence behavior of GFM-IBRs has not been sufficiently discussed. It is critical to investigate how the integration of GFM-IBR and its various control strategies affect the operation of the power system under unbalanced grid conditions.

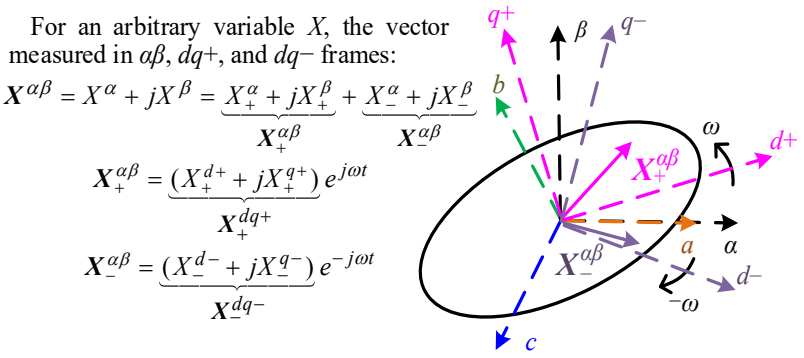

Fig. 1.4 Sequence components in $\alpha\beta$, $dq+$, and $dq-$ frames

The thesis focuses on the potential impacts of GFM-IBR on system dynamics, legacy protection, and FRT requirements under unbalanced grid conditions. Generic control structures for full converter-based GFM-IBR and GFM-DFIG are proposed to adapt to unbalanced grid conditions. Analysis and EMT simulation studies shed light on the merits and drawbacks of proposed FRT solutions under unbalanced grid conditions from perspectives of protection and dynamics. The prospects and new research ideas for future IBR accommodation are inspired.

1.2 Literature Review

1.2.1 System Dynamics

1.2.1.1 Small-signal stability

Fig. 1.5 shows the typical balanced positive sequence control (BPSC) scheme, also referred to as coupled-sequence control (CSC), of GFM-IBR in normal operation.

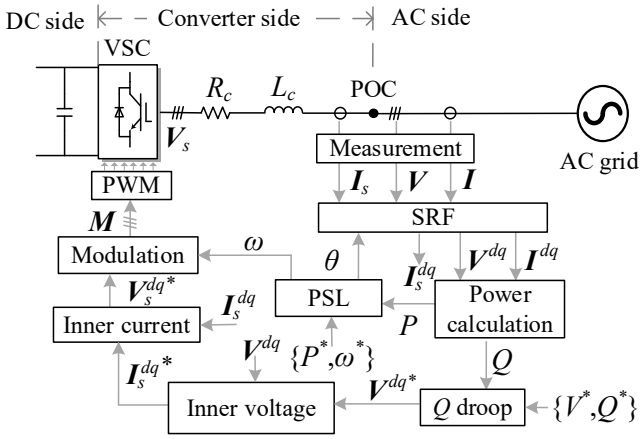

Fig. 1.5 BPSC structure of GFM-IBR

The notation is as follows: Superscript * denotes reference values, $\{\boldsymbol{V}_s, \boldsymbol{I}_s\}$: inverter terminal

voltages and currents, $\{\boldsymbol{V}, \boldsymbol{I}\}$: AC side voltages at the point of connection (POC) and currents, $\{\theta, \omega\}$: orientation angle and angular frequency. $\boldsymbol{M}$: modulation signals. $\{R_c, L_c\}$: choke resistance and inductance. In normal operation (actual GFM mode), IBR operates within its current and power limits and the criteria for FRT activation are not met. Therefore, CLM and additional FRT controls are not depicted in Fig. 1.5.

It's evident that GFM-IBR employs distinctive controllers compared to SG and GFL-IBR, challenging system dynamics. Significant research has been devoted to the small-signal stability analysis of GFM-IBR based on the assumption of balanced grid conditions, as summarized in Table 1-1 (Balanced perturbation). Nevertheless, in practical engineering, a small signal of imbalance often appears and deteriorates the stability of the power system. In the negative-sequence system, the conventional GFL controls can be equivalent to an open circuit [31]. However, since GFM controls incorporate additional PSLs, voltage reference generation, and inner voltage control compared to GFL controls, the dynamics of its negative-sequence behavior are distinctive and cannot be ignored simply [32]. There is a knowledge gap regarding the impacts of the negative-sequence behavior of GFM-IBRs on small-signal stability and dynamic performance under unbalanced small-signal disturbance.

Most existing dynamic modeling of GFM-IBRs for stability analysis solely considers the positive-sequence components. Under unbalanced small-signal disturbance, both positive-sequence and negative-sequence components will appear in the GFM controls, thus affecting the dynamics and stability of power systems. Therefore, these dynamic models may hinder stability issues caused by negative-sequence components under unbalanced small-signal disturbance. Some researchers are gradually working on decoupled-sequence modeling for GFM-IBRs [33]−[34]. Nevertheless, the typical GFM control structure is based on the synchronous reference frame (SRF) and only incorporates a single BPSC loop for *dq* components. These studies are specific to the proposed positive and negative sequence control (PNSC) schemes and do not address the negative-sequence mechanism and dynamic modeling of the typical BPSC for GFM-IBRs under unbalanced small-signal disturbance. The multiple-harmonic dynamic phasor model [35] exhibits considerable complexity due to the presence of multiple harmonic components, while the negative sequence components are not given primary emphasis. Furthermore, the impacts of negative sequence components from GFM-IBRs on system dynamics remain largely unexplored.

TABLE 1-1

Overview of Dynamic Analysis on GFM-IBR

Category		Contribution
Balanced perturbation	System level	Interaction of GFL- and GFM-IBR [15], [16]
		Comparison of GFL and GFM-based wind farms [17]
		Optimal placement of GFM-IBR [18]
		System stability with SGs and GFL- and GFM- IBR [19]
	Inverter control level	Advanced virtual-impedance controls [20], [21]
		Adaptive hybrid control [22]
		Power dynamic decoupling control [23]
		DC-link dynamic regulation [24]

		Inner control loops [26], [27]
		Control damping [28]
		Single-input single-out (SISO) stability [29]
		Adaptive droop mechanism [30]
Unbalanced perturbation	System level	Decoupled sequence *dq0* modeling based on the delayed signal cancellation method [34]
	Inverter control level	Sequence-decomposed modeling based on virtual admittance controls to study the impacts of sequence decomposition methods on stability [33]
		Multiple-harmonic dynamic phasor model to investigate the effects of DC offsets, second-harmonic content, six-step switching harmonics, and unbalance [35]

1.2.1.2 Transient stability

Replacing SGs with IBRs reduces rotational kinetic energy in the power system, leading to lower system inertia and adversely impacting the frequency stability [19], [36]. To provide inertia and improve frequency stability, PSLs assist GFM-IBRs in emulating the droop mechanism and swing feature of SGs. Unlike the previous GFL-IBRs that rely on a PLL and inject current into power grids, GFM-IBRs regulate orientation angle and internal voltage via the error between measurements and references of power.

Due to the rising short-circuit current and a breakdown in voltage regulation during symmetrical and asymmetrical short-circuit faults, GFM-IBR will switch from the actual GFM mode to the restricted mode. When the power reference cannot be achieved under large-signal disturbance, the GFM synchronization tends to be lost [37]. This may lead to transient instability issues stemming from the absence of a stable steady state or insufficient damping [38], as shown in Fig. 1.6.

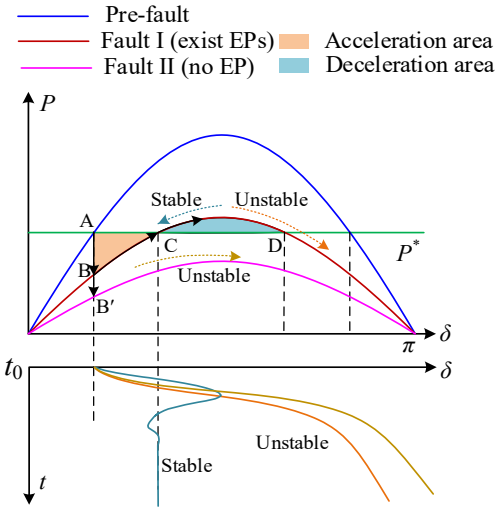

Fig. 1.6 *P*-*δ* curve of GFM-IBR under large-signal disturbance

When the power-angle (*P*-*δ*) curve of GFM-IBR is higher than the power reference P^* (Fault I), the stable and unstable equilibrium points, i.e., C and D, exist along with the deceleration area. The GFM operation can be retained unless the operation point crossover the D. However, when the *P*-*δ* curve is

lower than the P^* (Fault II), there are no EPs and deceleration area, so the GFM-IBR will lose the synchronism. The outcome is an oscillatory fault response, i.e., substantial variations in both voltages, currents, and power. In addition, phase angle jump is also present, challenging the existing synchronization loops [39].

To enhance the transient stability during faults, there are various improved grid synchronization techniques for GFM-IBRs [43]−[54], as summarized in Table 1-2. Researchers expect IBR to retain the GFM operation even under the current limiting mode [40]. When considering the power-electronic or microgrid scale, sustaining GFM operation is advantageous. However, at the broader power-system scale, retaining GFM operation may not be the optimal solution due to numerous constraints, such as compliance with grid codes or the fault's proximity. Depending on the severity of the fault, GFM-IBRs may still need to switch to GFL mode [41], [42]. In addition, most advanced techniques are developed based on balanced grid conditions. Hence, enhanced grid synchronization solutions to decompose positive and negative sequence components are still needed.

Switching from PSL to PLL is an effective option since the PLL can obtain the orientation angle from grid voltages, thus keeping the grid synchronization [52], [53]. However, the frequency response may oscillate over a long settling time under the conventional PLL. This may provoke instability issues when GFM-IBR is connected to weak grids [54]. To address this, robust multivariable PLLs are developed [55], [34]. The dynamic performance is improved but their parameter design is complicated. A simple and robust synchronization solution is needed for the restricted mode of GFM controls. Furthermore, most of the existing studies simplify the DC-side of GFM-IBR into a constant DC voltage source. This simplification neglects the DC-side dynamics and the couplings between the DC- and AC-sides, which might not reflect the accurate dynamics in synchronization [56], [57].

TABLE 1-2

Overview of Transient Stability Enhancement Techniques of GFM-IBR

Category	Contribution
Enhanced PSL	Hybrid synchronization control combining PLL and PSL to improve robustness against the weakening grid strength [43], [44]
	GFM vector current control [45]
	Power angle limiter [46], [47]
	Power freezer [48], [49]
	Adaptive power reference [50]
	Current synchronization control [51]
Switching from PSL to PLL	Generic PLL-based GFM control [52]
	Dual-mode/Two-stage switching control [53], [54]

1.2.2 Legacy System Protection

1.2.2.1 Negative sequence components-based protection element

Designing inverter controls to mimic SGs can ensure sufficient FRT capacities and eliminate the maloperation of negative sequence components-based protection elements [58], such as the instantaneous

negative sequence overcurrent (50Q), directional negative sequence overcurrent (67Q), and fault-identification (FID) elements. In [59], a GFL inverter with PNSC injects negative sequence reactive current (I2R) during unbalanced faults using the decoupled double SRF (DDSRF) [60]. However, the absence of a PLL in GFM controls may lead to non-zero q-axis voltage when the current limit is reached, which should be considered in reactive current injection schemes for GFM-IBR. Moreover, GFM control regulates voltage rather than current injection, with current references determined by inner voltage control when the current limit is not reached. The negative sequence behavior of the inverter is highly dependent on the control strategy [32], but the impact of inner voltage control on negative sequence components is not investigated. Consequently, GFM-IBR would generate fault current signatures different from SGs [61] potentially impacting negative sequence system [62], and causing maloperation of negative sequence components-based protection elements like GFL-IBR [63]−[66].

1.2.2.2 Distance protection

Distance protection forms the core of the protection system for transmission lines [67], [68]. The distance relay calculates the apparent impedance using locally measured current and voltage. This impedance is evenly distributed along the length of a transmission line. As a result, the distance relay can effectively differentiate fault zones by analyzing the apparent impedance during a fault. However, existing studies have found that GFM controls exhibit exclusive short-circuit fault characteristics [69], [70]. This potentially adversely affects the correct operation of the distance protection designed for SG-dominated systems. The impacts of GFL-IBR on various distance protection elements have also been explored [71]−[75], and various solutions [76]−[79] are proposed to enhance the correct operation. However, the impacts of GFM-IBR on distance protection remain largely unexplored [80]−[82] and lack in-depth analysis. From the overview in Table 1-3, there is a need to understand how integrating GFM-IBRs will affect the performance of conventional distance protection.

TABLE 1-3
Overview of Studies on IBR and Distance Protection

Category	Contribution
GFL-IBR	Impacts on the phase comparators [71]
	Impacts on the reactance method [72]
	Impacts on power swing function [73]
	Impacts on memory-polarized protection elements [74]
	Impacts on phase comparison line protection [75]
	Improved distance protection schemes [76], [77]
	Fault-coordinated control solutions [78], [79]
GFM-IBR	Tripping results of distance protection in a two-bus system with GFM-IBR using VI-based and CS-based CLMs [80], [81]
	Impacts on power swing function [82]

1.2.3 Fault Ride-Through Requirement Compliance

The IEEE 2800 standard provides minimum technical interconnection requirements for IBRs. As

transmission system operators and owners develop their IBR interconnection requirements and consider the adoption of IEEE 2800, it is essential to understand the implications of those requirements on the bulk power system to ensure reliable integration of IBRs.

To fulfill the grid code requirements regarding voltage support, IBRs need to be equipped with an FRT strategy. The FRT strategy is activated when the voltage deviation from operating conditions or nominal voltage exceeds the predefined value and deactivated when the voltage deviation reduces below the predefined value after a prespecified release time. During unbalanced faults, GFL-IBR is regarded as a controlled current source that injects a certain amount of positive and negative sequence reactive currents. However, GFM-IBR behaves as a voltage source in actual GFM mode. In the restricted mode, GFM-IBR is closer to current sources like conventional GFL-IBR [32], [41]. These features indicate that the equivalent impedance and control dynamics of GFM-IBRs differ from those of SGs and GFL-IBR. Per IEEE 2800, reactive current injection, AC voltage ride-through, and frequency ride-through are required for FRT. In addition, from the perspective of system reliability, the transition from one mode to another should be carefully designed [13].

1.2.3.1 Current Injection Requirement

Per IEEE 2800, an IBR plant shall be able to inject and absorb a minimum reactive power defined by $|Q_{min}| \geq 0.3287 \times$ IBR Continues Rating at the point of measurement (POM) when injecting active power into the grid under fault steady state conditions. Hence, GFM-IBRs should provide enough reactive power specified by IEEE 2800 in addition to supplying the reactive power consumption of the IBR transformer. Clause 7.2.2 of IEEE 2800 has specified the performance required of an IBR during FRT. The clause requires an IBR to inject positive sequence reactive current (I1R) and I2R during unbalanced faults. The incremental I1R shall not be reduced below incremental I2R. If the maximum current limit is reached, either I1R, or I2R, or both may be reduced with a preference of equal reduction in both currents. Moreover, the converter current capacity shall be fully utilized, and the I2 shall lead the negative sequence voltage (V2) at the POC by 90-100˚ for full converter-based IBRs and 90-150˚ for Type-III WTGs.

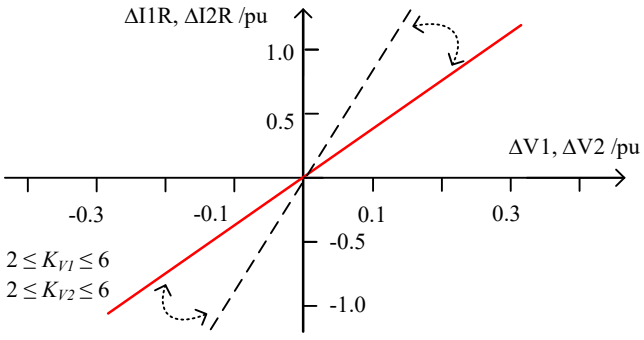

Fig. 1.7 K-factor–based proportional control in German VDE-A R-N 4120

When the FRT function is active, the IBR injects a positive sequence reactive current proportional to the deviation in voltage. In VDE-A R-N 4120 Technical Connection Rules [83], there is a typical K-factor-based proportional control, as shown in Fig. 1.7. The I1R is proportional to the voltage change in the positive sequence system by a factor abbreviated with K_{V1}. The I2R is proportional to the voltage change in the negative sequence system by a factor abbreviated with K_{V2}. These gains are adjustable but

may require additional converter capacity after a certain point. The implementation of the K-factor-based proportional control requires the use of a PNSC scheme.

Moreover, during balanced and unbalanced faults, IEEE 2800 requires a step response time of less than 2.5 cycles and a settling time of less than 4 cycles for the current contribution of full converter-based IBR units. For Type-III WTG, defining response time is not necessary since the response time is also affected by the machine parameters. The settling time should be within 6 cycles.

1.2.3.2 Voltage Ride-Through Requirement

IEEE 2800 standard requires an IBR to have voltage ride-through (VRT) capability during balanced and unbalanced faults. IBR shall not trip when its applicable voltage with the lowest magnitude is within the mandatory operation region and the applicable voltage with the greatest magnitude is within the mandatory operation region. Fig. 1.8 shows the low/high VRT curves used in different grid codes [84]−[86].

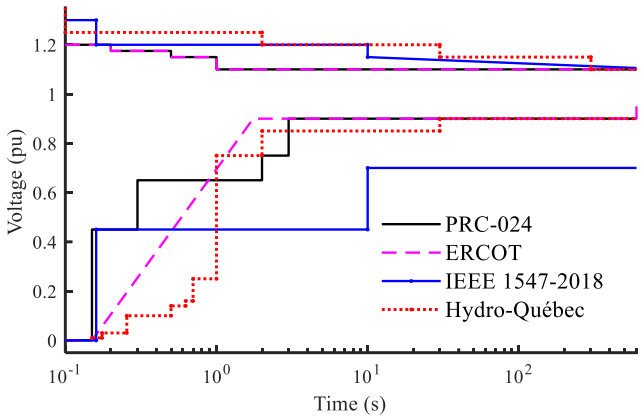

Fig. 1.8 VRT curves in different grid codes

The existing VRT technologies are typically based on GFL-IBRs. The outer-loop control of GFM-IBR generates an internal voltage different from that of GFL-IBR. The AC voltage support of GFM-IBR during faults may diverge under GFL standards, and there is a need for a detailed investigation of the VRT requirements of GFM-IBR under unbalanced faults. The integration of GFM-IBR will alter the unbalanced fault response of the power system, which might lead to the maloperation of system protection designed based on the hypothesis that GFM-IBRs can be modeled with equivalent SGs or GFL-IBRs.

1.2.3.3 Frequency Ride-Through Requirement

Under a large disturbance, an IBR plant shall be designed to provide the frequency ride-through capability. When the applicable frequency is within the required continuous operation region, as defined, the IBR plant shall exchange active and reactive power with the transmission system within its IBR Continues Rating and within the volts per hertz capability limits of IBR units, supplemental IBR devices, and transformers. In addition, IBRs need to provide active power-frequency response requirements of primary frequency response (PFR) and/or fast frequency response (FFR) as applicable. Fig. 1.9 shows frequency ride-through curves in different grid codes [85], [86]. As mentioned above, various synchronization techniques have been proposed to improve the frequency regulation of GFM-IBR. However, existing studies pay more attention to the stability perspective and lack the investigation of

active-power frequency response and frequency ride-through compliance of GFM-IBR under FRT mode.

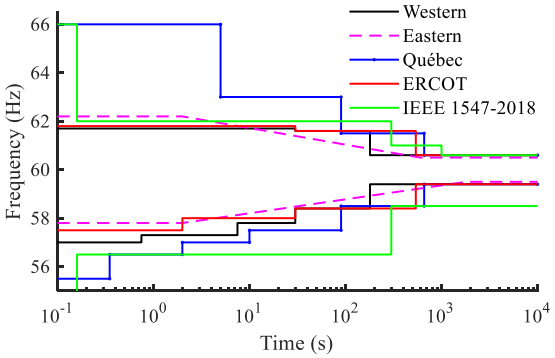

Fig. 1.9 Frequency ride-through curves in different grid codes

1.2.4 Control Solutions for Grid-Forming IBR

To better accommodate unbalanced grid conditions and fully achieve asymmetrical FRT requirements, the PNSC, also refers to decoupled-sequence control (DSC), is regarded as an effective control solution for IBRs. Compared to the BPSC of GFM-IBR, the PNSC of GFM-IBR incorporates the sequence decomposition method, CLM, supplementary negative sequence control, and current coordination. Virtual impedance-based (VI-based) or current saturation-based (CS-based) CLMs are employed to prevent overcurrent due to inverter capacity constraints. Relevant solutions are presented in this section.

1.2.4.1 Sequence Component Decomposition Method in Grid-Forming Control

To regulate positive- and negative-sequence components independently under unbalanced grid conditions, a number of sequence decomposition methods are reported in both GFL and GFM applications [60], [87]−[90], including filter-based methods or delayed-signal-based methods, where

- Delayed-signal-based methods provide quicker transient responses; however, they experience steady-state oscillations when exposed to deviations in the fundamental frequency if implemented at a fixed sampling rate.

- Filter-based methods exhibit slower convergence; however, they are devoid of steady-state errors, even when operating at fixed sampling rates [91].

For GFL- and GFM-IBRs, the DDSRF with low-pass filters is considered the representative sequence decomposition method, effectively used in industrial designs.

1.2.4.2 Current-Limiting Methods for Grid-Forming IBRs

To prevent overcurrent, achieve the current injection requirements, and enhance VRT capability, designing CLMs is a major focus for meeting FRT requirements as it primarily alters the current injection. However, most studies on CLMs in GFM control have focused on balanced grid conditions [8], [9]. Solutions for limiting sequence currents to achieve FRT for GFM-IBRs are limited and they prioritize innovations at the power-electronics level that might overlook the constraints imposed by the power system. State-of-the-art CLMs include virtual impedance-based (VI-based) and current saturation-based (CS-based) CLMs [40], [92]. To meet the IEEE 2800 standard, IBRs are expected to achieve the maximum reactive current injection within their capacity to support AC voltages under the FRT mode. After fault clearance, the restricted mode can be switched to the actual GFM mode. This may introduce

overcurrent issues during the transition due to the power variation [93]−[95]. However, there is no clear scheme specified for the post-fault behavior of GFM-IBR that improves fault recovery capability. There is still room for the improvement of CLMs for GFM-IBRs so that they are compatible with the grid codes on FRT requirements and applicable to a wide range of GFM control strategies.

The CS-based CLM can be applied to both GFL-IBR and GFM-IBR, enabling IBRs to behave like a current source during faults. Typical CS-based CLMs include instantaneous limiter, magnitude limiter, and priority-based limiter [92], [96], [97]. The current limiter is inserted prior to the inner current control to limit the fault current. The magnitude and phase angle of current references can be adjusted to improve the VRT capability [97]. However, once the current limit is reached while power references remain unchanged, the PSL will lose synchronism [99], [100]. The CS-based method can restrain the current within a few milliseconds at the inception of the fault [100]. Therefore, the CS-based method can be employed to avoid the impacts of transients on protective relays during faults.

The VI-based CLM is proposed for GFM-IBR, enabling GFM-IBR to retain internal voltage dynamics and keep the voltage source feature under FRT mode. The VI-based CLM limits the fault current by reducing the voltage reference, without modifying the current reference directly. For the VI-based method, the current references are restrained by adjusting the virtual impedance adaptively. It can keep the dynamics of inner voltage control but needs a tradeoff between stability and current limiting during faults [97]. Since this method relies on the PI controller to regulate the converter current to its maximum limit, this method may be subject to prolonged transient periods in the presence of significant short-circuit currents [101]. Moreover, current references cannot be specified by using this method making it inapplicable for achieving the reactive current injection requirements in some recent grid codes. In [102] and [103], advanced techniques such as adaptive sequence current decomposition and variable VI are employed to fulfill the reactive current injection requirements, making the application more complex and difficult to reproduce. The VI-based CLM can be implemented in positive sequence control channels only [104]−[107] or both in positive and negative sequence control channels [97], [102], [103]. When the VI-based CLM is employed in the positive sequence channel only, the equivalent positive-sequence fault circuit of the GFM-IBR is a voltage source with a VI, rather than a current source (like GFL-IBR) [106], [107]. In the negative sequence circuit, the equivalent circuit is a current source [97], [102], [103].

1.2.4.3 Negative Sequence Control

To regulate the uncontrolled negative-sequence components, six types of negative sequence control solutions for GFM-IBR are proposed, including: (a) Balanced three-phase voltage (BTPV) control [34]; (b) Balanced three-phase current (BTPC) control [108]; (c) Constant active power (Constant-P) control [109]; (d) Constant reactive power (Constant-Q) control [109]; (e) Negative sequence virtual impedance (NSVI) and negative sequence voltage vector (NSVC) control [110]; (f) Negative sequence current injection (NSCI) control [14].

1.2.4.4 Current Coordination Method

In the PNSC structure, the positive and negative current references are generated separately. A current coordination method is needed to prevent overcurrent. Based on the existing methods, two types of current coordination methods are developed to optimize the inverter current capacity utilization.

1) Current scaling method: To fully utilize the current capacity, the positive and negative sequence current references can be converted to phase current references. (a) *dq* current-based method [111]; (b) *αβ* current-based method [112]; (c) Active and reactive current-based method [103].

2) Adaptive current limit method: [102] proposed a positive and negative adaptive current limit distribution method to make phase current reach the current limit.

1.2.4.5 Fault Ride-Through Control Strategies for GFM-DFIG

In addition to the above control solutions for full converter-based GFM-IBR, the application of GFM control in the DFIG-based WTGs is also attractive. Under the regulation of the PSL, the DFIG-based WTG with GFM control can provide active power to support the grid frequency, emulating the inertia and damping characteristics of SGs [113]. The *Q*-droop strategy enables GFM-DFIG to work as a voltage source to build voltage for power grids, which is more suitable for weak grids [114]. However, studies on GFM-DFIG [115]−[120] are still under exploration, as summarized in Table 1-4 (GFM-DFIG). To ride through symmetrical voltage dips, GFM-DFIG may temporarily fall back to GFL mode. Moreover, improved schemes for symmetrical FRT are proposed [121], [122]. To the best knowledge of the authors, with the above GFM control strategies, DFIG-based WTGs cannot successfully deal with overstresses and provide the desired system services specified in recent gird code requirements and GFM capability definitions. The main reason is that, during asymmetrical faults, negative-sequence and transient components will interfere with the positive-sequence components through the coupled control loop and power calculation. Compared to balanced faults, the coordination of sequence components in unbalanced fault scenarios is more challenging for DFIG-based WTGs [123]. Researchers have proposed some control schemes [14], [124]−[131] for improving the FRT capability of conventional GFL-DFIG, as summarized in Table 1-4 (GFL-DFIG).

TABLE 1-4

Overview of Studies on GFM-DFIG and GFL-DFIG

Category	Contribution
GFM-DFIG	Virtual synchronous control for inertia support [115]: - Directly regulate the magnitude and phase angle of rotor voltage without using a current control loop. - Virtual resistance to limit current and ensure small-signal stability
	Virtual synchronous generator control with an inner-loop control for air-gap flux linkage [116]
	Small-signal stability of microgrids with high-penetration of GFM-DFIG [117]
	GFM control based on the orientation of the rotor flux [118]
	GFM control based on disturbance rejection stator flux [119]
	Hybrid synchronization control to improve the dynamics and oscillation issue [120]
	Virtual resistance and feedforward compensation methods to limit the

	forced component and natural component of fault currents [121]
	Air-gap flux feedback and rotor current limiting loops to accelerate the decay of transient components and avoid overcurrent [122]
GFL-DFIG	Current coordination method for grid code compliance [14]
	FRT control to mitigate risks of insulation failure [124]
	Transient stability enhancement [125]
	Demagnetization current and reactive current injection [126]
	Control for the required I2 angle [127]
	Enhance VRT capability [128], [129]
	Eliminate oscillations in electromagnetic torque [130], [131]

In summary, the literature review on the performance of GFM-IBR under unbalanced grid conditions can be drawn in Fig. 1.10.

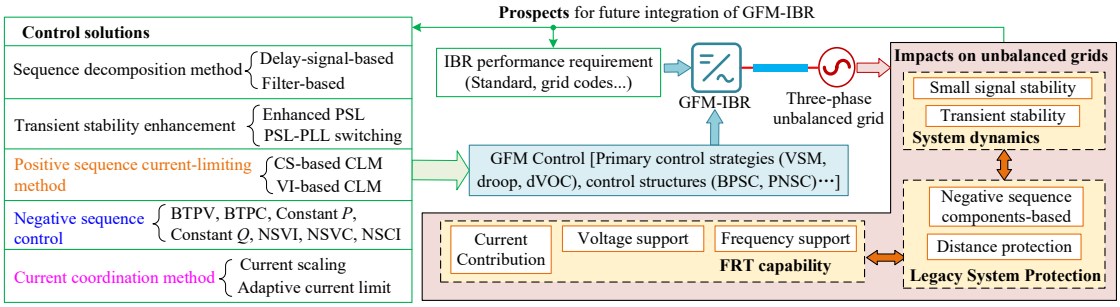

Fig. 1.10 Summary of literature review on GFM-IBR under unbalanced grid conditions

1.3 Research Gaps

Based on the above literature review, the main research gaps are drawn as follows:

1) The negative-sequence behavior of GFM-IBRs has not been sufficiently discussed. It is critical to investigate how the integration of GFM-IBRs and their various control strategies impact power system operations under unbalanced grid conditions, especially in comparison to SGs and GFL-IBRs.

2) Although the IEEE 2800 standard gives some room for new technologies such as GFM in terms of compliance, there is scope for the improvement of the existing FRT control solutions for GFM-IBRs so that they are compatible with the grid codes on FRT requirements, e.g. reactive current injection requirements, voltage ride-through requirements, and frequency ride-through requirements.

3) The computational intensity of detailed EMT models limits efficiency across multiple fault scenarios. Accurate short-circuit modeling for IBRs with various FRT strategies is crucial for future IBR-rich systems.

4) The integration of GFM-IBRs will alter the unbalanced fault response of the power system, which might lead to the maloperation of system protection. The impacts of GFM-IBRs on the performance of legacy protection are underexplored.

1.4 Contributions

To address these gaps, the thesis focuses on the potential impacts of GFM-IBRs on system dynamics, legacy protection, and FRT requirements under unbalanced grid conditions, providing innovative insights and control solutions for GFM-IBRs under unbalanced grid conditions. Key contributions of the thesis are:

(i) To clarify the fundamentals and impacting factors of GFM-IBRs in the negative sequence system:

- From the perspective of system dynamics, a decoupled-sequence dynamic model for GFM-IBRs is proposed to study the internal oscillatory modes in negative sequence systems, providing crucial insights into the behavior of negative-sequence components under unbalanced perturbations.

- From the perspective of steady state fault conditions, the equivalent negative-sequence impedance of GFM-IBRs is estimated, considering BPSC and PNSC strategies.

(ii) For full converter-based GFM-IBRs, a PNSC structure for GFM-IBRs is proposed to regulate sequence components independently, with flexibility in utilizing different power synchronization loops and CLMs.

- To prevent overcurrent, an enhanced CS-based CLM is developed for IEEE 2800 compliance, including reactive current injection and full utilization of current capacity during unbalanced faults. Another solution is the VI-based CLM, which updates the positive sequence internal voltage vectors to retain inner voltage dynamics.

- To improve the grid synchronization and voltage support capability, this thesis proposes a three-mode switching GFM control solution for Type-IV WTGs. A sequence-domain αβ voltage synchronization loop (VSL) is activated to enhance frequency stability and maintain synchronism, while the CS-based CLM is used to inject optimal reactive currents for low-voltage ride-through. After fault clearance, the VI-based CLM is employed to eliminate transient components for the WTG restoration in the transition mode.

(iii) For DFIG-based WTGs, this thesis proposes asymmetrical FRT controls for the GFM-DFIG based on the mechanism for forming the grid voltage.

- Internal voltage vectors are designed for the assessment of asymmetrical FRT capabilities. Then a PNSC is proposed to support the sequence components of internal voltage vectors for the GFM-DFIG.

- An asymmetrical FRT control structure is proposed, incorporating negative-sequence reactive current injection and two types of positive-sequence control schemes: the CS-based and the VI-based CLMs.

- A simplified calculation method for transient voltages is utilized to eliminate the impacts of transient flux leakage.

(iv) To facilitate rapid and accurate short-circuit fault analysis of the system with IBR:

- A comprehensive and efficient solver incorporating phasor domain short-circuit models of GFM- and GFL-IBRs is proposed for steady-state fault calculations considering various CLMs. The proposed approach is validated by comparing it with detailed EMT modeling and simulations using a modified IEEE 39 bus system with multi IBRs.

- The proposed solver platform enables system operators to perform rapid and accurate short-circuit

computations and protective relay studies in power systems with high penetration of IBRs, facilitating the assessment of FRT strategies and compliance with grid codes.

(v) To evaluate the performance of AC protective relays in systems with GFM-IBRs:

- The impacts of GFM-IBR on the apparent impedance measured by distance relays are elaborated analytically during unbalanced faults in a two-bus system. The analysis provides the first explanation for why GFM-IBR may alter the trajectory of the apparent impedance, potentially causing maloperation of distance protection. EMT simulations using the EPRI benchmark system are conducted to validate the analytical findings and provide in-depth investigations.

- In a modified IEEE PSRC D29 system with IBRs, the performance of distance protection is investigated under varying impact factors, including K factors, fault proximity, and fault resistance.

- The performance of the negative sequence components-based protective relays, i.e., the 50Q, 67Q, and FID elements, are tested in a system with IBRs with various FRT solutions, to identify potential maloperation issues.

1.5 Thesis Outline

The thesis focuses on the potential impacts of GFM-IBR on system dynamics, legacy protection, and FRT requirements under unbalanced grid conditions, providing innovative insights and control solutions for GFM-IBR under unbalanced grid conditions. The thesis is organized as follows:

In Chapter 2, the negative-sequence behavior of GFM-IBR and GFL-IBR is compared. From the perspective of dynamics, decoupled-sequence dynamic models of GFM-IBR with balanced positive sequence control (BPSC) and positive and negative sequence control (PNSC) are developed, to investigate the internal oscillatory modes caused by negative sequence components. For steady-state fault analysis, static analytical negative sequence modeling of GFM-IBR is developed to clarify the fundamentals and impacting factors of I2 injection.

In Chapter 3, FRT control solutions of GFM-IBR are proposed for grid code compliance during unbalanced faults.

3.1 For full converter-based GFM-IBR, a PNSC structure for GFM Type-IV WTG is proposed. When FRT detection logic triggers, WTGs operate in restricted mode. The sequence-domain $\alpha\beta$ voltage synchronization loop (VSL) activates to maintain synchronization and improve frequency stability. To avoid overcurrent, two CLM solutions are developed, including (i) current saturation-based (CS-based) CLM with a current scaling method for IEEE 2800 compliance. (ii) virtual impedance-based (VI-based) CLM with an adaptive current limit method.

3.2 For Type-III WTG, a PNSC structure is proposed to support the sequence components of internal voltage vectors for the GFM-DFIG. On this basis, an asymmetrical FRT control structure is proposed, incorporating negative-sequence reactive current injection and two types of positive-sequence control schemes: the CI-based CLM and VI-based CLM. A simplified calculation method for transient voltages is utilized to eliminate the impacts of transient flux leakage.

The proposed FRT controls for GFM-IBR are validated by using the EPRI benchmark system.

In Chapter 4, for short-circuit fault analysis of the system with IBR, a comprehensive and efficient solver incorporating phasor domain short-circuit models of GFM- and GFL-IBRs is proposed for steady-

state fault calculations considering various CLMs. The proposed approach is validated by comparing it with detailed EMT modeling and simulations using a modified IEEE 39 bus system with multi IBRs. The proposed solver platform enables system operators to perform rapid and accurate short-circuit computations and protective relay studies in power systems with high penetration of IBRs, facilitating the assessment of FRT strategies and compliance with grid codes.

In Chapter 5, the impacts of GFM-IBR on AC protection elements during unbalanced faults are investigated, including:

In 5.1, the impacts of GFM-IBR on the apparent impedance measured by distance relays are elaborated analytically during unbalanced faults in a two-bus system. The analysis provides the first explanation for why GFM-IBR may alter the trajectory of the apparent impedance, potentially causing maloperation of distance protection. EMT simulations using the EPRI benchmark system are conducted to validate the analytical findings and provide in-depth investigations. In a modified IEEE PSRC D29 system with IBRs, the performance of distance protection is investigated under varying impact factors, including K factors, fault proximity, and fault resistance.

In 5.2, the performance of the negative sequence components-based protective relays, i.e., the instantaneous negative sequence overcurrent (50Q), directional negative sequence overcurrent (67Q), and fault-identification (FID) elements, are tested in a modified IEEE PSRC D29 system with IBRs with various FRT solutions, to identify potential maloperation issues.

In Chapter 6, the conclusions of the thesis shed light on the merits and drawbacks of GFM-IBRs under unbalanced grid conditions. The suggestions and prospects for future IBR accommodation are inspired.

2 Negative Sequence Behavior of Grid-Forming IBR

The negative-sequence mechanisms and dynamics within GFM-IBRs under unbalanced grid conditions remain insufficiently understood. This lack of clarity can obscure the significance and objectives of developing GFM control strategies. Moreover, under the growing penetration of GFM-IBRs in power systems, the impacts of the negative-sequence behavior of GFM IBRs on power systems will be increasingly significant. To address this, this chapter contributes to developing dynamic and steady-state negative sequence models for studying negative-sequence components inside GFM-IBRs and exploring the negative-sequence behavior.

2.1 Dynamic Negative Sequence Modeling

2.1.1 Negative-Sequence Components inside GFM-IBR with BPSC

Fig. 2.1 depicts the structure of a typical GFM-IBR plant that incorporates N GFM-IBR units. For each GFM-IBR unit, balanced positive sequence control (BPSC) strategy is employed to regulate the measurements from IBR hardware and generate modulation signals to drive the voltage source converter (VSC). Under unbalanced perturbations, positive-, negative- and zero-sequence components of both voltages and currents are typically present in the AC grid. However, due to the presence of a delta-connected winding in the IBR transformer, only the positive- and negative-sequence components are present on the converter side.

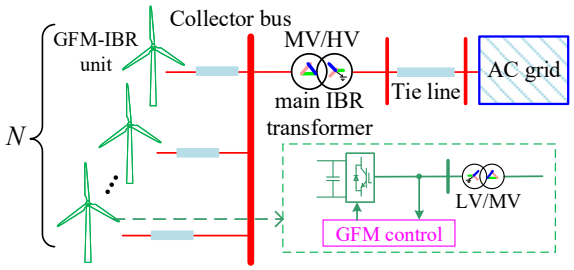

Fig. 2.1. GFM-IBR plant in power systems

Based on the synchronous reference frame (SRF), dq components of an arbitrary variable $\boldsymbol{X}$ in the BPSC loop can be derived as,

$$\boldsymbol{X}_{dq} = \begin{bmatrix} X_\alpha \cos(\theta) + X_\beta \sin(\theta) \\ X_\beta \cos(\theta) - X_\alpha \sin(\theta) \end{bmatrix} = \boldsymbol{X}_{dq}^{+} + \begin{bmatrix} X_d^{-} \cos(2\omega t) + X_q^{-} \sin(2\omega t) \\ X_q^{-} \cos(2\omega t) - X_d^{-} \sin(2\omega t) \end{bmatrix} = \boldsymbol{X}_{dq}^{+} + \tilde{\boldsymbol{X}}_{dq}^{-} \tag{2.1}$$

where $\tilde{\boldsymbol{X}}_{dq}^{-}$ denotes double-fundamental-frequency (2ω) negative-sequence dq components, and θ and ω are the orientation angle and angular frequency, respectively. Superscripts + and – also refer to positive- and negative-sequence components, respectively. For illustration, the diagram of sequence components inside GFM-IBRs under unbalanced perturbations is depicted in Fig. 2.2. I_{vsc} denotes the DC-link current on the converter side. In subscript, *set* refers to setpoints, while *dc* denotes DC-link components.

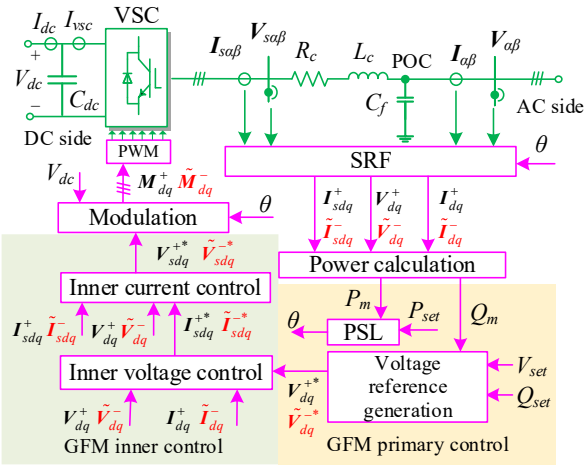

Fig. 2.2. Sequence components within typical GFM BPSC under unbalanced perturbations

2.1.2 Decoupled-Sequence Dynamic Modeling for GFM-IBR

2.1.2.1 Generic Decoupled-Sequence Dynamic Modeling Structure

To evaluate the influence of 2ω negative-sequence components within GFM controls, a decoupled-sequence dynamic modeling approach for GFM-IBRs is designed, which can be represented by a unified time-domain model, as follows

$$\begin{cases} \boldsymbol{x}(t)=\left[\boldsymbol{x}_{dq}^{+}(t) \quad \boldsymbol{x}_{dq}^{-}(t) \quad \boldsymbol{x}_{s}(t) \quad \boldsymbol{x}_{dc}(t)\right]^{\mathrm{T}} \\ \dot{\boldsymbol{x}}(t)=f(\boldsymbol{x}(t)) \end{cases} \tag{2.2}$$

where $\boldsymbol{x}_{dq}^{+}(t)$ and $\boldsymbol{x}_{dq}^{-}(t)$ represent the state variables of the positive- and negative-sequence dq components, respectively. $\boldsymbol{x}_{s}(t)$ and $\boldsymbol{x}_{dc}(t)$ represent the state variables of the GFM control system and DC system, respectively.

1) GFM BPSC System

GFM primary control:

The VSM control emulates the rotor motion and primary frequency regulation of SGs, enabling GFM-IBRs to exhibit the *P-f* droop mechanism and swing behavior, as given by,

$$\begin{cases} \dot{\omega}=((P_{set}-x_P)/\omega_n+D_p(\omega_n-\omega))/J \\ \dot{x}_P=\omega_f(P_m-x_P) \end{cases} \tag{2.3}$$

where J is the virtual inertia constant, D_p is the droop gain, and ω_n and ω_f are the nominal frequency and cut-off frequency, respectively. x_P is a state variable of the low-pass filter of active power. Under unbalanced grid conditions, the *d*-axis voltage is given by,

$$V_d=V_d^{+}+\tilde{V}_d^{-}=V_d^{+}+V_d^{-}\cos(2\omega t)+V_q^{-}\sin(2\omega t) \tag{2.4}$$

Then, the virtual flux leakage is derived as,

$$\psi_M=\psi_M^{+}+\tilde{\psi}_M^{-} \tag{2.5}$$

$$\begin{cases} \psi_M^{+}=k_{pvac}\underbrace{(V_{set}-V_d^{+})}_{\dot{x}_V^{+}}+k_{ivac}x_V^{+} \\ \tilde{\psi}_M^{-}=k_{pvac}\underbrace{(0-\tilde{V}_d^{-})}_{\dot{\tilde{x}}_V^{-}}+k_{ivac}\tilde{x}_V^{-} \end{cases} \tag{2.6}$$

where k_{pvac} and k_{ivac} are the PI-controller gains. x_V is a state variable of the PI controller for generating

virtual flux leakage. On this basis, the virtual voltage references are determined as,

$$\begin{cases} \boldsymbol{V}_{dq}^{+*} = \mathbf{T}_{dq}(\theta)\mathbf{T}_{\alpha\beta}\omega\psi_M^+ \sin(\hat{\theta}) \\ \tilde{\boldsymbol{V}}_{dq}^{-*} = \mathbf{T}_{dq}(\theta)\mathbf{T}_{\alpha\beta}\omega\tilde{\psi}_M^- \sin(\hat{\theta}) \\ \sin(\hat{\theta}) = \left[\sin(\theta) \quad \sin(\theta - 2\pi/3) \quad \sin(\theta - 4\pi/3)\right]^{\mathrm{T}} \end{cases} \tag{2.7}$$

where $\mathbf{T}_{dq}(\cdot) = \begin{bmatrix} \cos(\cdot) & \sin(\cdot) \\ -\sin(\cdot) & \cos(\cdot) \end{bmatrix}$ and $\mathbf{T}_{\alpha\beta} = \sqrt{\frac{2}{3}}\begin{bmatrix} 1 & -1/2 & -1/2 \\ 0 & \sqrt{3}/2 & -\sqrt{3}/2 \end{bmatrix}$.

The droop control replicates the speed droop characteristic of the synchronous generator (SG) governor and balances deviations in power injection. Frequency regulation is modeled with (2.8) and voltage reference regulation is modeled with (2.9) and (2.10), where m_p is the droop gain.

$$\omega = \omega_n - m_p(P_m - P_{set}) \tag{2.8}$$

$$\begin{cases} V_d^* = V_d^{+*} + \tilde{V}_d^{-*} \\ V_q^* = 0 \end{cases} \tag{2.9}$$

$$\begin{cases} V_d^{+*} = k_{pvac}\underbrace{(V_{set}^+ - V_d^+)}_{\dot{x}_V^+} + k_{ivac}x_V^+ \\ \tilde{V}_d^{-*} = k_{pvac}\underbrace{(0 - \tilde{V}_d^-)}_{\dot{\tilde{x}}_V^-} + k_{ivac}\tilde{x}_V^- \end{cases} \tag{2.10}$$

The dVOC function regulates active and reactive power separately, thus obtaining the amplitude and phase of virtual voltage references, as follows:

Frequency regulation:

$$\begin{cases} \omega = \omega_n + \kappa_1(P_{set}/(V_{set})^2 - x_P/(V_d^*)^2) \\ \dot{x}_P = \omega_f(P_m - x_P) \end{cases} \tag{2.11}$$

Voltage reference generation:

$$\begin{cases} \dot{V}_d^* = V_d^*\left(\kappa_1\left(\frac{Q_{set}}{(V_{set})^2} - \frac{x_Q}{(V_d^*)^2}\right) + \frac{\kappa_2(V_{set}^2 - (V_d^*)^2)}{V_{set}^2}\right) \\ \dot{x}_Q = \omega_f(Q_m - x_Q) \end{cases} \tag{2.12}$$

where κ_1 and κ_2 denote synchronization gains. x_Q is a state variable of the low-pass filter of reactive power. Since the dVOC regulates voltage references via the reactive power, $\tilde{V}_d^-$ does not affect voltage reference generation.

GFM inner control:

The inner control loop consists of the inner voltage and current control. Typical dual closed-loop design controllers with feedforward terms are employed. Under unbalanced grid conditions, the measured *dq* voltages and currents are given by,

$$\boldsymbol{X} = \{I, V, I_s\} \tag{2.13}$$

$$\boldsymbol{X}_{dq} = \boldsymbol{X}_{dq}^+ + \tilde{\boldsymbol{X}}_{dq}^- = \begin{bmatrix} X_d^+ + X_d^-\cos(2\omega t) + X_q^-\sin(2\omega t) \\ X_q^+ + X_q^-\cos(2\omega t) - X_d^-\sin(2\omega t) \end{bmatrix} \tag{2.14}$$

The formulas of inner voltage control are derived as,

$$\begin{cases} \boldsymbol{I}_{sdq}^{+*} = k_{iv}\boldsymbol{x}_{Vdq}^{+} + k_{pv}\underbrace{(\boldsymbol{V}_{dq}^{+*} - \boldsymbol{V}_{dq}^{+})}_{\dot{\boldsymbol{x}}_{Vdq}^{+}} + \underbrace{\boldsymbol{\gamma} C_f \boldsymbol{V}_{dq}^{+} + \boldsymbol{I}_{dq}^{+}}_{\text{feedforward}} \\ \tilde{\boldsymbol{I}}_{sdq}^{-*} = k_{iv}\tilde{\boldsymbol{x}}_{Vdq}^{-} + k_{pv}\underbrace{(\tilde{\boldsymbol{V}}_{dq}^{-*} - \tilde{\boldsymbol{V}}_{dq}^{-})}_{\dot{\tilde{\boldsymbol{x}}}_{Vdq}^{-}} + \underbrace{\boldsymbol{\gamma} C_f \tilde{\boldsymbol{V}}_{dq}^{-} + \tilde{\boldsymbol{I}}_{dq}^{-}}_{\text{feedforward}} \end{cases} \tag{2.15}$$

where $\boldsymbol{\gamma} = \begin{bmatrix} 0 & \omega \\ -\omega & 0 \end{bmatrix}$. k_{pv} and k_{iv} are PI-controller gains of the inner voltage control. $\boldsymbol{x}_{Vdq}$ denotes state variables of the PI controller of inner voltage control. The formulas of inner current control are derived as,

$$\begin{cases} \boldsymbol{V}_{sdq}^{+*} = k_{pi}\underbrace{(\boldsymbol{I}_{dq}^{+*} - \boldsymbol{I}_{dq}^{+})}_{\dot{\boldsymbol{x}}_{Idq}^{+}} + k_{ii}\boldsymbol{x}_{Idq}^{+} + \underbrace{\boldsymbol{\gamma} L_f \boldsymbol{I}_{dq}^{+} + \boldsymbol{V}_{dq}^{+}}_{\text{feedforward}} \\ \tilde{\boldsymbol{V}}_{sdq}^{-*} = k_{pi}\underbrace{(\tilde{\boldsymbol{I}}_{dq}^{-*} - \tilde{\boldsymbol{I}}_{dq}^{-})}_{\dot{\tilde{\boldsymbol{x}}}_{Idq}^{-}} + k_{ii}\tilde{\boldsymbol{x}}_{Idq}^{-} + \underbrace{\boldsymbol{\gamma} L_f \tilde{\boldsymbol{I}}_{dq}^{-} + \tilde{\boldsymbol{V}}_{dq}^{-}}_{\text{feedforward}} \end{cases} \tag{2.16}$$

where k_{pi} and k_{ii} are the PI-controller gains of the inner current control. $\boldsymbol{x}_{Idq}$ denotes state variables of the PI controller of inner voltage control. The modulation signals are generated by the inner current control, as follows:

$$\begin{cases} \boldsymbol{M}_{dq}^{+} = \dfrac{2}{V_{dc}}\boldsymbol{V}_{sdq}^{+*} \\ \tilde{\boldsymbol{M}}_{dq}^{-} = \dfrac{2}{V_{dc}}\tilde{\boldsymbol{V}}_{sdq}^{-*} \end{cases} \tag{2.17}$$

$$\boldsymbol{M}_{dq}^{-} = \begin{bmatrix} \tilde{M}_d^{-}\cos(2\omega t) - \tilde{M}_q^{-}\sin(2\omega t) \\ \tilde{M}_q^{-}\cos(2\omega t) + \tilde{M}_d^{-}\sin(2\omega t) \end{bmatrix} \tag{2.18}$$

2) GFM PNSC System

For regulating positive- and negative-sequence components independently, a GFM PNSC structure can be employed. In PNSC, sequence component extraction methods, such as delayed-signal-based method or filter-based method (see section 1.2.4.1), can be utilized to eliminate the effects of 2ω negative-sequence components of voltages and currents. In this way, the positive- and negative-sequence components can be separated. Hence, for PNSC, the 2ω negative-sequence components $\tilde{\boldsymbol{X}}_{dq}^{-}$ equal zero in (2.3)−(2.18). To address these uncontrolled negative-sequence components, two types of negative-sequence control solutions for GFM-IBRs are considered in this section, i.e., the balanced voltage control strategy given by (2.19) and balanced current control strategy given by (2.20).

$$\begin{cases} \boldsymbol{V}_{dq}^{-*} = 0 \\ \boldsymbol{I}_{sdq}^{-*} = (k_{pv} + k_{iv}/s)(\boldsymbol{V}_{dq}^{+*} - \boldsymbol{V}_{dq}^{+}) + \boldsymbol{\gamma} C_f \boldsymbol{V}_{dq}^{-} + \boldsymbol{I}_{dq}^{-} \\ \boldsymbol{V}_{sdq}^{-*} = (k_{pi} + k_{ii}/s)(\boldsymbol{I}_{sdq}^{-*} - \boldsymbol{I}_{sdq}^{-}) + \boldsymbol{\gamma} L_c \boldsymbol{I}_{sdq}^{-} + \boldsymbol{V}_{dq}^{-} \\ \boldsymbol{M}_{dq}^{-} = 2\boldsymbol{V}_{sdq}^{-*}/V_{dc} \end{cases} \tag{2.19}$$

$$\begin{cases} \boldsymbol{I}_{sdq}^{-*} = 0 \\ \boldsymbol{V}_{sdq}^{-*} = (k_{pi} + k_{ii}/s)(\boldsymbol{I}_{sdq}^{-*} - \boldsymbol{I}_{sdq}^{-}) + \boldsymbol{\gamma} L_c \boldsymbol{I}_{sdq}^{-} + \boldsymbol{V}_{dq}^{-} \\ \boldsymbol{M}_{dq}^{-} = 2\boldsymbol{V}_{sdq}^{-*}/V_{dc} \end{cases} \tag{2.20}$$

3) AC and DC systems

Since the section focuses on the negative-sequence behavior of GFM-IBRs on the AC side, the DC system can be simplified to a DC-voltage-controlled current source, as given by,

$$\begin{cases} \dot{I}_{dc} = (I_{dcset} - I_{dc})/T_{dc} = \left[k_{Vdc}(V_{dcset} - V_{dc}) - I_{dc}\right]/T_{dc} \\ \dot{V}_{dc} = (I_{dc} - I_{vsc})/C_{dc} = \left[I_{dc} - \frac{1}{2}(\boldsymbol{M}_{\alpha\beta})^{\mathrm{T}}\boldsymbol{I}_{s\alpha\beta}\right]/C_{dc} \end{cases} \tag{2.21}$$

where T_{dc} and k_{Vdc} denote the time delay constant and DC voltage control gain, respectively. For the AC system in Fig. 2.2, positive- and negative-sequence differential equations in *dq* coordinates are derived as,

$$\begin{cases} \dot{\boldsymbol{I}}^{+}_{sdq} = (\boldsymbol{V}^{+}_{sdq} - R_c\boldsymbol{I}^{+}_{sdq} - \boldsymbol{V}^{+}_{dq})/L_c + \boldsymbol{\gamma}\,\boldsymbol{I}^{+}_{sdq} \\ \dot{\boldsymbol{I}}^{-}_{sdq} = (\boldsymbol{V}^{-}_{sdq} - R_c\boldsymbol{I}^{-}_{sdq} - \boldsymbol{V}^{-}_{dq})/L_c + \boldsymbol{\gamma}\boldsymbol{I}^{-}_{sdq} \end{cases} \tag{2.22}$$

$$\begin{cases} \dot{\boldsymbol{V}}^{+}_{dq} = (\boldsymbol{I}^{+}_{sdq} - \boldsymbol{I}^{+}_{dq})/C_f + \boldsymbol{\gamma}\boldsymbol{V}^{+}_{dq} \\ \dot{\boldsymbol{V}}^{-}_{dq} = (\boldsymbol{I}^{-}_{sdq} - \boldsymbol{I}^{-}_{dq})/C_f + \boldsymbol{\gamma}\boldsymbol{V}^{-}_{dq} \end{cases} \tag{2.23}$$

4) Linearization

By linearizing the proposed dynamic model $\dot{\boldsymbol{x}}(t)=f(\boldsymbol{x}(t))$ at steady-state equilibrium, decoupled-sequence small-signal models of GFM-IBRs are derived as follows:

$$\begin{cases} \Delta\boldsymbol{x} = \left[\Delta\boldsymbol{x}^{+}_{dq} \quad \Delta\boldsymbol{x}^{-}_{dq} \quad \Delta\boldsymbol{x}_{s} \quad \Delta\boldsymbol{x}_{dc}\right]^{\mathrm{T}} \\ \Delta\dot{\boldsymbol{x}} = \boldsymbol{A}\Delta\boldsymbol{x} + \boldsymbol{B}\Delta\boldsymbol{u} \end{cases} \tag{2.24}$$

where $\boldsymbol{A}$ denotes the state-space matrix. $\boldsymbol{B}$ denotes the input matrix. The state variables are then given by

$$\begin{cases} \Delta\boldsymbol{x}^{+}_{dq} = \left[\underbrace{\Delta\boldsymbol{I}^{+}_{sdq} \quad \Delta\boldsymbol{V}^{+}_{dq}}_{\text{AC system}} \quad \underbrace{\Delta\boldsymbol{x}^{+}_{Vdq} \quad \Delta\boldsymbol{x}^{+}_{Idq}}_{\text{Inner control}}\right]^{\mathrm{T}} \\ \Delta\boldsymbol{x}^{-}_{dq} = \left[\underbrace{\Delta\boldsymbol{I}^{-}_{sdq} \quad \Delta\boldsymbol{V}^{-}_{dq}}_{\text{AC system}} \quad \underbrace{\Delta\boldsymbol{x}^{-}_{Vdq} \quad \Delta\boldsymbol{x}^{-}_{Idq}}_{\text{Inner control}}\right]^{\mathrm{T}} \\ \Delta\boldsymbol{x}_{dc} = \left[\underbrace{\Delta I_{dc} \quad \Delta V_{dc}}_{\text{DC system}}\right]^{\mathrm{T}} \end{cases} \tag{2.25}$$

For the VSM control strategy (GFM_VSM),

$$\begin{cases} \Delta\boldsymbol{x}_{s} = \left[\Delta\boldsymbol{x}^{+}_{V} \quad \Delta\boldsymbol{x}^{-}_{V} \quad \Delta\theta \quad \Delta\omega \quad \Delta x_{P}\right]^{\mathrm{T}} \\ \Delta\boldsymbol{u} = \left[\Delta\boldsymbol{I}^{+}_{dq} \quad \Delta\boldsymbol{I}^{-}_{dq} \quad \underbrace{\Delta P_{set} \quad \Delta V_{set}}_{\text{VSM control input}}\right]^{\mathrm{T}} \end{cases} \tag{2.26}$$

For the droop control strategy (GFM_droop),

$$\begin{cases} \Delta\boldsymbol{x}_{s} = \left[\Delta\boldsymbol{x}^{+}_{V} \quad \Delta\boldsymbol{x}^{-}_{V} \quad \Delta\theta \quad \Delta x_{P}\right]^{\mathrm{T}} \\ \Delta\boldsymbol{u} = \left[\Delta\boldsymbol{I}^{+}_{dq} \quad \Delta\boldsymbol{I}^{-}_{dq} \quad \underbrace{\Delta P_{set} \quad \Delta V_{set}}_{\text{droop control input}}\right]^{\mathrm{T}} \end{cases} \tag{2.27}$$

For the dVOC strategy (GFM_dVOC),

$$\begin{cases} \Delta \boldsymbol{x}_s = \begin{bmatrix} \Delta\theta & \Delta V_d^* & \Delta x_P & \Delta x_Q \end{bmatrix}^{\mathrm{T}} \\ \Delta \boldsymbol{u} = \begin{bmatrix} \Delta \boldsymbol{I}_{dq}^{+} & \Delta \boldsymbol{I}_{dq}^{-} & \underbrace{\Delta P_{set} \quad \Delta Q_{set} \quad \Delta V_{set}}_{\text{dVOC input}} \end{bmatrix}^{\mathrm{T}} \end{cases} \tag{2.28}$$

Overall, the proposed dynamic modeling approach provides a detailed illustration of the regulation of negative-sequence components within GFM-IBRs. The derived state-space matrix can be used to further analyze the impact of negative-sequence components on system dynamics through modal analysis.

5) Model Validation

To validate the proposed decoupled-sequence dynamic modeling approach of GFM-IBRs, a test system is implemented in an EMT-type tool, as shown in Fig. 2.3. The parameter configuration of GFM-IBRs is listed in Table 2-1. *Tr_m* and *Tr_u* denote the ratio of the main IBR transformer and IBR unit transformer, respectively.

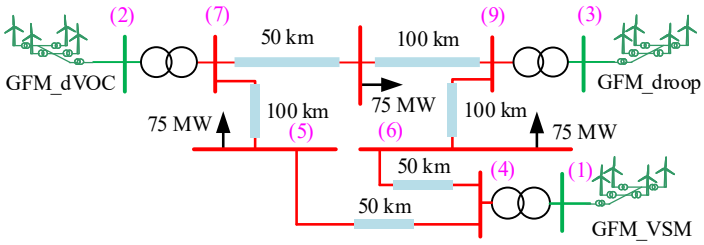

Fig. 2.3. Test system: 100% GFM-IBR-dominated system

TABLE 2-1

Parameter Configuration of GFM-IBRs

Parameter	Value	Parameter	Value
N	200	(k_{pvac}, k_{ivac})	(0.001, 0.0021)
(T_{dc}, k_{Vdc})	(0.05 s, 0.83)	(k_{pv}, k_{iv})	(0.52,232.2)
ω_n	314 rad/s	(k_{pi}, k_{ii})	(0.73, 0.0059)
ω_f	31.4 rad/s	(P_{set}, Q_{set})	(1 pu, 0 pu)
(D_p, J)	(1.01e5, 2.02e3)	(V_{set}, V_{dcset})	(1 pu, 2.45 kV)
(κ_1, κ_2)	(0.0209, 1.39e3)	m_p	3.14e-8
(R_c, L_c)	(5e-6 Ω, 1e-6 H)	(C_{dc}, C_f)	(1.6 F, 0.06 F)
Tr_m	230 kV /13.8 kV	*Tr_u*	13.8 kV/1 kV

In the test system, GFM-IBR operates at P_m=75 MW. For illustration, when t=15 s, a 75 MW unbalanced load is applied at Bus (6), resulting in the imbalance of grid voltages and currents. The negative-sequence components of grid voltages are shown in Fig. 2.4. Per IEEE 2800 standard, IBRs can continue to operate if the negative-sequence component of the applicable voltages is below 3% of the nominal voltage for less than 10 seconds, provided that the voltage imbalance is not caused or exacerbated by unbalanced currents from the IBR.

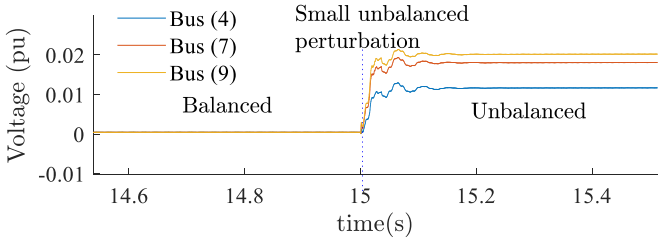

Fig. 2.4. Magnitude of negative-sequence grid voltages

The time step and simulation duration are set to 100 μs and 20 s, respectively. For GFM-IBRs with the BPSC strategy, Fig. 2.5 shows the numerical results of the EMT simulation, the existing dynamic model [34], and the proposed dynamic model for comparison. The existing dynamic model solely incorporates positive-sequence *dq* components in the BPSC system and ignores 2ω negative-sequence components.

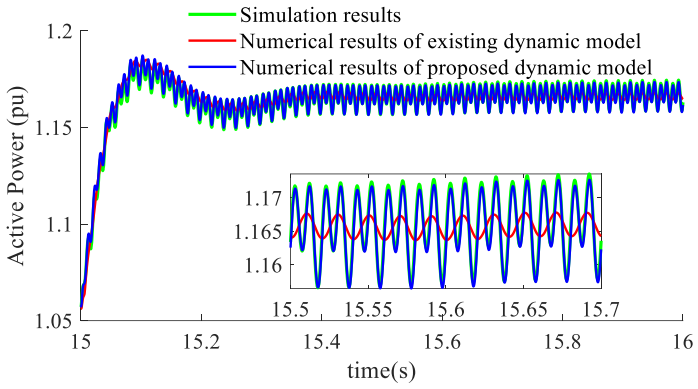

(a) GFM_VSM

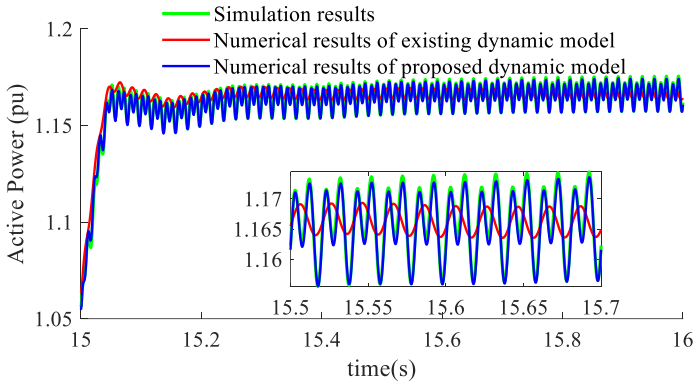

(b) GFM_droop

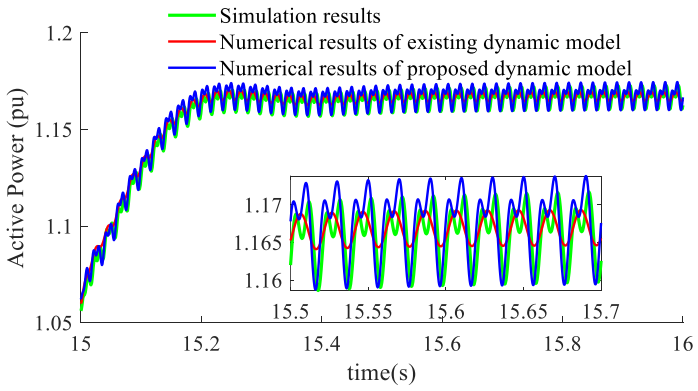

(c) GFM_dVOC

Fig. 2.5. Numerical results of active power responses of GFM-IBRs

During the interval t=15−15.2 s, the transient dynamics of active power differ among GFM-IBRs due to each plant's different primary control strategies. Under steady-state unbalanced grid conditions, the dynamics of the proposed model are highly consistent with the EMT simulations. In addition, Fig. 2.6 shows that the 100% GFM-IBR-dominated system can still provide a path for the flow of 2ω negative-sequence components.

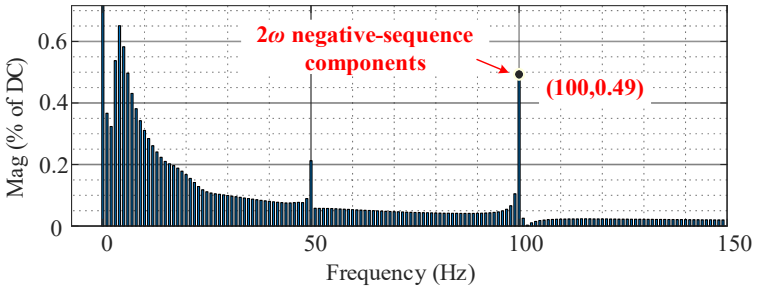

Fig. 2.6. FFT analysis for active power response of GFM_VSM

2.1.3 Modal Analysis for GFM-IBR under Small Unbalanced Perturbations

2.1.3.1 Oscillatory Modes of GFM-IBR under Small Unbalanced Perturbations

Based on the state-space matrix derived from the proposed dynamic model, the eigenvalue-based stability assessment (EBSA) is used to study the impacts of control settings and negative-sequence control solutions on oscillatory modes dominated by 2ω negative-sequence components. Oscillatory modes of the GFM_VSM are filtered out, as shown in Fig. 2.7. Participation factors are employed to identify the dominant variables. For illustration, the dominant variables are defined as the state variables that exhibit a participation factor exceeding 25%. The eigenvalue λ, damping ratio δ, oscillation frequency f, and dominant variables are listed in Table 2-2.

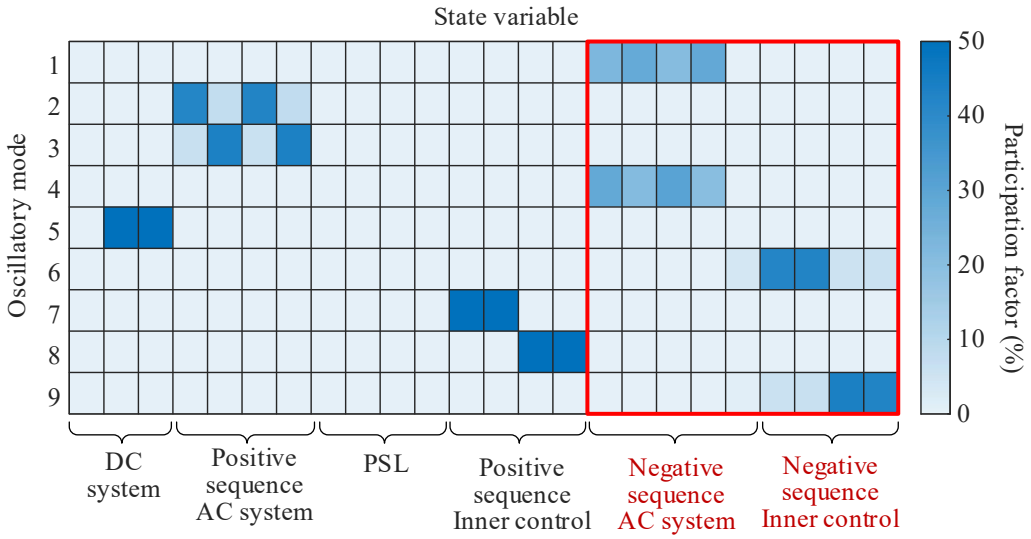

Fig. 2.7. Participation factors of GFM_VSM

TABLE 2-2

Oscillatory modes of GFM_VSM

Mode	*Λ*	*δ*	*f* /Hz	Dominant Variables
1	**-1719±2524i**	**0.56**	**401.82**	$\Delta \boldsymbol{I}_{sdq}^{-}$ $\Delta \boldsymbol{V}_{dq}^{-}$
2	-1931±2264i	0.65	360.45	ΔI_{sd}^{+} ΔV_{d}^{+}
3	-1763±1718i	0.72	273.55	ΔI_{sq}^{+} ΔV_{q}^{+}
4	**-1976±1457i**	**0.80**	**231.89**	$\Delta \boldsymbol{I}_{sdq}^{-}$ ΔV_{d}^{-}
5	-7.20±143.7i	0.05	22.88	ΔI_{dc} ΔV_{dc}
6	**-2.17±0.73i**	**0.95**	**0.12**	$\Delta \boldsymbol{x}_{Vdq}^{-}$

7	-2.23±0.0015i	1.00000	0.00025	Δx^{+}_{Vdq}
8	-1.61±0.0007i	1.00000	0.00012	Δx^{+}_{Idq}
9	**-1.53±0.0510i**	**0.99945**	**0.00812**	Δx^{-}_{Idq}

Table 2-2 indicates that under the regulation of the GFM control system, the 2ω negative-sequence components would lead to oscillations at various frequencies (0−0.12 Hz, 231 Hz, 225 Hz, 325 Hz, and 402 Hz), thus deteriorating the dynamic performance. This issue is usually hidden by the dynamic model without consideration of negative-sequence components.

For the DC side, there exists an oscillatory frequency of 22.88 Hz that is caused by the DC-link voltage and current, indicating that the DC-link voltage and current exhibit an oscillation at 22.88 Hz. The result is consistent with the FFT analysis of the DC-link voltage using EMT simulation, as shown in Fig. 2.8.

For the AC side, the oscillatory frequency caused by *dq* voltages and currents is within the range of 224 Hz to 402 Hz. The real parts of these eigenvalues are around -1800, indicating they are significantly distant from the imaginary axis. Hence, their impact on system stability is relatively minimal. The negative-sequence GFM inner control also generates oscillatory modes. The real parts of these eigenvalues are closer to the imaginary axis, potentially affecting the system's stable operation.

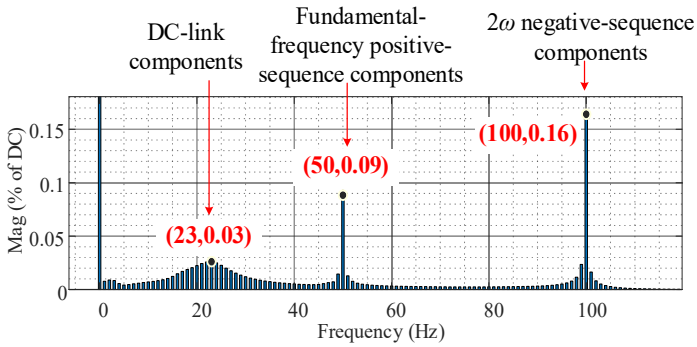

Fig. 2.8. FFT analysis based on simulation results of the DC-link voltage under small unbalanced perturbations

2.1.3.2 Impact of Negative-Sequence Control Solutions on Oscillatory Modes under Small Unbalanced Perturbations

For GFM_VSM with the PNSC strategy, the negative-sequence voltage at the POC and negative-sequence converter current are shown in Fig. 2.9. The balanced voltage control effectively suppresses the negative-sequence voltage, while the balanced current control effectively suppresses the negative-sequence current.

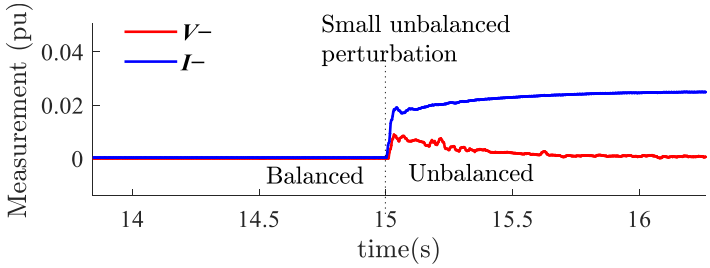

(a) Balanced voltage control strategy

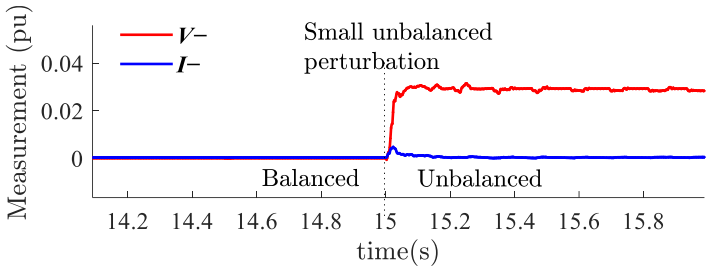

(b) Balanced current control strategy

Fig. 2.9. Simulation results with negative-sequence control solutions in PNSC

For comparison, the oscillatory modes dominated by $\Delta \boldsymbol{x}_{Vdq}^{-}$ and $\Delta \boldsymbol{x}_{Idq}^{-}$ under the original BPSC and negative-sequence control solutions are shown in Fig. 2.10. Since there are no negative-sequence voltages within the balanced current control loop, the oscillatory modes dominated by $\Delta \boldsymbol{x}_{Vdq}^{-}$ do not exist under the balanced current control. By using the balanced current control and balanced voltage control strategies, the oscillatory modes shifted to the left. The imaginary part of modes is reduced to zero under the regulation of negative-sequence control solutions. Hence, for the oscillatory modes dominated by $\Delta \boldsymbol{x}_{Vdq}^{-}$ and $\Delta \boldsymbol{x}_{Idq}^{-}$, using the negative-sequence control solutions increases the damping ratio while reducing the oscillation frequency. This indicates that the additional negative-sequence control solution can eliminate the oscillation, thus improving the control damping of GFM-IBRs.

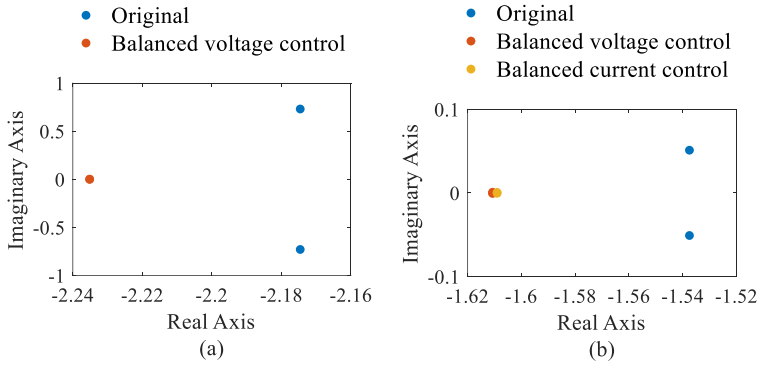

Fig. 2.10. Oscillatory modes dominated by negative-sequence components under BPSC and PNSC strategies: (a) Modes dominated by $\Delta \boldsymbol{x}_{Vdq}^{-}$; (b) Modes dominated by $\Delta \boldsymbol{x}_{Idq}^{-}$.

2.1.4 Conclusion

This section introduces a novel generic decoupled-sequence dynamic model for GFM-IBRs, providing crucial insights into the behavior of 2ω negative-sequence components within the GFM BPSC system under small, unbalanced perturbations. Our comprehensive modal analysis of GFM-IBR-dominated systems reveals several significant findings:

1. Impact of Negative Sequence Components: The 2ω negative-sequence components induce undesirable oscillations across various frequencies, substantially degrading system dynamic performance. This critical effect is often overlooked in conventional dynamic models that neglect negative-sequence components.

2. Effectiveness of Negative-Sequence Control: Implementing balanced current and voltage control

strategies shifts oscillatory modes leftward and reduces their imaginary components to zero. This finding suggests the adoption of supplementary negative-sequence controls in GFM-IBRs to enhance control damping under small, unbalanced perturbations.

The proposed model and analysis method provide a powerful methodology for understanding and mitigating the impacts of negative-sequence behavior on system dynamics in GFM-IBR-dominated grids. While this study employs EBSA to focus on oscillatory mode analysis rather than instability mechanisms, it lays a foundation for future research.

2.2 Static Negative Sequence Modeling

2.2.1 Steady-State Negative Sequence Modeling

Given the large-scale adoption of full-scale converters, the Type-IV WTG is considered as a representative example of IBRs. Fig. 2.11 illustrates the typical GFL-based and GFM-based BPSC structures in grid-side converters (GSCs) of Type-IV WTGs. Measurement filters are used to eliminate the harmonics. Combining Park's transformation, the PLL-based or PSL-based SRF is employed to obtain *dq* components. The details of the PLL and PSL are presented in Fig. 2.12(a) and Fig. 2.12(b). The PSL utilizes the virtual synchronous machine control. LPF denotes the low-pass filter. J and D_p denote virtual inertia and damping factor. K_V denotes the AC voltage droop coefficient.

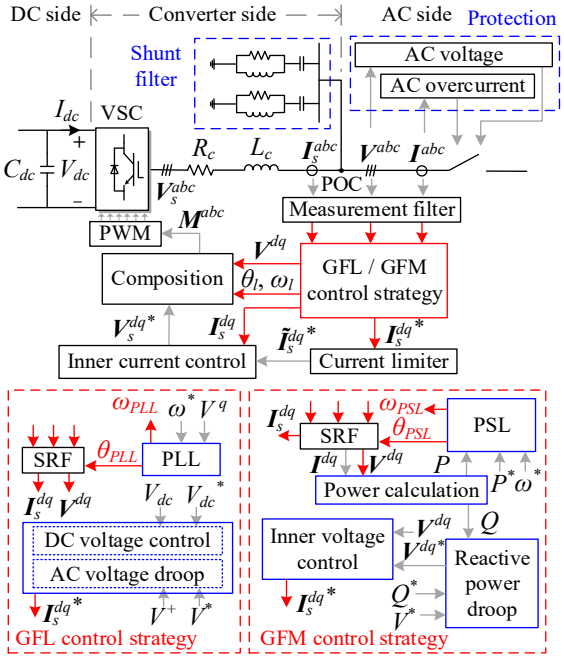

Fig. 2.11. Typical GFL and GFM BPSC structures in GSCs of Type-IV WTGs.

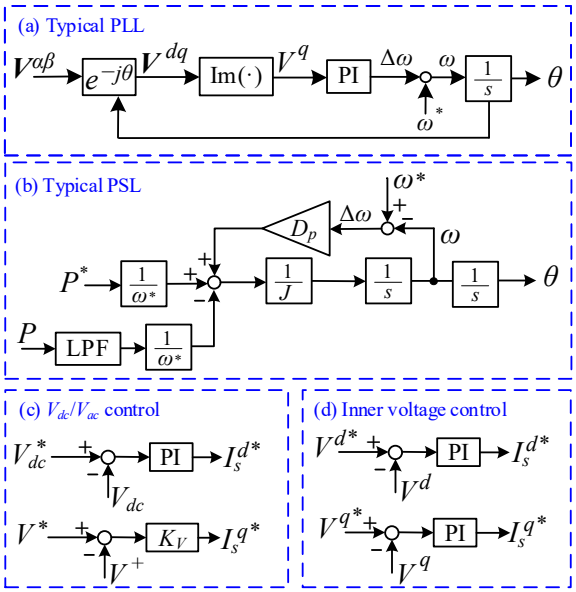

Fig. 2.12. Diagram of GFM and GFL control structure.

AC overcurrent and voltage protections are incorporated at the point of connection (POC) to protect the voltage source converter (VSC). As the zero-sequence components are blocked by the typically delta connected WTG transformer, the focus is on the positive and negative-sequence components of the voltages and currents. For an arbitrary variable X, the dq-, $\alpha\beta$-, and abc-vectors are denoted in bold and italics, as given by

$$\begin{cases} x = X\cos(\omega_n t + \theta_X) = X\angle\theta_X = x^+ + x^- \\ \boldsymbol{X}^{abc} = [x^a \ x^b \ x^c]^{\mathrm{T}} \\ \boldsymbol{X}^{\alpha\beta} = x^\alpha + jx^\beta \\ \boldsymbol{X}^{dq} = X^d + jX^q = Xe^{j\theta_X} \end{cases} \tag{2.29}$$

where $X = \sqrt{(X^d)^2 + (X^q)^2}$. $\theta_X = \arctan(X^q / X^d)$. θ and ω denote the phase angle and angular frequency. ω_n represents the nominal frequency. I and V denote currents and voltages at the POC. P and Q denote the active and reactive power. C_{dc}, R_c, and L_c denote the DC-link capacitor, choke resistance, and choke inductance. M denotes the modulation voltages. In superscripts, the symbol * indicates reference value. Superscripts + and – indicate positive sequence and negative sequence components. In subscripts, s and dc indicate converter-side and DC-side components. l = PLL or PSL denotes the components regulated by the PLL or PSL. The priority-based current limiter, which operates on the P priority during normal operation and Q priority in FRT mode, is utilized. $\tilde{\boldsymbol{I}}_s^{dq*}$ denotes dq current references regulated by current limiters.

Under unbalanced grid conditions, both positive sequence and negative sequence components are present on the AC side. Although there is no negative-sequence control loop in the BPSC system, negative sequence components would still be incorporated within dq components in the form of double-fundamental-frequency oscillation.

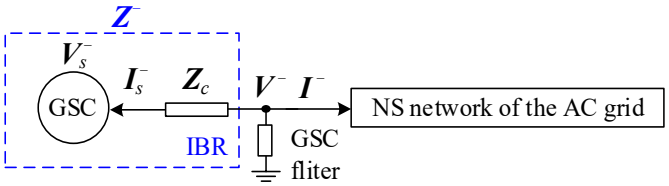

Fig. 2.13. Equivalent negative sequence (NS) network of a two-bus system connected to an IBR

To elaborate on the negative sequence behavior of GFL and GFM inverters under unbalanced grid conditions, an equivalent negative sequence network under an unbalanced steady state is established, as shown in Fig. 2.13. The equivalent negative sequence impedance ($\boldsymbol{Z}^-$) of IBRs is defined as

$$\boldsymbol{Z}^- = \boldsymbol{V}^- / \boldsymbol{I}_s^- = \boldsymbol{Z}_c + \boldsymbol{V}_s^- / \boldsymbol{I}_s^- \tag{2.30}$$

where $\boldsymbol{Z}_c = R_c + j\omega_n L_c$ .To facilitate the derivations, the GSC filter is not included in $\boldsymbol{Z}^-$.

Since the inner voltage control and inner current control are typically implemented by proportional-integral (PI) regulators, to simplify the expressions, denote the complex gain of a PI regulator as

$$\boldsymbol{R}_C^\omega = k_{pC} + k_{iC} / j\omega \tag{2.31}$$

where k_p and k_i are proportional and integral parameters. Superscript ω indicates the angular frequency of the phasor. Subscript $C = \{V, I\}$ represents the inner voltage control and inner current control. These PI regulators are typically equipped with output limiters. Given that these limiters have sufficient margin,

they would not affect the negative sequence behavior of inverter controls. The GFL and GFM controls can swiftly regulate the current references during the transient process. Thus, $\tilde{\boldsymbol{I}}_s^{dq*} = \boldsymbol{I}_s^{dq*}$. Therefore, in the inner current control (See Fig. 2.14), the relations between the $\boldsymbol{V}_s^{dq}$ and $\boldsymbol{V}^{dq}$ are established as

$$\boldsymbol{V}_s^{dq} = \boldsymbol{V}_s^{dq*} = \underbrace{\boldsymbol{\lambda}_f^{\omega}(\boldsymbol{V}^{dq} - \boldsymbol{Z}_c \boldsymbol{I}_s^{dq})}_{\text{feed-forward term}} - \underbrace{\boldsymbol{R}_I^{\omega}(\boldsymbol{I}_s^{dq*} - \boldsymbol{\lambda}_f^{\omega}\boldsymbol{I}_s^{dq})}_{\text{PI control}} \tag{2.32}$$

where $\boldsymbol{\lambda}_f^{\omega}$ denotes the complex gain of a measurement filter at the angular frequency ω. In (2.32), the generation of current references $\boldsymbol{I}_s^{dq*}$ differs between the GFL and GFM controls.

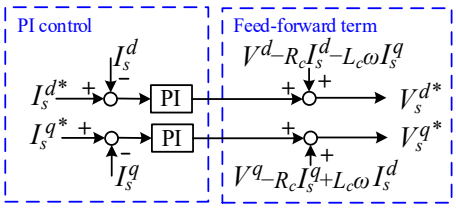

Fig. 2.14. Diagram of inner current control structure.

For GFL inverters, the *q*-axis current reference is regulated by the AC voltage droop control based on the measured positive sequence voltage magnitude, as shown in Fig. 2.12(c). The *d*-axis current reference is regulated by the DC voltage control, where double-fundamental-frequency oscillations appear in DC voltage under unbalanced grid conditions. Denote the apparent power as $\boldsymbol{S}$. During unbalanced grid conditions, the power outputs of the GSC are derived as

$$\begin{aligned}
\boldsymbol{S} &= P + jQ = \boldsymbol{V}^{dq}\hat{\boldsymbol{I}}_s^{dq} \\
&= (\boldsymbol{V}^{dq+} + \boldsymbol{V}^{dq-}e^{-j2\omega_n t})(\hat{\boldsymbol{I}}_s^{dq+} + \hat{\boldsymbol{I}}_s^{dq-}e^{j2\omega_n t}) \\
&= \boldsymbol{V}^{dq+}\hat{\boldsymbol{I}}_s^{dq+} + \boldsymbol{V}^{dq-}\hat{\boldsymbol{I}}_s^{dq-} + \underbrace{\boldsymbol{V}^{dq+}\hat{\boldsymbol{I}}_s^{dq-}e^{j2\omega_n t} + \boldsymbol{V}^{dq-}\hat{\boldsymbol{I}}_s^{dq+}e^{-j2\omega_n t}}_{\text{oscillations in power}}
\end{aligned} \tag{2.33}$$

where the symbol ^ denotes the conjugates of *dq* components. The DC-link components are given by

$$V_{dc}C_{dc}\frac{dV_{dc}}{dt} = P - P_{MSC} = \mathrm{Re}\left(\boldsymbol{V}^{dq}\hat{\boldsymbol{I}}_s^{dq}\right) - \mathrm{Re}\left(\boldsymbol{V}_{MSC}^{dq}\hat{\boldsymbol{I}}_{MSC}^{dq}\right) \tag{2.34}$$

where subscript *MSC* denotes the components in the machine-side converter (MSC) side. Since the MSC-side AC components are determined by the permanent magnetic synchronous generators (PMSGs), only positive sequence components exist. Therefore,

$$\begin{cases}
V_{dc}C_{dc}\,dV_{dc}/dt = \Delta P^{dc} + \Delta P^{2\omega_n} \\
\Delta P^{dc} = \mathrm{Re}\left(\boldsymbol{V}^{dq+}\hat{\boldsymbol{I}}_s^{dq+} - \boldsymbol{V}_{MSC}^{dq+}\hat{\boldsymbol{I}}_{MSC}^{dq+} + \boldsymbol{V}^{dq-}\hat{\boldsymbol{I}}_s^{dq-}\right) \\
\Delta P^{2\omega_n} = \mathrm{Re}\left(\boldsymbol{V}^{dq-}\hat{\boldsymbol{I}}_s^{dq+}e^{-j2\omega_n t} + \boldsymbol{V}^{dq+}\hat{\boldsymbol{I}}_s^{dq-}e^{j2\omega_n t}\right)
\end{cases} \tag{2.35}$$

From (2.35), double-fundamental-frequency oscillations appear in DC voltage under unbalanced grid condition. These oscillations are cut by the measurement filter and the PI regulator in the outer loop. For GFL inverters with other control modes, such as *P*/*Q* control or P/V_{ac} control, the double-fundamental-frequency oscillations in active and reactive power can also be eliminated by the measurement filter and PI regulator in the outer loop. Hence, there is almost no negative sequence component with double-fundamental-frequency oscillations in the current references. Remove the positive sequence components, (2.32) is rewritten as

$$\boldsymbol{V}_s^{dq-} = \boldsymbol{\lambda}_f^{\omega_n}(\boldsymbol{V}^{dq-} - \boldsymbol{Z}_c\boldsymbol{I}_s^{dq-} + \boldsymbol{R}_I^{2\omega_n}\boldsymbol{I}_s^{dq-}) \tag{2.36}$$

Combining (2.30) and (2.36), $\boldsymbol{Z}^-$ of GFL inverters is given by

$$\boldsymbol{Z}_{GFL}^- = \boldsymbol{V}^-/\boldsymbol{I}_s^- = (\boldsymbol{Z}_c(1-\boldsymbol{\lambda}_f^{\omega_n}) + \boldsymbol{\lambda}_f^{\omega_n}\boldsymbol{R}_I^{2\omega_n})/(1-\boldsymbol{\lambda}_f^{\omega_n}) = \boldsymbol{Z}_c + \boldsymbol{\lambda}_f^{\omega_n}\boldsymbol{R}_I^{2\omega_n}/(1-\boldsymbol{\lambda}_f^{\omega_n}) \tag{2.37}$$

where $\boldsymbol{\lambda}_f^{\omega_n} = e^{j\theta_{shift}} = 1\angle\theta_{shift}$. θ_{shift} denotes the phase shift caused by the measurement filter. To facilitate understanding, the 2nd-order Butterworth low-pass filter is taken as an example, the complex gain becomes

$$\boldsymbol{\lambda}_f^{\omega_n} = 1/(1+j\sqrt{2}r+(jr)^2) = -(r^2-1+j\sqrt{2}r)/(2r^2+(r^2-1)^2) = e^{j\theta_{shift}} \tag{2.38}$$

where $r = \dfrac{\omega_n}{2\pi f_m}$. f_m denotes the cut-off frequency in kHz. $\theta_{shift} = \arctan(\dfrac{\sqrt{2}r}{r^2-1})$. In (2.37), larger θ_{shift} leads to a larger denominator, thus reducing the magnitude of $\boldsymbol{Z}_{GFL}^-$. However, since the typical range of the cut-off frequency of the measurement filter is 2 to 5 kHz [74], θ_{shift} is minimal. Hence, $\boldsymbol{Z}_{GFL}^-$ becomes a large impedance. When there is no additional negative-sequence control loop for GFL inverters, the negative sequence current ($\boldsymbol{I}^-$) produced by GFL inverters is generally insignificant, to the point where it can be treated as an open circuit in the negative sequence system. For GFM inverters, the current references are regulated by the inner voltage control based on *dq* voltages (See Fig. 2.12(d)), as given by

$$\boldsymbol{I}_s^{dq*} = \boldsymbol{R}_V^{\omega}(\boldsymbol{V}^{dq*} - \boldsymbol{\lambda}_f^{\omega}\boldsymbol{V}^{dq}) \tag{2.39}$$

where the *q*-axis voltage reference is zero, while the *d*-axis voltage reference is generated by the reactive power droop control. Since the oscillations in reactive power are filtered by the low-pass filter, the voltage references are only positive sequence components. Therefore, the negative sequence components in $\boldsymbol{I}_s^{dq*}$ are conveyed by the $\boldsymbol{V}^{dq*}$. (2.32) can be rewritten as

$$\boldsymbol{V}_s^{dq-} = \boldsymbol{\lambda}_f^{\omega_n}(\boldsymbol{V}^{dq-} - \boldsymbol{Z}_c\boldsymbol{I}_s^{dq-} + \boldsymbol{R}_I^{2\omega_n}(\boldsymbol{R}_V^{2\omega_n}\boldsymbol{V}^{dq-} + \boldsymbol{I}_s^{dq-})) \tag{2.40}$$

Combining (2.30) and (2.40), $\boldsymbol{Z}^-$ of GFM inverters is given by

$$\boldsymbol{Z}_{GFM}^- = \frac{\boldsymbol{V}^-}{\boldsymbol{I}_s^-} = \frac{\boldsymbol{Z}_c(1-\boldsymbol{\lambda}_f^{\omega_n}) + \boldsymbol{\lambda}_f^{\omega_n}\boldsymbol{R}_I^{2\omega_n}}{1-\boldsymbol{\lambda}_f^{\omega_n} - \boldsymbol{R}_V^{2\omega_n}\boldsymbol{R}_I^{2\omega_n}\boldsymbol{\lambda}_f^{\omega_n}} \tag{2.41}$$

Since θ_{shift} is minimal, the denominator is approximately

$$\lim_{\theta_{shift}\to 0}\left|1-\boldsymbol{\lambda}_f^{\omega_n} - \boldsymbol{R}_V^{2\omega_n}\boldsymbol{R}_I^{2\omega_n}\boldsymbol{\lambda}_f^{\omega_n}\right| = \frac{\sqrt{(k_{iI}{}^2 + (2k_{pI}\,\omega_n)^2)(k_{iV}{}^2 + (2k_{pV}\,\omega_n)^2)}}{4\,\omega_n{}^2} \tag{2.42}$$

From (2.41) and (2.42), with respect to $\boldsymbol{Z}_{GFL}^-$, the magnitude of $\boldsymbol{Z}_{GFM}^-$ is relatively smaller. This indicates that GFM inverters can provide a lower impedance path for $\boldsymbol{I}^-$ circulation compared to GFL inverters. The magnitude and angle of $\boldsymbol{Z}_{GFM}^-$ are approximately given by

$$\lim_{\theta_{shift}\to 0} Z_{GFM}^- = \left|\frac{1}{\boldsymbol{R}_V^{2\omega_n}}\right| = \frac{2\omega_n}{\sqrt{k_{iV}{}^2 + (2k_{pV}\,\omega_n)^2}} \tag{2.43}$$

$$\lim_{\theta_{shift}\to 0} \theta_{Z_{GFM}}^- = \arctan\left(\frac{\mathrm{Im}(1/\boldsymbol{R}_V^{2\omega_n})}{\mathrm{Re}(1/\boldsymbol{R}_V^{2\omega_n})}\right) = \arctan\left(\frac{k_{iV}}{2k_{pV}\,\omega_n}\right) \tag{2.44}$$

From (2.43) and (2.44), the inner voltage control parameters have a significant impact on the magnitude and angle of $\boldsymbol{Z}_{GFM}^{-}$. The derivation also suggests that the currents produced by GFM inverters are generated by *dq* voltage references through inner voltage control, making the IBR more akin to a voltage source. This is a crucial characteristic of GFM controls. Conversely, in GFL inverters, the current references are calculated based on DC voltage and AC voltage drops, to inject the required active and reactive power into the grid, playing a role as a current injection source.

The analytical results are summarized in the following:

(i) The phase shift caused by the measurement filter largely determines $\boldsymbol{Z}_{GFL}^{-}$. As the phase shift becomes larger, the magnitude of $\boldsymbol{Z}_{GFL}^{-}$ reduces. Typically, a small phase shift leads to a large magnitude of $\boldsymbol{Z}_{GFL}^{-}$, to the point where it can be treated as an open circuit in the negative sequence system.

(ii) By incorporating voltage regulations, GFM inverters can provide a path for the $\boldsymbol{I}^{-}$ circulation. Hence, $\boldsymbol{Z}_{GFM}^{-}$ has a smaller magnitude in comparison to $\boldsymbol{Z}_{GFL}^{-}$. When the current references are regulated by the inner voltage control, the magnitude and angle of $\boldsymbol{Z}_{GFM}^{-}$ are primarily determined by the inner voltage control parameters. The inverter has the potential to provide sufficient $\boldsymbol{I}^{-}$ injection. A simplified impedance computation method based on (2.43) and (2.44) is proposed for $\boldsymbol{Z}_{GFM}^{-}$.

During FRT modes, IBRs are required to inject reactive current into the grid, as set forth by grid codes. The relations between *dq* components and active and reactive currents are illustrated as follows

$$P + jQ = \boldsymbol{V}^{dq}\hat{\boldsymbol{I}}^{dq} = Ve^{j\theta_V}Ie^{-j\theta_I} = V(\underbrace{I\cos(\theta_I - \theta_V)}_{I_P}) - j\underbrace{I\sin(\theta_I - \theta_V)}_{I_Q}) \tag{2.45}$$

$$\Rightarrow \begin{cases} I_P - jI_Q = \boldsymbol{I}^{dq}e^{-j\theta_V} \\ \boldsymbol{I}^{dq} = (I_P - jI_Q)e^{j\theta_V} \end{cases} \tag{2.46}$$

where $\hat{\boldsymbol{I}}^{dq}$ indicates the conjugates of *dq* currents. Subscripts P and Q denote active and reactive components, respectively. For GFL controls, the *q*-axis voltage is supposed to be regulated to zero by PLL, i.e., $V^q = 0$. Considering the phase of voltages $\theta_V = \arctan(\frac{V^q}{V^d})$, θ_V equals zero. Hence, the reactive current predominantly matches the *q*-axis current. Due to the absence of a PLL under certain GFM controls, the *q*-axis voltage is not necessarily zero. Hence, the phase of voltages θ_V might not be zero. The angular relation needs to be incorporated for reactive current injection of GFM inverters. Based on the characteristic curves for the reactive current injection of the *K*-factor-based method (see Fig. 1.7), under unbalanced grid conditions, I_Q^{-} shall be injected to reduce the negative sequence voltage ($\boldsymbol{V}^{-}$). Per IEEE Std. 2800-2022 7.2.2.3.4, some provisions are presented as follows:

Denote the pre-fault reactive current injection as I_Q^{pre}. The incremental positive sequence reactive current $\Delta I_Q = I_Q - I_Q^{pre}$. Note that ΔI_Q^{-} should not be increased above ΔI_Q^{+}.

Denote the angular relations between the $\boldsymbol{I}^{-}$ and $\boldsymbol{V}^{-}$ as $\Delta\theta^{-} = \theta_I^{-} - \theta_V^{-}$. For full-size converter-based IBR units, $\Delta\theta^{-}$ should be within a range of 90° to 100°.

The current capacity of IBRs is limited. The current limiter should restrict $\boldsymbol{I}^-$ to prevent semiconductor switches from being damaged by a sustained overcurrent.

To comply with these requirements, this section implements two FRT control solutions for BPSC and PNSC strategies, with detailed $\boldsymbol{I}^-$ injection mechanisms.

2.2.1.1 Fault Ride-Through Control Solution Design for BPSC Strategies

The equivalent impedance representation illustrates the negative sequence behavior of GFL and GFM inverters with BPSC strategies. Since the magnitude of $\boldsymbol{Z}_{GFL}^-$ is generally large, I_Q^- injection is not applicable to GFL BPSC strategies. For GFM BPSC strategies, the magnitude and angle of $\boldsymbol{Z}_{GFM}^-$ are primarily determined by the inner voltage control parameters. Based on (2.39) and (2.46), the injected active and reactive currents are derived as

$$I_P^* - jI_Q^* = \boldsymbol{R}_V^{\omega}(\boldsymbol{V}^{dq*} - \boldsymbol{\lambda}_f^{\omega}\boldsymbol{V}^{dq})e^{-j\theta_V} \tag{2.47}$$

The injected $\boldsymbol{I}^-$ is determined as

$$I_P^{-*} - jI_Q^{-*} = \boldsymbol{I}_s^{dq-*}e^{-j\theta_V} = -\boldsymbol{R}_V^{2\omega_n}\boldsymbol{\lambda}_f^{\omega_n}\boldsymbol{V}^{dq-}e^{-j\theta_V} \tag{2.48}$$

To comply with FRT requirements, the angle of $\boldsymbol{Z}_{GFM}^-$ should range from 90˚ to 100˚. According to the reference direction of current in Fig. 2.13, (2.44) yields

$$\theta_{Z_{GFM}}^- \approx \arctan\left(\frac{k_{iV}}{2k_{pV}\omega_n}\right) = \pi/2 \tag{2.49}$$

which requires

$$\frac{k_{iV}}{2k_{pV}\omega_n} = \infty \tag{2.50}$$

From (2.49) and (2.50), when $k_{iV} \gg k_{pV}$, $\theta_{Z_{GFM}}^-$ approximately equals π/2. Since $\theta_{Z_{GFM}}^- = \theta_V^- - \theta_{I_s}^-$, the phase angle between $-\boldsymbol{I}_s^-$ and $\boldsymbol{V}^-$ is close to 90˚, indicating that the $\boldsymbol{I}^-$ injection leads $\boldsymbol{V}^-$ by 90˚, i.e., $\theta_I^- - \theta_V^- = \pi/2$. Hence, from (2.46), I_Q^- is prioritized.

When the current limit is reached, the current limiter based on *Q* priority is activated to avoid overcurrent and ensure sufficient reactive current injection, as given by

$$\begin{cases} \left|I_Q^*\right| \le I_s^{lim} \\ \left|I_P^*\right| \le \sqrt{(I_s^{lim})^2 - (I_Q^*)^2} \end{cases} \tag{2.51}$$

where superscript *lim* denotes the current limit. The designated priority current can reach the maximum value. Then the current references from the current limiter are determined as

$$\tilde{\boldsymbol{I}}_s^{dq*} = (\tilde{I}_P^* - j\tilde{I}_Q^*)e^{j\theta_V} \tag{2.52}$$

Assume $I_P^{-*} \approx 0$, from (2.43), the relation between inner voltage control parameters and the *K*-factor (K_Q^-) (see Fig. 1.7) is approximately as

$$K_Q^- \approx \frac{\sqrt{{k_{iV}}^2 + (2k_{pV}\omega_n)^2}}{2\omega_n} \tag{2.53}$$

To facilitate understanding, an FRT control solution for GFM BPSC strategies is depicted in Fig. 2.15.

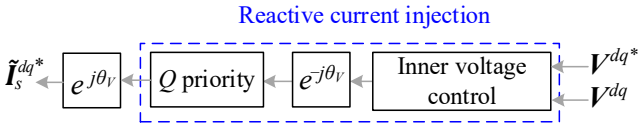

Fig. 2.15. FRT control solution for GFM BPSC strategies

This analysis shows that the negative sequence response of GFM with BPSC is sensitive to inner controller parameters. On the other hand, these parameters must be primarily tuned for system stability. They cannot be freely adjusted just to meet negative sequence current requirements as this could compromise system stability, dynamic response, and overall power quality.

2.2.1.2 Fault Ride-Through Solution for PNSC Strategies

To separate sequence components, the decoupled double SRF (DDSRF) is employed to eliminate the coupling of double-fundamental-frequency oscillations, as given by

$$\boldsymbol{X}^{dq-} = \boldsymbol{X}^{\alpha\beta} e^{j\theta_l} - \left(\zeta_f^{j\omega} \boldsymbol{X}^{\alpha\beta} e^{-j\theta_l}\right) e^{-j2\theta_l} \tag{2.54}$$

where $\zeta_f^{j\omega} = \omega_{lp} / (j\omega + \omega_{lp})$. $\zeta_f^{j\omega}$ and ω_{lp} denote the complex gain and cut-off angular frequency of a low-pass filter, respectively. In (2.54), to implement the DDSRF in GFL controls, the PLLs regulate the phase angle θ_l as the input of the DDSRF. Whereas, in GFM controls, the phase angle is regulated using PSLs, which preserves the frequency regulation ability of GFM controls.

When $\left|K_Q^+ \Delta V^+\right| + \left|K_Q^- \Delta V^-\right| \le I_s^{lim}$, the IBR can inject required reactive currents. To meet the FRT requirements, ΔI_Q^- is prescribed as

$$\Delta I_Q^- = K_Q^- \Delta V^- \le \Delta I_Q^+ \tag{2.55}$$

To ensure converter currents below the capacity limits, the current limiter is designed by incorporating the sequence components, as follows:

$$\begin{cases} I_P^{-*} = 0 \\ \left|I_Q^{-*}\right| = \left|I_s^{-*}\right| \le I_s^{lim} \end{cases} \tag{2.56}$$

where I_P^{-*} is set to zero to spare the current capacity for the reactive current injection and ensure the range of $\Delta\theta^-$ being 90˚ to 100˚. Similar to (2.51), the positive sequence components are constrained by the current limiter based on Q priority.

To fully utilize the maximum current capacity, a current scaling method is employed. First, the coordinate system of current references is converted from the *dq* frame to the *abc* frame. Then a scale factor K_{scale} is established to multiply the current references, ensuring that the faulty phase current can reach the current limit, as given by

$$\tilde{\boldsymbol{I}}_s^{dq-*} = K_{scale} K_Q^- \Delta V^- e^{j(\theta_V^- + \frac{\pi}{2})} = \tilde{I}_Q^{-*} e^{j(\theta_V^- + \frac{\pi}{2})} \tag{2.57}$$

where $K_{scale} = I_s^{lim} / \max(I_s^{a*}, I_s^{b*}, I_s^{c*})$. θ_V^- denotes the angle of $\boldsymbol{V}^-$. Then the magnitude and angle of $\boldsymbol{Z}^-$ can be approximately determined as

$$\begin{cases} Z^- \approx K_{scale} K_Q^- \\ \theta_Z^- \approx -\pi/2 \end{cases} \tag{2.58}$$

To this end, the FRT control solution for PNSC strategies, as depicted in Fig. 2.16, implements an

accurate I_Q^- injection.

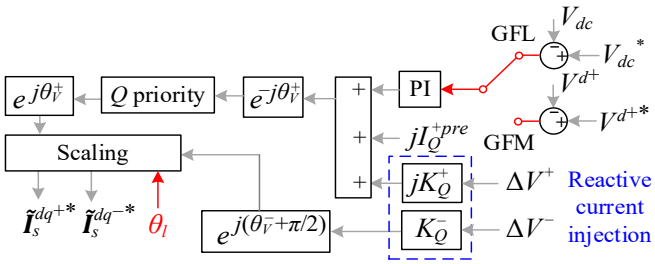

Fig. 2.16. FRT control solution for GFL and GFM PNSC strategies

2.2.2 Comparative Studies

To conduct comprehensive studies on the negative sequence behavior of GFL and GFM inverters, a 230 kV/60 Hz IEEE PSRC D29 system with two Type-IV WPs is built using an EMT-type tool, as displayed in Fig. 2.17. To investigate the overall negative sequence behavior of the IBR rather than the detailed operations of each individual unit, aggregated models are used for improving simulation efficiency. The measurement filter is the 2nd order Butterworth. The virtual synchronous machine (VSM) control is employed as the PSL for GFM inverters. The fault location is set at 71% of the total length of the 70-mile tie lines. The fault occurs at t = 2 s and its duration is set to 0.5 s for illustration purposes. The system parameters can be found in Table A1 of the Appendix.

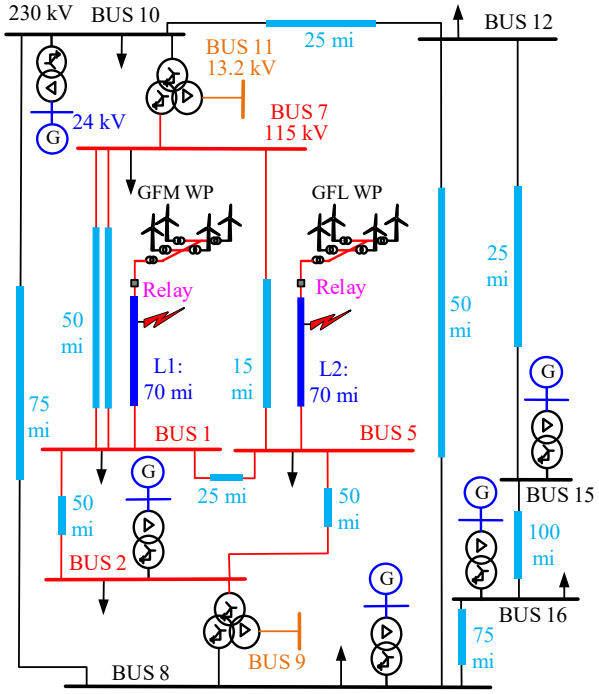

Fig. 2.17. IEEE PSRC D29 system with GFM and GFL WPs

To simplify the representations, GFL-BPSC and GFM-BPSC denote GFL and GFM inverters with BPSC strategies, respectively while GFL-PNSC and GFM-PNSC denote GFL and GFM inverters with PNSC strategies, respectively.

To validate the FRT capacities of GFL and GFM inverters, the control parameters are set as f_m=2.5

kHz, $K_Q^+ = K_Q^-$ =2, I_s^{lim} =1.2 pu. For GFM-PNSC, k_{pv} =1, and k_{iv} =200. For GFM-BPSC, k_{pv} =0.8, and k_{iv} =1500. The FRT control solutions are implemented in the GFM-BPSC, GFL-PNSC, and GFM-PNSC. During a line-A-to-ground (AG) fault, negative sequence components measured at the POC are displayed in phasor representation, as shown in Fig. 2.18. The GFL-BPSC has a minor $\boldsymbol{I}^-$ contribution compared to other GFM and GFL control strategies, where it is significant. The angular relation $\Delta\theta^-$ of the GFL-BPSC exceeds 100˚, while under other GFM and GFL control strategies, it falls within the range of 90˚ to 100˚. This shows that the GFL-BPSC cannot produce the required magnitude and angle of the $\boldsymbol{I}^-$.

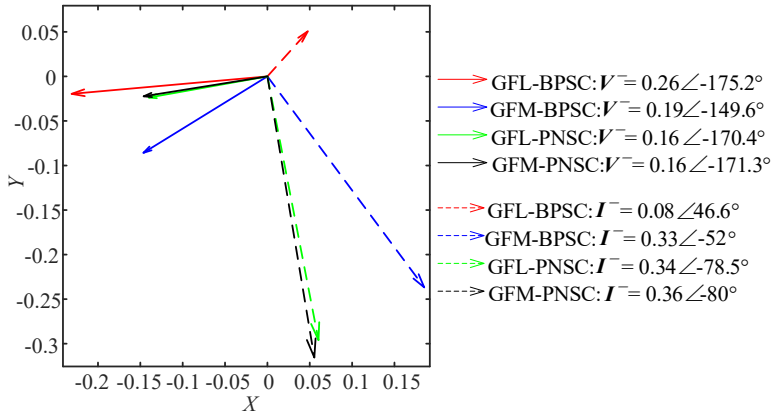

Fig. 2.18. Phasor representation of negative sequence components for different GFM and GFL control strategies

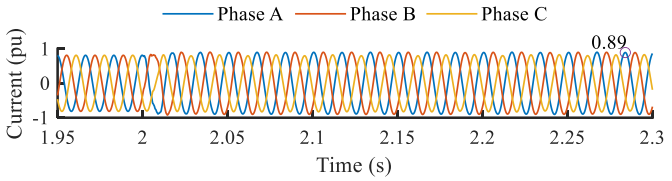

(a) GFL-BPSC

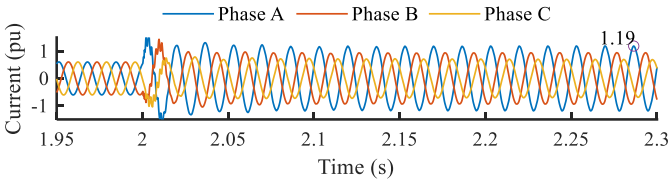

(b) GFM-BPSC

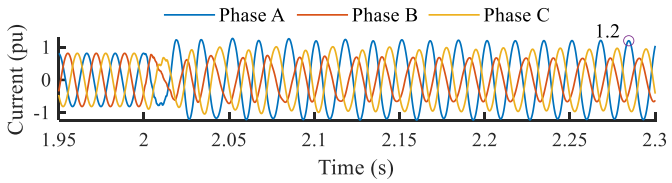

(c) GFL-PNSC

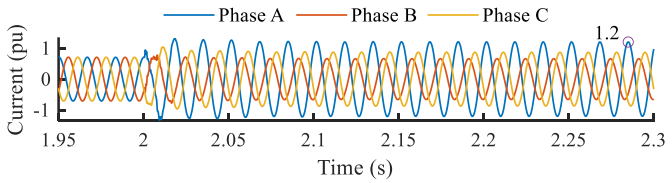

(d) GFM-PNSC

Fig. 2.19. Converter current waveforms for different GFM and GFL control strategies

The converter current waveforms are displayed in Fig. 2.19. The fault current outputs of WPs in steady state under various fault scenarios are shown in Table I. From Fig. 2.19(a), given the large magnitude of $\boldsymbol{Z}^{-}$ under the GFL-BPSC scheme, the positive sequence currents utilize nearly all converter capacities. Therefore, the converter current outputs are almost balanced. Fig. 2.19(b) illustrates the significant imbalance in the three-phase current waveforms under GFM-BPSC, indicating the contribution of negative-sequence current from the GFM inverter. From the highlighted results in Table I and Fig. 2.19(c) and Fig. 2.19(d), the faulted phase current can reach the current limits for the GFM-PNSC and GFL-PNSC. This indicates that the scaling method achieves the full utilization of converter capacities. In the FRT solution for PNSC strategies, the scale factor K_{scale} is determined by three-phase currents. In Fig. 2.19(c) and Fig. 2.19(d), the angle and transients in phase currents of the GFL-PNSC and GFM-PNSC are not identical. This leads to inconsistent K_{scale} (K_{scale} =1.11 for GFM-PNSC, K_{scale} =1.08 for GFL-PNSC). Therefore, there is a slight difference in $\boldsymbol{I}^{-}$ outputs of the GFL-BPSC and GFM-PNSC, as observed in Fig. 2.18 and Table 2-3.

TABLE 2-3

Phase Currents and the Active and Reactive Currents

Type	Fault	I_s^a	I_s^b	I_s^c	$I_P^+ + jI_Q^+$	$I_P^- + jI_Q^-$	$\Delta\theta^-$
GFL-BPSC	AG	0.90	0.90	0.83	0.96+*j*0.26	-0.07-j0.05	216.9
	BG	0.83	0.90	0.90	0.96+*j*0.26	-0.07-j0.05	216.3
	CG	0.90	0.83	0.90	0.96+*j*0.26	-0.07-j0.05	215.1
GFM-BPSC	AG	1.19	0.94	0.70	0.51+*j*0.70	-0.05+*j***0.33**	**97.7**
	BG	0.70	1.19	0.95	0.51+*j*0.70	-0.05+*j***0.33**	**97.7**
	CG	0.95	0.70	1.19	0.51+*j*0.70	-0.05+*j***0.33**	**97.7**
GFL-PNSC	AG	**1.20**	0.66	0.96	0.98+*j*0.37	0.00+*j***0.33**	**90.6**
	BG	0.96	**1.20**	0.66	0.97+*j*0.38	0.00+*j***0.34**	**90.6**
	CG	0.66	0.96	**1.20**	0.97+*j*0.38	0.00+*j***0.34**	**90.6**
GFM-PNSC	AG	**1.20**	0.66	0.87	0.89+*j*0.51	-0.01+*j***0.35**	**91.3**
	BG	0.87	**1.20**	0.66	0.89+*j*0.51	-0.01+*j***0.35**	**91.3**
	CG	0.66	0.87	**1.20**	0.89+*j*0.51	-0.01+*j***0.35**	**91.3**

To validate the analytical results, for the GFL-BPSC, simulation results of $\boldsymbol{Z}^{-}$ and phase shift under different cut-off frequencies are displayed in Fig. 2.20. As f_m rises, the $\left|\theta_{shift}\right|$ decreases while the Z_{GFL}^{-} increases. Fig. 2.21 shows that the *dq* converter currents exhibit double-fundamental-frequency oscillations while there are no oscillations in the *dq* current references. These relations and characteristics match the analytical result (i) in Section 2.2.1.

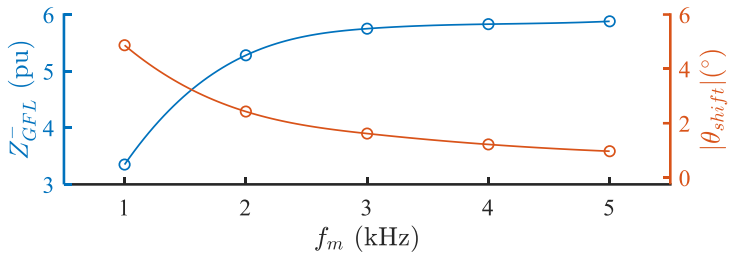

Fig. 2.20. $\boldsymbol{Z}^{-}$ and phase shift for the GFL-BPSC

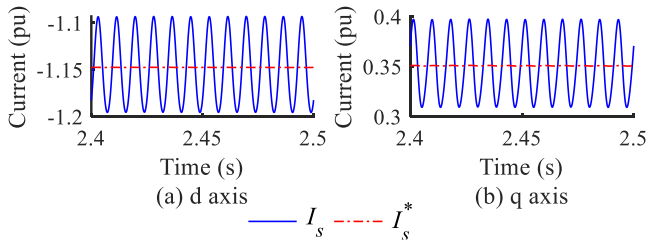

Fig. 2.21. Simulation results of *dq* converter currents and current references for the GFL-BPSC

For the GFM-BPSC, when k_{pv} is set to 1, simulation results of $\boldsymbol{Z}^{-}$ under different k_{iv} are demonstrated in Table 2-4. As k_{iv} increases, Z_{GFM}^{-} reduces while $\theta_{Z_{GFM}}^{-}$ gradually approaches -90°. These features match the analytical result (ii) in Section 2.2.1. Additionally, based on the simplified calculation in (2.43) and (2.44), the calculation and simulation results in Fig. 2.22 are approximately consistent. The simplified calculation assumes a phase shift of zero. This causes the error. In Fig. 2.23, the *dq* voltages exhibit double-fundamental-frequency oscillations, while there are no oscillations in the *dq* voltage references.

TABLE 2-4

$\boldsymbol{Z}^{-}$ of the GFM-BPSC

k_{iv}	200	800	1400	2000	2400
Z_{GFM}^{-}	1.03	0.76	0.52	0.38	0.34
$\theta_{Z_{GFM}}^{-}$	-156.7	-121.1	-104.2	-95.8	-93.2

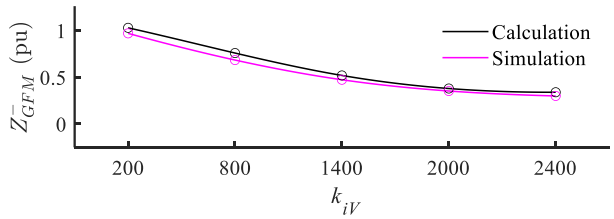

(a) Magnitude

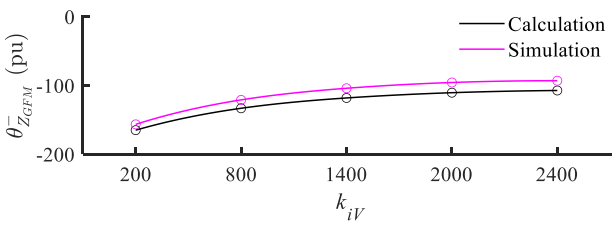

(b) Angle

Fig. 2.22. Calculation and simulation results of $\boldsymbol{Z}^{-}$ for the GFM-BPSC

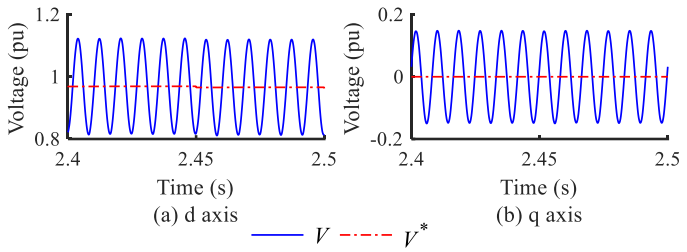

Fig. 2.23. Simulated *dq* voltages and its references – GFM-BPSC

The simulation results show that negative sequence current and voltage phasors in GFM-BPSC are highly sensitive to inner control parameters (Fig. 2.24), leading to variations in negative sequence impedance. For instance, with k_{iv} = 200, the phase angle between negative sequence current and voltage is 156.7°, well outside the 90°-100° range required by IEEE Std. 2800-2022. This demonstrates that GFM-BPSC fails to meet FRT requirements under certain inner control parameter settings.

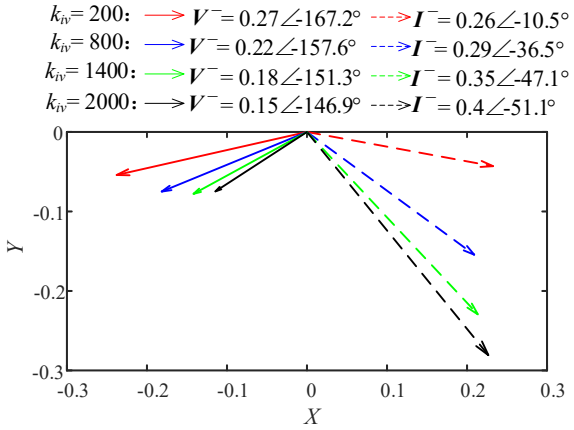

Fig. 2.24. Phasor representation of the $\boldsymbol{I}^-$ and $\boldsymbol{V}^-$ for the GFM-BPSC under different inner control parameters

Furthermore, inner control parameters significantly impact dynamic performance. Fig. 2.25 shows substantial current oscillations in GFM-BPSC under different parameter settings. While adjusting these parameters theoretically could achieve desired negative sequence behavior, they must be primarily tuned for system stability. Therefore, inner control parameters cannot be freely modified to meet negative sequence current requirements, as this would compromise fundamental control objectives including stability, dynamic response, and power quality.

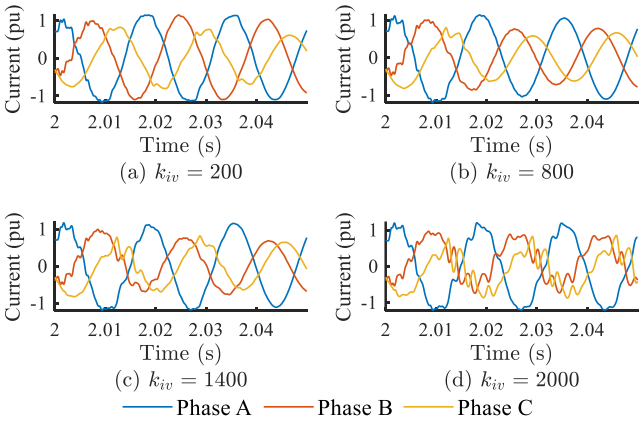

Fig. 2.25. Converter currents for the GFM-BPSC under different inner control parameters

For GFM-PNSC, the positive and negative sequence components have been separated by using DDSRF. The inner voltage control is only employed for the regulation of positive sequence components in normal operation and positive sequence residual current capacity during faults. Hence, the inner voltage control cannot affect the $\boldsymbol{I}^-$ outputs under GFM-PNSC fundamentally. Therefore, the $\boldsymbol{I}^-$ outputs and current waveforms under GFM-PNSC are consistent for different inner control parameters, as shown in Fig. 2.26 and Fig. 2.27.

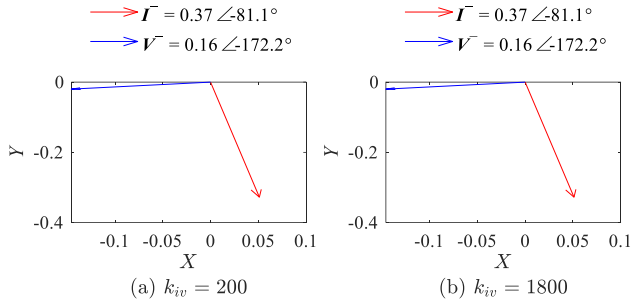

Fig. 2.26. Phasor representation of the $\boldsymbol{I}^-$ and $\boldsymbol{V}^-$ for the GFM-PNSC under different inner control parameters

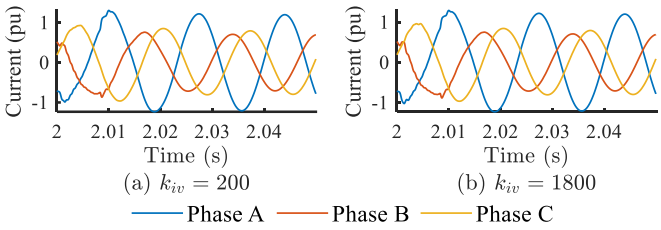

Fig. 2.27. Converter currents for the GFM-PNSC under different inner control parameters

The analysis in Section 2.2.1 is based on the hypothesis that the current capacity is sufficient. When the current references reach the current limit, the current limiter will be in service. Consequently, the current references are cut by the current limit. Hence, the impact of current limits on the negative sequence behavior of the GFM-BPSC cannot be ignored. By adjusting the current limits, simulation results of converter currents are shown in Fig. 2.28. As the current limit decreases, the distortion of the three-phase converter currents for the GFM-BPSC becomes increasingly noticeable, failing to regulate stable three-phase currents. Fig. 2.29 shows that under the 1.1 pu current limit, the GFL-PNSC and GFM-PNSC can still produce stabilized currents.

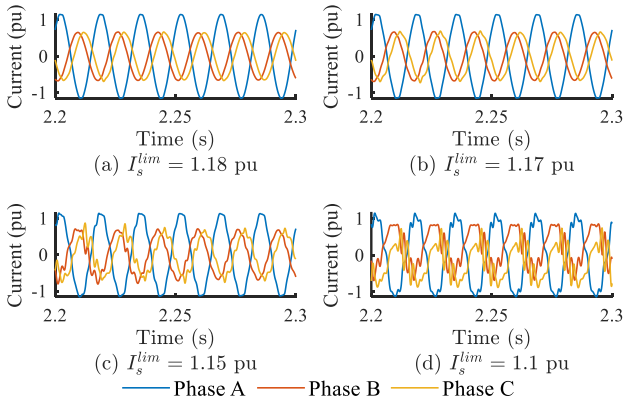

Fig. 2.28. Converter currents for the GFM-BPSC under different current limits

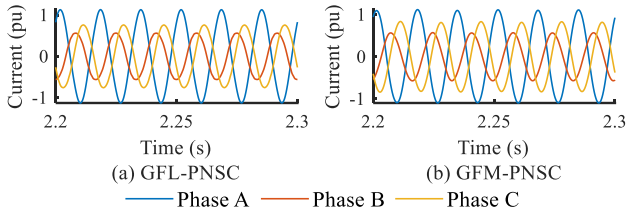

Fig. 2.29. Converter currents for the GFL-PNSC and GFM-PNSC (I_s^{lim}=1.1 pu)

Additionally, Fig. 2.30 shows the performance of GFM-BPSC under varying fault distances. For near-end faults, the voltage variation is significant, leading to a high fault current. Consequently, the insufficient current capacity of the inverter causes current distortion. For remote-end faults, the current capacity of the inverter is sufficient for the current injection to respond to the voltage variation. Hence, the phase currents are sinusoidal and stable. For the GFL-PNSC and GFM-PNSC, there is no distortion in phase currents under varying fault distances, as shown in Fig. 2.31 and Fig. 2.32, since the sequence components of currents are regulated in coordination.

Therefore, when the current capacity of the inverter is not sufficient, the currents regulated by the GFM-BPSC are distorted. The IBR should rely on PNSC strategies to regulate stable responses in the desired manner.

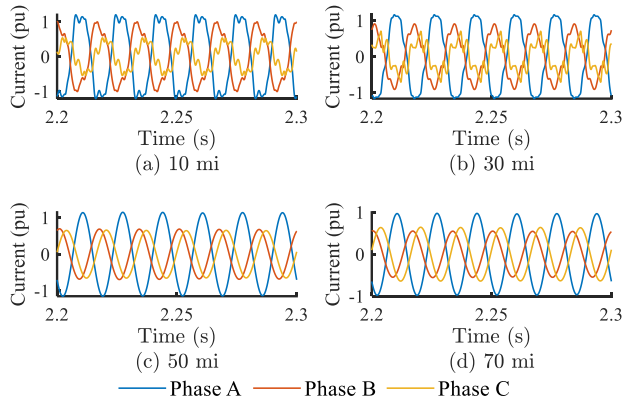

Fig. 2.30. Converter currents for the GFM-BPSC under varying fault distances

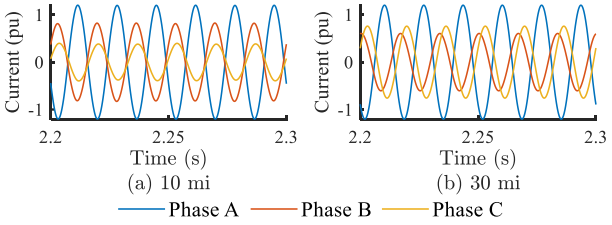

Fig. 2.31. Converter currents for the GFM-PNSC under varying fault distances

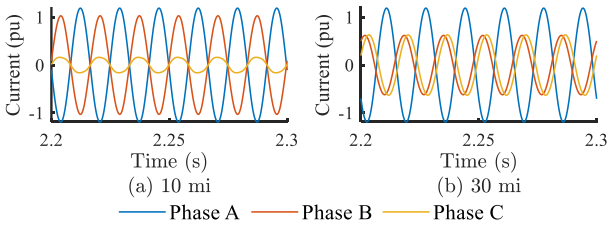

Fig. 2.32. Converter currents for the GFL-PNSC under varying fault distances

2.2.3 Conclusion

This section presents comparative studies on the negative sequence behavior of GFL and GFM inverters, considering negative sequence requirements in IEEE Std. 2800-2022. Key conclusions are drawn as follows:

i. Impacts of GFL-BPSC and GFM-BPSC on negative sequence impedance ($\boldsymbol{Z}^{-}$):

For GFL-BPSC, the magnitude and angle of $\boldsymbol{Z}^{-}$ are primarily determined by the phase shift in measurement filters. Typically, a small phase shift results in a large impedance, leading to GFL inverter being an open circuit approximation in the negative sequence network. For GFM-BPSC, the current references are typically generated by the inner voltage control. While the magnitude and angle of $\boldsymbol{Z}^{-}$ are influenced by the inner voltage control parameters $\{k_{pv}, k_{iv}\}$, these parameters must be primarily tuned for system stability and cannot be freely adjusted to meet negative sequence current requirements. The proposed simplified impedance computation method helps explain the relationship between control parameters and $\boldsymbol{Z}^{-}$.

ii. Advantages and limitations of FRT solutions:

The FRT control solutions show varying performance under different conditions. GFM-BPSC exhibits significant limitations including current distortion and high sensitivity to inner control parameters, current limits, and fault proximity. Furthermore, FRT compliance cannot be guaranteed for all conditions with BPSC due to the constraints on inner controller tuning. PNSC strategies are strongly recommended as they enable independent control of sequence components and optimal utilization of converter capacity through current scaling, providing more reliable FRT compliance without compromising stability.

3 Fault Ride-Through Control Solutions for Grid-Forming IBR

3.1 For Full Converter-based GFM-IBR

3.1.1 PNSC design of Grid-Forming Type-IV WTG

Fig. 3.1(a) shows the basic topology of Type-IV WTGs within a wind park (WP). The central wind park controller (WPC) manages reactive power at the point of interconnection (POI). Fig. 3.1(b) depicts the GSC and MSC control structures for GFM Type-IV WTGs operating in actual GFM mode. The current limiting methods, omitted from Fig. 3.1(b), are detailed later in the discussion of restricted mode operation.

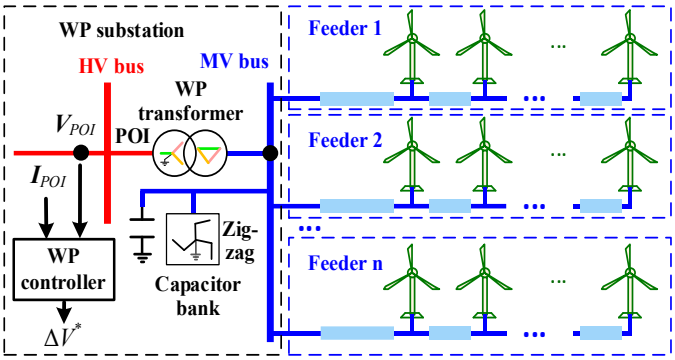

(a) Type-IV WTGs in a WP

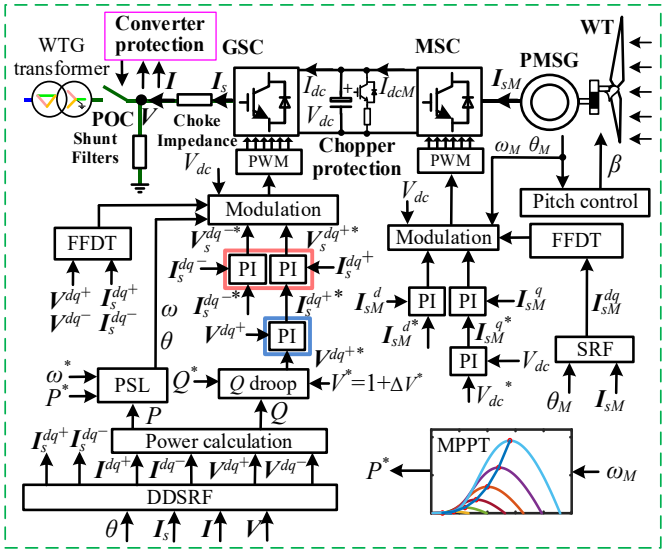

(b) Control structure of GFM Type-IV WTG

Fig. 3.1. Topology and control of GFM Type-IV WTGs in a WP.

Under unbalanced grid conditions, the GSC control regulates positive and negative sequence components through PSL implementation in the decoupled double synchronous reference frame (DDSRF). The WPC supplies voltage reference to the Q droop control. The blue and red boxes highlight the inner voltage and current structures, respectively. The FFDT block calculates feedforward terms. Each IBR unit includes AC overcurrent protection, voltage ride-through protection, and DC chopper protection to prevent overcurrent, meet voltage ride-through requirements, and maintain acceptable DC

voltage levels. The wind turbine system uses a permanent magnet synchronous generator (PMSG). An R-L choke impedance circuit serves as a filter to improve power quality.

This section uses italic letters to represent scalar variables, while complex vectors are denoted in bold. θ and ω denote phase angle and angular frequency, respectively. I and V denote the currents and voltages at the point of connection (POC), respectively. P and Q denote active and reactive power, respectively. Superscripts $\alpha\beta$ and dq represent vectors under the stationary reference frame and synchronous reference frame, respectively. Symbols + and – indicate positive and negative sequence components, respectively. The symbol * denotes the reference of controlled variables. Subscripts M, s, and dc indicate the components of MSC, GSC, and DC link, respectively.

During normal operation, conventional WTGs use the GSC control to regulate the DC-link voltage, with maximum power point tracking (MPPT) implemented through the MSC control. In GFM Type-IV WTGs, however, MPPT provides power reference to the PSL within the GSC control, as the PSL regulates active power and frequency in actual GFM mode. This relationship is expressed as:

$$\begin{cases} P^* = C_{p\max}\rho A(R/\lambda_{op}\,\omega_M)^3/2 \\ P = V^{d+}I^{d+} + V^{q+}I^{q+} + V^{d-}I^{d-} + V^{q-}I^{q-} \\ \dot{\theta} = \omega = K_\omega\omega^* + K_P(P^* - P) \end{cases} \tag{3.1}$$

where ρ: air density, ω_M: wind turbine rotational speed, R: blade radius, $C_{p\max}$: maximum power coefficient, λ_{op}: optimal tip-speed ratio, and A: rotor swept area. Different PSL implementations are given by:

$$\begin{bmatrix} K_\omega & K_P \end{bmatrix} = \begin{cases} \begin{bmatrix} \dfrac{D_\omega}{Js + D_\omega} & \dfrac{\lambda_f(s)}{Js + D_\omega} \end{bmatrix} & \text{VSM} \\ \begin{bmatrix} 1 & D_P\lambda_f(s) \end{bmatrix} & \text{droop} \\ \begin{bmatrix} 1 & \dfrac{\omega^*\kappa_1\lambda_f(s)}{(V^{d+*})^2} \end{bmatrix} & \text{dVOC} \end{cases} \tag{3.2}$$

where J: inertia constant, κ_1: synchronization control gain, D_ω: damping coefficient for frequency, D_P: damping coefficient for active power, $\lambda_f(s)$: low-pass filter. The control details and parameter design can be found in [9] and [12]. In GFM Type-IV WTGs, the MSC control regulates q-axis current reference based on the deviation in DC-link. The d-axis current reference maintains zero value to achieve unity power factor. These relationships are expressed as:

$$\begin{cases} I_{sM}^{d*} = 0 \\ I_{sM}^{q*} = \left(k_{pVdc} + k_{iVdc}/s\right)\left(V_{dc} - V_{dc}^*\right) \end{cases} \tag{3.3}$$

In addition, the DC chopper protection should be considered to prevent DC overvoltage, as shown in Fig. 3.2. It activates when V_{dc} exceeds $V_{\text{chopperON}}$ and deactivates when V_{dc} falls below $V_{\text{chopperOFF}}$.

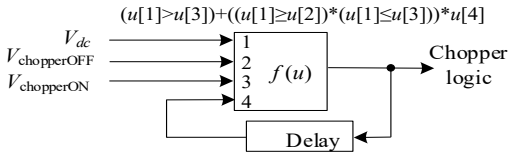

Fig. 3.2. Control strategy of DC chopper.

The active power output from the GSC in a single WTG infinite bus system is given by:

$$P = \frac{V_s V \sin\left(\theta - \theta_{grid}\right)}{X_{WTG}} \tag{3.4}$$

where X_{WTG} : equivalent reactance of WTG, θ_{grid} : phase angle of the AC grid. The GSC-MSC active power difference is:

$$\begin{aligned} \Delta P &= P_M - P = P_M - \frac{V_s V}{X_{WTG}} \sin\left(\theta - \theta_{grid}\right) \\ &= \left(I_{dcM} - I_{dc}\right) V_{dc} = \Delta I_{dc} V_{dc} \end{aligned} \tag{3.5}$$

where P_M : active power output from the MSC, ΔI_{dc} : DC-link current difference.

In actual GFM mode, under the PSL regulation, $P^*=P=P_M$. During grid faults, the GFM control may switch to restricted mode. Sharp active power variations can prevent following the power reference, causing θ divergence. This leads to P_M losing synchronization with P. While V_{dc} remains regulated by the MSC and restricted by DC chopper protection, ΔI_{dc} diverges. Active power imbalance weakens WTG synchronization. After fault clearance, power variations resurface during recovery, with potential current oscillations during transition risking overcurrent. To address these issues, two key improvements are proposed as follows:

1) Fault operation: The additional synchronization control regulates the orientation angle, maintaining a stable angular difference. The reactive current injection supports voltages, reducing power variation.

2) Post-fault recovery: The current limiting methods eliminate current transients and enable a smooth transition from restricted to actual GFM mode.

3.1.2 Current Saturation-based CLM

In existing studies, the positive sequence components can be constrained by the three prevailing current limiters, as follows:

- Instantaneous Limiter

$$\begin{cases} \left|I_Q^{+*}\right| \le k_q I_s^{+lim} \\ \left|I_P^{+*}\right| \le k_d I_s^{+lim} \end{cases} \tag{3.6}$$

In this section, under FRT mode, k_q= k_d =0.5.

- Magnitude Limiter

$$\sqrt{(I_P^{+*})^2 + (I_Q^{+*})^2} \le I_s^{+lim} \tag{3.7}$$

- Priority-based Limiter

$$\begin{cases} \left|I_Q^{+*}\right| \le I_s^{+lim} \\ \left|I_P^{+*}\right| \le \sqrt{(I_s^{+lim})^2 - (I_Q^{+*})^2} \end{cases} \tag{3.8}$$

These existing current limiters are employed in the proposed PNSC based on the assumption that $I_Q^{+*} \approx I_s^{q+*}$ and $I_P^{+*} \approx I_s^{d+*}$.

Compliance with grid codes requires considering the relationship between the reactive current injection and sequence components of voltages. According to the IEEE 2800 standard, all IBRs must have the capability to generate reactive current under unbalanced grid conditions. Specifically, the

standard mandates that the phase angle of the I2 phasor leads that of the negative sequence voltage (V2) phasor by an angle between 90° and 100° in IBRs with full-scale converters. Additionally, the full utilization of the converter current capacity is needed. In this work, the current limiters for I1 and I2 are implemented considering these features. In the positive sequence system, active and reactive powers delivered at the POC can be expressed by

$$\begin{aligned} P^+ + jQ^+ &= V^+ e^{j\theta_{V+}} I^+ e^{-j\theta_{I+}} \\ &= V^+ (\underbrace{I^+ \cos(\theta_{I+} - \theta_{V+})}_{I_P^+} - j \underbrace{I^+ \sin(\theta_{I+} - \theta_{V+})}_{I_Q^+}) \end{aligned} \tag{3.9}$$

where subscripts P and Q denote active and reactive components, respectively. Therefore, I1R and I2R are given by

$$I_P^+ - jI_Q^+ = (I^{d+} - jI^{q+}) e^{-j\arctan\left(\frac{V^{q+}}{V^{d+}}\right)} \tag{3.10}$$

For GFL-IBRs, due to the regulation of phase-locked loop (PLL), V^{q+}=0. Based on (3.10), I1R predominantly matches I^{q+}.

For GFM-IBRs, when the current limiter is activated in the FRT mode, V^{q+} may not be regulated to zero by the inner voltage controller. Since the orientation angle regulated by the PSL is the angle of the internal voltage vector, the positive sequence voltage (V1) at the POC has both d+ and q+ components. Hence, the implementation of reactive current injection in GFM-IBRs might not be consistent with that in GFL-IBRs. To realize the accurate current injection, the relation between dq+ currents and reactive currents of GFM-IBRs needs to be considered. The detailed relations are graphically illustrated in Fig. 3.3. In the sequence domain, the active and reactive power can be expressed as follows:

$$\begin{cases} P = P^+ + P^- = V^+ I_P^+ + V^- I_P^- \\ Q = Q^+ + Q^- = -V^+ I_Q^+ - V^- I_Q^- \end{cases} \tag{3.11}$$

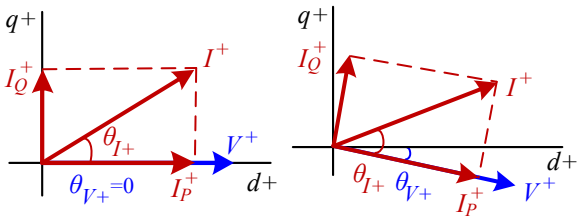

(a) GFL-IBR (b) GFM-IBR

Fig. 3.3. Phasor diagram of V1 and I1 in the dq+ frame.

Combining (3.9) and (3.11) yields:

$$\begin{cases} I^{d+} = V^{d+} I_P^+ / V^+ + V^{q+} I_Q^+ / V^+ \\ I^{d-} = V^{d-} I_P^- / V^- + V^{q-} I_Q^- / V^- \\ I^{q+} = -V^{q+} I_P^+ / V^+ + V^{d+} I_Q^+ / V^+ \\ I^{q-} = -V^{q-} I_P^- / V^- + V^{d-} I_Q^- / V^- \end{cases} \tag{3.12}$$

The requirements for reactive current injection of IBRs are set forth by the IEEE 2800 standard. Under unbalanced grid conditions, I1R and I2R shall be regulated to support V1 and reduce V2, respectively. Based on the K-factor-based method in Fig. 1.7, the incremental I1R and I2R are determined by the variation of V1 and V2, as follows:

$$\begin{cases} \Delta I_Q^+ = K_Q^+ \Delta V^+ = K_Q^+ (1 - V^+) \\ \Delta I_Q^- = K_Q^- \Delta V^- = K_Q^- V^- \end{cases} \tag{3.13}$$

where the coefficients $K_Q^+ = K_Q^-$ =2. Per IEEE 2800 standard, ΔI_Q^+ shall not be negative under balanced fault conditions. Under unbalanced fault conditions, $\left|\Delta I_Q^+\right|$ shall not be decreased below $\left|\Delta I_Q^-\right|$, i.e., $\left|\Delta I_Q^+\right| \geq \left|\Delta I_Q^-\right|$. To prevent the incremental reactive currents from exceeding the current limit I_s^{lim}, when $\left|K_Q^+ \Delta V^+\right| + \left|K_Q^- \Delta V^-\right| > I_s^{lim}$, the incremental reactive currents are determined as

$$\begin{cases} \Delta I_Q^+ = I_s^{lim} K_Q^+ \Delta V^+ \Big/ \left(\left|K_Q^+ \Delta V^+\right| + \left|K_Q^- \Delta V^-\right|\right) \\ \Delta I_Q^- = I_s^{lim} K_Q^- \Delta V^- \Big/ \left(\left|K_Q^+ \Delta V^+\right| + \left|K_Q^- \Delta V^-\right|\right) \end{cases} \tag{3.14}$$

To regulate the expected current, the reactive current references can be configured by the current injection method. During normal operation, the inner voltage control regulates the V^{q+} to zero. Hence, the pre-fault I1R matches pre-fault I_s^{q+}. To facilitate the absorption of reactive currents by IBRs, the references of reactive currents are derived as follows:

$$\begin{cases} I_Q^{+*} = I_s^{q+pre} + \Delta I_Q^+ \\ I_Q^{-*} = \Delta I_Q^- \end{cases} \tag{3.15}$$

where superscript *pre* denotes the pre-fault value. Under unbalanced grid conditions, the $d+$ axis current continues to be governed by the inner voltage controller, as given by

$$I_s^{d+*} = R_v^+(s)(V^{d+*} - V^{d+}) \tag{3.16}$$

where $R_v^+(s) = k_{pv}^+ + k_{iv}^+ / s$. Due to the additional reactive current injection, an incremental amount of I1R is also superimposed onto the $d+$ axis, as illustrated in Fig. 3.4.

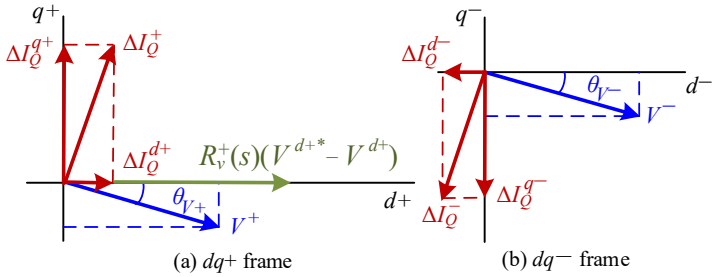

(a) $dq+$ frame (b) $dq-$ frame

Fig. 3.4. I1 and I2 injection of GFM-IBRs in the FRT mode.

Therefore, based on (3.9), (3.12), and (3.13), the dq current references for GFM-IBRs can be established by incorporating the relations between reactive currents and dq components, as follows:

$$\begin{cases} I_s^{d+*} = \underbrace{V^{q+} \Delta I_Q^+ / V^+}_{\Delta I_Q^{d+}} + R_v^+(s)(V^{d+*} - V^{d+}) \\ I_s^{q+*} = \underbrace{V^{d+} \Delta I_Q^+ / V^+}_{\Delta I_Q^{q+}} + I_s^{q+pre} \\ I_s^{d-*} = V^{q-} \Delta I_Q^- / V^- \\ I_s^{q-*} = V^{d-} \Delta I_Q^- / V^- \end{cases} \tag{3.17}$$

The active and reactive current references during unbalanced faults are given by

$$\begin{cases} I_P^{+*} = V^{d+} R_v^+(s)(V^{d+*} - V^{d+}) / V^+ \\ I_Q^{+*} = I_s^{q+pre} + \Delta I_Q^+ + V^{q+} R_v^+(s)(V^{d+*} - V^{d+}) / V^+ \\ I_P^{-*} = 0 \\ I_Q^{-*} = \Delta I_Q^- \end{cases} \tag{3.18}$$

where I_P^{-*} is set to zero to ensure that the negative sequence current leads the negative sequence voltage by 90°. I_Q^{-*} equals the negative sequence incremental reactive current. I_P^{+*} is derived from the output of *d*-axis inner voltage controller by considering the angular difference between *d*-axis and positive sequence voltage. I_Q^{+*} consists of the pre-fault reactive current, positive sequence incremental reactive current, and contribution of the *d*-axis inner voltage controller caused by the angular difference. The setting rules for incremental reactive currents $\left\{\Delta I_Q^+, \Delta I_Q^-\right\}$ are drawn as follows:

a) Per IEEE 2800 standard, $\left|\Delta I_Q^+\right| \geq \left|\Delta I_Q^-\right|$.

b) When $\left|K_Q^+ \Delta V^+\right| + \left|K_Q^- \Delta V^-\right| \leq I_s^{lim}$, based on the *K*-factor-based method, $\left\{\Delta I_Q^+, \Delta I_Q^-\right\}$ is determined by (3.13).

c) When $\left|K_Q^+ \Delta V^+\right| + \left|K_Q^- \Delta V^-\right| > I_s^{lim}$, to prevent the incremental reactive currents from exceeding the current limit, $\left\{\Delta I_Q^+, \Delta I_Q^-\right\}$ is determined by (3.14).

The block diagram of the proposed current reference generation is shown in Fig. 3.5.

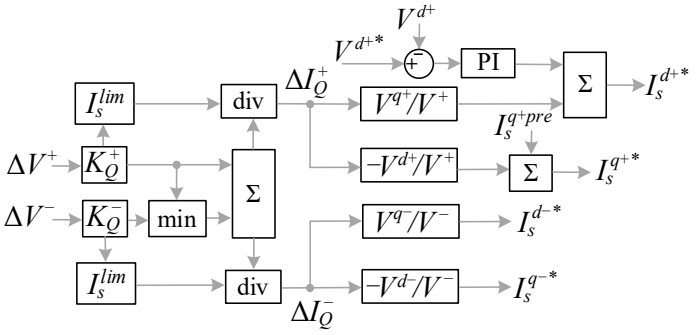

Fig. 3.5. Reference generation of I1 and I2 for GFM-IBR.

To achieve sufficient I2R contribution and reduce V2 on the grid side, I2 can be restrained as follows:

$$\begin{cases} \left|I_Q^{-*}\right| = \left|I_s^{-*}\right| \leq I_s^{lim} \\ I_s^{+lim} \leq I_s^{lim} - \left|I_s^{-*}\right| \end{cases} \tag{3.19}$$

The priority of I1 is given by:

$$\begin{cases} \left|V^{d+} \Delta I_Q^+ / V^+\right| \leq I_s^{+lim} - I_s^{q+pre} \\ \left|(V^{d+*} - V^{d+}) R_v^+(s)\right| \leq \sqrt{(I_s^{+lim})^2 - (I_s^{q+*})^2} - \dfrac{V^{q+} \Delta I_Q^+}{V^+} \end{cases} \tag{3.20}$$

Per IEEE 2800 standard, IBRs are expected to fully utilize the maximum current capacity and achieve optimal reactive current injection. To that end, a scaling method based on [111] is employed First, the coordinate system of current references is converted from the *dq* reference frame to the *abc* frame.

$$\begin{cases} \mathbf{I}_s^{\alpha\beta+*} = \mathbf{T}^{dq}(-\theta)\mathbf{I}_s^{dq+*} \\ \mathbf{I}_s^{\alpha\beta-*} = \mathbf{T}^{dq}(\theta)\mathbf{I}_s^{dq-*} \end{cases} \tag{3.21}$$

$$\mathbf{I}_s^{abc*} = (\mathbf{T}^{\alpha\beta})^{-1}(\mathbf{I}_s^{\alpha\beta+*} + \mathbf{I}_s^{\alpha\beta-*}) \tag{3.22}$$

Next, a scaling factor μ is established based on the ratio of the current limit over the maximum absolute value of phase currents, as follows:

$$\mu = I_s^{lim} \Big/ \max(\left|I_s^{a*}\right|, \left|I_s^{b*}\right|, \left|I_s^{c*}\right|) \tag{3.23}$$

To achieve the full utilization of converter current capacities, μ is utilized to multiply the current references, ensuring that the faulty phase current can reach the current limit, as given by

$$\begin{cases} \tilde{\mathbf{I}}_s^{dq+*} = \mu\mathbf{I}_s^{dq+*} \\ \tilde{\mathbf{I}}_s^{dq-*} = \mu\mathbf{I}_s^{dq-*} \end{cases} \tag{3.24}$$

where the symbol tilde (~) denotes the current references after scaling. Fig. 3.6 illustrates the control block diagram of the proposed CS-based CLM.

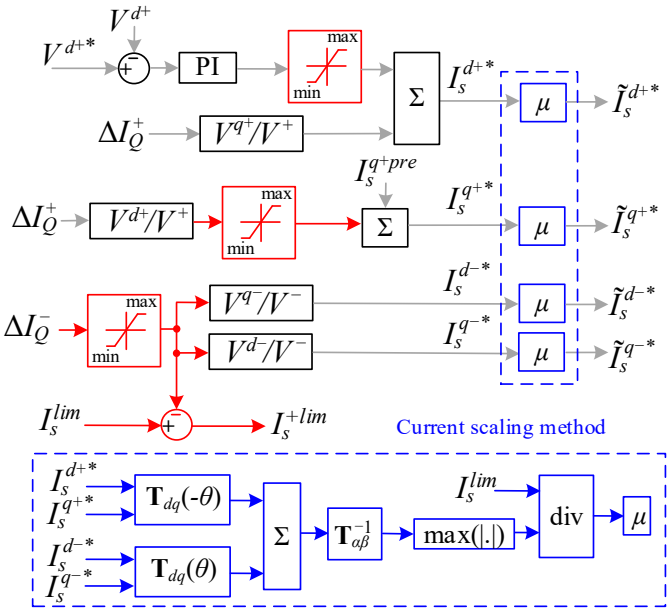

Fig. 3.6. Improved current limiter of GFM-IBRs.

3.1.3 Virtual Impedance-based CLM

Fig. 3.7 shows the basic control block diagram of a GFM that is used to incorporate the proposed virtual impedance-based (VI-based) CLM. Key components are positive sequence control with virtual impedance, negative sequence control following grid codes, power synchronization via P-droop, and voltage regulation via Q-droop. ω_0 is the angular frequency, k_f and k_v are droop coefficients for frequency and voltage control, v and i represent voltage and current components, and P and Q denote active and reactive powers. Subscript ref denotes reference values. 1 and 2 represent positive and negative sequences, and E_{dc} is the DC voltage. The DDSRF performs sequence separation. Unlike GFL inverters that use PLL, the phase angle θ is derived from P-droop control. The inner current loop includes coupling terms to prevent dq axis interactions. During normal operation, voltage control generates positive-sequence current references, with v_{1dref} from Q-droop and v_{1qref} set to zero. Negative-sequence control maintains only the current loop, with zero references pre-fault. During unbalanced faults, VI-based CLM limits the

positive-sequence current while negative-sequence references can be adjusted to follow grid codes. *P*-droop is disabled during faults to maintain angle stability, while *Q*-droop remains active.

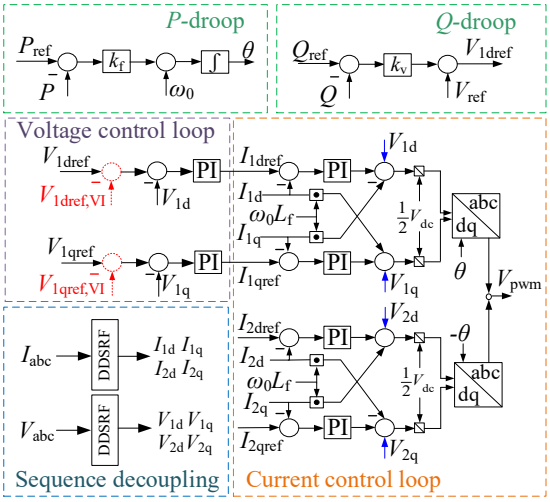

Fig. 3.7. The control block diagram of a GFM inverter.

The VI-based CLM limits the fault current by reducing voltage references, $v_{1\mathrm{dref,VI}}$ and $v_{1\mathrm{qref,VI}}$ (marked in red):

$$\begin{cases} v_{1\mathrm{dref,VI}} = R_{\mathrm{VI}} i_{1\mathrm{d}} - X_{\mathrm{VI}} i_{1\mathrm{q}} \\ v_{1\mathrm{qref,VI}} = R_{\mathrm{VI}} i_{1\mathrm{q}} + X_{\mathrm{VI}} i_{1\mathrm{d}} \end{cases} \tag{3.25}$$

where R_{VI} and X_{VI} are the resistance and reactance components of the virtual impedance, as given by

$$\begin{cases} R_{\mathrm{VI}} = R_{\mathrm{VI}}^{0} + \Delta R_{\mathrm{VI}} \\ X_{\mathrm{VI}} = X_{\mathrm{VI}}^{0} + \Delta X_{\mathrm{VI}} \end{cases} \tag{3.26}$$

where R_{VI}^{0} and X_{VI}^{0} are the rated resistance and reactance for load sharing, (usually taken as 0 during a fault), ΔR_{VI} and ΔX_{VI} are their additional components during a fault, and they are adjusted adaptively based on the fault current, as follows:

$$\begin{cases} \Delta R_{\mathrm{VI}} = \max\left\{ k_{\mathrm{p}} \left(\sqrt{i_{1\mathrm{dref}}^{2} + i_{1\mathrm{qref}}^{2}} - I_{\mathrm{thres}} \right), 0 \right\} \\ \Delta X_{\mathrm{VI}} = \Delta R_{\mathrm{VI}} \cdot \Delta_{X/R} \end{cases} \tag{3.27}$$

where I_{thres} is the current threshold value, and $\Delta_{X/R}$ is the virtual impedance ratio. The coefficient k_{p} is determined as

$$\begin{cases} k_{\mathrm{p}} = \dfrac{V_{\mathrm{drop}}}{I_{1\max} \Delta I_{\mathrm{thres}} \sqrt{1 + \Delta_{X/R}^{2}}} \\ \Delta I_{\mathrm{thres}} = \left(I_{1\max} - I_{\mathrm{thres}} \right) \end{cases} \tag{3.28}$$

where V_{drop} is the voltage drop across the virtual impedance, and $I_{1\max}$ is the positive-sequence current limiting value of the GFM-IBR. To fix the positive-sequence fault current at $I_{1\max}$, V_{drop} is adjusted by the proportional-integral (PI) controller, as shown in Fig. 3.8.

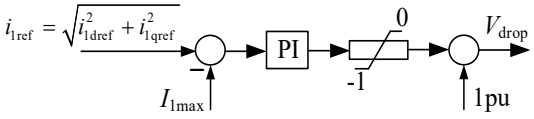

Fig. 3.8. The block diagram to generate U_{drop}.

VI-based CLM activates when i_{1ref} exceeds I_{1max}, setting V_{drop} to control current limiting. When i_{1ref} is below I_{1max}, V_{drop} remains zero and VIC stays inactive. During activation, fault current maximization is achieved through sequence current coordination. Using a *K*-factor approach, the negative-sequence reactive current is determined based on voltage variation during faults.

IEEE Std 2800-2022 specifies that negative sequence current should lead voltage by 90° to 100°. Using 90° for simplicity, the *dq* current references are calculated as follows:

$$\begin{cases} i_{2dr} = k\sqrt{v_{2d}^2 + v_{2q}^2} \cdot \dfrac{v_{2q}}{\sqrt{v_{2d}^2 + v_{2q}^2}} = kv_{2q} \\ i_{2qr} = k\sqrt{v_{2d}^2 + v_{2q}^2} \cdot \dfrac{-v_{2d}}{\sqrt{v_{2d}^2 + v_{2q}^2}} = -kv_{2d} \end{cases} \tag{3.29}$$

where *k* is the reactive coefficient from 2 to 6. To maximize converter capacity utilization, the relationship between phase and sequence currents are given by

$$\left|\bar{I}_{abc}\right| = \left(\left|\bar{I}_1\right|^2 + \left|\bar{I}_2\right|^2 + 2\left|\bar{I}_1\right|\left|\bar{I}_2\right| \cdot \cos\Delta\delta_{abc}\right)^{\frac{1}{2}} \tag{3.30}$$

where $\bar{I}_{abc}$ denotes phase currents. The angle difference is:

$$\Delta\delta_{abc} = \begin{bmatrix} \delta_{i1} - \delta_{i2} \\ \delta_{i1} - \delta_{i2} + 2\pi/3 \\ \delta_{i1} - \delta_{i2} - 2\pi/3 \end{bmatrix} \tag{3.31}$$

$$\delta_{i2} = \delta_{v2} + \frac{\pi}{2} \tag{3.32}$$

where δ_{i1} and δ_{i2} are positive and negative-sequence current angles and δ_{v2} is the negative-sequence voltage angle at the transformer LV side. The previous method [102] distributed current limits as:

$$\begin{cases} I_{2max} = I_{max}\left[\eta_{12}^2 + 2\eta_{12}\max(\cos(\Delta\delta_{abc})) + 1\right]^{-1/2} \\ I_{1max} = \eta_{12} I_{2max} \end{cases} \tag{3.33}$$

where I_{max} is total current limit, η_{12} is sequence current ratio, and I_{1max}, I_{2max} are sequence limits. This approach has limitations: I_{2max} may not be reached for small negative sequence voltages and becomes unstable for balanced faults. Hence, a new adaptive current limit is proposed, as given by

$$I_{2max} = I_{max}/2 \tag{3.34}$$

$$\begin{cases} I_{1max} = -\left|\bar{I}_2\right|\max(\cos\Delta\delta_{abc}) + \sqrt{\left|\bar{I}_2\right|^2 \cdot \left(\max(\cos\Delta\delta_{abc})\right)^2 - \left|\bar{I}_2\right|^2 + I_{max}^2} \\ \left|\bar{I}_2\right| = \sqrt{i_{2dref}^2 + i_{2qref}^2} \end{cases} \tag{3.35}$$

This new approach:

- Automatically adjusts I_{1max} based on actual $\bar{I}_2$
- Maintains SG-like behavior ($\left|\bar{I}_1\right| > \left|\bar{I}_2\right|$)
- Handles balanced faults without additional logic
- Maximizes current utilization while meeting codes

A key consideration is that while IEEE Std 2800-2022 requires positive sequence reactive current to exceed negative sequence, this may need re-examination for GFM inverters that maintain voltage source characteristics.

3.1.4 Asymmetrical FRT Control with Three Mode Switching

This section presents a three-mode switching synchronization control scheme for WTG operation:

(1) Actual GFM mode

(2) Restricted mode featuring:

- The advanced VSL using sequence-domain $\alpha\beta$ voltages for enhanced frequency stability and voltage component detection

- Dual-sequence reactive current injection to support positive sequence voltage and suppress negative sequence voltage

(3) Transition mode implementation:

The VI-based current limiting to control post-fault current transients

3.1.4.1 Design of the Synchronization Loop

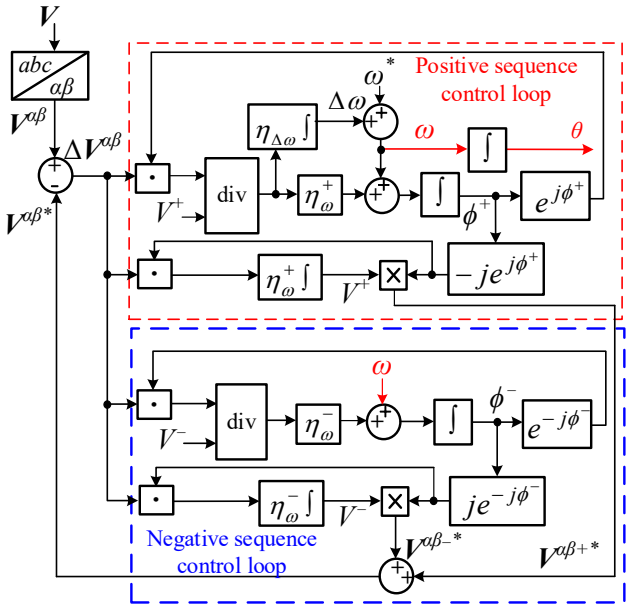

Fig. 3.9. Sequence domain $\alpha\beta$ voltage synchronization loop (VSL)

The VSL employs a unified three-phase signal processor [133], [134] (Fig. 3.9). Unlike conventional synchronous reference frame PLLs, the VSL computes $\alpha\beta$ voltage errors in stationary reference frame:

$$\Delta \boldsymbol{V}^{\alpha\beta} = \boldsymbol{V}^{\alpha\beta} - \boldsymbol{V}^{\alpha\beta *} \tag{3.36}$$

Under asymmetrical grid conditions, integrated positive/ negative sequence control loops generate $\alpha\beta$ voltage references:

$$\boldsymbol{V}^{\alpha\beta *} = \underbrace{-V^{+} j e^{j\phi^{+}}}_{\boldsymbol{V}^{\alpha\beta *+}} + \underbrace{V^{-} j e^{-j\phi^{-}}}_{\boldsymbol{V}^{\alpha\beta *-}} \tag{3.37}$$

where

$$\begin{cases} \dot{V}^{+} = -\eta_{\omega}^{+}(\Delta \boldsymbol{V}^{\alpha\beta} \bullet j e^{j\phi^{+}}) \\ \dot{V}^{-} = \eta_{\omega}^{-}(\Delta \boldsymbol{V}^{\alpha\beta} \bullet j e^{-j\phi^{-}}) \\ \dot{\phi}^{+} = \dot{V}^{+} / V^{+} + \omega \\ \dot{\phi}^{-} = \dot{V}^{-} / V^{-} + \omega \end{cases} \tag{3.38}$$

Note that ($\bullet$) represents dot product operation.

The frequency regulation occurs in the positive sequence control loop:

$$\begin{cases} \Delta\dot{\omega} = \eta_{\Delta\omega}(\Delta \boldsymbol{V}^{\alpha\beta} \bullet e^{j\phi^+}) \big/ V^+ \\ \dot{\theta} = \omega = \Delta\omega + \omega^* \end{cases} \tag{3.39}$$

(3.37) leads to $\alpha\beta$ voltage reference derivation,

$$\begin{cases} \dot{\boldsymbol{V}}^{\alpha\beta+*} = -\dot{V}^+ j e^{j\phi^+} + V^+ \dot{\phi}^+ e^{j\phi^+} \\ \dot{\boldsymbol{V}}^{\alpha\beta-*} = \dot{V}^- j e^{-j\phi^-} + V^- \dot{\phi}^- e^{-j\phi^-} \end{cases} \tag{3.40}$$

Combining (3.37), (3.38), and (3.40) yields:

$$\begin{bmatrix} \dot{\boldsymbol{V}}^{\alpha\beta+*} \\ \dot{\boldsymbol{V}}^{\alpha\beta-*} \end{bmatrix} = \mathbf{A} \begin{bmatrix} \boldsymbol{V}^{\alpha\beta+*} \\ \boldsymbol{V}^{\alpha\beta-*} \end{bmatrix} + \begin{bmatrix} \eta_\omega^+ \\ \eta_\omega^- \end{bmatrix} \begin{bmatrix} \boldsymbol{V}^{\alpha\beta+} \\ \boldsymbol{V}^{\alpha\beta-} \end{bmatrix} \tag{3.41}$$

where $\mathbf{A} = \begin{bmatrix} j\omega - \eta_\omega^+ & -\eta_\omega^+ \\ -\eta_\omega^- & -j\omega - \eta_\omega^- \end{bmatrix}$. The characteristic equation becomes

$$\left| s\mathbf{I} - \mathbf{A} \right| = s^2 + (\eta_\omega^+ + \eta_\omega^-)s + \omega^2 + j\omega(\eta_\omega^+ - \eta_\omega^-) = 0 \tag{3.42}$$

Let $\eta_\omega^+ = \eta_\omega^- = \xi_\omega \omega$. (3.42) yields

$$s = -\xi_\omega \omega \pm j\omega\sqrt{1 - \xi_\omega^{\,2}} \tag{3.43}$$

where ξ_ω: damping ratio of frequency. (3.43) enables design of η_ω^+ and η_ω^- through ξ_ω. Combining (3.38) and (3.39) yields

$$\dot{\phi}^+ = \omega + \underbrace{(\eta_\omega^+ / \eta_{\Delta\omega})}_{\xi_{\Delta\omega}} \Delta\dot{\omega} \tag{3.44}$$

where $\xi_{\Delta\omega}$: damping ratio of frequency deviation. When $\eta_\omega^+ = \eta_\omega^- = \xi_\omega \omega$, $\eta_{\Delta\omega}$ design is given by

$$\eta_{\Delta\omega} = \xi_\omega \omega / \xi_{\Delta\omega} \tag{3.45}$$

The frequency regulation in (3.1) can be rewritten for synchronization loop switching:

$$\omega = K_\omega \omega^* + K_P(P^* - P) + K_{\Delta\omega}\Delta\omega \tag{3.46}$$

where the frequency deviation coefficient $K_{\Delta\omega}$ equals 0 in actual GFM mode. In restricted mode, K_ω=$K_{\Delta\omega}$=1, and K_P=0. The proposed synchronization loop structure appears in Fig. 3.10.

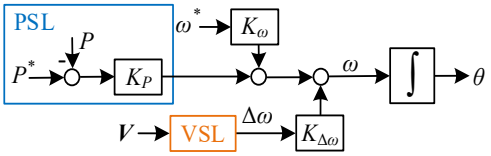

Fig. 3.10. Proposed synchronization loop for GFM Type-IV WTGs.

3.1.4.2 Current Reference Coordination in the Restricted Mode

The *K* factor-based method from German grid codes calculates the required positive/negative sequence reactive currents $\{I_Q^+, I_Q^-\}$ using the VSL-derived sequence voltage magnitudes:

$$\begin{cases} I_Q^+ = I_s^{q+pre} + K_Q^+ \left(V^* - V^+ \right) \\ I_Q^- = K_Q^- V^- \end{cases} \tag{3.47}$$

where I_s^{q+pre}: pre-fault positive sequence *q*-axis current, $\{K_Q^+, K_Q^-\}$: reactive current injection gains that typically range from 2 to 6. The sequence current limits $\{I_s^{+lim}, I_s^{-lim}\}$ are determined by:

$$\begin{cases} I_s^{-lim} = \min\left\{\eta I_Q^-, I_Q^+\right\} \\ I_s^{+lim} = I_s^{lim} - \left|I_s^{-lim}\right| \end{cases} \tag{3.48}$$

where $\eta = \dfrac{I_s^{lim}}{\left(\left|I_Q^-\right| + \left|I_Q^+\right|\right)}$. The VSL aligns the positive sequence voltage vector with the *d*-axis. Hence, $I_s^{q+*} = I_Q^+$. The priority settings of current references are shown in Fig. 5. Current priority hierarchy has three levels:

Level 1: Reactive current allocation

Level 2: The remaining capacity assigned to *d*-axis current reference

Level 3: The current scaling method maximizes converter capacity

The scaling process applies a factor K_{scale} to align current references with the total current limit:

$$\begin{cases} K_{scale} = I_s^{lim} / \max\{\boldsymbol{I}_s^{abc*}\} \\ \tilde{\boldsymbol{I}}_s^{dq+*} = K_{scale} \boldsymbol{I}_s^{dq+*} \\ \tilde{\boldsymbol{I}}_s^{dq-*} = K_{scale} \boldsymbol{I}_s^{dq-*} \end{cases} \tag{3.49}$$

where $\tilde{\boldsymbol{I}}_s^*$ represent scaled current references after scaling.

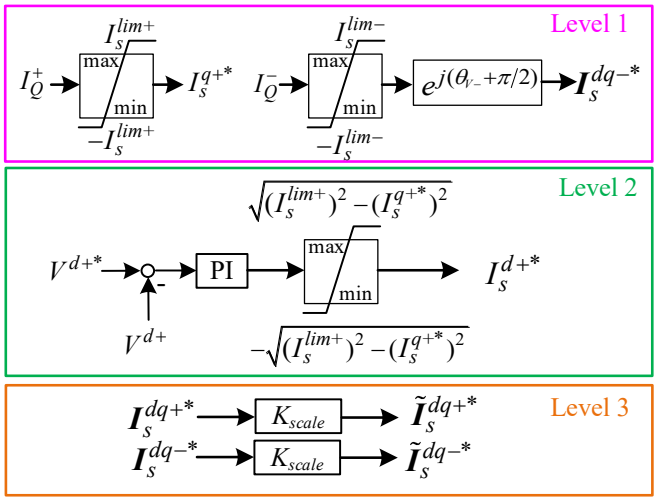

Fig. 3.11. Priority settings of current references in the restricted mode.

3.1.4.3 Virtual Impedance-based Method for WTG Restoration

After fault clearance, the WTG transitions from restricted mode back to actual GFM mode. $K_{\Delta\omega}$ equals zero in this transition mode. K_P and K_ω equal the coefficients of the employed PSL. No negative sequence component exists, thus $\boldsymbol{I}_s^{dq-*} = 0$. To prevent variations in restore outputs from causing the FRT to malfunction, during the active power recovery period, which ranges from 1 s to 10 s per IEEE 2800, the FRT logic is disabled. The WTG is protected by a VI-based method to prevent overcurrent resulting from restoration or additional disturbances. The VI-based method updates voltage references, as shown in Fig. 3.12. $\Delta_{X/R}$: ratio of virtual reactance over virtual resistance, with a typical range from 0.5 to 5 [102], [104]. I_s: converter current magnitude. I_s^{th}: current threshold for the VI-based method activation. $\boldsymbol{V}_{VI}$: voltage drop across the VI. The VI-based method generates updated *dq* voltage references:

$$Z_{VI} = \frac{k_{th}\left[V^* - \left(k_{pVI} + k_{iVI}/\mathrm{s}\right)\left(I_s - I_s^{th}\right)\right]}{I_s^{th}} \tag{3.50}$$

$$\begin{cases} \boldsymbol{V}_{VI} = \boldsymbol{I}_s^{dq+}\boldsymbol{Z}_{VI} = \boldsymbol{I}_s^{dq+} Z_{VI} e^{j\arctan\left(\Delta_{X/R}\right)} \\ \tilde{\boldsymbol{V}}^{dq+*} = \boldsymbol{V}^{dq+*} - \boldsymbol{V}_{VI} \end{cases} \tag{3.51}$$

where $k_{th} = \max\left(\dfrac{I_s - I_s^{th}}{I_s^{lim} - I_s^{th}}, 0\right)$. During the active power recovery time, when I_s exceeds I_s^{th}, the VI activates. To mitigate the risk of transients leading to the deactivation of the VI, a pre-defined transition time is strategically employed. After a pre-defined transition time, the VI deactivates if I_s stabilizes at the I_s^{th}, i.e., $Z_{VI} = 0$.

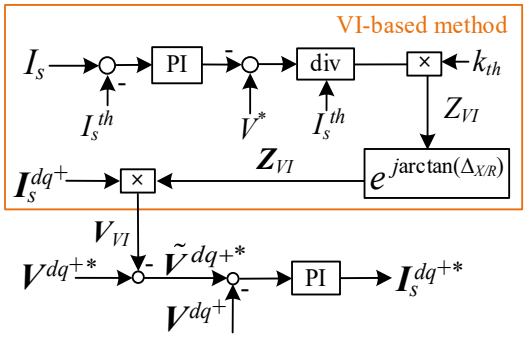

Fig. 3.12. VI-based method in transition mode.

3.1.4.4 Detection and Transition of Control Modes

Per IEEE 2800, the IBR plant shall be designed to provide voltage disturbance ride-through capability. During low-voltage disturbances, e.g., balanced and unbalanced faults, the low-voltage variations can be detected by the FRT detection logic. In the FRT detection logic, the variation in V_{POI}, denoted as ΔV_{POI}, enables sensitive detection of abnormal grid conditions [135], as shown in Fig. 3.13. Time integral block output resets to the reset value (rv) when the reset control (rc) exceeds 0. For low-voltage ride-through, the relevant voltage shall be the lowest magnitude fundamental frequency phasor component relative to the corresponding nominal voltage [86]. Hence, the lowest RMS value of phase voltages is used for FRT detection in the proposed control strategy.

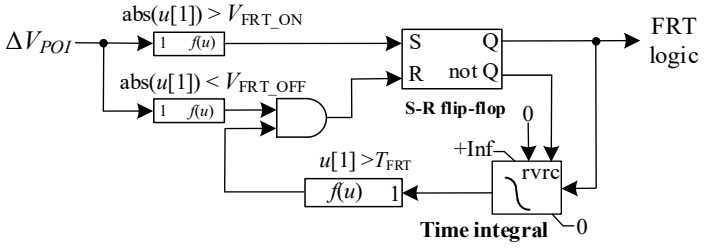

Fig. 3.13. FRT detection logic.

The coordination of three operation modes for GFM Type-IV WTGs is summarized as follows:

(i) Actual GFM mode: The PSL regulates frequency while the VSL remains deactivated. $\boldsymbol{I}_s^{dq+*}$ are regulated by the inner voltage control while $\boldsymbol{I}_s^{dq-*} = 0$. The steady-state values are listed in Table 3-1. The power difference $\Delta P = P_M - P = 0$ pu, and the DC current difference $\Delta I_{dc} = I_{dcM} - I_{dc} = 0$ pu.

TABLE 3-1
Initialization of GFM Type-IV WTG

Variable	ΔP, ΔI_{dc}, Q	P_M, P, I_{dcM}, ω, V_{dc}, I_{dc}, V, I
Initial value	0 pu	1 pu

(ii) Restricted mode: When $|\Delta V_{POI}|$ exceeds a predefined activation threshold ($V_{\text{FRT\_ON}}$), FRT logic activates. The WTG operates in the restricted mode. The PSL and the inner voltage control are disengaged while the VSL activates for enhancing frequency responses, and the current coordination method activates for reactive current injection with three priority levels. Note that these three levels represent the sequential priority without requiring any judgment or switching.

(iii) Transition mode: When $|\Delta V_{POI}|$ falls below a predefined deactivation threshold ($V_{\text{FRT\_OFF}}$) after a pre-defined release time (T_{FRT}), the VI-based method, PSL, and inner voltage control activate, $\boldsymbol{I}_s^{dq-*} = 0$. During the active power recovery time, when the converter current magnitude exceeds the current threshold, the VI activates, and the WTG operates in transition mode. After a pre-defined transition time, the VI deactivates if the converter current magnitude stabilizes at the current threshold. Then, the WTG operates in actual GFM mode.

For clarity, Fig. 3.14 shows the flow chart of the proposed three-mode switching synchronization control solution. Table 3-2 presents activated control blocks in each operation mode of GFM Type-IV WTGs, where "√" indicates activated and "×" indicates deactivated.

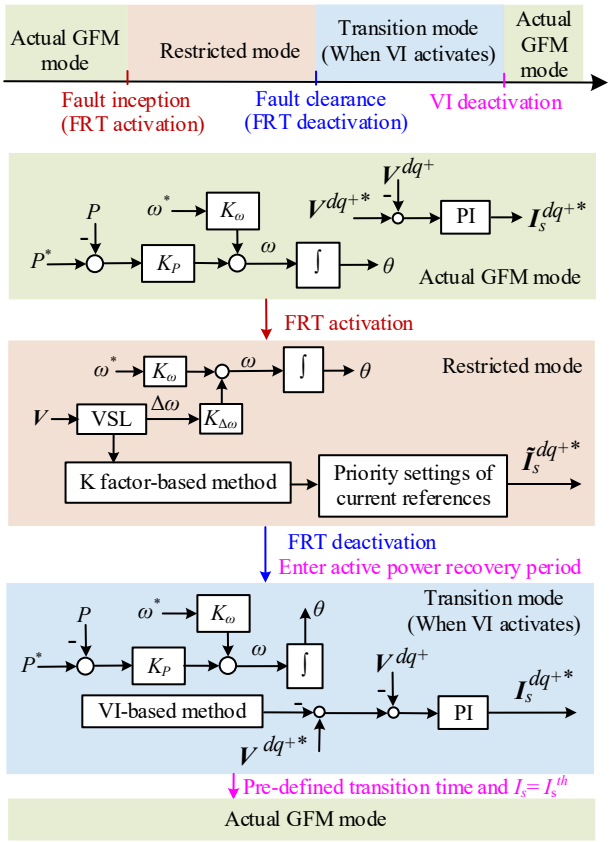

Fig. 3.14. Flow chart of the proposed three-mode switching control solution for GFM Type-IV WTGs.

TABLE 3-2

Three Operation Modes of GFM Type-IV WTGs

Control	Actual GFM mode	Restricted mode	Transition mode
PSL	√	×	√
VSL	×	√	×
Inner voltage control	√	×	√
K factor-based method	×	√	×
Scaling factor	×	√	×
Priority setting	×	√	×
VI-based method	×	×	√

3.1.5 Case Studies

3.1.5.1 Validation of Current saturation-based CLM

To validate the proposed current limiting strategy, a modified EPRI benchmark system is built using an EMT-type tool, as displayed in Fig. 3.15. A wind park with aggregated GFM-IBRs is connected to the power grid at Bus 1. The VSM control is the default choice of PSLs for the GFM-IBR. Unbalanced faults are applied when t = 2 s. The fault duration is 0.5 s. This is not a practical fault duration, but it is helpful for illustration purposes. The system parameters can be found in Table A2 of the Appendix.

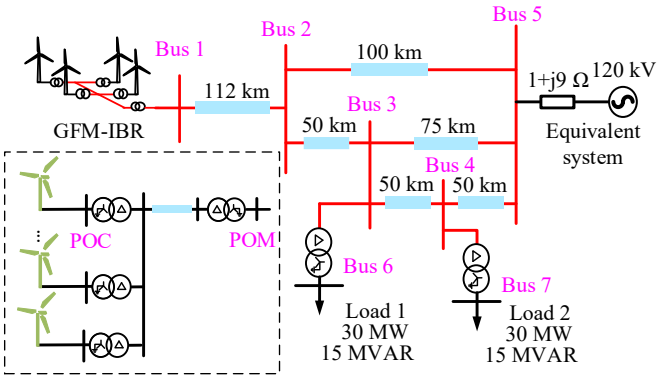

Fig. 3.15. EPRI benchmark system with aggregated GFM-IBRs.

a) Performance under Different Current limiters

To provide insights into deciding on the choice of the current limiters, the unbalanced fault types, including single-line-to-ground (SLG) and line-to-line (LL), are simulated under different current limiters. Taking a phase-A-to-ground (AG) fault at Bus 2 as an example, the phase currents under different current limiters are shown in Fig. 3.16. Currents reach a steady state rapidly once the fault is triggered on the grid side. By comparing the performance of existing current limiters and the improved current limiter (before scaling) in Fig. 3.16(a)−(d), the maximum current magnitude under the improved current limiter (before scaling) is the highest. Moreover, by using the scaling method, as shown in Fig. 3.16(e), the current in the faulty phase reaches the current limit set to 1.2 pu under the improved current limiter (after scaling). Scaling ensures the full utilization of the current capacity.

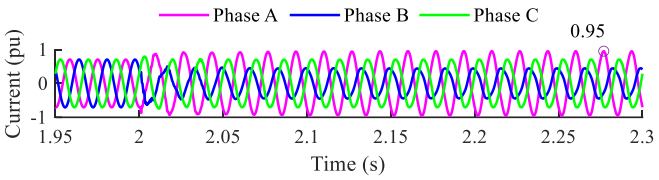

(a) Instantaneous limiter

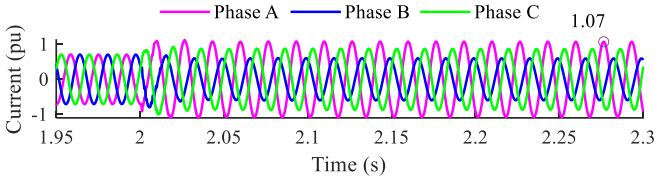

(b) Magnitude limiter

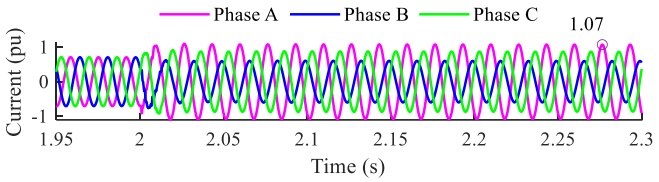

(c) Priority-based limiter

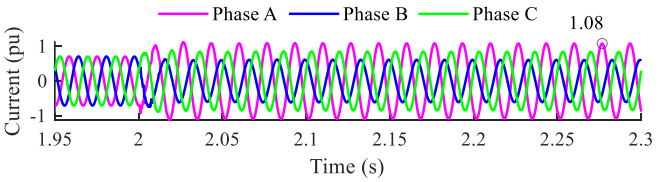

(d) Improved current limiter (before scaling)

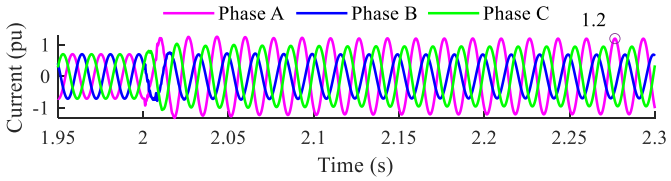

(e) Improved current limiter (after scaling)

Fig. 3.16. Phase converter currents under an AG fault.

Fig. 3.17 shows I1R and I2R components considering different current limiters. The injected I1R is the largest under the improved current limiter (after scaling). The incremental I1R is not negative, and it is higher than the injected I2R, as stipulated in the IEEE 2800 standard. The magnitude of V1 and V2 at the POC are shown in Fig. 3.18. The improved current limiter, after scaling, exhibits the highest magnitude of V1, indicating that this method is the most effective in providing voltage support.

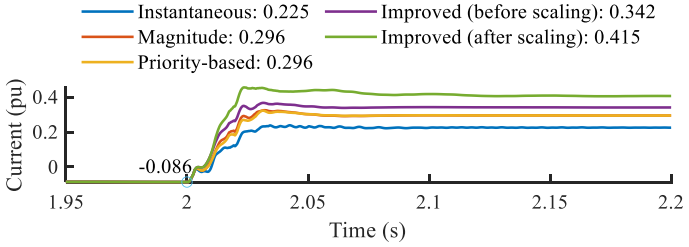

(a) I1R

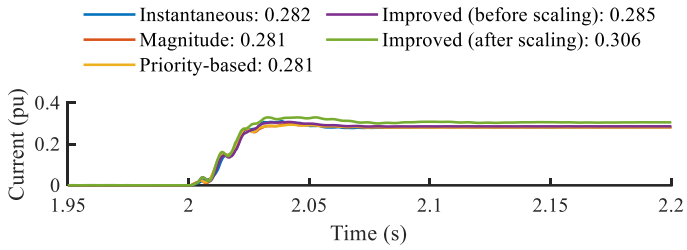

(b) I2R

Fig. 3.17. Reactive current injection under an AG fault.

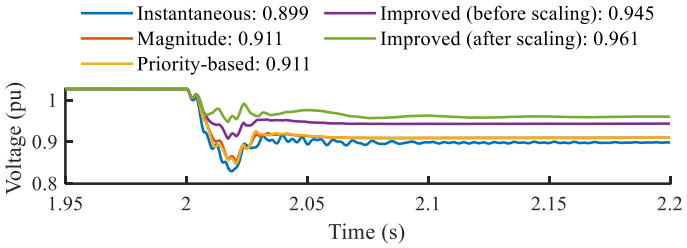

(a) V1

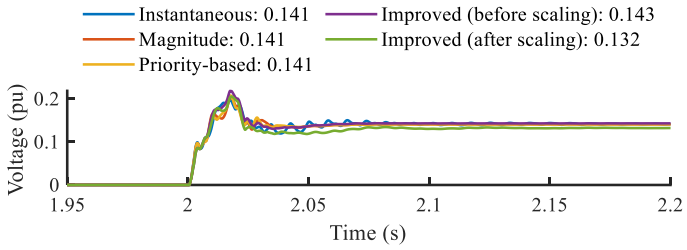

(b) V2

Fig. 3.18. Magnitude of V1 and V2 at the POC under an AG fault.

The detailed simulation results of sequence components of currents and voltages at the POC are demonstrated in Table 3-3, using a format indicating “magnitude (angle)”. The units of magnitude and angle are in pu and degrees, respectively. ∠I2/V2 denotes the angular difference between I2 and V2. Values highlighted in bold signify that, by using the current limiter for I2 in (12), I2 leads V2 by 90°. Based on the results in Table 3-3 and Fig. 3.16−Fig. 3.18, the current limiters can alter the injected current of the GFM-IBR, consequently impacting the AC voltages and currents during unbalanced faults.

TABLE 3-3

Sequence Components of Currents and Voltages at the POC under Different Current Limiters

Current limiter	I1	I2	V1	V2	∠I2/V2
Instantaneous limiter	0.665 (-28.8)	0.283 (-55.9)	0.899 (-8.9)	0.141 (-146)	**90.0**
Magnitude limiter	0.819 (-24)	0.282 (-53.8)	0.911 (-3)	0.141 (-143.8)	**90.0**
Priority-based limiter	0.819 (-24)	0.282 (-53.8)	0.911 (-3)	0.141 (-143.8)	**90.0**
Improved limiter (Before scaling)	0.815 (-29.1)	0.286 (-54.1)	**0.945** (-4.4)	**0.143** (-144.1)	**90.0**
Improved limiter (After scaling)	0.921 (-26.9)	0.306 (-52.4)	**0.961** (-0.8)	**0.132** (-142.4)	**90.0**

Overall, the improved current limiter exhibits the optimal utilization of converter current capacities,

the largest reactive current injection, and the maximum voltage support ability. The simulation results demonstrate that the proposed current limiting strategy conforms with the following FRT requirements:

(a) $\Delta I_Q^+ \geq \Delta I_Q^-$ during unbalanced faults.

(b) I2 leads V2 by 90°.

(c) $\max(|I_s^a|, |I_s^b|, |I_s^c|) = I_s^{lim}$.

In this section, the pre-fault I1R and I2R are −0.086 pu and 0 pu, respectively, as shown in Fig. 3.17. Hence, $\Delta I_Q^+ = I_Q^{+*} + 0.0086$ pu and $\Delta I_Q^- = I_Q^{-*}$. The subsequent case studies focus on the performance evaluation of the proposed GFM PNSC structure with the enhanced current limiting strategy under various scenarios, and its validation against the above FRT requirements (a)−(c).

b) Performance under Different Power Synchronization Loops

Under an AG fault at Bus 2, using the proposed current limiting strategy, the currents and voltages produced by GFM-IBRs are simulated with different PSLs, as demonstrated in Tables 3-4 and 3-5. The superscript *max* denotes the maximum absolute value of the current under fault steady state conditions. Values in bold fonts indicate that the proposed current limiting strategy meets the requirements (a)−(c) no matter what the PSL strategy.

TABLE 3-4

Phase Currents and the Active and Reactive Currents under Different PSLs

PSL	$I_s^{a\max}$	$I_s^{b\max}$	$I_s^{c\max}$	I_P^+	I_Q^+	I_P^-	I_Q^-
VSM	**1.200**	0.693	0.945	0.827	**0.405**	0.000	**0.306**
droop	**1.199**	0.691	0.944	0.826	**0.404**	0.000	**0.306**
dVOC	**1.200**	0.697	0.950	0.831	**0.404**	0.000	**0.302**

TABLE 3-5

Sequence Components of Currents and Voltages at the POC under Different PSLs

PSL	I1	I2	V1	V2	∠I2/V2
VSM	0.921 (-26.9)	0.306 (-52.4)	0.961 (-0.8)	0.132 (-142.4)	**90.0**
droop	0.919 (-26.9)	0.306 (-52.4)	0.961 (-0.8)	0.132 (-142.4)	**90.0**
dVOC	0.924 (-26.5)	0.302 (-52.4)	0.96 (-0.6)	0.134 (-142.4)	**90.0**

c) Comparison between the Proposed and Existing Control Strategies

During faults, the existing GFM controls typically employ a power freezer and a single balanced positive sequence control loop. The priority-based current limiter is employed based on *Q* priority without additional reactive current injection.

To validate the improvements provided by the proposed current limiting strategy, an AG fault is applied at Bus 2, and the currents and voltages associated with the GFM-IBR are simulated with the proposed GFM control and existing GFM control, as shown in Tables 3-6 and 3-7. The highlighted value in bold indicates that the existing GFM control cannot meet requirements (b) and (c). Moreover, since the existing GFM control does not provide a negative sequence control loop, there is not sufficient I2R injection. The magnitudes of V1 and V2 at the POC are shown in Fig. 3.19. Due to the additional reactive current injection by the proposed GFM control, the magnitude of V1 is enhanced while that of V2 is

reduced compared to the existing GFM control. Overall, the proposed GFM control effectively addresses these issues associated with the existing GFM control. Note that the GFM PNSC structure provides the positive and negative sequence control loops. The proposed current limiting strategy is key to improving the performance, and it is established on the GFM PNSC structure for regulating I1 and I2 independently.

TABLE 3-6

Phase Currents and the Active and Reactive Currents under the Proposed and Existing Control Strategies

Strategy	$I_s^{a\max}$	$I_s^{b\max}$	$I_s^{c\max}$	I_P^+	I_Q^+	I_P^-	I_Q^-
Existing	**1.072**	0.832	0.705	0.821	**0.241**	**-0.224**	**0.032**
Proposed	**1.200**	0.693	0.945	0.827	**0.405**	0.000	**0.306**

TABLE 3-7

Sequence Components of Currents and Voltages at the POC under the Proposed and Existing Control Strategies

Strategy	I1	I2	V1	V2	∠I2/V2
Existing	0.855(-17.7)	0.226(-0.7)	0.873(-1.3)	0.231(-172.4)	**171.8**
Proposed	0.921(-26.9)	0.306(-52.4)	0.961(-0.8)	0.132(-142.4)	**90.0**

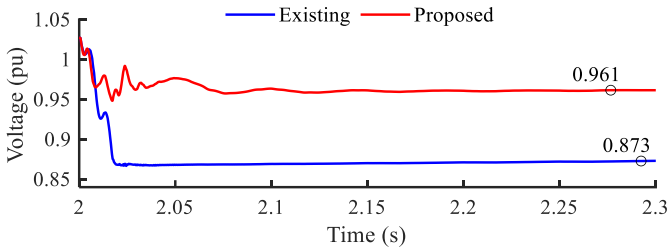

(a) V1

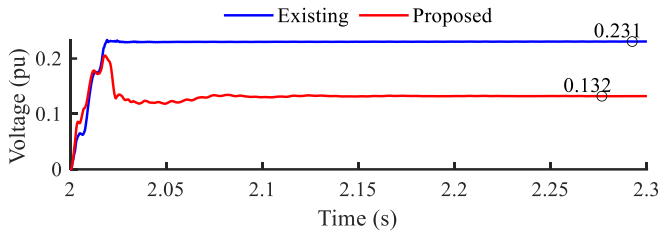

(b) V2

Fig. 3.19. Magnitude of V1 and V2 at the POC under the existing GFM control and proposed GFM control.

d) Performance under Different Unbalanced Fault Scenarios

To create a scenario for a severe grid fault for GFM-IBRs, SLG and LL faults at Bus 1 are studied. The converter currents are shown in Table 3-8. Comparisons of the currents before and after scaling reveal that the residual current capacity of the converter is effectively utilized when the scaling method is used. Additionally, the relations between the sequence components of currents and voltages at the POC after scaling are illustrated graphically in Fig. 3.20. Values highlighted in bold indicate that the proposed current limiting strategy can achieve the full utilization of converter current capacity under different

unbalanced fault scenarios. From Tables 3-8 and Fig. 3.20, the performances of reactive current injections and voltage support abilities are consistent under different unbalanced faulty phases. Overall, the proposed current limiting strategy under different unbalanced fault scenarios meets the requirements (a)−(c).

TABLE 3-8

Phase Currents and the Active and Reactive Currents under Various Fault Scenarios

Strategy	Fault Type	$I_s^{a\max}$	$I_s^{b\max}$	$I_s^{c\max}$	I_P^+	I_Q^+	I_P^-	I_Q^-
before scaling	AG	**1.120**	0.940	0.193	0.182	**0.614**	0.000	**0.560**
	BG	0.193	**1.119**	0.940	0.182	**0.614**	0.000	**0.560**
	CG	0.940	0.193	**1.120**	0.182	**0.614**	0.000	**0.560**
	AB	0.754	**1.188**	0.449	0.188	**0.626**	0.000	**0.547**
	BC	0.448	0.753	**1.188**	0.188	**0.626**	0.000	**0.547**
	CA	**1.188**	0.449	0.754	0.187	**0.626**	0.000	**0.547**
after scaling	AG	**1.200**	1.012	0.201	0.191	**0.656**	0.000	**0.604**
	BG	0.201	**1.200**	1.012	0.191	**0.656**	0.000	**0.604**
	CG	1.011	0.201	**1.200**	0.190	**0.656**	0.000	**0.604**
	AB	0.760	**1.200**	0.452	0.190	**0.632**	0.000	**0.553**
	BC	0.452	0.760	**1.200**	0.190	**0.632**	0.000	**0.553**
	CA	**1.200**	0.452	0.760	0.190	**0.632**	0.000	**0.553**

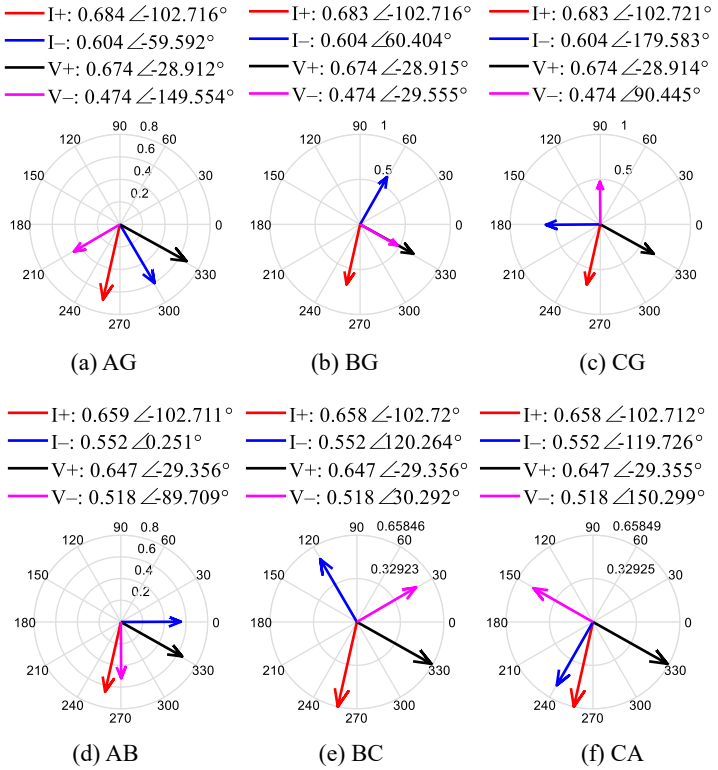

Fig. 3.20. Phasor of currents and voltages at the POC under various fault scenarios (after scaling)

e) Significance of I2R Injection

To show the significance of I2R injection, Fig. 3.21 shows the phasor representation of V2 and I2 at the POM under an AG fault at Bus 2. These results are produced by the SG, existing GFM control, and proposed GFM control.

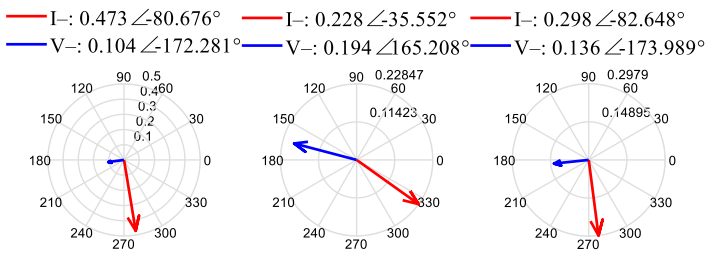

(a) (b) (c)

Fig. 3.21. Phasor of I2 and V2 at the POM: (a) SG; (b) Existing GFM control; (c) Proposed GFM control.

Under steady-state fault conditions, the SG in the negative sequence system shows a behavior close to an inductance. Its I2 contribution is highly reactive. Currently, there is no strict requirement for GFM-IBRs in the negative sequence system. However, the performance of system protection elements that rely on negative sequence components can be affected under the influence of IBRs. Uncontrolled negative sequence behavior of GFM-IBRs may cause maloperation of these protection elements. With the proposed GFM control, the negative sequence behavior of GFM-IBRs is close to that of SGs. Hence, the proposed current reference generation is beneficial for GFM-IBRs to emulate the negative sequence behavior of SGs.

A. Performance under Varying Short-Circuit Ratio

To show the effectiveness of the proposed control in voltage support over a wide range of short-circuit ratio (SCR) conditions, the sequence components of voltages at the POC under varying SCRs are shown in Fig. 3.22.

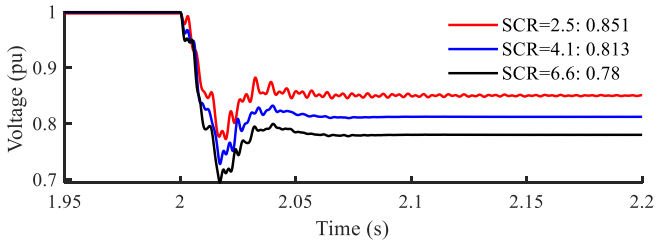

(a) V1

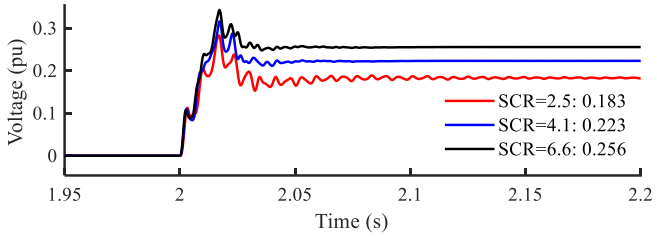

(b) V2

Fig. 3.22. Magnitude of V1 and V2 at the POC under varying SCRs.

From Fig. 3.22, under steady state fault conditions, the magnitude of V1 and V2 varies with different SCRs due to the proximity of faults. For instance, when SCR=2.5, the equivalent system impedance is the highest. Therefore, the magnitude of V1 is highest while that of V2 is lowest. For the stronger grid (SCR>3), the voltages can be stabilized faster. As the grid strength decreases (when SCR=2.5), there are minor fluctuations in both V1 and V2. Overall, the proposed control solution enables GFM-IBRs to

support terminal voltage across diverse grid strength conditions.

3.1.5.2 Validation of Virtual impedance-based CLM

To validate the proposed VI-based CLM, a modified 120kV/60 Hz EPRI benchmark system is built in an EMT-type tool, as shown in Fig. 3-2-3. The parameter configuration is presented in Table 3-9. For illustration, an unbalanced fault (Fault I or II) is applied during t = 3-4 s. The fault scenarios are below:

- Fault I: Line-A-to-ground (AG) fault at Bus (3).
- Fault II: Line-A-to-line-B (AB) fault at Bus (2).

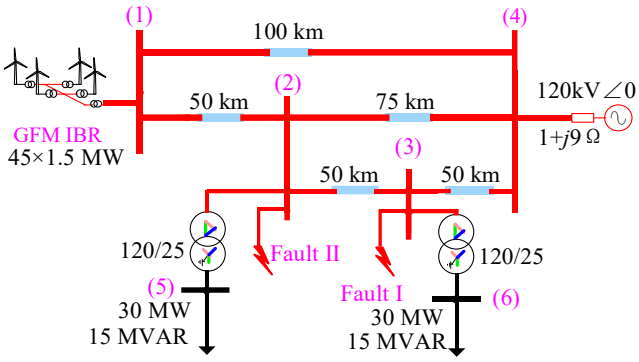

Fig. 3.23. EPRI benchmark system integrated by the GFM IBR

TABLE 3-9

PARAMETER CONFIGURATION OF VI-BASED CLM

Parameters	Value	Parameters	Value
Rated capacity	1 MW	k	3
Number	45	k_v	0.04
PI (current loop)	0.4588, 8.5163	k_f	0.0033
PI (voltage loop)	1, 200	σ	1
PI (V_{drop} loop)	0.45, 57.5	ΔI_{thres}	0.2
Filter capacitor	1.8052e-5 F	I_{max}	1.2
Filter inductor L_f	2.9234e-6 H	DC capacitance	0.0276 F
Switch frequency	4500 Hz	DC voltage	1.2 kV

The original GFM control is the current saturation-based VSM control scheme under the synchronous reference frame. The current limiter gives priority to reactive current during faults. The simulation results under Fault I and Fault II are shown in Fig. 3.24. With the original control, the active power (P_{I} and P_{II}) and frequency (ω_{I} and ω_{II}) oscillate intensively since the uncontrolled negative-sequence dq components appear within the control loop. The angular difference δ_{I} remains stable whereas δ_{II} diverges under fault steady state and fault clearance conditions.

In contrast, the proposed VI-based CLM effectively retain synchronization for various PSLs under Fault II. At the fault inception, the VI-based CLM is activated by the FRT detection. Since the positive- and negative-sequence dq components are decomposed via the DDSRF, the oscillations in power and frequency are removed, as shown in Fig. 3.25 (b) and Fig. 3.25 (c). In Fig. 3.25 (e), the current coordination achieves optimal utilization of current capacity (1.2 pu). The three-phase instantaneous voltages quickly stabilize in less than two cycles after fault inception, as shown in Fig. 3.25 (a). After fault clearance, the normal operation recovered gradually. The simulation results corroborate the analysis presented in Fig. 3-2-2 (b), which accounts for the stability enhancement.

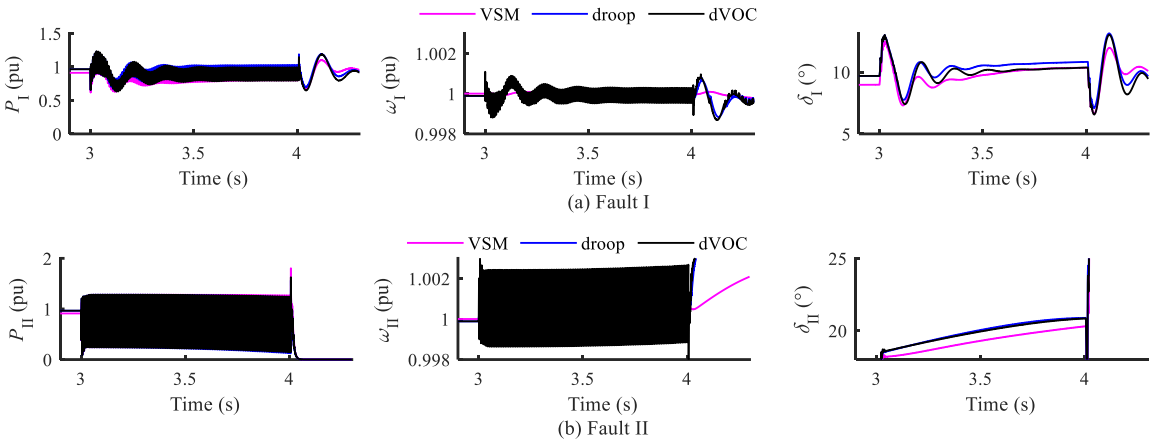

Fig. 3.24. Simulation results of original GFM control under Fault I and Fault II.

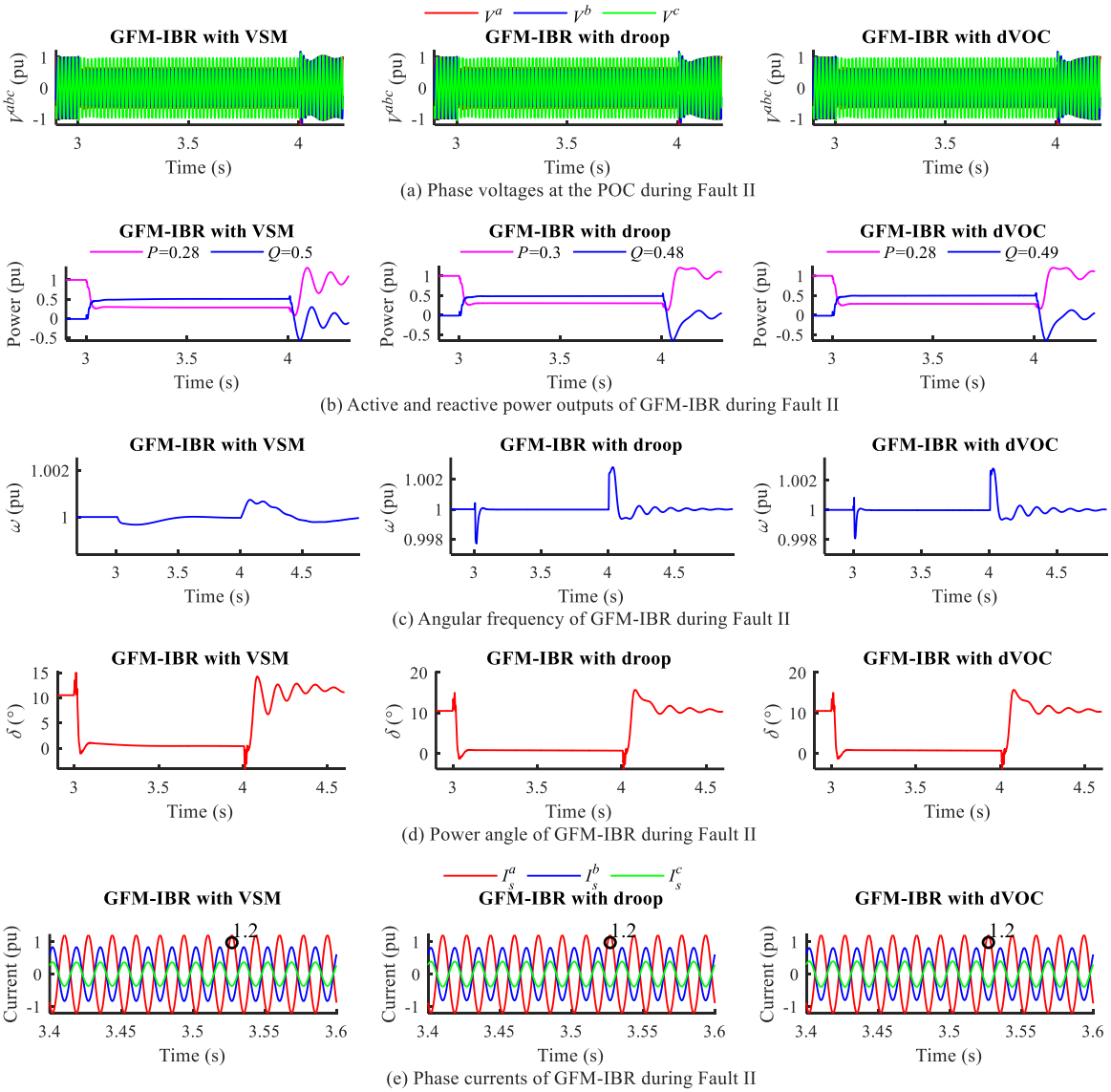

Fig. 3.25. Simulation results of proposed VI-based CLM under Fault II.

3.1.5.3 Validation of Three Mode-switching Control

The proposed three-mode switching control solution is validated using a modified EPRI benchmark system, as shown in Fig. 3.26. The converter's current limit is set to 1.2 pu. AC voltage protections follow practical technical requirements, using three-phase RMS voltages as the basis. The VSM control serves as the default PSL. All WTGs maintain consistent initialization in the following studies.

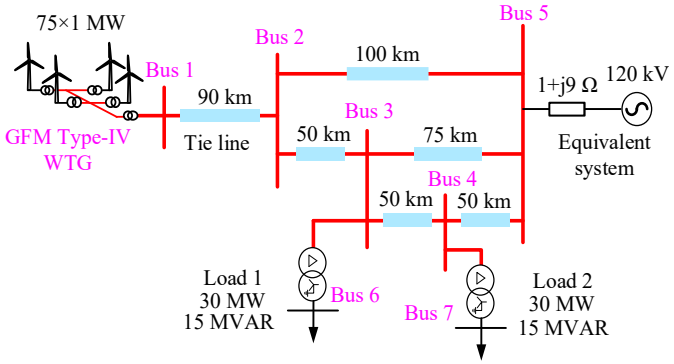

Fig. 3.26. EPRI benchmark system connected to GFM Type-IV WTGs.

a) Performance under the Original GFM Control

At t=2 s, a severe bolted line-A-to-ground (AG) fault occurs at Bus 2. The original GFM control uses priority-based current limiting to prevent overcurrent and supply reactive current. Fig. 3.27 demonstrates the LOS issue across the original GFM control strategies, including VSM control, droop control, and dVOC. All three GFM primary controls exhibit instability despite varying performance under different control parameters.

In Fig. 3.27(a), the angular frequency deviates from the nominal value under PSLs, indicating the GSC active power fails to follow the MPPT power reference. Power synchronization deteriorates due to improperly controlled GSC active power. Consequently, the active power difference between the GSC and the MSC (ΔP) increases substantially, as shown by the diverging waveform in Fig. 3.27(b). According to (3.1), with a K_P value of approximately 0.0033, the angular frequency deviation remains below 0.005 pu despite ΔP exceeding 0.6 pu.

The AC-side coupling affects the DC-side WTG operation. While the DC-link voltage maintains approximately 1 pu under MSC control regulation, the DC-link current difference diverges due to LOS, as shown in Fig. 3.27(c) and Fig. 3.27(d). Double-fundamental-frequency (2ω) oscillations persist in Fig. 3.27 due to negative-sequence components, consistent with previous studies [136], [137]. ΔI_{dc}, determined by $C_{dc}(dV_{dc}/dt)$, also exhibits 2ω oscillations.

The AC voltage protection implements overvoltage and undervoltage requirements. Fig. 3.27(e) shows continuously rising RMS voltages triggering the AC voltage protection and subsequent WTG disconnection from the power grid. The fault tolerance duration reaches approximately 1.4 s under VSM control and 1.1 s under droop control and dVOC. WTGs using the original GFM control fail to maintain GFM operation in this fault scenario. These responses validate the analysis in Section II and demonstrate the need for an enhanced synchronization loop in GFM control.

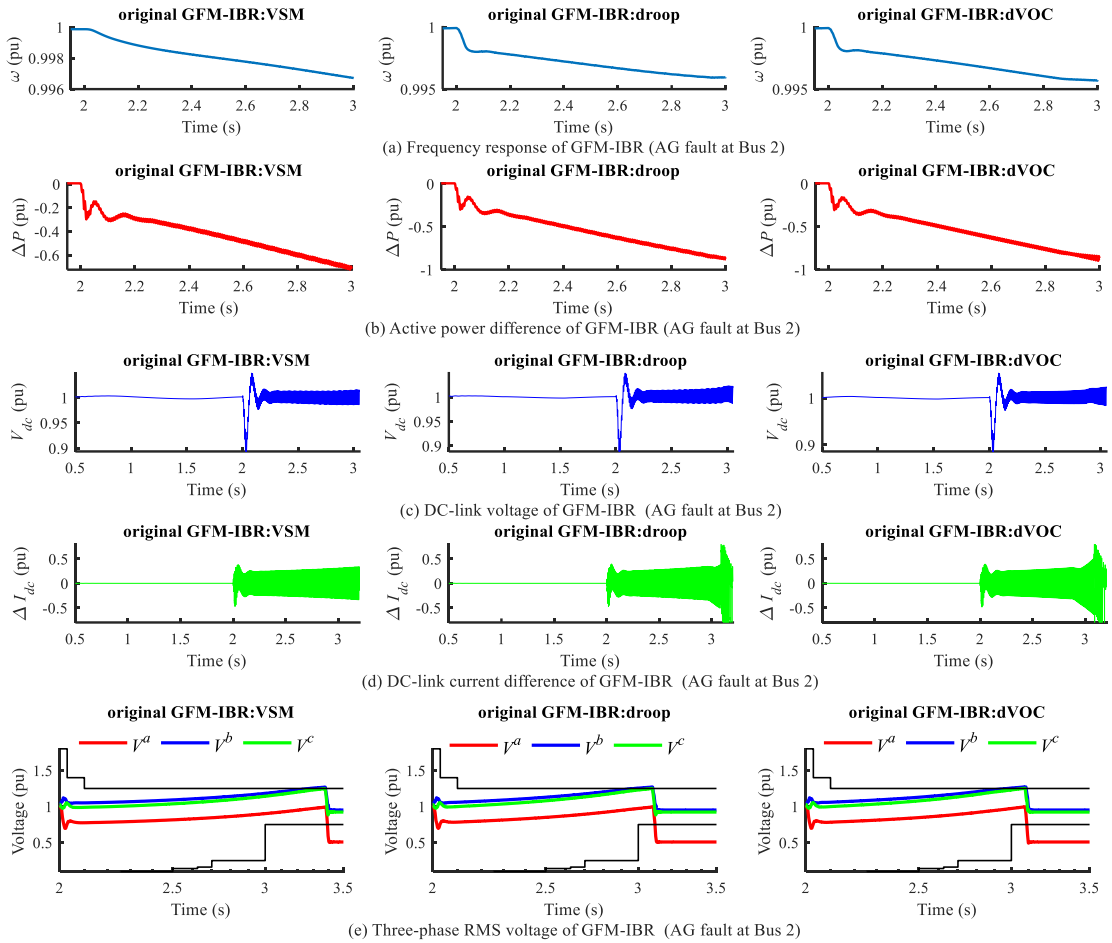

Fig. 3.27. Responses of the original GFM control under AG fault at the Bus 2.

b) Performance under the Proposed GFM Control

Fig. 3.28 and Fig. 3.29 demonstrate the proposed GFM control responses during AG faults at Bus 2 and Bus 3, respectively. The fault duration is set to 1 s and the transition mode duration to 0.2 s for clear demonstration.

Fig. 3.28(a) and Fig. 3.29(a) show the angular frequency maintaining the nominal value during both steady state fault conditions and fault clearance, confirming WTG synchronization retention through the proposed synchronization loop. As a result:

- The active power difference remains near zero

- The DC-link voltage maintains approximately 1 pu in both restricted and post-fault actual GFM modes (Fig. 3.28(b), Fig. 3.28(c), Fig. 3.29(b), and Fig. 3.29(c))

- Double-fundamental-frequency oscillations appear in waveforms due to asymmetrical fault negative sequence components

- Three-phase RMS voltages receive support through the proposed current reference coordination and the VSL (Fig. 3.28(d) and Fig. 3.29(d))

- At the fault inception (t=2 s), the low-voltage variation in phase A is detected by the FRT logic. Then WTG enters FRT mode within 0.5 cycles. After fault recovery (t=3 s), FRT logic deactivates within one cycle. (Fig. 3.30(a) and Fig. 3.30(b))

- In transition mode, the magnitude of $\boldsymbol{Z}_{VI}$ reduces to zero, indicating that I_s stabilizes at I_s^{th}. Then

WTG enters the actual GFM mode after 0.2 s. (Fig. 3.30(c))

- After fault recovery, the DC chopper effectively attenuates DC overvoltage to levels below 1.1 pu. The DC chopper effect does not adversely affect the synchronization. (Fig. 3.31)

WTGs maintain grid connection while meeting voltage ride-through requirements. The proposed control operates beyond specific frequency bands, regulating both voltage and frequency dynamics with operational timescales exceeding 1 ms [19].

The proposed GFM control achieves:

- Electrical variable stabilization across operation modes
- The resolution of the original GFM control instability
- Enhanced synchronization during asymmetrical faults

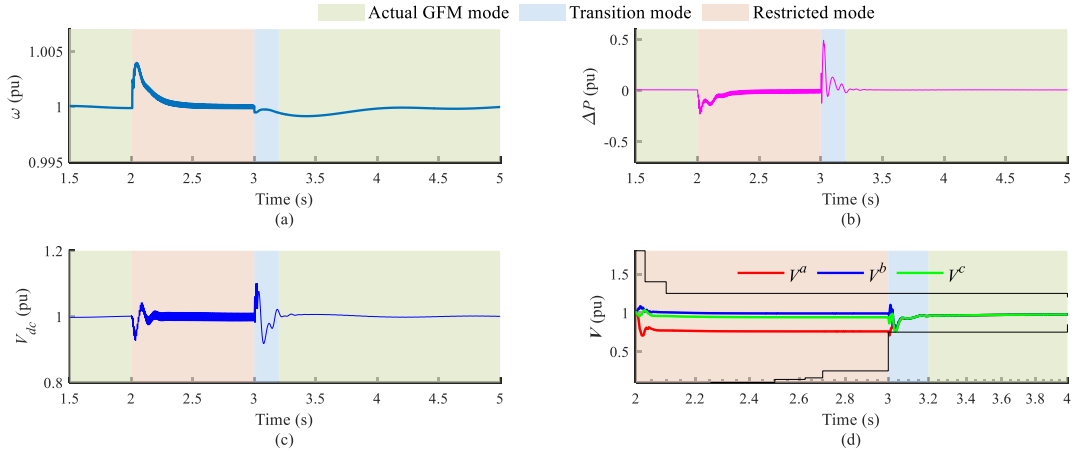

Fig. 3.28. Responses of the proposed GFM control under an AG fault at Bus 2: (a) Frequency response; (b) Active power difference; (c) DC-link voltage; (d) Three-phase RMS voltage.

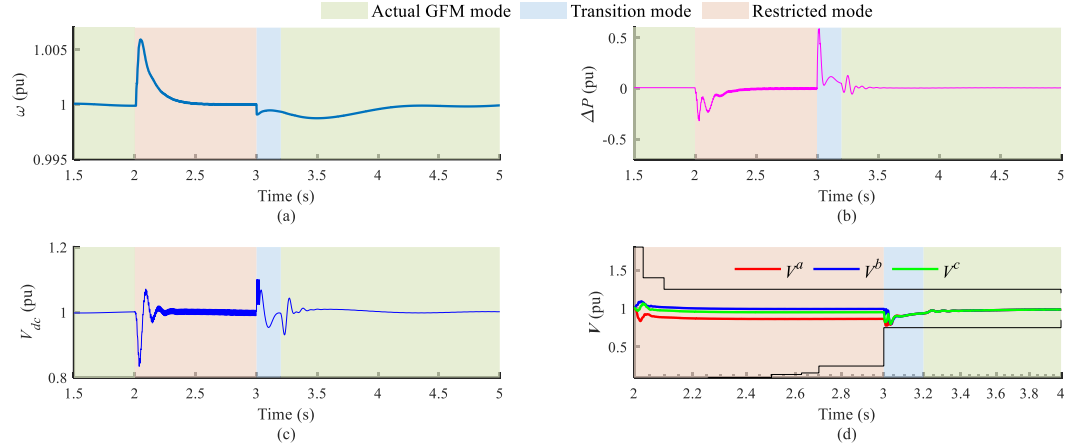

Fig. 3.29. Proposed GFM control response under an AG fault at Bus 3: (a) Frequency response; (b) Active power difference; (c) DC-link voltage; (d) Three-phase RMS voltage.

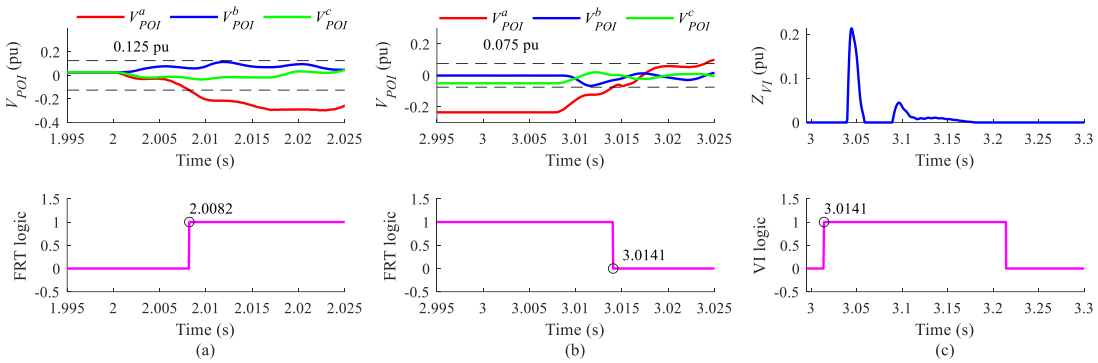

Fig. 3.30. Control mode detection under an AG fault at Bus 2: (a) FRT activation; (b) FRT deactivation; (c) VI response.

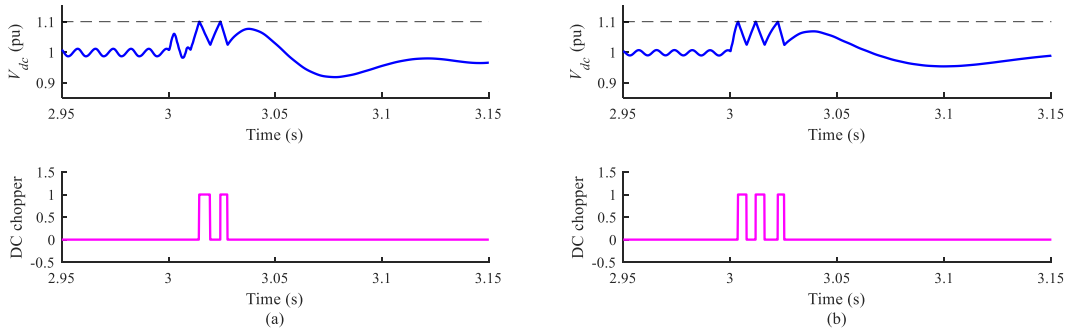

Fig. 3.31. DC chopper effects: (a) AG fault at Bus 2; (b) AG fault at Bus 3.

c) Comparison with Grid-Following FRT Control

To compare the dynamic performance of the proposed GFM synchronization control and GFL-based FRT control, the frequency responses under different asymmetrical fault scenarios are presented in Fig. 3.32. Each subplot carries the title "Fault Location (Fault Type)," where (AB) indicates a bolted line-A-to-line-B fault. The GFL-based FRT control incorporates the conventional DDSRF-PLL and the decoupled-sequence control that complies with VDE-AR-N 4120 [135]. Under GFL-based FRT control, the frequency experiences significant oscillations with peaks exceeding the continuous frequency ride-through range, whereas under the proposed GFM synchronization control, it converges within a short transient period without significant overshoot. This behavior demonstrates the robust performance of the proposed synchronization loop under asymmetrical grid conditions. Overall, results indicate that the proposed GFM synchronization control delivers superior dynamic performance compared to GFL-based FRT control, thereby enhancing frequency stability during asymmetrical faults.

For additional comparison, Fig. 3.33 illustrates the reactive power outputs across various fault scenarios. Because the current coordination method in the proposed GFM control maximizes converter current capacity utilization, Fig. 3.33(a) demonstrates its superior reactive power support compared to GFL-based FRT control. As shown in Fig. 3.33(d), during three-phase short circuit faults, GFL-based FRT control experiences LOS while the proposed GFM control maintains stability. Although the proposed current coordination with scaling could enhance reactive power support in GFL-based FRT control, it would not improve its synchronization capabilities.

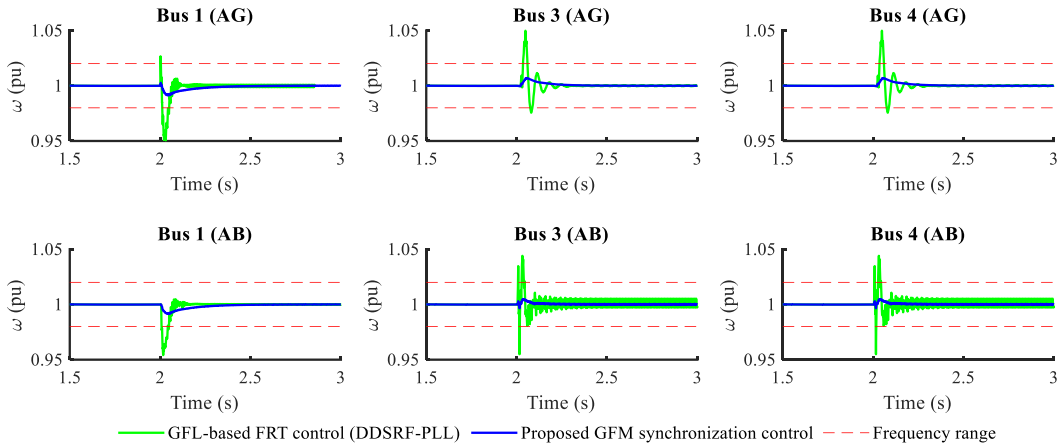

Fig. 3.32. Frequency responses under the GFL-based FRT control and proposed GFM control in different fault scenarios

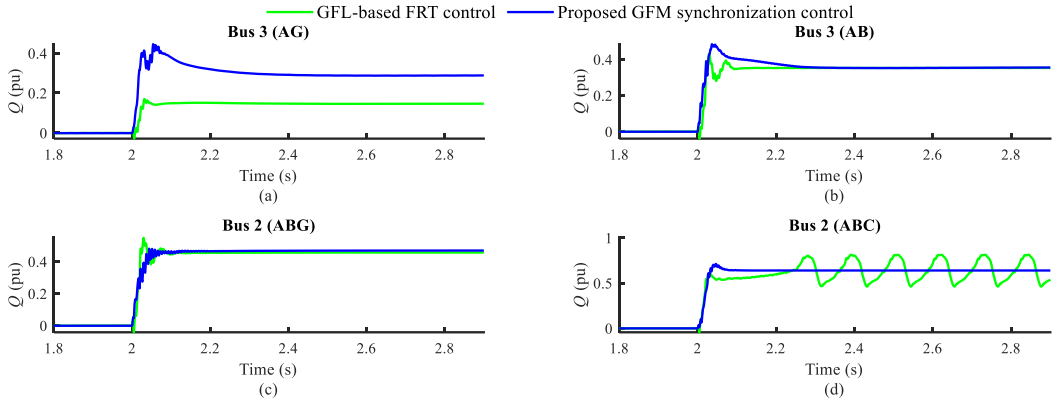

Fig. 3.33. Reactive power responses under the GFL-based FRT control and proposed GFM control in different fault scenarios

d) Performance of WTG restoration

Fig. 3.34 and Fig. 3.35 demonstrate three-phase RMS current performance during WTG restoration under AG faults at Bus 2 and Bus 3, respectively. The current reference coordination enables the faulted phase current to reach the current limit (1.2 pu) during restricted mode.

After fault clearance, WTGs transition from restricted mode to transition mode. In Fig. 3.34(a) and Fig. 3.35(a), without the VI-based method implementation, the currents exhibit oscillation, and their first peak exceeds the current limit. This indicates that overcurrent issues emerge during the transition process despite fault clearance. With the VI-based method illustrated, the current transients are eliminated through *dq* voltage reference adjustments in transition mode, as shown in Fig. 3.34(b) and Fig. 3.35(b). This demonstrates that the VI-based method effectively resolves the overcurrent issue in transition mode.

Table 3-10 provides comparative numerical results in restricted mode, including the maximum deviation $\Delta_{max}(.)$, the frequency settling time T_s, the phase current maximum, and voltage ride-through capability (three-phase RMS voltages at t = 3 s). Under the original GFM control, voltage exceeds 1 pu and diverges as frequency decreases. With GFL-based FRT control, the frequency oscillates under PLL regulation. The proposed GFM control effectively resolves these issues.

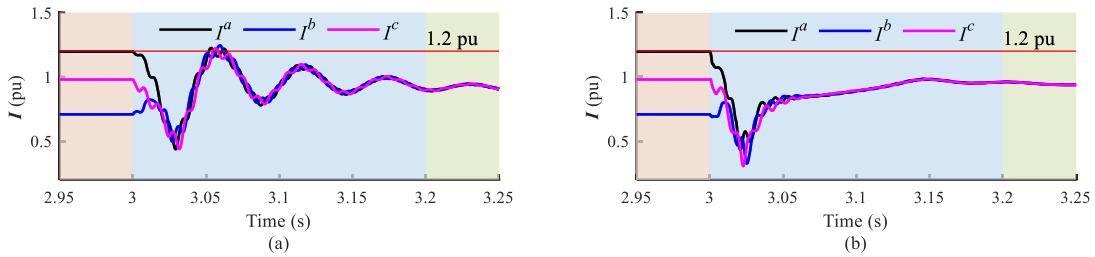

Fig. 3.34. Three-phase RMS currents under an AG fault at Bus 2: (a) Without the VI-based method; (b) With the VI-based method.

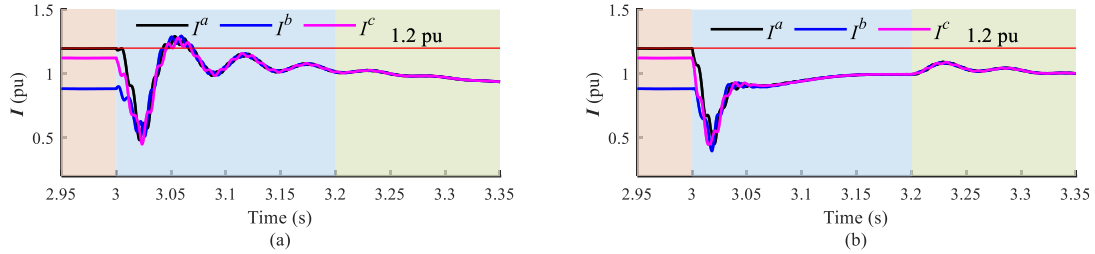

Fig. 3.35. Three-phase RMS currents under an AG fault at Bus 3: (a) Without the VI-based method; (b) With the VI-based method.

TABLE 3-10

Comparative Studies on the Proposed GFM Control and Other Control Strategies (Bus 2 (AG))

Control Strategy	$\Delta_{max}(\omega)$	$\Delta_{max}(\Delta P)$	$\Delta_{max}(V_{dc})$	V^a	V^b	V^c	T_s	I_s^a	I_s^b	I_s^c
Proposed GFM Control	0.0048	0.3083	0.0626	0.72	0.99	0.92	0.5 s	1.20	0.78	1.05
Original GFM Control	Descend	0.7239	0.1063	0.84	1.14	1.09	Diverge	1.12	0.71	0.83
GFL-based FRT Control	0.1108	0.1224	0.0893	0.60	0.92	0.99	Oscillate	1.21	1.07	1.05

3.1.6 Conclusion

This section proposes enhanced FRT control solutions for full converter-based GFM-IBRs. The key proposals include an advanced reactive current injection method using the *K*-factor, an improved CS-based CLM by using a current scaling method, an adaptive VI-based CLM, and a three mode-switching control solution. The proposed GFM PNSC structure exhibits the flexibility of selecting different synchronization loops and current limiters. The main conclusions are summarized as follows:

1) The proposed current reference generation implements the I1R and I2R injection per IEEE 2800 standard. The improved current limiter incorporates the angular relations between *dq* components and reactive currents of GFM-IBRs and a current scaling method to achieve full converter capacity utilization. Under different unbalanced fault scenarios, the proposed current limiting strategy effectively meets current injection requirements during ride-through modes per IEEE 2800. The CS-based CLM enables GFM-IBRs to provide optimal I1R and I2R injection, fully utilize current capacity, and emulate the negative sequence behavior of SGs during unbalanced faults. Overall, the proposed GFM PNSC structure and enhanced current limiting strategy represent a significant step toward the integration of GFM-IBRs in modern grid systems.

2) Under unbalanced large-signal disturbance, the GFM IBR is prone to LOS and FRT capacity. The adaptive VI-based CLM is activated at the fault inception to avoid overcurrent and update the internal

voltage vectors to retain voltage dynamics. Various PSLs (VSM, droop, and dVOC) can be flexibly used in the proposed GFM control, and angular difference and frequency remain stabilized under fault steady state and fault clearance conditions. The FRT capability of GFM-IBRs is effectively enhanced due to the increased reactive power caused by positive- and negative-sequence reactive current injection per recent grid codes. This control solution also achieves optimal utilization of current capacity via adaptive decoupled-sequence current limits. Moreover, the three-phase instantaneous voltages exhibit great transient responses, achieving stabilization in less than two cycles after fault inception.

3) A three-mode switching control solution is proposed for GFM Type-IV WTGs, enhancing synchronization during asymmetrical faults. In actual GFM mode, the PSL is employed in the GSC control, using active power reference obtained from MPPT. The DC-link voltage remains regulated by the MSC control. In restricted mode, the VSL and current reference coordination manage frequency regulation, reactive current injection, and current limiting. In transition mode, the VI-based method eliminates transients. Mode switching relies on the FRT start-up block using voltage variation at POI. Compared with the original controls, the merits of the proposed control solution are summarized as follows:

3.1) The proposed synchronization loop reduces the complexity of multiple parameter design and demonstrates robustness under asymmetrical grid conditions. In restricted mode, the VSL addresses imbalance between the wind turbine power output and the grid power demand, preventing the divergence of DC-link components. Compared with the GFL-WTG employing DDSRF-PLL, the proposed GFM synchronization control converges quickly without notable overshoot, enhancing frequency ride-through.

3.2) During asymmetrical faults, the reactive current injection and the current scaling method maximize voltage support capabilities of WTGs, fulfilling overvoltage/undervoltage ride-through requirements. Following fault clearance, the VI-based method effectively eliminates current transients, preventing overcurrent issues during the transition process, thus improving the dynamic performance of WTG restoration and the safety of converter devices.

3.2 For Type-III WTG: GFM-DFIG

3.2.1 PNSC design of Grid-Forming DFIG

3.2.1.1 Mechanism of DFIG During Asymmetrical Faults

The topology of a typical DFIG-based WTG is depicted in Fig. 3.36. The rotor speed ω_r and rotor angle θ_r are controlled by the pitch regulator. The grid-side converter (GSC) control is typically employed to regulate the DC-link voltage V_{dc}. $\boldsymbol{V}$, $\boldsymbol{I}$, and $\boldsymbol{M}$ denote the voltages, currents, and modulation signals, respectively. Subscripts s and r denote the stator- and rotor-side components, respectively. During asymmetrical faults, since the zero-sequence components on the grid side are separated by a delta-connected WTG transformer, the instantaneous three-phase components in the DFIG can be represented using dq or $\alpha\beta$ complex vectors. In this section, superscripts $d+$ and $q+$ denote d-axis and q-axis components in the $dq+$ frame that rotate at the nominal frequency ω_n, respectively. Superscripts $d-$ and $q-$ denote d-axis and q-axis components in the $dq-$ frame that rotate at the nominal frequency $-\omega_n$, respectively.

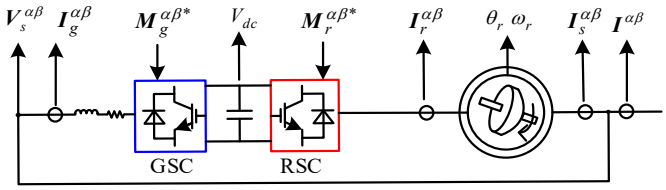

Fig. 3.36. Basic topology of a DFIG-based WTG.

The stator voltage $\boldsymbol{V}_s$ and stator flux linkage $\boldsymbol{\psi}_s$ are given by

$$\begin{cases} \boldsymbol{V}_{s+}^{dq+} = R_s \boldsymbol{I}_{s+}^{dq+} + d\boldsymbol{\psi}_{s+}^{dq+}/dt + j\omega_n \boldsymbol{\psi}_{s+}^{dq+} \\ \boldsymbol{V}_{s-}^{dq-} = R_s \boldsymbol{I}_{s-}^{dq-} + d\boldsymbol{\psi}_{s-}^{dq-}/dt - j\omega_n \boldsymbol{\psi}_{s-}^{dq-} \\ \boldsymbol{\psi}_{s+}^{dq+} = L_s \boldsymbol{I}_{s+}^{dq+} + L_m \boldsymbol{I}_{r+}^{dq+} \\ \boldsymbol{\psi}_{s-}^{dq-} = L_s \boldsymbol{I}_{s-}^{dq-} + L_m \boldsymbol{I}_{r-}^{dq-} \end{cases} \tag{3.52}$$

where R and L denote resistance and inductance, respectively. Subscript m denotes the magnetizing components. Subscripts + and − denote the positive- and negative-sequence components, respectively. Similarly, the rotor voltage $\boldsymbol{V}_r$ and rotor flux linkage $\boldsymbol{\psi}_r$ are given by

$$\begin{cases} \boldsymbol{V}_{r+}^{dq+} = R_r \boldsymbol{I}_{r+}^{dq+} + d\boldsymbol{\psi}_{r+}^{dq+}/dt + js\omega_n \boldsymbol{\psi}_{r+}^{dq+} \\ \boldsymbol{V}_{r-}^{dq-} = R_r \boldsymbol{I}_{r-}^{dq-} + d\boldsymbol{\psi}_{r-}^{dq-}/dt - j(2-s)\omega_n \boldsymbol{\psi}_{r-}^{dq-} \\ s = (\omega_n - \omega_r)/\omega_n \\ \boldsymbol{\psi}_{r+}^{dq+} = L_m \boldsymbol{I}_{s+}^{dq+} + L_r \boldsymbol{I}_{r+}^{dq+} \\ \boldsymbol{\psi}_{r-}^{dq-} = L_m \boldsymbol{I}_{s-}^{dq-} + L_r \boldsymbol{I}_{r-}^{dq-} \end{cases} \tag{3.53}$$

where s denotes the slip factor. Based on (3.52) and (3.53), the stator- and rotor-side voltages consist of the rotor speed and the stator- and rotor-side resistance, inductance, currents, and flux leakage. The complexity involved in expressing these voltage vectors restricts their usefulness for evaluating FRT performance. To convert these voltage vectors into a simpler form, an internal voltage vector is defined based on the derivation of the rotor-side flux leakage. By using $\alpha\beta$ complex vectors, the stator voltages

can be expressed by the stator current and rotor flux linkage as follows:

$$\boldsymbol{V}_s^{\alpha\beta} = R_s \boldsymbol{I}_s^{\alpha\beta} + \frac{L_m}{L_r}\frac{d\boldsymbol{\psi}_r^{\alpha\beta}}{dt} + \sigma L_s \frac{d\boldsymbol{I}_s^{\alpha\beta}}{dt} \tag{3.54}$$

where the leakage factor σ equals

$$\sigma = 1 - \frac{L_m^2}{L_s L_r} \tag{3.55}$$

From (3.54), the internal voltage vector is defined as

$$\begin{aligned} \boldsymbol{E}_s^{\alpha\beta} &= \boldsymbol{V}_s^{\alpha\beta} - R_s \boldsymbol{I}_s^{\alpha\beta} - \sigma L_s \frac{d\boldsymbol{I}_s^{\alpha\beta}}{dt} \\ &= \frac{L_m}{L_r}\frac{d\boldsymbol{\psi}_r^{\alpha\beta}}{dt} \end{aligned} \tag{3.56}$$

During asymmetrical faults, the rotor flux linkage can be separated into positive-sequence, negative-sequence, and transient component, as follows:

$$\boldsymbol{\psi}_r^{\alpha\beta} = \boldsymbol{\psi}_{r+}^{dq+} e^{j\omega_n t} + \boldsymbol{\psi}_{r-}^{dq-} e^{-j\omega_n t} + \boldsymbol{\psi}_r'^{\alpha\beta} \tag{3.57}$$

Hence, the internal voltage vector is separated as

$$\begin{cases} \boldsymbol{E}_s^{\alpha\beta} = \boldsymbol{E}_{s+}^{dq+} e^{j\omega_n t} + \boldsymbol{E}_{s-}^{dq-} e^{-j\omega_n t} + \boldsymbol{E}_s'^{\alpha\beta} \\ \boldsymbol{E}_{s+}^{dq+} = \underbrace{\frac{L_m}{L_r}\frac{d\boldsymbol{\psi}_{r+}^{dq+}}{dt}}_{\text{transient}} + \underbrace{\frac{j\omega_n L_m \boldsymbol{\psi}_{r+}^{dq+}}{L_r}}_{\text{steady state}} \approx \frac{j\omega_n L_m \boldsymbol{\psi}_{r+}^{dq+}}{L_r} \\ \boldsymbol{E}_{s-}^{dq-} = \underbrace{\frac{L_m}{L_r}\frac{d\boldsymbol{\psi}_{r-}^{dq-}}{dt}}_{\text{transient}} + \underbrace{\frac{-j\omega_n L_m \boldsymbol{\psi}_{r-}^{dq-}}{L_r}}_{\text{steady state}} \approx \frac{-j\omega_n L_m \boldsymbol{\psi}_{r-}^{dq-}}{L_r} \\ \boldsymbol{E}_s'^{\alpha\beta} = \frac{L_m}{L_r}\frac{d\boldsymbol{\psi}_r'^{\alpha\beta}}{dt} \end{cases} \tag{3.58}$$

From the above analysis, various sequence components produced by DFIG-based WTG appear during asymmetrical faults. To support the sequence components of internal voltage vectors, the design of the RSC and GSC control systems should enable independent control over both positive- and negative-sequence components. In this section, GFM control is implemented for the RSC to support the stator voltage and frequency.

3.2.1.2 Sequence Component Division and Power Control

The decoupled double synchronous reference frame (DDSRF) is employed to separate the sequence components from the measurements, offering *dq*+ and *dq*− frames that rotate at the regulated frequency. As shown in Fig. 3.37, the GSC control follows the traditional GFL mode, utilizing the phase angle regulated by a PLL (θ_{PLL}) as the input of the DDSRF. The RSC control employs GFM mode with the phase angle regulated by a PSL (θ_{PSL}) as the input of the DDSRF. This preserves the distinctive features of GFM controls.

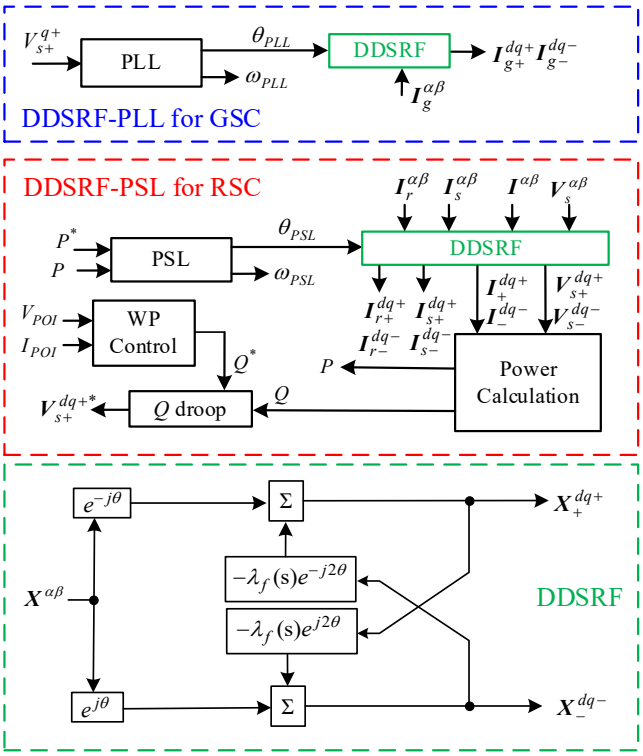

Fig. 3.37. Sequence component division and outer-loop frequency and power control of the proposed GFM-DFIG.

In Fig. 3.37, the reference of the active power P^* is obtained by the maximum power point tracking (MPPT) strategy. In this section, the virtual synchronous machine control is used as the most representative PSL, as given by

$$\begin{cases} P^* = C_{p\max}\rho A(R_b/\lambda_{op}\,\omega_r)^3/2 \\ \dfrac{d\theta_{PSL}}{dt} = \omega_{PSL} \\ J\dfrac{d\omega_{PSL}}{dt} = D_\omega\left(\omega_n - \omega_{PSL}\right) + \lambda_f(\mathrm{s})(P^* - P) \end{cases} \tag{3.59}$$

where $C_{p\max}$ denotes the maximum power coefficient. ρ is the air density. R_b denotes the blade radius of the wind turbine. λ_{op} and A denote the optimal tip-speed ratio and the swept area of the rotor, respectively. J and D_ω denote the inertia constant and damping factor for frequency. The instantaneous active and reactive powers are utilized as the inputs of PSLs and reactive power droop (Q droop) control, as given by

$$\begin{cases} P = V_{s+}^{d+}I_+^{d+} + V_{s+}^{q+}I_+^{q+} + V_{s-}^{d-}I_-^{d-} + V_{s-}^{q-}I_-^{q-} \\ Q = V_{s+}^{q+}I_+^{d+} - V_{s+}^{d+}I_+^{q+} + V_{s-}^{q-}I_-^{d-} - V_{s-}^{d-}I_-^{q-} \end{cases} \tag{3.60}$$

The Q droop control is employed to obtain the positive-sequence virtual voltage references for the inner voltage control. To align the d-axis with the voltage, the q-axis virtual voltage reference V_{s+}^{q+*} is set to zero. The d-axis virtual voltage reference is established as follows:

$$V_{s+}^{d+*} = V^* + D_Q\lambda_f(\mathrm{s})(Q^* - Q) \tag{3.61}$$

where D_Q denotes the damping factor for reactive power.

3.2.1.3 Inner Control Loop and Modulation

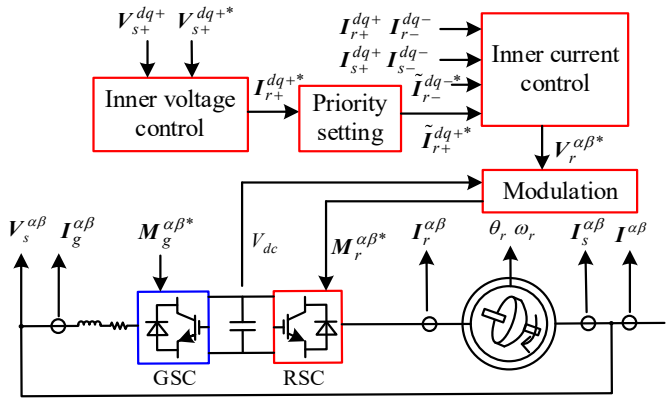

Fig. 3.38. PNSC of the GFM-DFIG in normal operation.

In normal operation, the system is in a balanced condition, which implies that there are no negative-sequence components that necessitate control. Hence, the references for negative-sequence rotor currents should be set to zero, i.e., $\boldsymbol{I}_{r+}^{dq-*}=0$. To support the stator voltage, the references for positive-sequence rotor currents are generated by the inner voltage control, as given by

$$\boldsymbol{I}_{r+}^{dq+*}=\left(k_{pV}+k_{iV}/\mathrm{s}\right)\left(\boldsymbol{V}_{s+}^{dq+*}-\boldsymbol{V}_{s+}^{dq+}\right) \tag{3.62}$$

where k_{pV} and k_{iV} are the inner voltage control parameters. To avoid overcurrent, a current limiter based on priority settings of I1A and I1R is in service. For simplicity, denote the I1A and I1R as *PQ* currents. The transformation between *PQ* currents and *dq* currents is given by

$$\begin{cases} I_{r+}^{P*}-jI_{r+}^{Q*}=\boldsymbol{I}_{r+}^{dq+*}e^{-j\theta_{V_s^+}} \\ \theta_{V_s^+}=\arctan\left(V_{s+}^{q+}/V_{s+}^{d+}\right) \end{cases} \tag{3.63}$$

where I^P and I^Q denote active current and reactive current, respectively. The current references under the priority setting, denoted as $\tilde{\boldsymbol{I}}$, are determined as

$$\begin{cases} \left|\tilde{I}_{r+}^{P*}\right|\le I_r^{lim} \\ \left|\tilde{I}_{r+}^{Q*}\right|\le\sqrt{(I_r^{lim})^2-(\tilde{I}_{r+}^{P*})^2} \\ \tilde{\boldsymbol{I}}_{r+}^{dq+*}=(\tilde{I}_{r+}^{P+*}-j\tilde{I}_{r+}^{Q*})e^{j\theta_{V_{r+}}} \\ \theta_{V_{r+}}=\arctan\left(V_{r+}^{q+}/V_{r+}^{d+}\right) \end{cases} \tag{3.64}$$

where superscript *lim* denotes the current limits. The inner current control is separated into positive- and negative-sequence loops, as follows:

$$\begin{cases} \boldsymbol{V}_{r+}^{dq+*}=\left(k_{pC}+k_{iC}/\mathrm{s}\right)\left(\boldsymbol{I}_{r+}^{dq+*}-\boldsymbol{I}_{r+}^{dq+}\right)+js\omega_n\boldsymbol{\psi}_{r+}^{dq+} \\ \boldsymbol{V}_{r-}^{dq-*}=\left(k_{pC}+k_{iC}/\mathrm{s}\right)\left(\boldsymbol{I}_{r-}^{dq-*}-\boldsymbol{I}_{r-}^{dq-}\right)-j(2-s)\omega_n\boldsymbol{\psi}_{r-}^{dq-} \\ s=(\omega_n-\omega_r)/\omega_n \end{cases} \tag{3.65}$$

$$\begin{aligned} \boldsymbol{V}_r^{\alpha\beta*}&=\boldsymbol{V}_{r+}^{\alpha\beta*}+\boldsymbol{V}_{r-}^{\alpha\beta*} \\ &=\boldsymbol{V}_{r+}^{dq+*}e^{j(\theta_{PSL}-\theta_r)}+\boldsymbol{V}_{r-}^{dq-*}e^{-j(\theta_{PSL}+\theta_r)} \end{aligned} \tag{3.66}$$

where k_{pC} and k_{iC} are the inner current control parameters. In normal operation, the regulation is focused solely on the positive-sequence components. On this basis, the modulation signal is established as follows:

$$\boldsymbol{M}_r^{\alpha\beta*} = \frac{2\boldsymbol{V}_r^{\alpha\beta*} N_r/N_s}{V_{dc}} \tag{3.67}$$

where N_r/N_s denotes the turn ratio between rotor and stator windings. Based on the proposed PNSC as shown in Fig. 3.38, during asymmetrical faults, the potential challenges are summarized as follows:

For the positive-sequence loop, the stator voltage will be sharply disturbed. Moreover, due to overcurrent, the current limiter will cut the current references. This leads to the inner voltage control not being able to regulate the positive-sequence stator voltage properly.

Moreover, the negative-sequence and transient components typically induce rotor EMF that exceeds the rotor voltage capability. The negative-sequence internal voltage vectors are generated and uncontrolled. This is likely to increase the voltage unbalance and overvoltage on the healthy phase, which introduces risks of insulation failure and protection maloperation.

Besides, to comply with the recent grid codes, it is required to offer a low-reactance path in the negative-sequence system and implement reactive current injection. Since the flux linkages cannot instantaneously vary, transient components are induced together with positive- and negative-sequence components. This brings severe over-modulation issues.

To this end, there is a need to design an asymmetrical FRT control solution for GFM-DFIG. This will be illustrated in the next section.

3.2.2 Asymmetrical FRT Control to Establish Internal Voltage Vectors

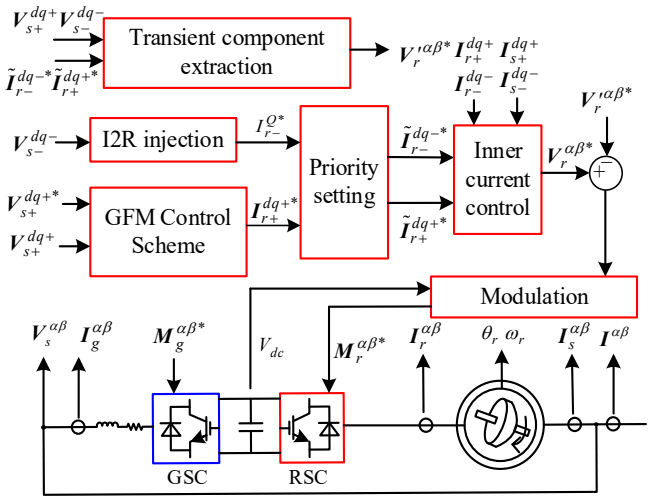

Fig. 3.39. Asymmetrical FRT control of the GFM-DFIG.

Fig. 3.39 illustrates the structure of the proposed asymmetrical FRT control for the GFM-DFIG. Based on this, Fig. 3.40 depicts a closed-loop system to establish positive- and negative-sequence internal voltage vectors.

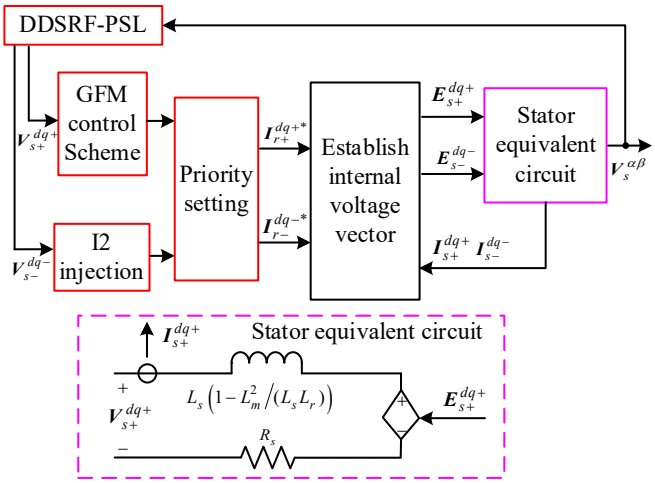

Fig. 3.40. Closed-loop system to establish positive- and negative-sequence internal voltage vectors.

Assume $\omega_{PSL}=\omega_n$, the positive- and negative-sequence internal voltage vectors under fault steady state conditions are determined as

$$\begin{cases} \boldsymbol{E}_s^{dq+} \approx \dfrac{j\omega_n L_m \boldsymbol{\psi}_{r+}^{dq+}}{L_r} = \dfrac{j\omega_n L_m \left(L_m \boldsymbol{I}_{s+}^{dq+} + L_r \boldsymbol{I}_{r+}^{dq+*}\right)}{L_r\left[1+\left(L_r/k_{pC}\right)\mathrm{s}\right]} \\ \boldsymbol{E}_{s-}^{dq-} \approx \dfrac{-j\omega_n L_m \boldsymbol{\psi}_{r-}^{dq-}}{L_r} = \dfrac{-j\omega_n L_m \left(L_m \boldsymbol{I}_{s-}^{dq-} + L_r \boldsymbol{I}_{r-}^{dq-*}\right)}{L_r\left[1+\left(L_r/k_{pC}\right)\mathrm{s}\right]} \end{cases} \tag{3.68}$$

In (3.68) and Fig. 3.40, the internal voltage vectors can be regulated by adjusting the rotor current references. For the proposed control structure in Fig. 3.39, the positive-sequence rotor current references are regulated by the GFM control scheme, while the negative-sequence rotor current references are regulated by the I2R injection. In the FRT mode, priority settings should be specified to coordinate the current references. Hence, the details of control strategies and priority settings for establishing internal voltage vectors are illustrated in this section.

3.2.2.1 Negative-Sequence Control

Based on the recent grid codes, the required I2R equals

$$I_-^Q = K_-^Q V_{s-} \tag{3.69}$$

where K_-^Q is the gain for I2R injection. Then the negative-sequence rotor current references are given by

$$\begin{cases} I_{r-}^{Q*} = \left(\dfrac{1}{\omega_n L_m} - \dfrac{L_s K_-^Q}{L_m}\right) V_{s-} \\ I_{r-}^{P*} = 0 \end{cases} \tag{3.70}$$

where I_{r-}^{P*} is set to zero to conform with the IEEE Std. 2800-2022 and spare the current capacity for the I2R injection.

On this basis, the injected I2R from the stator winding is

$$I_{s-}^Q = -\frac{L_m}{L_s}\tilde{I}_{r-}^{Q*} + \frac{V_{s-}}{\omega_n L_s} \tag{3.71}$$

Finally, the GSC will inject the rest of the required I2R, as given by

$$I_{g-}^{Q*} = I_{-}^{Q} - I_{s-}^{Q} = K_{-}^{Q} V_{s-} + \frac{L_m}{L_s} \tilde{I}_{r-}^{Q*} - \frac{V_{s-}}{\omega_n L_s} \tag{3.72}$$

3.2.2.2 Positive-Sequence Control

In comparison to conventional GFL-based DFIGs, the most significant difference in the GFM-DFIG is the positive-sequence control. This section proposes two GFM control schemes for asymmetrical FRT to support the positive-sequence internal voltage vector of the DFIG.

1) Current Saturation-based Method

The proposed current saturation-based method implements the I1R injection in conventional GFL-based DFIGs. The incremental I1R is given by

$$\Delta I_{r+}^{Q*} = -\frac{L_s}{L_m} K_{+}^{Q} (V_{s+}^{*} - V_{s+}) - \frac{V_{s+}}{\omega_n L_m} \tag{3.73}$$

where K_{+}^{Q} is the gain for I1R injection. Since there is no PLL in the RSC control, the *q*-axis voltage is not zero, the I1R injection in the RSC control needs to incorporate the relations between incremental I1R and *dq* currents as follows:

$$\begin{cases} I_{r+}^{P*} = \left(k_{pV} + k_{iV}/\mathrm{s}\right)(V_{s+}^{d+*} - V_{s+}^{d+}) \\ I_{r+}^{Q*} = I_{r+}^{q+pre} + \Delta I_{r+}^{Q*} \end{cases} \tag{3.74}$$

where superscript *pre* denotes the pre-fault component. To restrict the positive-sequence rotor currents, a current limiter based on *Q* priority is employed, as given by

$$\begin{cases} \left|\tilde{I}_{r+}^{Q*}\right| \le I_r^{lim} \\ \left|\tilde{I}_{r+}^{P*}\right| \le \sqrt{\left(I_r^{lim} - \left|\tilde{I}_{r-}^{Q*}\right|\right)^2 - \left(\tilde{I}_{r+}^{Q*}\right)^2} \end{cases} \tag{3.75}$$

To prioritize the I1R, the I2R is constrained as

$$\left|\tilde{I}_{r-}^{Q*}\right| \le I_r^{lim} - \left|\tilde{I}_{r+}^{Q*}\right| \tag{3.76}$$

2) Virtual Impedance-based Method

To ensure the rotor current can be limited and regulated by the inner voltage control during asymmetrical faults, a virtual impedance-based method is proposed. Firstly, adaptive virtual voltage references $\tilde{\boldsymbol{V}}_{s+}^{dq+*}$ are defined by subtracting the voltage drop on the virtual rotor impedance $\boldsymbol{Z}_{rVI}$, as given by

$$\begin{aligned} \tilde{\boldsymbol{V}}_{s+}^{dq+*} &= \boldsymbol{V}_{s+}^{dq+*} - \boldsymbol{Z}_{rVI} \boldsymbol{I}_{r+}^{dq+*} \\ &= \boldsymbol{V}_{s+}^{dq+*} - \left(R_{rVI} + jX_{rVI}\right) \boldsymbol{I}_{r+}^{dq+*} \end{aligned} \tag{3.77}$$

where R_{rVI} and X_{rVI} denote the virtual rotor resistance and reactance, respectively. To suppress the current, a PI controller is employed to regulate the current reference tracking the current limit. Then the magnitude of the virtual rotor impedance is determined as

$$\left|\boldsymbol{Z}_{rVI}\right| = Z_{rVI} = \frac{\Delta V_{s+}}{I_r^{lim}} = \frac{V_{s+}^{*} - \left(k_{pVI} + k_{iVI}/\mathrm{s}\right)(I_r^{lim} - I_{r+}^{*})}{I_r^{lim}} \tag{3.78}$$

where k_{pVI} and k_{iVI} are the control parameters. Denote $\Delta_{X/R}$ as the ratio of reactance to resistance, the angle of the virtual rotor impedance is determined as

$$\theta_{\boldsymbol{Z}_{rVI}} = \arctan(\Delta_{X/R}) \tag{3.79}$$

Based on the adaptive virtual voltage references, the positive-sequence rotor currents can be regulated by the inner voltage control, as given by

$$\boldsymbol{I}_{r+}^{dq+*} = \left(k_{pV} + k_{iV}/\mathrm{s}\right)\left(\tilde{\boldsymbol{V}}_{s}^{dq+*} - \boldsymbol{V}_{s}^{dq+}\right) \tag{3.80}$$

Since the virtual impedance-based method does not rely on current limiters and priority settings in the positive-sequence control, the I2R is constrained as

$$\left|\tilde{I}_{r-}^{Q*}\right| \le I_{r}^{lim} - \left|\tilde{I}_{r+}^{*}\right| \tag{3.81}$$

3.2.2.3 Transient Component Extraction

To avoid over-modulation issues caused by transient components during asymmetrical faults, prior to modulation, a simplified calculation method is employed to remove the transient components in the rotor voltage references.

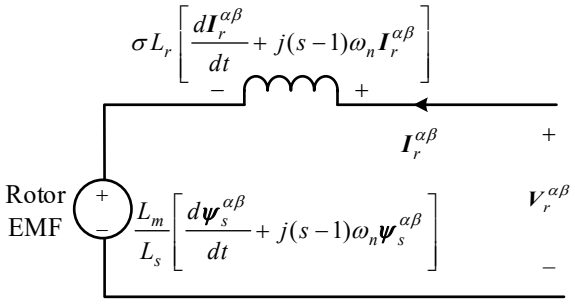

Fig. 3.41. Rotor equivalent circuit.

Firstly, the transient stator flux leakage is determined as

$$\begin{cases} \boldsymbol{\psi}_{s}^{\alpha\beta} = \boldsymbol{\psi}_{s}^{\prime\alpha\beta} + \boldsymbol{\psi}_{s+}^{dq+} e^{j\omega_n t} + \boldsymbol{\psi}_{s-}^{dq-} e^{-j\omega_n t} \\ \boldsymbol{\psi}_{s}^{\prime\alpha\beta} = L_s \boldsymbol{I}_{s}^{\prime\alpha\beta} + L_m \boldsymbol{I}_{r}^{\prime\alpha\beta} \\ \boldsymbol{\psi}_{s+}^{dq+} = \dfrac{L_s \boldsymbol{V}_{s+}^{dq+} + R_s L_m \tilde{\boldsymbol{I}}_{r+}^{dq+*}}{R_s + j\omega_n L_s} \\ \boldsymbol{\psi}_{s-}^{dq-} = \dfrac{L_s \boldsymbol{V}_{s-}^{dq-} + R_s L_m \tilde{\boldsymbol{I}}_{r-}^{dq-*}}{R_s - j\omega_n L_s} \end{cases} \tag{3.82}$$

During faults, if the RSC's equivalent impedance behaves as an inductor with a positive magnitude, the rotor current can be limited with a lesser rotor voltage. Denote L_{RSC} as the equivalent impedance of the RSC, combining (3.55) and (3.82) yields

$$\begin{cases} \boldsymbol{I}_{r}^{\prime\alpha\beta} = -\dfrac{L_m}{L_s\left(\sigma L_r + L_{RSC}\right)} \boldsymbol{\psi}_{s}^{\prime\alpha\beta} \\ \boldsymbol{I}_{s}^{\prime\alpha\beta} = \dfrac{L_r + L_{RSC}}{L_s\left(\sigma L_r + L_{RSC}\right)} \boldsymbol{\psi}_{s}^{\prime\alpha\beta} \end{cases} \tag{3.83}$$

Based on the rotor equivalent circuit in Fig. 3.41, by ignoring the derivation terms, the transient component of rotor voltages is approximately given by

$$\boldsymbol{V}_r'^{\alpha\beta} \cong j\omega_n(s-1)\left[\left(L_m/L_s\right)\boldsymbol{\psi}_s'^{\alpha\beta} + \sigma L_r \boldsymbol{I}_r'^{\alpha\beta}\right] \tag{3.84}$$

Combining (3.82)-(3.84) yields

$$\begin{aligned}\boldsymbol{V}_r'^{\alpha\beta*} &= j\omega_n\left(s-1\right)\frac{L_{RSC}L_m}{\left(L_rL_s - L_m^2 + L_sL_{RSC}\right)}\boldsymbol{\psi}_s'^{\alpha\beta} \\ &= -\frac{j\omega_r L_{RSC}L_m}{\left(L_rL_s - L_m^2 + L_sL_{RSC}\right)}\boldsymbol{\psi}_s'^{\alpha\beta}\end{aligned} \tag{3.85}$$

On this basis, the modulation signal is given by

$$\boldsymbol{M}_r^{\alpha\beta*} = \frac{2(\boldsymbol{V}_r^{\alpha\beta*} - \boldsymbol{V}_r'^{\alpha\beta*})\,N_r/N_s}{V_{dc}} \tag{3.86}$$

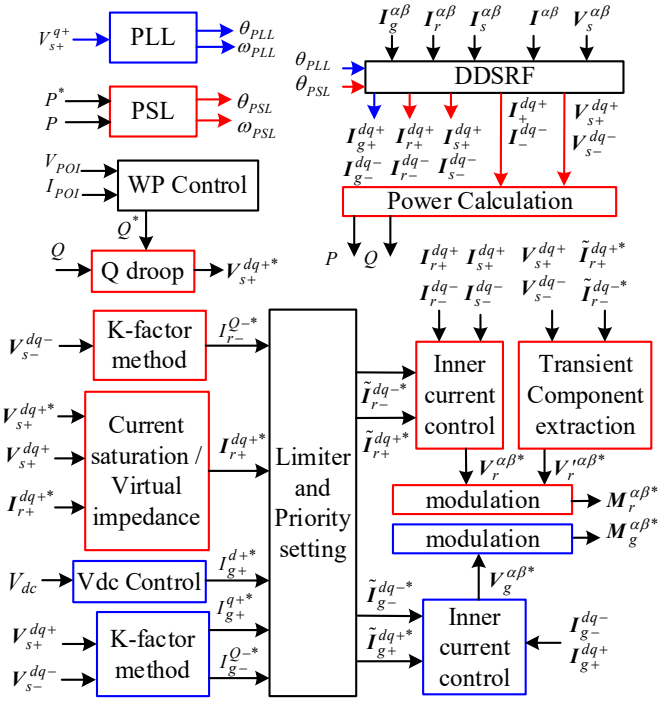

Fig. 3.42. Proposed asymmetrical FRT control solution of the GFM-DFIG.

To this end, a diagram of the FRT control for the GFM-DFIG is shown in Fig. 3.42. Initially, the AC measurements are separated into positive- and negative-sequence components using the DDSRF-PSL and DDSRF-PLL in RSC and GSC controls. To enhance transient stability, the frequency regulated by the DDSRF-PSL can be frozen during faults [49]. Next, to establish internal voltage vectors, two types of GFM control solutions are designed in the positive-sequence control in RSC control, while the negative-sequence control implements I2R injection.

To avoid overcurrent, the priority settings, as depicted in Fig. 3.43, are implemented to coordinate the current references within RSC and GSC controls. Since the virtual impedance-based method does not limit the current directly, there is no need to configure the positive-sequence current limiter with priority settings in RSC. The positive-sequence current limiter with priority settings in RSC is employed for the current saturation-based method. Finally, transient component extraction is utilized to eliminate the transient components in the rotor voltage references to address over-modulation issues.

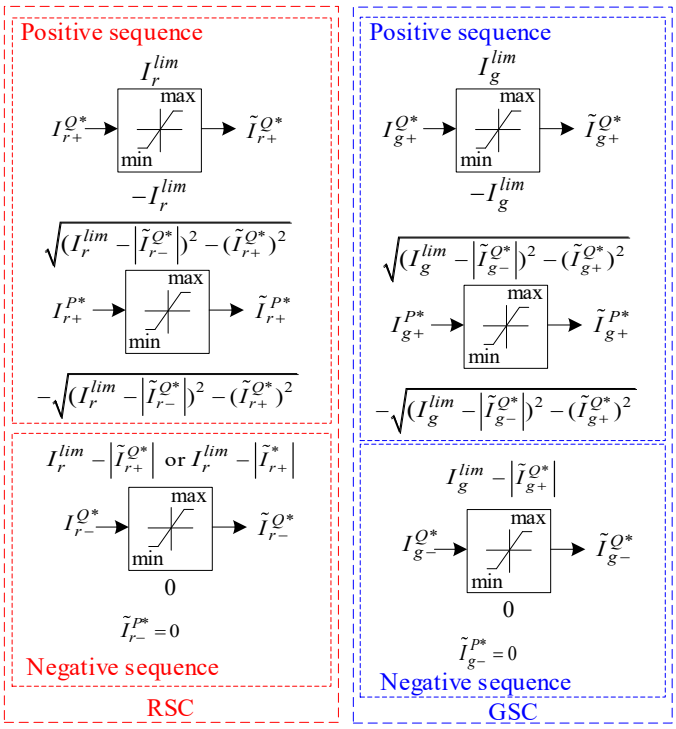

Fig. 3.43. Priority settings in asymmetrical FRT control solution of the GFM-DFIG.

3.2.3 Case Studies

In this section, the comparative studies on the current saturation-based method and virtual impedance-based method are performed with EMT simulations. The proposed GFM-DFIG and asymmetrical FRT controls are validated. In Fig. 3.44, the 120 kV 60 Hz EPRI benchmark system is connected to 45×1.5 MW DFIG-based WTGs. The RSC control parameters are presented in Table 3-11.

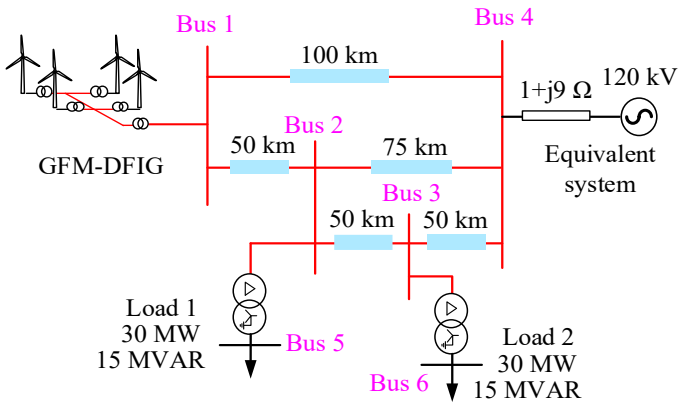

Fig. 3.44. EPRI Benchmark system connected to a GFM-DFIG.

TABLE 3-11

Parameters of RSC Control

Parameter	Value	Parameter	Value
J , D_ω	0.15, 0.8038	K_+^Q , K_-^Q	2
k_{pC}, k_{iC}	0.82, 12.13	V^*	1 pu
k_{pV}, k_{iV}	1, 200	$\Delta_{X/R}$	1
k_{pVI}, k_{iVI}	0.2, 65	I_r^{lim} , I_g^{lim}	1.2 pu, 0.36 pu

3.2.3.1 Internal Voltage Vector

To investigate the performance of the GFM-DFIG during asymmetrical faults, bolted line-A-to-ground (AG) fault and line-A-to-line-B (AB) fault are applied at Bus 2 when t = 2 s, respectively. The fault duration is set to 1 s for illustration. The simulation results of positive- and negative-sequence internal voltage vectors are displayed in Fig. 3.45−Fig. 3.48.

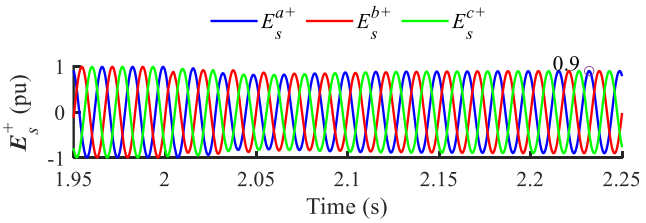

(a) Current saturation-based method

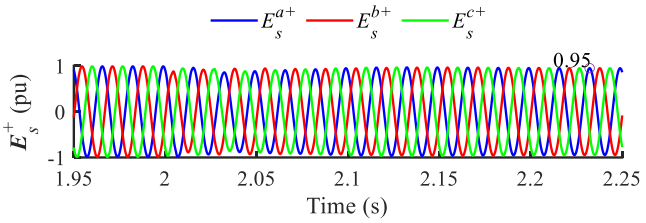

(b) Virtual impedance-based method

Fig. 3.45. Positive-sequence internal voltage vectors (AG fault).

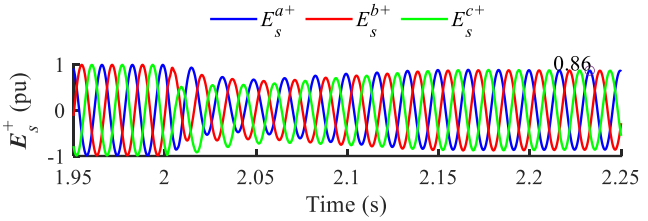

(a) Current saturation-based method

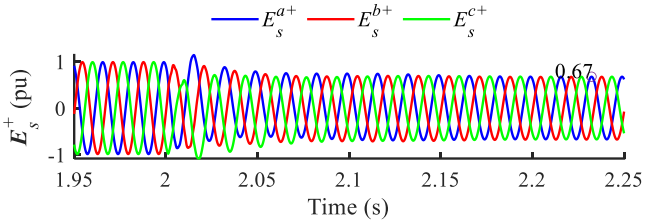

(b) Virtual impedance-based method

Fig. 3.46. Positive-sequence internal voltage vectors (AB fault).

For the positive-sequence internal voltage vectors:

Fig. 3.45 and Fig. 3.46 demonstrate that the current saturation-based and virtual impedance-based methods significantly influence the positive-sequence internal voltage vectors. Under the pre-fault conditions, the magnitude of positive-sequence internal voltage vectors equals 1 pu. In Fig. 3.45, during an AG fault, due to the I1R injection in the current saturation-based method, the magnitude of the positive-sequence internal voltage vectors is maintained at 0.9 pu under steady state fault conditions. Under the virtual impedance-based method, the magnitude of the positive-sequence internal voltage vectors remains at 0.95 pu by using the adaptive virtual voltage references. This is close to the nominal

value. In Fig. 3.46, during an AB fault, the magnitude of the positive-sequence internal voltage vectors is maintained at 0.86 pu under steady state fault conditions by using the current saturation-based method. The value is a bit lower than that during an AG fault. However, under the virtual impedance-based method, the magnitude of the internal voltage drops to 0.67 pu by subtracting the voltage drop on the virtual rotor impedance during an AB fault. These results indicate that the current saturation-based method exhibits great capability in supporting the positive-sequence internal voltage vectors due to the I1R injection, while the virtual impedance-based method lowers the positive-sequence internal voltage by adjusting the adaptive voltage references.

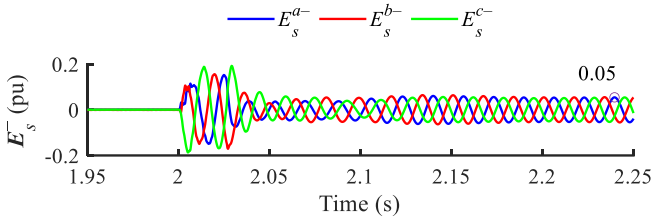

(a) Current saturation-based method

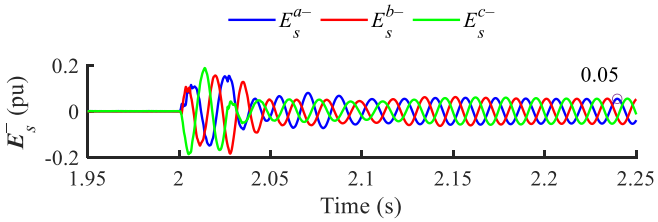

(b) Virtual impedance-based method

Fig. 3.47. Negative-sequence internal voltage vectors (AG fault).

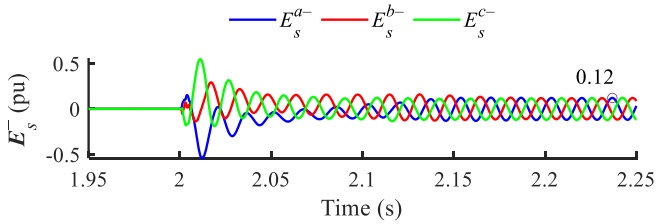

(a) Current saturation-based method

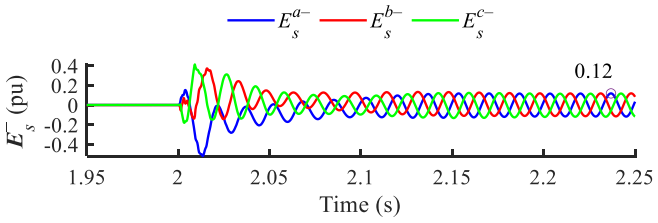

(b) Virtual impedance-based method

Fig. 3.48. Negative-sequence internal voltage vectors (AB fault).

For the negative-sequence internal voltage vectors:

Under the pre-fault conditions, the magnitude of negative-sequence internal voltage vectors equals 0 pu since the grid condition is balanced, as shown in Fig. 3.47 and Fig. 3.48. At the inception of asymmetrical faults, the negative-sequence internal voltage vectors oscillate due to the generation of transient components. Since the two control schemes implement the I2R injection in negative-sequence

control loops, the negative-sequence internal voltage vectors gradually stabilize. Under steady state fault conditions, the magnitude of negative-sequence internal voltage vectors is nearly consistent by using the two methods.

The simulation results indicate that the internal voltage vectors are determined by the current reference generation. Employing the two different positive-sequence current reference generation methods results in varying positive-sequence internal voltage vectors, while the negative-sequence internal voltage vectors are identical by using the same I2R injection method.

3.2.3.2 Active and Reactive Current Injection

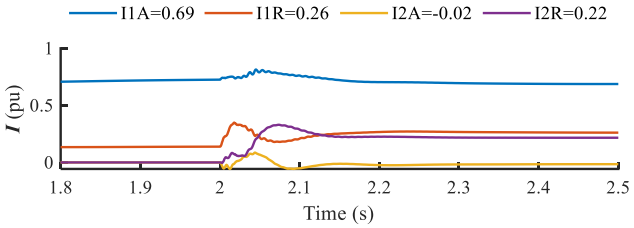

(a) Current saturation-based method

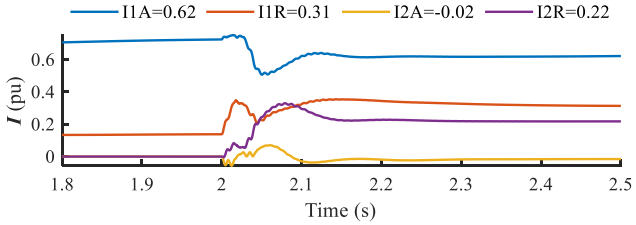

(b) Virtual impedance-based method

Fig. 3.49. Active and reactive WTG current injection (AG fault).

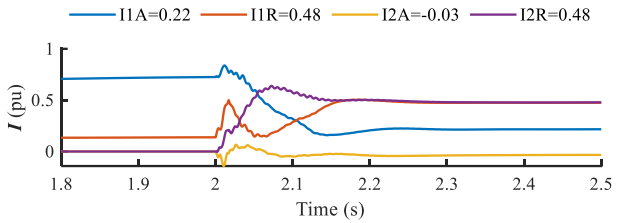

(a) Current saturation-based method

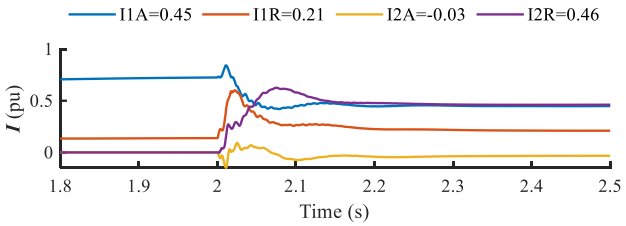

(b) Virtual impedance-based method

Fig. 3.50. Active and reactive WTG current injection (AB fault).

To validate the current coordination of the proposed FRT scheme for the GFM-DFIG during asymmetrical faults at Bus 2, the simulation results of the active and reactive current injection are shown in Fig. 3.49 and Fig. 3.50. The magnitudes of the I2A and I2R under the two control schemes are almost consistent due to the same I2R injection method. The difference lies in the injection of the I1A and I1R.

By using the K factor-based method, the I1R increases significantly under the current saturation-based method in various fault scenarios. Under the virtual impedance-based method, there is no additional I1R injection. Compared to the AG fault, the magnitude of the I1R gets lower during an AB fault. The I1R injection cannot be guaranteed since it is regulated by adjusting the virtual voltage references.

In the proposed control, the current saturation-based method prioritizes the I1R while the virtual impedance-based method prioritizes the I2R to optimize the utilization of current capacity. For the scenario of the most severe grid fault for GFM-DFIG, the simulations under a bolted AB and ABG fault at Bus 1 are carried out in Fig. 3.51 and Fig. 3.52, respectively. The results indicate that both the positive- and negative-sequence currents can be injected, even when faults occur at the point of interconnection.

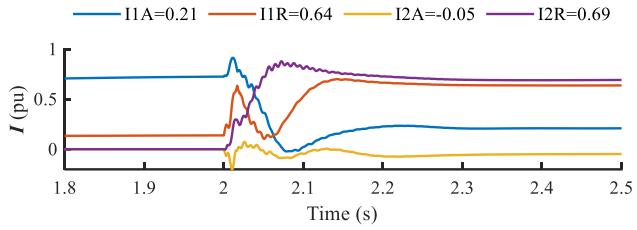

(a) Current saturation-based method

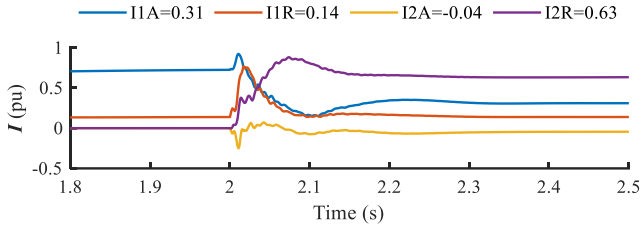

(b) Virtual impedance-based method

Fig. 3.51. Active and reactive WTG current injection (AB fault at Bus 1).

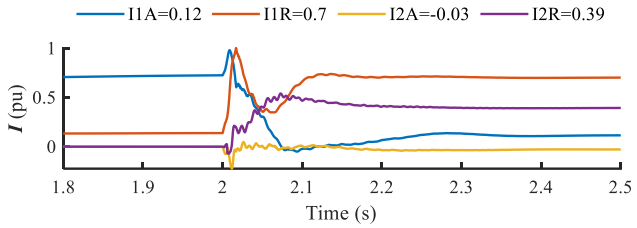

(a) Current saturation-based method

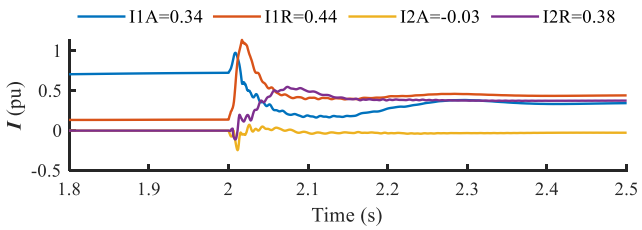

(b) Virtual impedance-based method

Fig. 3.52. Active and reactive WTG current injection (ABG fault at Bus 1).

To study the relations between sequence-domain stator voltage vectors and WTG current vectors, their phasor representation during faults at Bus 2 is shown in Fig. 3.53 and Fig. 3.54. Under the two control schemes, the negative-sequence WTG current leads the negative-sequence stator voltage by 90-

95 degrees. This angular relation matches the requirements in recent grid codes. The magnitude of negative-sequence WTG current is approximately 2 times that of negative-sequence stator voltage. This matches the specified K factor of the I2R injection. Compared to the virtual impedance-based method, the magnitude of stator voltages is higher due to the injection of the I1R under the current saturation-based method. Moreover, the two control schemes lead to different phase angles of positive-sequence stator voltage vectors and WTG current vectors. This may affect the sensitivity and faulted phase selection of protective relaying.

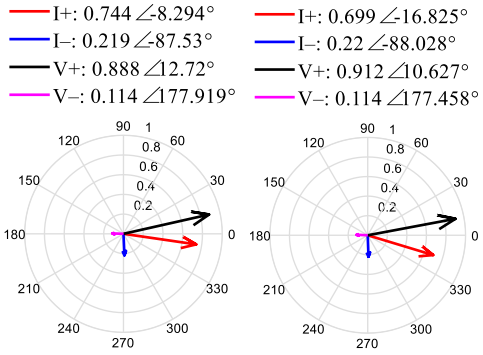

(a) Current saturation (b) Virtual impedance

Fig. 3.53. Phasor of sequence components of WTG currents and stator voltages (AG fault).

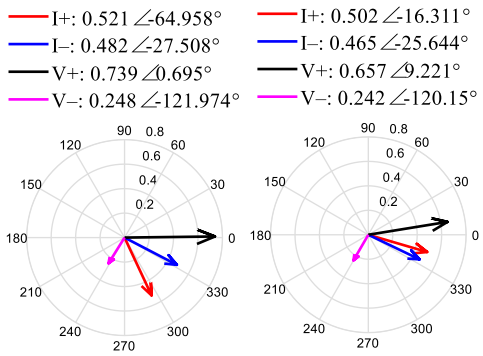

(a) Current saturation (b) Virtual impedance

Fig. 3.54. Phasor of sequence components of WTG currents and stator voltages (AB fault).

3.2.3.3 LVRT Capability

To validate the LVRT capability of the proposed FRT scheme for the GFM-DFIG, Fig. 3.55−Fig. 3.57 show the RMS voltage responses during various types of faults at Bus 2 in comparison with the voltage ride-through requirements of Hydro-Quebec. From Fig. 3.55−Fig. 3.57, the three-phase voltages can stabilize and remain within the range required for continuous operation. This indicates that the proposed control scheme enables the GFM-DFIG to maintain stable operation during the asymmetrical faults within 1 s. In Fig. 3.56 and Fig. 3.57, the current saturation-based method enhances the magnitude of three-phase voltages more effectively than the virtual impedance-based method, demonstrating superior performance in voltage support compared to the latter. Fig. 3.57 shows that although the FRT control is developed for the asymmetrical fault ride-though, it is also effective for GFM-DFIG to ride through symmetrical faults.

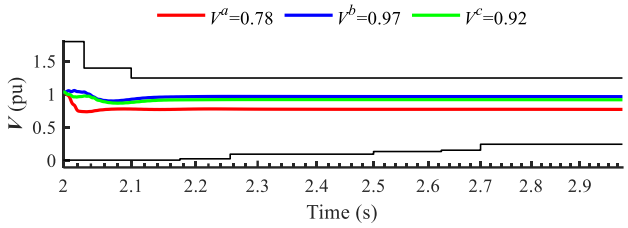

(a) Current saturation-based method

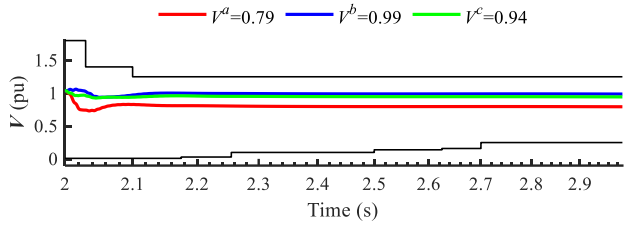

(b) Virtual impedance-based method

Fig. 3.55. Three-phase RMS voltages during an AG fault

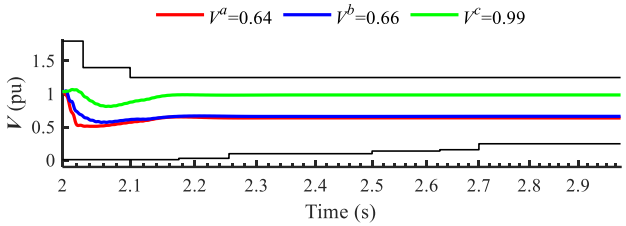

(a) Current saturation-based method

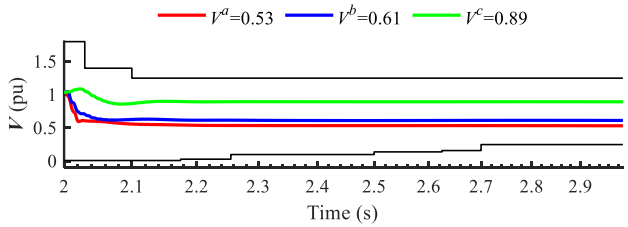

(b) Virtual impedance-based method

Fig. 3.56. Three-phase RMS voltages during an AB fault

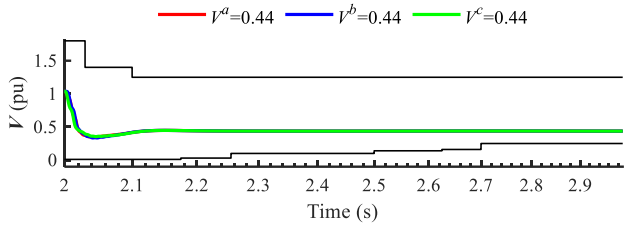

(a) Current saturation-based method

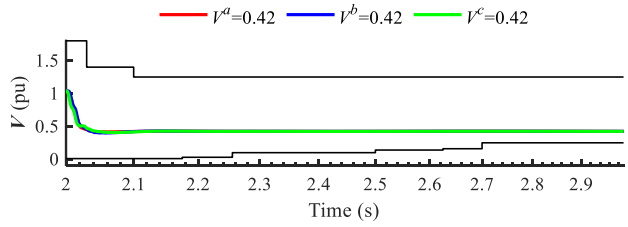

(b) Virtual impedance-based method

Fig. 3.57. Three-phase RMS voltages during a three-phase short circuit fault

3.2.3.4 Rotor Current and Volage Limit

To investigate the overcurrent issue, Fig. 3.58 and Fig. 3.59 show the three-phase rotor currents and their bounds. The magnitude of rotor currents does not exceed the current limit under steady state fault conditions. This validates the proposed priority settings under the current saturation-based method. In the virtual impedance-based method, the reduction in adaptive virtual voltage references leads to a decrease in the magnitude of rotor currents, thereby mitigating the risk of overcurrent. Compared to the current saturation-based method, the rotor current capacity is more sufficient under the virtual impedance-based method. Overall, the proposed FRT controls effectively meet the limits of rotor current capacity.

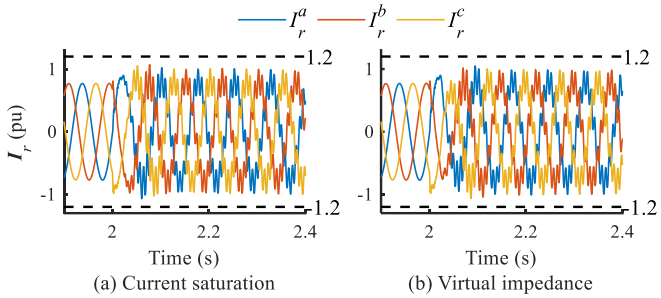

Fig. 3.58. Rotor currents during an AG fault

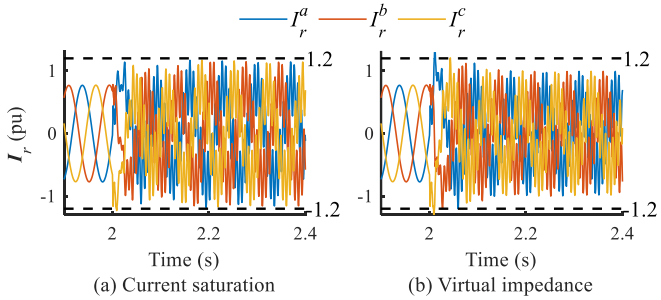

Fig. 3.59. Rotor currents during an AB fault

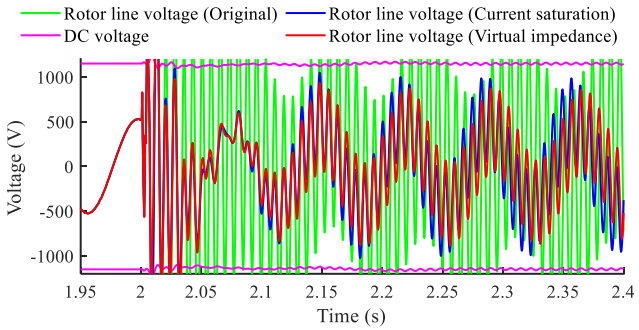

Fig. 3.60. Rotor line voltage and DC voltage during an AB fault

To investigate the overmodulation issue, during AB faults, the rotor line voltages and the DC voltage are demonstrated in Fig. 3.60. Under the original control, the magnitude of the rotor line voltage frequently surpasses the DC voltage. The rotor voltage references cannot be achieved so the rotor currents would be out of control. This may lead to the activation of crowbar protection in practical engineering. Under the proposed FRT controls, the magnitude of rotor line voltages is lower than the DC voltage under steady state fault conditions. Additionally, the transient process is shortened with fewer overshoots. The rotor voltage demand under the virtual impedance-based method is smaller than that under the current saturation-based method. Overall, the proposed FRT controls effectively decrease transient components

and avoid overmodulation under steady state fault conditions.

3.2.3.5 Electromagnetic Torque

In addition to the grid-side and converter responses, the machine-side responses should also be investigated since they are critical to the stable operation of the GFM-DFIG. During an AB fault at Bus 2, the electromagnetic torque T_{em} is shown in Fig. 3.61 and Fig. 3.62. During an AG fault, the oscillation magnitude of T_{em} under the two control schemes is nearly consistent. During an AB fault, the oscillation magnitude of T_{em} under the virtual impedance-based method is much smaller than that under the current saturation-based method. The double-grid-frequency oscillation in T_{em} is caused by the interaction between the positive and negative sequence components [127], [131]. The elimination of these oscillations is advantageous but is not necessary, and it is achieved at the expense of violating the current injection requirements in grid codes [127]. Since the proposed GFM control is specified for meeting FRT requirements in grid codes, the solution for eliminating these oscillations is not considered in the proposed control. Overall, compared to the current saturation-based method, the virtual impedance-based method exhibits better performance in reducing electromagnetic stress.

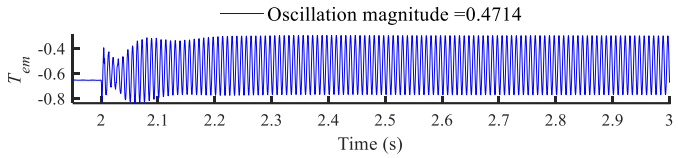

(a) Current saturation-based method

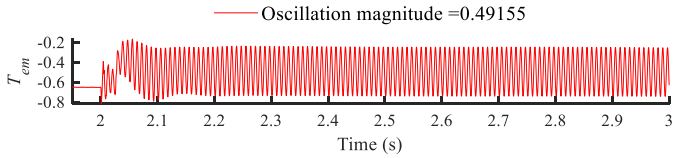

(b) Virtual impedance-based method

Fig. 3.61. Electromagnetic torque during an AG fault

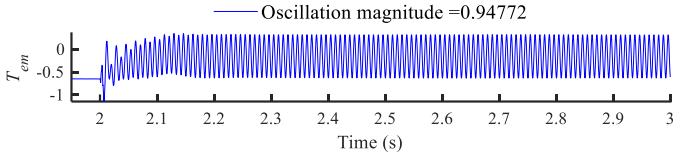

(a) Current saturation-based method

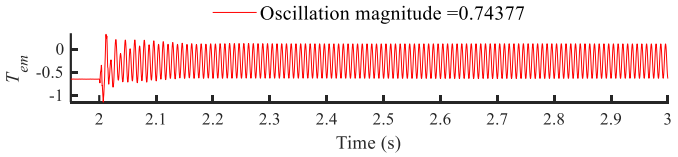

(b) Virtual impedance-based method

Fig. 3.62. Electromagnetic torque during an AB fault

3.2.4 Conclusion

This section proposes novel asymmetrical FRT controls in a PNSC structure for the GFM-DFIG.

The proposed FRT controls incorporate the I2R injection, transient component extraction, and positive-sequence control with the current saturation-based method and virtual impedance-based method. The current-limiting methods and priority settings are designed for the coordination of rotor currents and stator currents. The internal voltage vectors are used as the control object to evaluate the FRT capabilities of the GFM-DFIG. Based on detailed EMT studies, the main conclusions are summarized as follows:

(1) The internal voltage vectors are determined by the current reference generation. The current saturation-based and virtual impedance-based methods significantly influence the positive-sequence internal voltage vectors, while the negative-sequence internal voltage vectors are identical by using the same I2R injection method.

(2) Under the proposed FRT controls, both the positive- and negative-sequence WTG currents can be injected. The negative-sequence WTG current leads the negative-sequence stator voltage by 90-95 degrees. The magnitude of negative-sequence WTG current is approximately 2 times that of negative-sequence stator voltage. This matches the specified K factor in line with the requirements in recent grid codes. Hence, the GFM-DFIG can achieve the required negative-sequence behavior during asymmetrical faults.

(3) The proposed control scheme enables the GFM-DFIG to meet the LVRT requirements during the asymmetrical and symmetrical faults. In addition, the GFM-DFIG effectively meets the rotor current capacity, decreases transient components, and maintains the rotor line voltage lower than the DC voltage under steady state fault conditions, thus addressing the overcurrent and overmodulation issues. Although the FRT control of GFM-DFIG is developed for the asymmetrical fault ride-though, it is also effective for GFM-DFIG to ride through symmetrical faults.

(4) The current saturation-based method exhibits great capability in supporting the positive-sequence internal voltage vectors due to the I1R injection, while the virtual impedance-based method lowers the positive-sequence internal voltage by adjusting the adaptive voltage references. The I1R injection under the virtual impedance-based method cannot be guaranteed since it is regulated by adjusting the virtual voltage references. Compared to the current saturation-based method, the virtual impedance-based method exhibits better performance in reducing electromagnetic stress and rotor voltage demand and optimizing rotor current capacity.

4 Short-Circuit Fault Analysis of IBR-Rich System

Accurate short-circuit modeling for IBRs with various FRT strategies is crucial for future IBR-rich systems. While detailed electromagnetic transient (EMT) models exist [135], [138], their computational intensity limits efficiency across multiple fault scenarios. Research has produced simplified models to improve analysis efficiency: For GFL-IBRs, phasor domain models incorporating FRT strategies have been developed for Type-III [139], [140] and Type-IV [141] wind turbines. The analysis employs modified augmented nodal analysis (MANA) with fixed-point solver [142], [143], though these solvers show slower convergence compared to derivative-based solvers. This chapter integrates the Newton-based approach of [144], [145] into MANA formulation for improved numerical convergence under IBRs.

Recent research has produced various GFM models: RMS models under synchronous reference frame [146], equivalent models covering transient and steady-state responses [147] positive and negative sequence equivalent circuits [148] implemented in OpenDSS [149], and positive sequence and per-phase phasor models [150], [151]. However, these models generally lack consideration of decoupled-sequence FRT strategies.

The key contribution of this chapter includes a comprehensive solver with MANA formulation incorporating static IBR models with various FRT strategies, GFM/GFL controls, and current limiters, demonstrating scalability and new insights for future high-IBR grids.

4.1 Phasor Domain Short-Circuit Model for IBRs Considering FRT Control Strategies

4.1.1 Basic Topology and PNSC structure of GFL- and GFM-IBR

Fig. 4.1 shows a typical full-size-type IBR plant, where the power generated by the IBRs is transmitted to the point of interconnection (POI) via a medium-voltage (MV) collector grid, a main IBR transformer, and a high-voltage (HV) bus. In this chapter, superscript * denotes the reference. Subscripts + and – denote positive and negative sequences, respectively. Fig. 4.2 shows the typical topology of a grid-side converter (GSC) of an IBR unit. The choke circuit, shunt filters, and unit transformer are connected at the point of connection (POC) on the low-voltage (LV) side. $\boldsymbol{V}_{LV}$ denotes the LV-side voltage phasor. $\boldsymbol{I}_{IBR}$ denotes the current phasor provided by IBRs. The subscript *gsc* denotes the component on the GSC side.

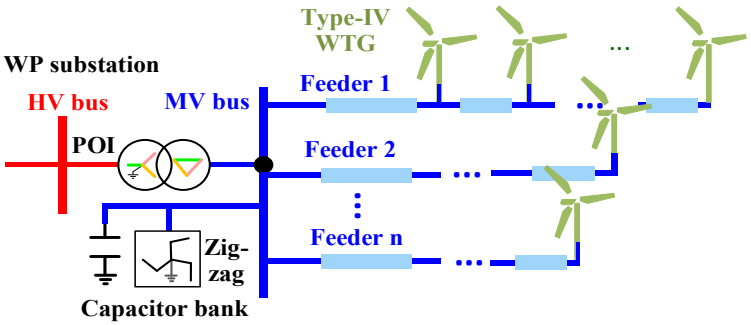

Fig. 4.1. Diagram of a full-size-type IBR plant.

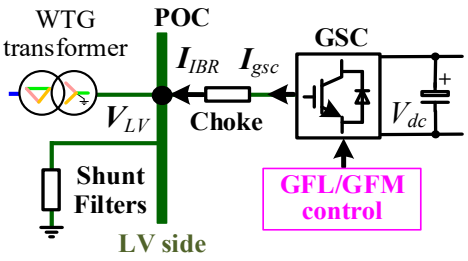

Fig. 4.2. Topology of IBR unit.

To ensure stable operation in normal operation, the GFL control typically includes PLL, DC voltage control, AC voltage droop control, and inner current regulation (blue box), while the GFM control typically incorporates PSL, Q-droop control, inner voltage regulation (red box), and inner current regulation (blue box), as illustrated in Fig. 4.3. The PNSC structure aims to appropriately regulate both positive and negative sequence components to comply with current capability and current injection requirements per grid codes. $\{\theta, \omega\}$ denotes the orientation angle and angular frequency. $\{P, Q\}$ denotes the active and reactive powers. Under unbalanced grid conditions, since the zero-sequence components on the grid side are usually separated by a delta-connected IBR transformer, the instantaneous abc vectors of IBR can be transformed into $dq+$ and $dq-$ vectors. Superscript $dq+$ denotes components in the $dq+$ coordinate that rotates at the nominal frequency ω_n. Superscript $dq-$ denotes components in the $dq-$ frame that rotates at the nominal frequency $-\omega_n$.

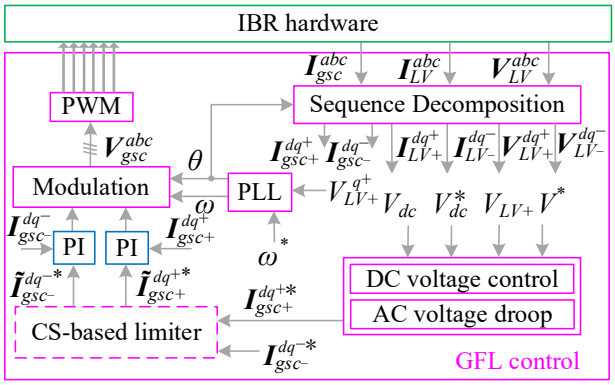

(a) GFL-IBR.

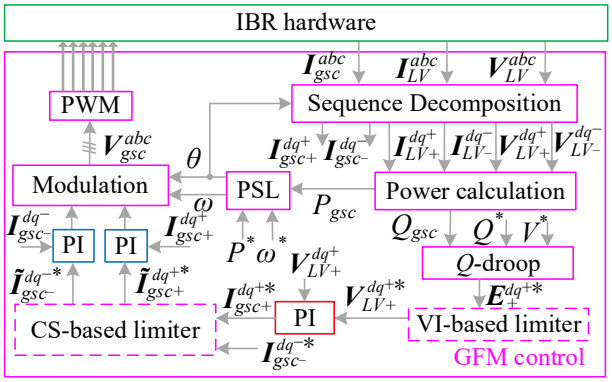

(b) GFM-IBR.

Fig. 4.3. PNSC structure for the grid-side converter of IBR.

Fig. 4.4(a) illustrates the angular relations between V_+ and coordinates. Fig. 4.4(b) illustrates the phasor representation of positive sequence active and reactive current (I1A and I1R). Fig. 4.4(c)

illustrates the phasor representation of negative sequence active and reactive current (I2A and I2R). These current phasors are given by:

$$\begin{cases} I_+^P + jI_+^Q = I_+ e^{j(\theta_{I+}-\theta_{V+})} \\ I_-^P + jI_-^Q = I_- e^{j(\theta_{I-}-\theta_{V-})} \end{cases} \tag{4.1}$$

where $\{I_+^P, I_-^P\}$ denotes I1A and I2A. $\{I_+^Q, I_-^Q\}$ denotes I1R and I2R. In Fig. 4.4, θ_0 denotes the power angle of IBR, which is frozen in FRT mode for the purpose of short-circuit calculation. For clarity, positive and negative sequence voltages are abbreviated as V1 and V2. Positive and negative sequence currents are abbreviated as I1 and I2.

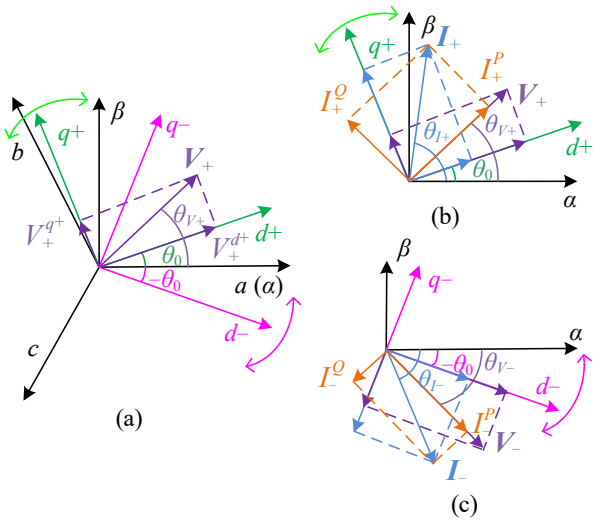

Fig. 4.4. Relations between the coordinates for IBR.

4.1.2 Current Injection of IBR under FRT mode

Under unbalanced grid conditions, I1R is regulated to support V1 and I2R to reduce V2. By using a *K*-factor-based method, the incremental reactive currents are determined by the variation of V1 and V2 as follows:

$$\begin{cases} \Delta I_{gsc+}^{Q*} = K_+^Q \Delta V_{LV+} = K_+^Q (V^* - V_{LV+}) \\ \Delta I_{gsc-}^{Q*} = K_-^Q \Delta V_{LV-} = K_-^Q V_{LV-} \end{cases} \tag{4.2}$$

where $\{K_+^Q, K_-^Q\}$ denotes the *K* factor for reactive current injection. In normal operation, the inner voltage regulation suppresses V_{LV+}^{q+} to zero. Based on Fig. 4.5, $I_{gsc+}^{Q} = I_{gsc+}^{q+}$. Therefore, the references of I1R and I2R are determined as

$$\begin{cases} I_{gsc+}^{Q*} = I_{gsc+}^{Qpre} + \Delta I_{gsc+}^{Q*} = I_{gsc+}^{q+pre} + \Delta I_{gsc+}^{Q*} \\ I_{gsc-}^{Q*} = \Delta I_{gsc-}^{Q*} \end{cases} \tag{4.3}$$

where superscript *pre* denotes the pre-fault value.

To emulate the negative sequence behavior of SGs, I2 is injected leading V2 by 90°. Hence, I2A can be set to zero to spare the current capacity for I2R injection. Fig. 4.5 depicts the generation of I2R, where $\tilde{I}^*$ denotes the updated current reference. I^{lim} denotes the current limit. Based on the relations in Fig. 4.4, the $dq-$ current references are derived as

$$\begin{cases} \tilde{I}_{gsc-}^{d-*} = V_{LV-}^{q-}\tilde{I}_{gsc-}^{Q*} \big/ V_{LV}^{-} \\ \tilde{I}_{gsc-}^{q-*} = -V_{LV-}^{d-}\tilde{I}_{gsc-}^{Q*} \big/ V_{LV}^{-} \end{cases} \tag{4.4}$$

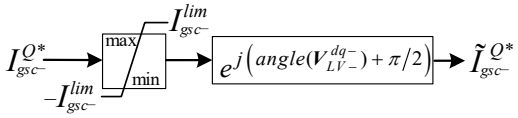

Fig. 4.5. Negative sequence current limiter design

The equivalent positive sequence system integrated with IBR under CS-based and VI-based limiters is shown in Fig. 4.6, where $\boldsymbol{Z}_{eq+}$ and $\boldsymbol{V}_{eq+}$ denote the equivalent positive sequence impedance and voltage source of AC networks.

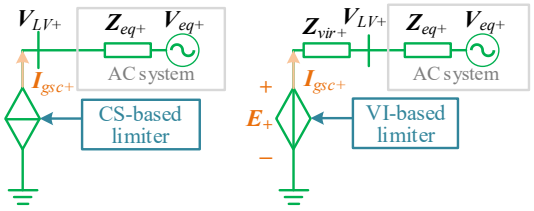

(a) (b)

Fig. 4.6. Equivalent positive sequence system integrated with IBR under CS-based and VI-based limiters

Under CS-based limiter, an IBR is equivalent to a current source. Hence, IBR I1 injection is determined by the FRT strategy as a function of the terminal voltage (LV-side voltage phasor) which is retrieved from the iterative solver at each step. The CS-based limiters can be applied to both GFL-IBR and GFM-IBR. For GFL-IBR, due to the regulation of SRF-PLL, $V_{LV+}^{q+} = 0$ and $\theta_{V+} = \theta_0$. For GFM-IBR, in the absence of a PLL, $\theta_{V+} \neq \theta_0$. Since the angular relation $(\theta_{V+} - \theta_0)$ of GFM-IBR and GFL-IBR is different, their reaction to I1A and I1R injection will be different. The IEEE 2800 compliant limiter considers this angular relation to address this.

For an IBR under VI-based limiter, the I1 injection is determined by the equivalent voltage source, the virtual impedance of the IBR, and the equivalent network impedance, as given by

$$\boldsymbol{I}_{gsc+} = \frac{\boldsymbol{E}_+ - \boldsymbol{V}_{eq+}}{\boldsymbol{Z}_{vir+} + \boldsymbol{Z}_{eq+}} \tag{4.5}$$

The VI-based limiter is only implemented in GFM-IBR.

4.1.2.1 Current Saturation-based Limiters for GFL- and GFM-IBR

Assuming the output active power remains constant during short circuit faults, I_{gsc+}^{d+*} is approximated by

$$I_{gsc+}^{d+*} = \frac{P_{gsc}^{pre}}{V_{LV+}\cos(\theta_{LV+} - \theta_0)} \tag{4.6}$$

To avoid overcurrent, four types of current limiters are studied and compared in this chapter, as below:

a) Instantaneous Limiter

The current limiting thresholds are respectively set for $d+$ and $q+$ current references in this type of limiters, as shown in Fig. 4.7. Hence, the performance is usually conservative, resulting in underuse of

the converter's current capacity.

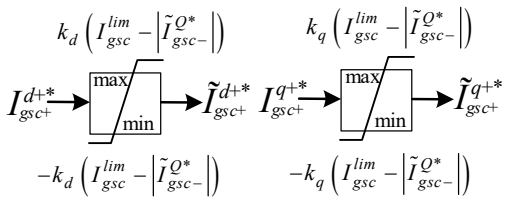

Fig. 4.7. Instantaneous current limiter design.

b) Magnitude Limiter

In this limiter, the magnitude of I1 references is constrained to avoid overcurrent, but its angle would not be affected, as shown in Fig. 4.8.

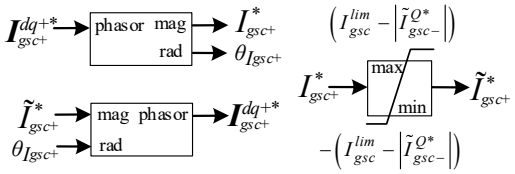

Fig. 4.8. Magnitude current limiter design.

c) Priority-based Limiter

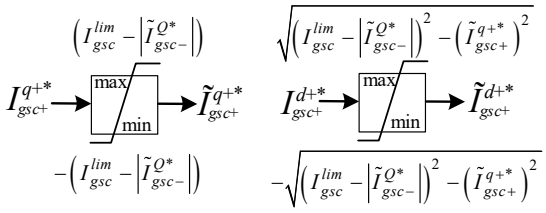

Fig. 4.9. Priority-based current limiter design.

This limiter allows the designated priority current to reach the maximum limit. Generally, priority is given to the $q+$ current reference in the FRT mode, as shown in Fig. 4.9.

d) IEEE 2800 Compliant Limiter

The IEEE 2800 compliant limiter (2800 limiter) is developed to enable IBRs to comply with current injection requirements in the IEEE 2800 standard. With this angular difference $(\theta_{V+}-\theta_0)$, the relations in (4.1) need to be reconsidered:

$$\begin{cases} I_{gsc+}^{d+*}=V_{LV+}^{d+}I_{gsc+}^{P*}\big/V_{LV+}+V_{LV+}^{q+}I_{gsc+}^{Q*}\big/V_{LV+} \\ I_{gsc+}^{q+*}=V_{LV+}^{q+}I_{gsc+}^{P*}\big/V_{LV+}-V_{LV+}^{d+}I_{gsc+}^{Q*}\big/V_{LV+} \end{cases} \tag{4.7}$$

Per IEEE 2800 standard, the coordination for I1R and I2R is given by

$$\begin{cases} \Delta I_{gsc+}^{Q*}\geq 0 & \text{During balanced faults} \\ \left|\Delta I_{gsc+}^{Q*}\right|\geq\left|\Delta I_{gsc-}^{Q*}\right| & \text{During unbalanced faults} \end{cases} \tag{4.8}$$

To ensure that the incremental reactive currents do not exceed the current limit, when $\left|K_+^Q\Delta V_{LV+}\right|+\left|K_-^Q\Delta V_{LV-}\right|>I_{gsc}^{lim}$, the incremental reactive current references are determined as

$$\begin{cases} \left\{\Delta I_{gsc+}^{Q*},\Delta I_{gsc-}^{Q*}\right\}=\left\{\eta K_+^Q\Delta V_{LV+},\eta K_-^Q\Delta V_{LV-}\right\} \\ \eta=I_{gsc}^{lim}\Big/\left(\left|K_+^Q\Delta V_{LV+}\right|+\left|K_-^Q\Delta V_{LV-}\right|\right) \end{cases} \tag{4.9}$$

Combining (4.2), (4.3), and (4.7) yields:

$$\begin{cases} I_{gsc+}^{d+*} = \dfrac{V_{LV+}^{q+}\Delta I_{gsc+}^{Q*}}{V_{LV+}} + \dfrac{P_{gsc}^{pre}}{V_{LV+}\cos(\theta_{LV+}-\theta_0)} \\ I_{gsc+}^{q+*} = -V_{LV+}^{d+}\Delta I_{gsc+}^{Q*} \Big/ V_{LV+} + I_{gsc+}^{q+pre} \end{cases} \tag{4.10}$$

Then the positive sequence limiter in Fig. 4.9 and negative-sequence limiter in Fig. 4.5 are employed to avoid overcurrent. Per IEEE 2800 standard, IBRs are expected to fully utilize the maximum current capacity. Hence, a scaling method [111] is employed to ensure that the faulty phase current can reach the current limit, as given by

$$K_{scale} = I_{gsc}^{lim} \Big/ \max\left(\left|I_{gsc}^{a*}\right|, \left|I_{gsc}^{b*}\right|, \left|I_{gsc}^{c*}\right|\right) \tag{4.11}$$

$$\begin{cases} \tilde{\boldsymbol{I}}_{gsc}^{dq+*} = K_{scale}\boldsymbol{I}_{gsc}^{dq+*} \\ \tilde{\boldsymbol{I}}_{gsc}^{dq-*} = K_{scale}\boldsymbol{I}_{gsc}^{dq-*} \end{cases} \tag{4.12}$$

4.1.2.2 Virtual Impedance-based Limiter for GFM-IBR

For GFM-IBRs, the Q-droop control can be expressed as

$$\begin{cases} E_{+}^{d+*} = V^{*} + D_Q(Q^{*} - Q_{gsc}) \\ E_{+}^{q+*} = 0 \end{cases} \tag{4.13}$$

where D_Q denotes control gain. The VI-based limiter restrains fault currents by modifying voltage references:

$$\begin{cases} V_{LV+}^{d+*} = E_{+}^{d+*} - R_{vir+}I_{gsc+}^{d+*} + X_{vir+}I_{gsc+}^{q+*} \\ V_{LV+}^{q+*} = E_{+}^{q+*} - R_{vir+}I_{gsc+}^{q+*} - X_{vir+}I_{gsc+}^{d+*} \end{cases} \tag{4.14}$$

where $\{R_{vir+}, X_{vir+}\}$ denotes the virtual resistance and reactance. When I_{gsc+} exceeds I_{gsc+}^{lim}, the virtual impedance is given by

$$\boldsymbol{Z}_{vir+} = R_{vir+} + jX_{vir+} = \frac{\Delta V_{+}(1+j\sigma)}{I_{gsc+}^{lim}\sqrt{1+\sigma^2}} \tag{4.15}$$

where σ denotes the pre-defined ratio of X_{vir+} over R_{vir+}. ΔV denotes the positive sequence voltage drop across the $\boldsymbol{Z}_{vir+}$. To ensure I1 reaches I_{gsc+}^{lim} under FRT mode, a PI controller is employed to regulate the current reference tracking the current limit. The details of control loops can be found in section 3.1.3.

4.2 Short-Circuit Solver

4.2.1 Framework of Short-Circuit Solver

The proposed short-circuit solver is illustrated in the framework of Fig. 4.10. First, set the IBR location and read user inputs, including IBR configuration and selection of FRT strategies. Fault scenario is selected to generate the system matrix **A** that includes the fault represented with switches, then compute sequence domain equivalent impedance ($\boldsymbol{Z}_{eq}$) and equivalent voltage source ($\boldsymbol{V}_{eq}$) of the network as seen from GFM-IBR locations with VI-based limiters. The $\boldsymbol{Z}_{eq}$ and $\boldsymbol{V}_{eq}$ are used to compute I1 injection by (4.5). For IBRs with CS-based limiters, the current injection is determined by the FRT strategy. Once the

phasors I1 and I2 are computed for each IBR, they are converted in the *abc* domain for updating system voltages using the MANA formulation [142], [152].

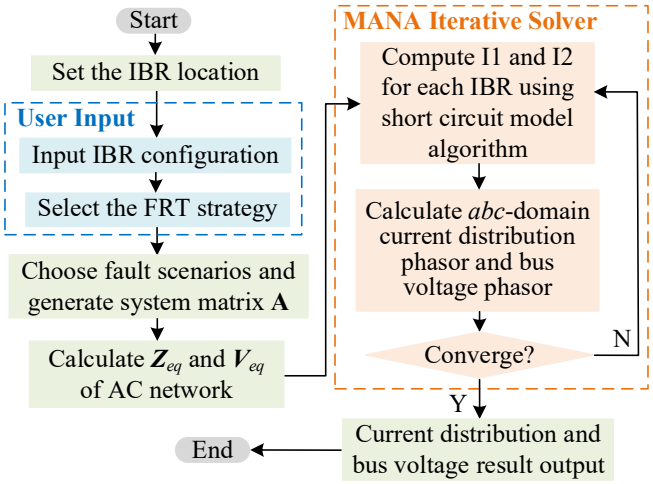

Fig. 4.10. Framework of the proposed short-circuit solver.

B. Phasor Domain Short-Circuit Model Algorithm

The main short-circuit solver algorithm encompasses the following aspects:

1. User Input:

1.1. Input IBR configuration, including:

- IBR parameter: I_{gsc}^{lim}, I_{gsc}^{lim-}, K_{+}^{Q}, K_{-}^{Q}, D_Q, V^*, Q^*, σ, k_d, k_q.

- Pre-fault value (steady state value in normal operation): θ_0, I_{gsc+}^{q+pre}, and P_{gsc}^{pre}.

1.2. Select the employed FRT strategy or limiter, including:

1-Instantaneous limiter; 2-Magnitude limiter; 3-Priority-based limiter; 4-2800 limiter; 5-VI-based limiter for GFM-IBR only.

2. Short-circuit model algorithm:

2.1. Current reference generation:

IF the employed limiter==4

Calculate ΔI_{gsc+}^{Q*} and ΔI_{gsc-}^{Q*} by (4.9);

ELSE

Calculate I_{gsc+}^{Q*} and I_{gsc-}^{Q*} by (4.2) and (4.3);

END

Calculate I_{gsc+}^{d+*} by (4.6).

2.2. Negative sequence current limiter:

IF $I_{gsc-}^{Q*} > I_{gsc-}^{lim}$

$I_{gsc-}^{Q*} = I_{gsc-}^{lim}$;

END

$I_{gsc+}^{lim} = I_{gsc}^{lim} - |\tilde{I}_{gsc-}^{Q*}|$;

Calculate $\tilde{I}_{gsc-}^{d-*}$ and $\tilde{I}_{gsc-}^{q-*}$ by (4.4);

$$\tilde{\boldsymbol{I}}_{gsc-}^{*} = abs\left(\tilde{I}_{gsc-}^{d-*} + j\tilde{I}_{gsc-}^{q-*}\right)e^{j\left(\theta_0 - angle\left(\tilde{I}_{gsc-}^{d-*} + j\tilde{I}_{gsc-}^{q-*}\right)\right)}.$$

2.3. Positive sequence current limiter:

The details of each current limiter are presented as below:

Algorithm 1 Instantaneous limiter

$\{I_{gsc+}^{d+lim}, I_{gsc+}^{q+lim}\} = \{k_d I_{gsc+}^{lim*}, k_q I_{gsc+}^{lim*}\}$;
IF $I_{gsc+}^{q+*} > I_{gsc+}^{q+lim}$
$I_{gsc+}^{q+*} = I_{gsc+}^{q+lim}$;
ELSE IF $I_{gsc+}^{q+*} < -I_{gsc+}^{q+lim}$
$I_{gsc+}^{q+*} = -I_{gsc+}^{q+lim}$;
END
END
IF $I_{gsc+}^{d+*} > I_{gsc+}^{d+lim}$
$I_{gsc+}^{d+*} = I_{gsc+}^{d+lim}$;
ELSE IF $I_{gsc+}^{d+*} < -I_{gsc+}^{d+lim}$
$I_{gsc+}^{d+*} = -I_{gsc+}^{d+lim}$;
END
END
$\{\tilde{I}_{gsc+}^{d+*}, \tilde{I}_{gsc+}^{q+*}\} = \{I_{gsc+}^{d+*}, I_{gsc+}^{q+*}\}$; $\tilde{\boldsymbol{I}}_{gsc+}^{*} = \left(\tilde{I}_{gsc+}^{d+*} + j\tilde{I}_{gsc+}^{q+*}\right)e^{j\theta_0}$;
RETURN $\tilde{\boldsymbol{I}}_{gsc+}^{*}$

Algorithm 2 Magnitude limiter

$I_{gsc+}^{*} = abs(\boldsymbol{I}_{gsc+}^{dq+*})$;
IF $I_{gsc+}^{*} > I_{gsc+}^{lim}$
$I_{gsc+}^{*} = I_{gsc+}^{lim}$;
END
$\tilde{I}_{gsc+}^{*} = I_{gsc+}^{*}$; $\tilde{\boldsymbol{I}}_{gsc+}^{*} = \tilde{I}_{gsc+}^{*} e^{j\left(\theta_0 + angle\left(I_{gsc+}^{dq+*}\right)\right)}$;
RETURN $\tilde{\boldsymbol{I}}_{gsc+}^{*}$

Algorithm 3 Priority-based limiter

IF $I_{gsc+}^{q+*} > I_{gsc+}^{lim}$
$I_{gsc+}^{q+*} = I_{gsc+}^{lim}$;
ELSE IF $I_{gsc+}^{q+*} < -I_{gsc+}^{lim}$
$I_{gsc+}^{q+*} = -I_{gsc+}^{lim}$;
END
END
IF $I_{gsc+}^{d+*} > \sqrt{\left(I_{gsc+}^{lim}\right)^2 - \left(\tilde{I}_{gsc+}^{q+*}\right)^2}$
$I_{gsc+}^{d+*} = \sqrt{\left(I_{gsc+}^{lim}\right)^2 - \left(\tilde{I}_{gsc+}^{q+*}\right)^2}$;
ELSE IF $I_{gsc+}^{d+*} < -\sqrt{\left(I_{gsc+}^{lim}\right)^2 - \left(\tilde{I}_{gsc+}^{q+*}\right)^2}$
$I_{gsc+}^{d+*} = -\sqrt{\left(I_{gsc+}^{lim}\right)^2 - \left(\tilde{I}_{gsc+}^{q+*}\right)^2}$;
END
END
$\{\tilde{I}_{gsc+}^{d+*}, \tilde{I}_{gsc+}^{q+*}\} = \{I_{gsc+}^{d+*}, I_{gsc+}^{q+*}\}$; $\tilde{\boldsymbol{I}}_{gsc+}^{*} = \left(\tilde{I}_{gsc+}^{d+*} + j\tilde{I}_{gsc+}^{q+*}\right)e^{j\theta_0}$;
RETURN $\tilde{\boldsymbol{I}}_{gsc+}^{*}$

Algorithm 4 IEEE 2800 compliant limiter

Calculate $\{I_{gsc+}^{d+*}, I_{gsc+}^{q+*}, I_{gsc-}^{d-*}, I_{gsc-}^{q-*}\}$ by (4.4) and (4.10);
IF $I_{gsc+}^{q+*} > I_{gsc+}^{lim}$

$I_{gsc+}^{q+*} = I_{gsc+}^{lim}$;
ELSE IF $I_{gsc+}^{q+*} < -I_{gsc+}^{lim}$
$I_{gsc+}^{q+*} = -I_{gsc+}^{lim}$;
END
END
IF $I_{gsc+}^{d+*} > \sqrt{\left(I_{gsc+}^{lim}\right)^2 - \left(\tilde{I}_{gsc+}^{q+*}\right)^2}$
$I_{gsc+}^{d+*} = \sqrt{\left(I_{gsc+}^{lim}\right)^2 - \left(\tilde{I}_{gsc+}^{q+*}\right)^2}$;
ELSE IF $I_{gsc+}^{d+*} < -\sqrt{\left(I_{gsc+}^{lim}\right)^2 - \left(\tilde{I}_{gsc+}^{q+*}\right)^2}$
$I_{gsc+}^{d+*} = -\sqrt{\left(I_{gsc+}^{lim}\right)^2 - \left(\tilde{I}_{gsc+}^{q+*}\right)^2}$;
END
END
$\tilde{\boldsymbol{I}}_{gsc+}^{*} = \left(I_{gsc+}^{d+*} + jI_{gsc+}^{q+*}\right)e^{j\theta_0}$;
$\tilde{\boldsymbol{I}}_{gsc-}^{*} = abs\left(\tilde{I}_{gsc-}^{d-*} + j\tilde{I}_{gsc-}^{q-*}\right)e^{j\left(\theta_0 - angle\left(\tilde{I}_{gsc-}^{d-*} + j\tilde{I}_{gsc-}^{q-*}\right)\right)}$;
$\boldsymbol{I}_{gsc}^{0+-*} = \begin{bmatrix} 0 & \tilde{\boldsymbol{I}}_{gsc+}^{*} & \tilde{\boldsymbol{I}}_{gsc-}^{*} \end{bmatrix}$;
$\alpha = e^{j\frac{2\pi}{3}}$; $\boldsymbol{A} = [1 \quad 1 \quad 1; 1 \quad \alpha^2 \quad \alpha; 1 \quad \alpha \quad \alpha^2]$;
$\boldsymbol{I}_{gsc}^{abc*} = \boldsymbol{A}\boldsymbol{I}_{gsc}^{0+-*}$; $K_{scale} = \frac{I_{gsc}^{lim}}{max\left(abs\left(I_{gsc}^{abc*}\right)\right)}$;
$\tilde{\boldsymbol{I}}_{gsc+}^{*} := K_{scale}\tilde{\boldsymbol{I}}_{gsc+}^{*}$; $\tilde{\boldsymbol{I}}_{gsc-}^{*} := K_{scale}\tilde{\boldsymbol{I}}_{gsc-}^{*}$;
RETURN $\tilde{\boldsymbol{I}}_{gsc+}^{*}, \tilde{\boldsymbol{I}}_{gsc-}^{*}$

Algorithm 5 Virtual Impedance-based limiter

Assume $\boldsymbol{Z}_{vir+} = 0$, calculate $\boldsymbol{I}_{gsc+}$ by (4.5);
IF $abs\left(\boldsymbol{I}_{gsc+}\right) \le I_{gsc+}^{lim}$
$R_{vir+} = 0$; $\tilde{\boldsymbol{I}}_{gsc+}^{*} = \boldsymbol{I}_{gsc+}$;
ELSE IF $abs\left(\boldsymbol{I}_{gsc+}\right) > I_{gsc+}^{lim}$
Calculate E_{+}^{d+*} by (4.13);
$R_{vir+} = abs\left(\left(\frac{E_{+}^{d+*}e^{j\theta_0} - \boldsymbol{V}_{eq+}}{I_{gsc+}^{lim}} - \boldsymbol{Z}_{eq+}\right)/(1 + j\sigma)\right)$;
$\tilde{\boldsymbol{I}}_{gsc+}^{*} = I_{gsc+}^{lim}e^{j\left(angle\left(\frac{E_{+}^{d+*}e^{j\theta_0} - V_{eq+}}{R_{vir+}(1+j\sigma)+Z_{eq+}}\right)\right)}$;
END
END
RETURN $\tilde{\boldsymbol{I}}_{gsc+}^{*}$

The VI-based limiter is only used in GFM-IBR. The CS-based limiters are applicable to both GFL- and GFM-IBRs. Since the pre-fault values θ_0 and I_{gsc+}^{q+pre} for GFL- and GFM-IBRs differ, their outputs will not be identical even when using the same CS-based limiter.

2.4. Updating LV-side current phasor:

$$\begin{cases} \tilde{\boldsymbol{I}}_{IBR+} = \tilde{\boldsymbol{I}}_{gsc+}^{*} - \boldsymbol{V}_{LV+} \big/ \boldsymbol{Z}_{f+} \\ \tilde{\boldsymbol{I}}_{IBR-} = \tilde{\boldsymbol{I}}_{gsc-}^{*} - \boldsymbol{V}_{LV-} \big/ \boldsymbol{Z}_{f-} \end{cases} \tag{4.16}$$

where $\left\{\boldsymbol{Z}_{f+}, \boldsymbol{Z}_{f-}\right\}$ denotes the phasor domain equivalent impedance of shunt filters.

4.2.2 Iterative Solver

The proposed short-circuit models can be implemented within a MANA-based iterative solver. For

each fault scenario, a sparse system matrix **A** is built in the phase domain that can also handle unbalanced distribution systems. The iterative process is described as follows:

Step 1. Compute currents in the sequence domain and transform: The set of $\{\tilde{\boldsymbol{I}}_{IBR+}, \tilde{\boldsymbol{I}}_{IBR-}\}$ is calculated using the proposed short-circuit models, and transformed into three-phase currents $\tilde{\boldsymbol{I}}_{IBR}$ and populated into **b**. Hence, $\mathbf{b} = [\tilde{\boldsymbol{I}}_{IBR} \ \ \boldsymbol{V}_b \ \ \mathbf{0}]^{\mathrm{T}}$. $\boldsymbol{V}_b$ denotes the known voltage sources in the system.

Step 2. Calculate current distribution phasor and bus voltage phasor**:** Using sparse LU factorization, the equation $\mathbf{Ax} = \mathbf{b}$ is solved to update nodal voltage phasors $\boldsymbol{V}$ and LV-side voltage phasors $\{\boldsymbol{V}_{LV+}, \boldsymbol{V}_{LV-}\}$. The $dq+$ and $dq-$ components of LV-side voltage phasors:

$$\begin{cases} \delta_{V+} = angle(\boldsymbol{V}_{LV+}) - \theta_0 \\ \delta_{V-} = \theta_0 - angle(\boldsymbol{V}_{LV-}) \\ \left\{V_{LV+}^{d+} \quad V_{LV+}^{q+}\right\} = abs(\boldsymbol{V}_{LV+})\left\{\cos\delta_{V+} \quad \sin\delta_{V+}\right\} \\ \left\{V_{LV-}^{d-} \quad V_{LV-}^{q-}\right\} = abs(\boldsymbol{V}_{LV-})\left\{\cos\delta_{V-} \quad \sin\delta_{V-}\right\} \end{cases} \tag{4.17}$$

Then go to step 1 for the next iteration until the convergence criterion (4.18) is satisfied. ε denotes the predefined tolerance for convergence. For the *k*-th iteration,

$$\begin{cases} \Delta V_{LV+} = abs(\boldsymbol{V}_{LV+}^{(k+1)}) - abs(\boldsymbol{V}_{LV+}^{(k)}) < \varepsilon \\ \Delta V_{LV-} = abs(\boldsymbol{V}_{LV-}^{(k+1)}) - abs(\boldsymbol{V}_{LV-}^{(k)}) < \varepsilon \end{cases} \tag{4.18}$$

When integrating high-penetration IBRs, the nonlinearity of FRT strategies can compromise the numerical stability of iterative mechanisms, potentially causing non-convergence. To address the challenge, this chapter integrates the secant-based variation of Newton's method proposed in [144] into MANA formulation, which represents IBRs by a Norton equivalent in each iteration. The Newton-Raphson-based solver [144], [145] linearizes the short-circuit model of IBRs $\tilde{\boldsymbol{I}}_{IBR} = f(\boldsymbol{V}_{LV})$ around the solution of the *k*-th iteration (*k*>1), as given by

$$\tilde{\boldsymbol{I}}_{IBR} = \tilde{\boldsymbol{I}}_{IBR}^{(k)} + \frac{\partial f(\boldsymbol{V}_{LV})}{\partial \boldsymbol{V}_{LV}^{(k)}}\left(\boldsymbol{V}_{LV} - \boldsymbol{V}_{LV}^{(k)}\right) \tag{4.19}$$

From (4.19), the IBR model can be linearized to a Norton equivalent, i.e., a virtual admittance $\boldsymbol{Y}_{IBR} = \partial f(\boldsymbol{V}_{LV})/\partial \boldsymbol{V}_{LV}$ in parallel with an ideal current source. This added linearity allows for seamless integration of the IBR model equations with the network's linear equations. For the *k*-th iteration (*k*>1), the virtual admittance can be determined as

$$\boldsymbol{Y}_{IBR}^{(k)} = -\frac{\partial f(\boldsymbol{V}_{LV})}{\partial \boldsymbol{V}_{LV}^{(k)}} = -\frac{\tilde{\boldsymbol{I}}_{IBR}^{(k)} - \tilde{\boldsymbol{I}}_{IBR}^{(k-1)}}{\boldsymbol{V}_{LV}^{(k)} - \boldsymbol{V}_{LV}^{(k-1)}} \tag{4.20}$$

Assuming the Norton admittance in the *k*-th iteration (*k*>1) to be given by $\boldsymbol{Y}_{IBR}^{(k)}$, an additional admittance matrix can be denoted as

$$\mathbf{Y} = \mathrm{diag}\left\{\left[\boldsymbol{Y}_{IBR}^{(k)} \quad \mathbf{0}\right]\right\} \tag{4.21}$$

The system equation becomes

$$\mathbf{A}\left[\boldsymbol{V}_{LV}^{(k+1)} \quad \boldsymbol{I}_m^{(k+1)}\right]^{\mathrm{T}} = \begin{bmatrix} \tilde{\boldsymbol{I}}_{IBR}^{(k)} - \boldsymbol{Y}_{IBR}^{(k)}\left(\boldsymbol{V}_{LV}^{(k+1)} - \boldsymbol{V}_{LV}^{(k)}\right) \\ \boldsymbol{V}_b \\ \mathbf{0} \end{bmatrix} \tag{4.22}$$

$$\left[\mathbf{A}+\mathbf{Y}\right]\left[\boldsymbol{V}_{LV}^{(k+1)} \quad \boldsymbol{I}_{m}^{(k+1)}\right]^{\mathrm{T}}=\begin{bmatrix}\tilde{\boldsymbol{I}}_{IBR}^{(k)}+\boldsymbol{Y}_{IBR}^{(k)}\boldsymbol{V}_{LV}^{(k)}\\ \boldsymbol{V}_{b}\\ \mathbf{0}\end{bmatrix} \tag{4.23}$$

The solver updates node voltage phasors until criterion (4.18) is satisfied.

4.3 IBR Short Circuit Model and Solver Verification

4.3.1 Test System and Fault Cases

In this section, the proposed IBR short-circuit models and solver are verified by comparing the iterative solution with EMT simulation results. A modified 500 kV/60 Hz IEEE 39 bus system integrated with GFM- and GFL-IBRs is used, as shown in Fig. 4.11. Each IBR plant contains an aggregated model of full-size-type IBR units with the PNSC scheme. Droop control is employed as the GFM primary control. The IBR configuration can be found in Table 4-1. For demonstration purposes, two combination schemes of FRT strategies are set in this system:

Scheme I: IBR1 (GFM mode, magnitude limiter); IBR2 (GFM mode, Instantaneous limiter); IBR3 (GFL mode, priority-based limiter).

Scheme II: IBR1 (GFM mode, 2800 limiter); IBR2 (GFM mode, VI-based limiter); IBR3 (GFL mode, priority-based limiter).

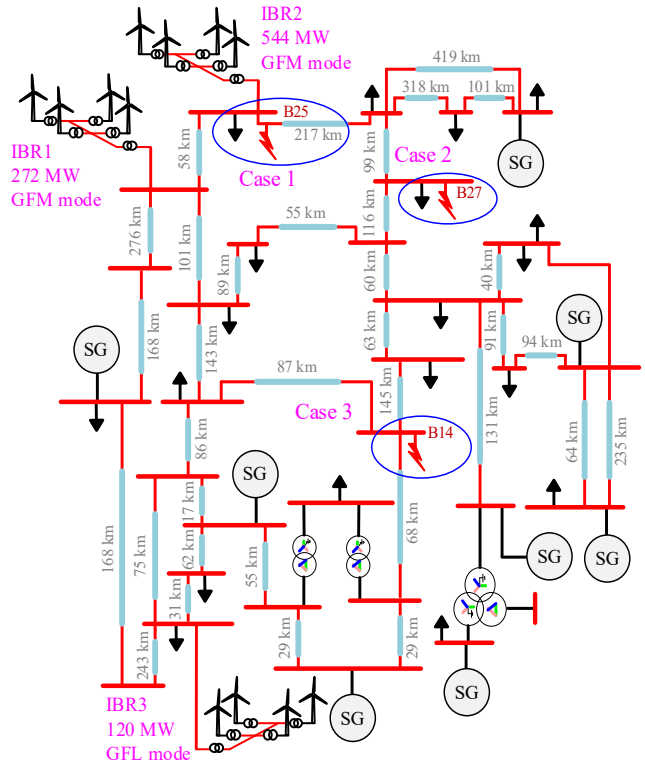

Fig. 4.11. Modified IEEE 39 bus system integrated with GFM-IBR and GFL-IBR

TABLE 4-1

Configurations of IBRs

Parameter	Value
DC voltage, DC capacitor	1.15 kV, 15 kJ/MVA

Parameter	Value
Choke impedance, Shunt filter impedance	0.01+0.15j pu, -11.107j pu
I_{gsc-}^{lim}, I_{gsc}^{lim}	0.6 pu, 1.2 pu
Pre-fault I1R	0.022 pu
K factor	3
k_d, k_q	0.5, 0.5
D_Q, σ	0.04, 1

To demonstrate the accuracy and efficiency of the proposed model, three typical fault scenarios are performed, as below:

Case 1: Bolted line-A-to-ground (AG) fault at B25.

Case 2: 10 Ω line-A-to-line-B-to-ground (ABG) fault at B27.

Case 3: 5 Ω line-B-to-line-C (BC) fault at B14.

In system matrix **A**, the switches can be set to 0 (open) or 1 (closed) for changing fault scenarios, including any type and number of simultaneous shunt or series faults. The sparsity pattern of matrix **A** is shown in Fig. 4.12.

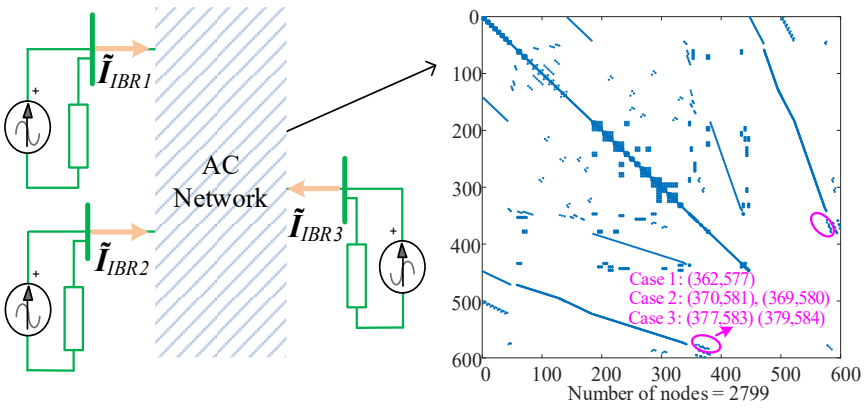

Fig. 4.12. Visualized sparsity pattern of matrix **A**

4.3.2 Accuracy under Various FRT Strategies

Table 4-2−Table 4-6 present the voltage and current phasors, formatted as "magnitude (angle)". The magnitude is expressed in per unit (pu) and the angle in degrees. The predefined tolerance for convergence is set to 0.0005 pu. In EMT simulation, FRT strategies are activated at the inception of faults and continue to operate without interruption for validation purposes.

The comparison of the iterative solver with EMT simulations shows that the proposed models accurately estimate the current contribution and voltage support capability of multi-IBRs under various FRT strategies. The absolute error is within 0.01 pu in magnitude and 2.1° in angle, caused by the tolerance for convergence, pre-fault conditions of IBRs, and the simplifications in IBR controllers.

TABLE 4-2

Phasors of IBR1 under Magnitude Limiter (Scheme I)

Case	Variable	EMT	Short-circuit Model	Mag. Absolute error	Mag. Relative error	Ang. Absolute error	Ang. Relative error
1	V_{LVa}	0.553 (17.411°)	0.553 (17.447°)	0.001	0.11%	-0.04°	-0.20%

	V_{LVb}	0.799 (-87.518°)	0.798 (-87.478°)	0.000	0.01%	-0.04°	0.05%
	V_{LVc}	0.846 (131.664°)	0.846 (131.668°)	0.000	0.03%	0°	0.00%
	I_{IBRa}	1.067 (-27.526°)	1.065 (-27.352°)	0.002	0.20%	-0.17°	0.63%
	I_{IBRb}	0.166 (-139.702°)	0.163 (-138.333°)	0.003	1.65%	-1.37°	0.98%
	I_{IBRc}	1.016 (143.759°)	1.018 (144.022°)	-0.002	-0.19%	-0.26°	-0.18%
2	V_{LVa}	0.803 (22.192°)	0.807 (22.027°)	-0.004	-0.44%	0.17°	0.75%
	V_{LVb}	0.804 (-87.319°)	0.807 (-87.532°)	-0.003	-0.39%	0.21°	-0.24%
	V_{LVc}	0.928 (147.392°)	0.931 (147.225°)	-0.003	-0.35%	0.17°	0.11%
	I_{IBRa}	1.195 (6.874°)	1.196 (5.902°)	-0.001	-0.06%	0.97°	14.14%
	I_{IBRb}	0.796 (-124.158°)	0.801 (-125.555°)	-0.005	-0.62%	1.4°	-1.13%
	I_{IBRc}	0.902 (145.112°)	0.897 (143.849°)	0.005	0.59%	1.26°	0.87%

TABLE 4-3

Phasors of IBR2 under Instantaneous Limiter (Scheme I)

Case	Variable	EMT	Short-circuit Model	Mag. Absolute error	Mag. Relative error	Ang. Absolute error	Ang. Relative error
1	V_{LVa}	0.351 (21.437°)	0.352 (21.254°)	-0.001	-0.17%	0.18°	0.85%
	V_{LVb}	0.75 (-80.812°)	0.752 (-80.911°)	-0.001	-0.15%	0.1°	-0.12%
	V_{LVc}	0.758 (126.094°)	0.76 (125.989°)	-0.002	-0.22%	0.11°	0.08%
	I_{IBRa}	0.915 (-44.249°)	0.918 (-44.561°)	-0.003	-0.29%	0.31°	-0.70%
	I_{IBRb}	0.183 (66.768°)	0.184 (68.335°)	-0.002	-0.99%	-1.57°	-2.35%
	I_{IBRc}	0.866 (147.096°)	0.863 (146.794°)	0.004	0.42%	0.3°	0.21%
2	V_{LVa}	0.802 (18.675°)	0.803 (18.527°)	-0.001	-0.17%	0.15°	0.79%
	V_{LVb}	0.797 (-89.908°)	0.798 (-90.087°)	-0.001	-0.10%	0.18°	-0.20%
	V_{LVc}	0.933 (144.63°)	0.934 (144.493°)	-0.001	-0.10%	0.14°	0.09%
	I_{IBRa}	0.922 (-9.26°)	0.919 (-9.628°)	0.003	0.32%	0.37°	-3.97%
	I_{IBRb}	0.601 (-156.672°)	0.602 (-157.25°)	-0.001	-0.11%	0.58°	-0.37%
	I_{IBRc}	0.527 (132.876°)	0.523 (132.318°)	0.005	0.88%	0.56°	0.42%

TABLE 4-4

Phasors of IBR3 under Priority-based Limiter (Scheme I)

Case	Variable	EMT	Short-circuit Model	Mag. Absolute error	Mag. Relative error	Ang. Absolute error	Ang. Relative error
1	V_{LVa}	0.93 (31.518°)	0.932 (31.477°)	-0.002	-0.26%	0.04°	0.13%
	V_{LVb}	0.988 (-87.723°)	0.991 (-87.745°)	-0.003	-0.34%	0.02°	-0.02%
	V_{LVc}	0.971 (148.949°)	0.974 (148.882°)	-0.003	-0.33%	0.07°	0.05%
	I_{IBRa}	1 (10.946°)	1 (10.395°)	0.000	-0.03%	0.55°	5.03%
	I_{IBRb}	0.943 (-103.3°)	0.942 (-103.816°)	0.001	0.10%	0.52°	-0.50%
	I_{IBRc}	1.056 (136.439°)	1.056 (135.96°)	0.000	-0.02%	0.48°	0.35%
2	V_{LVa}	0.937 (30.007°)	0.939 (29.99°)	-0.002	-0.25%	0.02°	0.06%
	V_{LVb}	0.952 (-86.849°)	0.955 (-86.833°)	-0.003	-0.29%	-0.02°	0.02%
	V_{LVc}	0.989 (150.819°)	0.992 (150.799°)	-0.003	-0.32%	0.02°	0.01%
	I_{IBRa}	1.051 (13.096°)	1.053 (12.655°)	-0.003	-0.25%	0.44°	3.37%
	I_{IBRb}	0.947 (-107.113°)	0.949 (-107.523°)	-0.002	-0.21%	0.41°	-0.38%
	I_{IBRc}	1 (138.135°)	1.003 (137.727°)	-0.003	-0.28%	0.41°	0.30%

TABLE 4-5

Phasors of IBR1 under 2800 Limiter (Scheme II)

Case	Variable	EMT	Short-circuit Model	Mag. Absolute error	Mag. Relative error	Ang. Absolute error	Ang. Relative error
2	V_{LVa}	0.817 (23.408°)	0.82 (23.302°)	-0.002	-0.26%	0.11°	0.45%

	$\boldsymbol{V}_{LVb}$	0.819 (-86.257°)	0.821 (-86.364°)	-0.002	-0.27%	0.11°	-0.12%
	$\boldsymbol{V}_{LVc}$	0.942 (148.511°)	0.945 (148.398°)	-0.002	-0.27%	0.11°	0.08%
	$\boldsymbol{I}_{IBRa}$	1.2 (3.181°)	1.2 (3.034°)	0.000	0.01%	0.15°	4.64%
	$\boldsymbol{I}_{IBRb}$	0.82 (-129.951°)	0.819 (-130.141°)	0.001	0.11%	0.19°	-0.15%
	$\boldsymbol{I}_{IBRc}$	0.876 (140.087°)	0.875 (139.992°)	0.001	0.09%	0.09°	0.07%
3	$\boldsymbol{V}_{LVa}$	0.984 (29.606°)	0.987 (29.527°)	-0.002	-0.23%	0.08°	0.26%
	$\boldsymbol{V}_{LVb}$	0.828 (-93.745°)	0.83 (-93.804°)	-0.001	-0.18%	0.06°	-0.06%
	$\boldsymbol{V}_{LVc}$	0.871 (157.006°)	0.873 (156.962°)	-0.002	-0.24%	0.04°	0.03%
	$\boldsymbol{I}_{IBRa}$	0.944 (28.485°)	0.943 (28.361°)	0.001	0.11%	0.12°	0.43%
	$\boldsymbol{I}_{IBRb}$	1.2 (-114.944°)	1.2 (-115.181°)	0.000	0.02%	0.24°	-0.21%
	$\boldsymbol{I}_{IBRc}$	0.715 (116.926°)	0.713 (116.612°)	0.002	0.27%	0.31°	0.27%

TABLE 4-6

Phasors of IBR2 under VI-based Limiter (Scheme II)

Case	Variable	EMT	Short-circuit Model	Mag. Absolute error	Mag. Relative error	Ang. Absolute error	Ang. Relative error
2	$\boldsymbol{V}_{LVa}$	0.822 (25.545°)	0.828 (25.124°)	-0.006	-0.74%	0.42°	1.65%
	$\boldsymbol{V}_{LVb}$	0.833 (-83.418°)	0.839 (-83.888°)	-0.005	-0.65%	0.47°	-0.56%
	$\boldsymbol{V}_{LVc}$	0.962 (150.529°)	0.968 (150.119°)	-0.006	-0.64%	0.41°	0.27%
	$\boldsymbol{I}_{IBRa}$	1.199 (2.003°)	1.199 (0.528°)	0.000	-0.04%	1.47°	73.64%
	$\boldsymbol{I}_{IBRb}$	0.792 (-132.874°)	0.799 (-134.958°)	-0.007	-0.85%	2.08°	-1.57%
	$\boldsymbol{I}_{IBRc}$	0.851 (140.764°)	0.843 (138.893°)	0.009	1.00%	1.87°	1.33%
3	$\boldsymbol{V}_{LVa}$	1.031 (31.438°)	1.035 (31.254°)	-0.004	-0.38%	0.18°	0.59%
	$\boldsymbol{V}_{LVb}$	0.906 (-91.469°)	0.909 (-91.618°)	-0.003	-0.34%	0.15°	-0.16%
	$\boldsymbol{V}_{LVc}$	0.932 (156.743°)	0.936 (156.592°)	-0.004	-0.42%	0.15°	0.10%
	$\boldsymbol{I}_{IBRa}$	0.95 (23.944°)	0.947 (23.22°)	0.002	0.26%	0.72°	3.03%
	$\boldsymbol{I}_{IBRb}$	1.19 (-113.511°)	1.191 (-114.266°)	0.000	-0.02%	0.76°	-0.67%
	$\boldsymbol{I}_{IBRc}$	0.808 (119.096°)	0.808 (118.157°)	0.001	0.07%	0.94°	0.79%

To examine the performance of FRT strategies, Case 2 (Scheme I) is taken as an example. The current injection requirements specified in the IEEE 2800 standard are summarized as below:

(a) IBRs shall be capable of injecting current up to the maximum current limit under FRT mode.

(b) For full-size-type IBR, I2 shall lead V2 by 90°−100°.

(c) During unbalanced faults, the incremental I1R shall not be lower than the incremental I2R.

Table 4-7 shows the phase currents of IBR2 under different FRT strategies. With the 2800 limiter, the current in the faulty phase reaches the current limit (1.2 pu), fully utilizing the converter's current capacity. The active and reactive current contributions of IBR2 under different FRT strategies can be calculated by (4.1), as shown in Table 4-8.

TABLE 4-7

Phase Currents under Different Current Limiters

Current limiter	$\boldsymbol{I}_{IBRa}$	$\boldsymbol{I}_{IBRb}$	$\boldsymbol{I}_{IBRc}$
Instantaneous limiter	0.917 (-9.47°)	-9.468 (0.6°)	0.597 (-157.25°)
Magnitude limiter	1.195 (7°)	6.996 (0.77°)	0.766 (-125.48°)
Priority-based limiter	1.197 (4.45°)	4.446 (0.78°)	0.779 (-129.29°)
2800 limiter	**1.2** (4.51°)	4.515 (0.78°)	0.781 (-129.18°)
VI-based limiter	1.199 (0.57°)	0.566 (0.8°)	0.799 (-134.98°)

TABLE 4-8

Active and Reactive Currents under Different Current Limiters

Current limiter	I^{P}_{IBR+}	I^{Q}_{IBR+}	I^{P}_{IBR-}	I^{Q}_{IBR-}	$\boldsymbol{V}_{LV+}$	$\boldsymbol{V}_{LV-}$
Instantaneous limiter	0.52	0.38	0.00	0.28	0.844 (24.241°)	0.092 (-93.923°)
Magnitude limiter	0.85	0.35	0.00	0.28	0.849 (32.297°)	0.092 (-92.716°)
Priority-based limiter	0.84	0.39	0.00	0.28	0.86 (31.594°)	0.092 (-92.802°)
2800 limiter	0.84	0.39	0.00	0.28	0.86 (31.648°)	0.092 (-92.782°)
VI-based limiter	0.81	**0.45**	0.00	0.28	**0.875** (30.454°)	0.092 (-92.952°)

With the magnitude limiter, the incremental I1R is lower than the incremental I2R, violating the IEEE 2800 standard. In addition, with these FRT strategies, I2A equals 0, indicating that I2 leads V2 by 90°, meeting the IEEE 2800 standard. The VI-based limiter demonstrates the highest magnitude of V1, indicating that it is the most effective method for providing voltage support. Overall, following the steps of the proposed short-circuit calculation method, the system operator can efficiently perform short-circuit analysis of IBR-rich systems for protective relaying studies and the evaluation of FRT strategies.

4.3.3 Robust Convergence

The section shows that the Newton-based iterative solver shows superior convergence characteristics and addresses the non-convergence issue under the conventional fixed point-based solver. Fig. 4.13−Fig. 4.15 shows the iteration process. Fig. 4.16 shows the comparison between the Newton-based iterative solver and the fixed-point iterative solver using MANA. Table 4-9 presents the iteration numbers for various scenarios.

TABLE 4-9

Comparison of Iterations of Short-Circuit Solvers

Case	Number of iterations	
	Fixed-point solver	Newton-based solver
1	12	7
2	103	10
3	Non-convergence	11

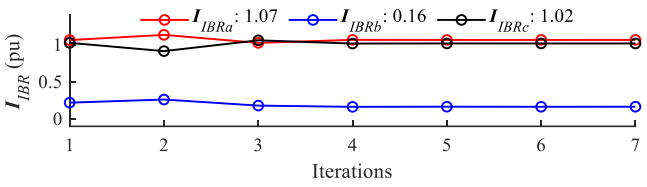

(a) Magnitude limiter

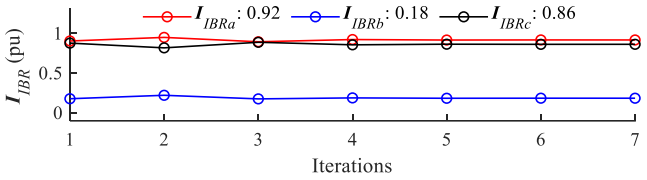

(b) Instantaneous limiter

Fig. 4.13. Current contribution of IBRs in Case 1 (Scheme I)

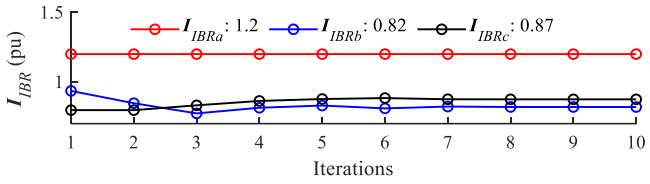

(a) 2800 limiter

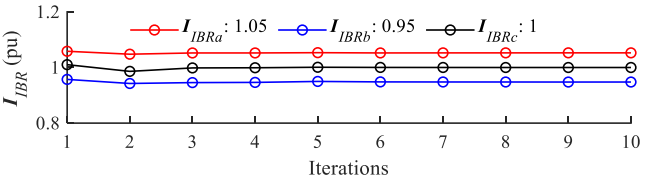

(b) Priority-based limiter

Fig. 4.14. Current contribution of IBRs in Case 2 (Scheme I)

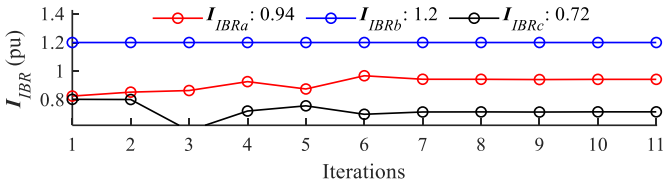

(a) 2800 limiter

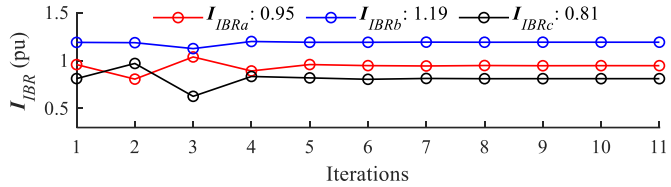

(b) VI-based limiter

Fig. 4.15. Current contribution of IBRs in Case 3 (Scheme II)

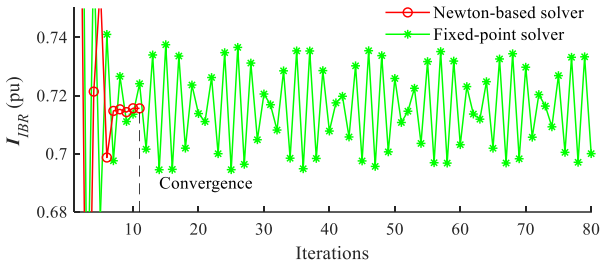

Fig. 4.16. Phase C current contribution of IBR1 under different solvers (Case 3, Scheme II)

4.4 Conclusion

Modern grid codes require IBRs to implement specific FRT strategies, which introduces complexity in current limiter design and short-circuit analysis. This chapter addresses these challenges by proposing phasor domain short-circuit models of IBRs incorporating various FRT strategies and an iterative solver for rapid short-circuit calculation in IBR-integrated power systems, combining a modified Newton algorithm with MANA formulation. The key findings demonstrate:

(a) With the CS-based limiter, the current contribution of IBRs is determined by their FRT strategies. With the VI-based limiter, the current injection of IBRs is determined by the equivalent voltage and impedance of IBRs and AC systems.

(b) The proposed short-circuit model accurately estimates the current contribution and voltage support capability under steady-state fault conditions. The MANA formulation with Newton-based iterative solver shows superior convergence and addresses non-convergence issues when compared to the MANA formulation with fixed-point solver.

(c) From the comparative studies on these FRT strategies, the IEEE 2800 compliant limiter fully utilizes converter current capacity, and the VI-based limiter enhances the voltage support capability. The proposed short-circuit models enable protection engineers to efficiently analyze short-circuit behavior in IBR-integrated systems, support FRT strategy development, and conduct comprehensive protective relaying studies.

5 Impact of Grid-Forming IBR on Protection Elements

5.1 Impacts of GFM-IBR on Apparent Impedance Measured by Distance Relays

5.1.1 Impacts of Grid-Forming BPSC on Apparent Impedance

In this section, boldface letters denote vectors. Italic letters denote complex space vectors. The symbol notation is given by

$$\begin{cases} x = e^{j\theta_x} = \mathrm{Re}(x) + j\,\mathrm{Im}(x) \\ \theta_x = \measuredangle x = \arctan(\mathrm{Im}(x)/\mathrm{Re}(x)) \end{cases} \tag{5.1}$$

$$\begin{cases} \mathbf{x}^{+-0} = \begin{bmatrix} x^+ & x^- & x^0 \end{bmatrix}^{\mathrm{T}} \\ \mathbf{x}^{dq} = \begin{bmatrix} x^d & x^q \end{bmatrix}^{\mathrm{T}} \\ \mathbf{x}^{abc} = \begin{bmatrix} x^a & x^b & x^c \end{bmatrix}^{\mathrm{T}} \end{cases} \tag{5.2}$$

where +, −, and 0 denote the positive, negative, and zero sequence components, respectively. *dq* and *abc* denote *dq* components and three-phase components, respectively. By using the symmetrical component method, the transformation between the sequence components and phase components is defined as

$$\mathbf{T}_{+-0}^{abc} = \begin{matrix} \\ a \\ b \\ c \end{matrix} \begin{matrix} \begin{matrix} + & - & 0 \end{matrix} \\ \begin{bmatrix} 1 & 1 & 1 \\ e^{j240^\circ} & e^{j120^\circ} & 1 \\ e^{j120^\circ} & e^{j240^\circ} & 1 \end{bmatrix} \end{matrix} = \begin{bmatrix} T_+^a & T_-^a & T_0^a \\ T_+^b & T_-^b & T_0^b \\ T_+^c & T_-^c & T_0^c \end{bmatrix} \tag{5.3}$$

The sequence components for each phase (ϕ=*a*, *b*, or *c*) are derived as

$$x^\phi = \mathbf{T}_{+-0}^{\phi}\mathbf{x}^{+-0} = T_+^\phi x^+ + T_-^\phi x^- + x^0 = x^{\phi+} + x^{\phi-} + x^{\phi 0} \tag{5.4}$$

To analyze the impacts of GFM-IBRs on protection systems, a typical two-bus transmission system integrated by GFM-IBRs is displayed in Fig. 5.1. The distance protective relay is installed on bus M. The apparent impedance equals the ratio of the locally measured voltage v_m over the locally measured current i_m. Considering the influence of R_f, the apparent impedance equals

$$z_m = \frac{v_m}{i_m} = z_l d + \frac{i_f}{i_m} R_f \tag{5.5}$$

where R_f and i_f denote the fault resistance and current, respectively. z_{tr} denotes the impedance of the main IBR transformer. z_l denotes the unit impedance of the transmission line. *l* and *d* denote the line length and fault distance, respectively.

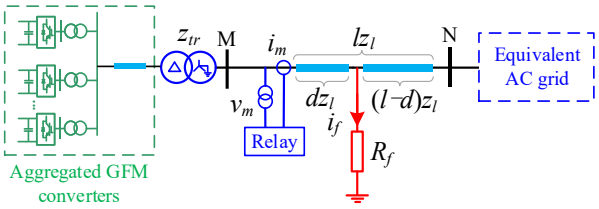

Fig. 5.1. Two-bus transmission system integrated by GFM-IBRs during faults.

To calculate the apparent impedance for ground faults and phase faults, assume the line-A-to-ground (AG) and line-A-to-line-B (AB) faults:

$$z_m^a = z_l^+ d + \frac{i_f}{\mathbf{T}_{+-0}^a \mathbf{i}_m^{+-0} + k_0 i_m^0} R_f \tag{5.6}$$

$$z_m^{ab} = z_l^+ d + \frac{i_f}{\mathbf{T}_{+-0}^a \mathbf{i}_m^{+-0} - \mathbf{T}_{+-0}^b \mathbf{i}_m^{+-0}} R_f \tag{5.7}$$

where k_0 denotes the coefficient for the zero-sequence compensation. From (5.6) and (5.7), considering the influence of fault resistance, the sequence behavior of GFM-IBRs will affect the impedance trajectory. Due to the hardware limits, IBRs may not be able to operate as GFM-IBRs that maintain voltage and frequency support during faults. According to IEEE Std. 2800-2022, GFM controls have two operation modes: Actual GFM mode, which requires adequate headroom in current and energy, and Restricted mode, which is activated when hardware limits are reached. In this section, the impacts of GFM BPSC in the two modes are discussed separately.

5.1.1.1 In the Actual Grid-Forming Mode

During unbalanced faults, three-phase measured voltages are expressed as

$$\begin{cases} v_m^\phi = v_m^{\phi+} + v_m^{\phi-} \\ v_m^{\phi+} = V_m^+ \cos\left(\omega_n t + \measuredangle v_m^+ + \delta^\phi\right) \\ v_m^{\phi-} = V_m^- \cos\left(\omega_n t + \measuredangle v_m^- - \delta^\phi\right) \end{cases} \tag{5.8}$$

where $\delta^a = 0°$, $\delta^b = -120°$, and $\delta^c = 120°$. ω_n denotes the nominal angular frequency.

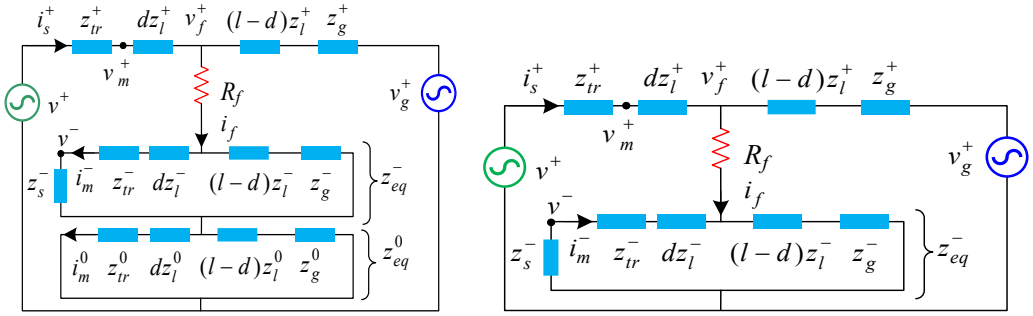

(a) AG fault (b) AB fault

Fig. 5.2. Equivalent sequence network integrated by GFM-IBRs.

In the fault steady state, when the converter currents are below the current limits, the current limiter is inactive. The positive sequence terminal voltages of GFM-IBRs are supported by the inner voltage control, thus

$$V^{d+} + jV^{q+} = V^{d+*} + jV^{q+*} = V^* + D_Q\left(Q^* - Q\right) \tag{5.9}$$

where Q denotes the reactive power. D_Q denotes the damping coefficient of the reactive power. The superscript * denotes reference. The phase voltage is given by

$$v^{\phi+} = V^+ \cos\left(\omega_l t + \measuredangle v^+ + \delta^\phi\right) \tag{5.10}$$

$$\begin{cases} V^{+}=\sqrt{\left(V^{d+}\right)^{2}+\left(V^{q+}\right)^{2}} \\ \measuredangle v^{\phi+}=\arctan\left(V^{q+}/V^{d+}\right) \end{cases} \tag{5.11}$$

where ω_l equals ω_n. For AG and AB faults, the equivalent sequence network is established in Fig. 2 (a) and (b), respectively.

From Fig. 5.2 (a), the AG fault current equals

$$i_f=\frac{v_f^{+}}{R_f+z_{eq}^{-}+z_{eq}^{0}}=\frac{v_g^{+}-i_g^{+}\left((l-d)z_l^{+}+z_g^{+}\right)}{R_f+z_{eq}^{-}+z_{eq}^{0}} \tag{5.12}$$

where z_{eq} denotes the equivalent impedance. The sequence-domain equivalent impedances are determined as

$$z_{eq}^{+}=\frac{\left(z_{tr}^{+}+dz_l^{+}\right)\left((l-d)z_l^{+}+z_g^{+}\right)}{z_{tr}^{+}+lz_l^{+}+z_g^{+}} \tag{5.13}$$

$$z_{eq}^{-}=\frac{\left(z_s^{-}+z_{tr}^{-}+dz_l^{-}\right)\left((l-d)z_l^{-}+z_g^{-}\right)}{z_s^{-}+z_{tr}^{-}+lz_l^{-}+z_g^{-}} \tag{5.14}$$

$$z_{eq}^{0}=\frac{\left(z_{tr}^{0}+dz_l^{0}\right)\left((l-d)z_l^{0}+z_g^{0}\right)}{z_{tr}^{0}+lz_l^{0}+z_g^{0}} \tag{5.15}$$

The sequence components of measured currents are determined as

$$i_m^{+}=i_s^{+}=\frac{v^{+}-v_g^{+}+i_g^{+}\left((l-d)z_l^{+}+z_g^{+}\right)}{z_{eq}^{+}} \tag{5.16}$$

$$i_m^{-}=i_s^{-}=\frac{i_f z_{eq}^{-}}{z_s^{-}+z_{tr}^{-}+dz_l^{-}}=\frac{i_f\left((l-d)z_l^{-}+z_g^{-}\right)}{z_s^{-}+z_{tr}^{-}+lz_l^{-}+z_g^{-}} \tag{5.17}$$

$$i_m^{0}=i_s^{0}=\frac{i_f z_{eq}^{0}}{z_{tr}^{0}+dz_l^{0}} \tag{5.18}$$

From (5.12) and (5.17), the fault current and measured current are related to the negative sequence impedance of GFM-IBRs. Combining (5.12) to (5.18) yields

$$\begin{aligned} \frac{i_m^{a}}{i_f}&=\frac{i_m^{+}}{i_f}+\underbrace{\left(\frac{\left((l-d)z_l^{-}+z_g^{-}\right)}{z_s^{-}+z_{tr}^{-}+lz_l^{-}+z_g^{-}}\right)}_{x}+\frac{(1+k_0)z_{eq}^{0}}{z_{tr}^{0}+dz_l^{0}} \\ &=\frac{\left(v^{+}-v_f^{+}\right)\left(R_f+z_{eq}^{0}+z_{eq}^{-}\right)}{z_{eq}^{+}v_f^{+}}+x+\frac{(1+k_0)z_{eq}^{0}}{z_{tr}^{0}+dz_l^{0}} \end{aligned} \tag{5.19}$$

$$z_{eq}^{-}=(1-x)\left((l-d)z_l^{-}+z_g^{-}\right) \tag{5.20}$$

Similarly, from Fig. 5.2 (b), the zero sequence equivalent impedance and fault current are given by

$$\begin{cases} z_{eq}^{0}=0 \\ i_f=v_f^{+}/\left(R_f+z_{eq}^{-}\right) \end{cases} \tag{5.21}$$

$$\begin{aligned}\frac{i_m^{ab}}{i_f} &= \frac{i_m^+}{i_f}\left(1-e^{j240^\circ}\right)-x\left(1-e^{j120^\circ}\right)\\ &= \frac{\left(v^+-v_f^+\right)\left(R_f+(1-x)\left((l-d)z_l^-+z_g^-\right)\right)\sqrt{3}e^{j30^\circ}}{z_{eq}^+ v_f^+}-x\sqrt{3}e^{-j30^\circ}\end{aligned} \tag{5.22}$$

Therefore, i_m^a/i_f and i_m^{ab}/i_f are closely related to the term x containing z_s^-. This indicates the z_s^- will affect the apparent impedance under unbalanced faults with a resistance.

Under the synchronous reference frame, double-frequency negative sequence components exist in the GFM control loop. The current references are regulated by the inner voltage control based on *dq* voltages, as given by

$$i_s^{-*} = R_v^{j2\omega_n}\left(v^* - \lambda_f^{j\omega_n} v^-\right) \tag{5.23}$$

where $\lambda_f^{j\omega_n} = e^{j\theta_{shift}}$ denotes the complex gain of measurement filters under the system frequency. $R_C^{j2\omega_n} = k_{pC} + k_{iC}/j2\omega_n$ denotes the complex gain of PI regulators under the double frequency. *C*=*i* and *v* denote the inner current control and inner voltage control, respectively.

Since the voltage references are only positive sequence components, the double-frequency oscillations in i_s^{-*} are conveyed by the v^-. The double-frequency negative sequence components of converter voltages are determined as

$$v_s^- = \lambda_f^{j\omega_n}\left(v^- - z_c i_s^- + R_i^{j2\omega_n}\left(R_v^{j2\omega_n} v^- + i_s^-\right)\right) \tag{5.24}$$

The equivalent negative sequence impedance is given by

$$z_s^- = \frac{v^-}{i_s^-} = \frac{z_c\left(1-\lambda_f^{j\omega_n}\right)+\lambda_f^{j\omega_n} R_i^{j2\omega_n}}{1-\lambda_f^{j\omega_n}-R_v^{j2\omega_n} R_i^{j2\omega_n}\lambda_f^{j\omega_n}} \tag{5.25}$$

Since the phase shift is relatively minimal, the angle of the equivalent negative sequence impedance is approximately given by

$$z_s^- \approx -1/R_v^{j2\omega_n} \tag{5.26}$$

$$Z_s^- \approx \frac{2\omega_n}{\sqrt{(k_{pv})^2+\left(k_{iv}/(2\omega_n)\right)^2}} \tag{5.27}$$

$$\angle z_s^- = \angle\left(-1/R_v^{j2\omega_n}\right) = \arctan\left(k_{iv}/2\omega_n k_{pv}\right) \tag{5.28}$$

From (5.27) and (5.28), considering the influence of fault resistances, the trajectory of the apparent impedance can be altered by the parameters of the inner voltage control. The sensitivity of distance protection may be reduced by improper inner control parameters.

5.1.1.2 In the Restricted Mode

Under severe grid faults, the converter currents can exceed the current limits. Then the current limiter is active to suppress the converter currents. The magnitude and angle of the total current are

$$\begin{cases} I_s^{lim} \geq \left|i_s^+ + i_s^-\right| \\ \angle i_s = \angle\left(i_s^+ + i_s^-\right) \end{cases} \tag{5.29}$$

From (5.29), the current references are modified by the CLM. The inner voltage control is not able to influence the negative sequence impedance, as the current output is limited. Consequently, advanced FRT solutions, such as current saturation-based and virtual impedance-based methods, are developed to improve the FRT capacities. Assuming that the current capacity is fully utilized, i.e., $i_m \approx I_s^{lim} \angle i_s$, we have

$$\frac{i_m^a}{i_f} = \frac{i_m}{i_f} - \frac{z_{eq}^0}{z_{tr}^0 + dz_l^0} \approx \frac{I_s^{lim} \angle i_s}{i_f} - \frac{z_{eq}^0}{z_{tr}^0 + dz_l^0} \tag{5.30}$$

$$\frac{i_m^{ab}}{i_f} = \frac{i_m}{i_f} - \frac{\left(e^{j240°} i_s^+ + e^{j120°} i_s^-\right)}{i_f} \approx \frac{I_s^{lim} \angle i_s}{i_f} - \frac{\left(e^{j240°} i_s^+ + e^{j120°} i_s^-\right)}{i_f} \tag{5.31}$$

where i_s^+ and i_s^- are determined by FRT solutions for current limiting. From (5.30) and (5.31), the apparent impedance in fault steady state changes as I_s^{lim} varies. $\angle i_s$ can be altered by different FRT solutions, ultimately affecting the trajectory of the apparent impedance.

5.1.2 Interaction between Fault Ride-Through Control and Apparent Impedance

IBRs can be equivalent to controlled current sources under FRT mode since they are required to inject specified current per grid codes. Fig. 5.3 shows a simple transmission system with an IBR and its equivalent circuit for the purpose of illustration. $\{\boldsymbol{V}_M, \boldsymbol{I}_M\}$ denotes voltage and current vectors measured by the distance relay at the IBR terminal. $\boldsymbol{Z}_s$ denotes the equivalent impedance of IBR. $\boldsymbol{I}_G$ denotes the current contribution from the external grid. R_F denotes the fault resistance. $\{\boldsymbol{Z}_{L1}, \boldsymbol{Z}_{L2}\}$ denotes the equivalent impedance from fault points to each terminal.

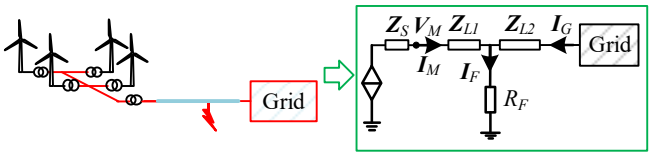

Fig. 5.3. Transmission system with IBR and the equivalent circuit

From Fig. 5.3, the apparent impedance measured by the distance relay can be derived as

$$\boldsymbol{Z}_M = \frac{\boldsymbol{V}_M}{\boldsymbol{I}_M} = \frac{\boldsymbol{I}_M \boldsymbol{Z}_{L1} + \boldsymbol{I}_F R_F}{\boldsymbol{I}_M} = \boldsymbol{Z}_{L1} + \frac{(\boldsymbol{I}_M + \boldsymbol{I}_G) R_F}{\boldsymbol{I}_M} = \boldsymbol{Z}_{L1} + \left(1 + \frac{\boldsymbol{I}_G}{\boldsymbol{I}_M}\right) R_F \tag{5.32}$$

where $\boldsymbol{I}_M$ is determined by the current limiting scheme, as given by

$$\begin{cases} |\boldsymbol{I}_M| = \left|i_g^+ + i_g^-\right| \\ \angle \boldsymbol{I}_M = \angle\left(i_g^+ + i_g^-\right) \end{cases} \tag{5.33}$$

where $|\boldsymbol{I}_M|$ and $\angle \boldsymbol{I}_M$ denotes the magnitude and angle of $\boldsymbol{I}_M$. With the specified scheme, the current capacity can be fully utilized. Hence, (5.33) can be rewritten as

$$\begin{cases} |\boldsymbol{I}_M| = i_{\max} \\ \angle \boldsymbol{I}_M = \angle\left(\boldsymbol{I}_P + \boldsymbol{I}_Q\right) \end{cases} \tag{5.34}$$

where $\boldsymbol{I}_P$ and $\boldsymbol{I}_Q$ denote active and reactive currents. The derivation indicates that the reactive current injection can alter the angle of the current vector, affecting the trajectory of the apparent impedance. To

enable I2 to lead V2 by 90˚, $\boldsymbol{I}_P^- = 0$. For the CS-based CLM, (5.34) yields

$$\begin{cases} \measuredangle \boldsymbol{I}_M = \measuredangle\left(\boldsymbol{I}_P^+ + \boldsymbol{I}_Q^+ + \boldsymbol{I}_Q^-\right) \\ \left|\boldsymbol{I}_Q^+\right| = K_{scale-ph}\left(K_{scaleQ}K^+\left(1-V_g^+\right)+i_Q^{+pre}\right) \\ \left|\boldsymbol{I}_Q^-\right| = K_{scale-ph}K_{scaleQ}K^-V_g^- \\ K_{scaleQ} == \left(i_{\max}-i_Q^{+pre}\right)\Big/\left(\left|K^+\left(1-V_g^+\right)\right|+\left|K^-V_g^-\right|\right) \\ K_{scale-ph} = i_{\max}/\max(\boldsymbol{i}_{abc}) \end{cases} \tag{5.35}$$

where i_{max} denotes the maximum current limit. K_{scaleQ} denotes the scaling factor for reactive current. i_Q^{+pre} denotes the pre-fault I1R. $K_{scale\text{-}ph}$ denotes the scaling factor for phase current.

From (5.32)−(5.35), the apparent impedance $\boldsymbol{Z}_M$ can be altered by the $\boldsymbol{Z}_{L1}$, R_F, and $\{K^+, K^-\}$. These impact factors represent the fault proximity, fault resistance, and K factors for reactive current injection, respectively. Since the interaction between these parameters and $\boldsymbol{Z}_M$ is nonlinear and complicated, EMT-type tools can be used to analyze the performance of distance protection under these varying impact factors. For the VI-based CLM, (5.33) yields

$$\begin{cases} \left|\boldsymbol{I}_M\right| = \left|\dfrac{i_{\max}^+\left(k_{pV}+k_{iV}/s\right)\left(\boldsymbol{v}_g^{+*}-\boldsymbol{v}_g^+\right)}{i_{\max}^+ + \left(k_{pV}+k_{iV}/s\right)\Delta V} + i_g^-\right| \\ \measuredangle \boldsymbol{I}_M = \measuredangle\left(\dfrac{i_{\max}^+\left(k_{pV}+k_{iV}/s\right)\left(\boldsymbol{v}_g^{+*}-\boldsymbol{v}_g^+\right)}{i_{\max}^+ + \left(k_{pV}+k_{iV}/s\right)\Delta V} + i_g^-\right) \\ \Delta V = \left[v_g^{+*} - \left(k_{pVI}+k_{iVI}/s\right)\left(i_{\max}^+ - i_g^{+*}\right)\right]e^{j\tan^{-1}(\Delta_{X/R})} \\ i_{\max}^+ = \eta_{12}i_{\max}\left[\eta_{12}^2 + 2\eta_{12}\max(\cos(\boldsymbol{\delta}_{abc}))+1\right]^{-1/2} \end{cases} \tag{5.36}$$

where $\{k_{pV}, k_{iV}\}$ denotes PI parameters of the inner voltage control of GFM-IBRs. $\Delta_{X/R}$: virtual impedance ratio. $\{k_{pVI}, k_{iVI}\}$ denotes PI parameters of the VI-based limiter. η_{12} is the current limiter ratio.

The current contribution and apparent impedance $\boldsymbol{Z}_M$ can be altered by the PI parameters, virtual impedance ratio, and current limit ratio. Since the interaction between these parameters and $\boldsymbol{Z}_M$ is nonlinear and complicated, EMT-type tools can be used to analyze the performance of distance protection under these varying impact factors.

5.1.3 Case Studies

5.1.3.1 Performance of Apparent Impedance Near IBRs with the BPSC

To validate the impacts of GFM BPSC on the apparent impedance during unbalanced faults, four illustrative examples are presented based on the EPRI benchmark system integrated by a GFM wind park (WP) in EMTP as shown in Fig. 5.4. The default FRT solution is the CS-based CLM.

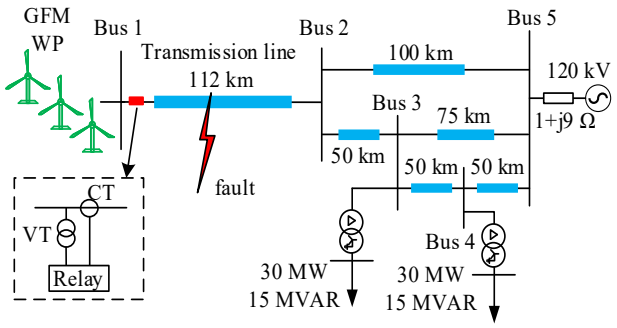

Fig. 5.4. EPRI benchmark system integrated by GFM-IBRs.

In the test system, z_l^+ =0.028+*j*0.325 Ω, *l*=112 km. The fault point is located at 86 km of the transmission line (77% of the total length). The magnitude and angle of the total positive sequence line impedance are 36.5348 Ω and 85.0759˚, respectively. The reach of zone 1 and zone 2 is 29.2279 Ω and 43.8418 Ω, respectively.

a) Performance under Different Inner Control Parameters

During an AG fault, when R_f = 5 Ω, 10 Ω, 50 Ω, and 100 Ω, the negative sequence impedance of GFM-IBRs and apparent impedance are measured under different inner control parameters based on EMT simulation. Since k_{pv} is sensitive to the stability, k_{iv} is taken as the tuning parameter for illustration. From Fig. 5.5, under different fault resistance, as k_{iv} increases, Z_s^- reduces while $\theta_{Z_s^-}$ gradually approaches −100˚. This shows that the inner control parameters have a significant impact on the negative sequence impedance of GFM-IBRs.

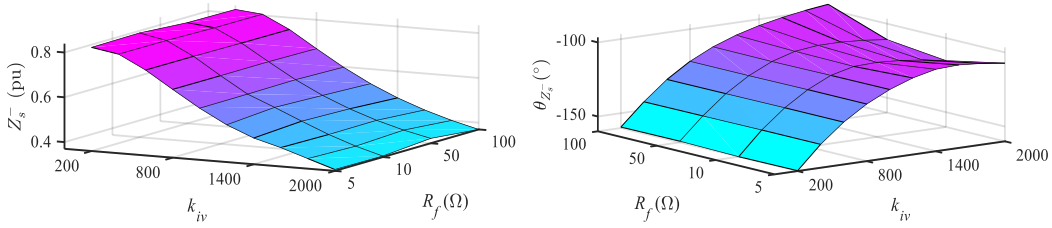

(a) Magnitude (b) Angle

Fig. 5.5. Equivalent negative sequence impedance of GFM-IBRs under different inner control parameters.

In Fig. 5.6, during an AG fault with R_f =50 Ω, the trajectory of the apparent impedance is altered saliently by different inner control parameters. Smaller k_{iv} reduces the apparent impedance of the GFM-IBR. This validates the analysis in section 5.1.1. In Fig. 5.7, a maloperation issue of the distance protection caused by the improper inner control parameters is identified. During an AG fault with R_f =7 Ω, the apparent impedance locus cannot enter the protection zone 1, causing incorrect operation when k_{pv}=0.9 and k_{iv} =2000. Overall, the apparent impedance measured by the distance relay varies under different inner control parameters, leading to reduce the sensitivity of the distance protection.

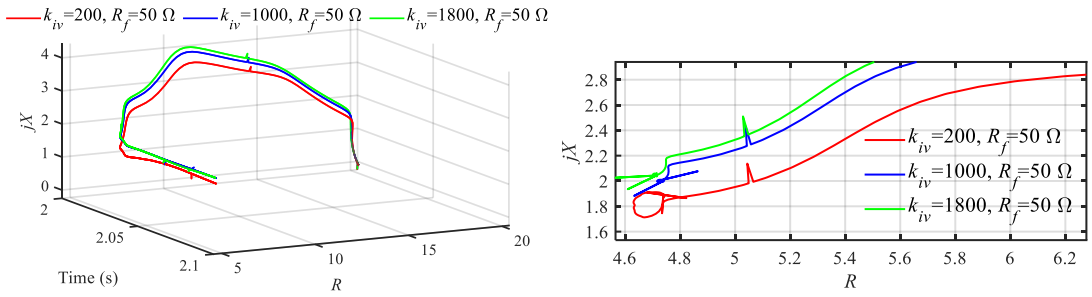

(a) Time-varying apparent impedance (b) Apparent impedance in the *R*-*X* diagram

Fig. 5.6. Apparent impedance under different inner control parameters.

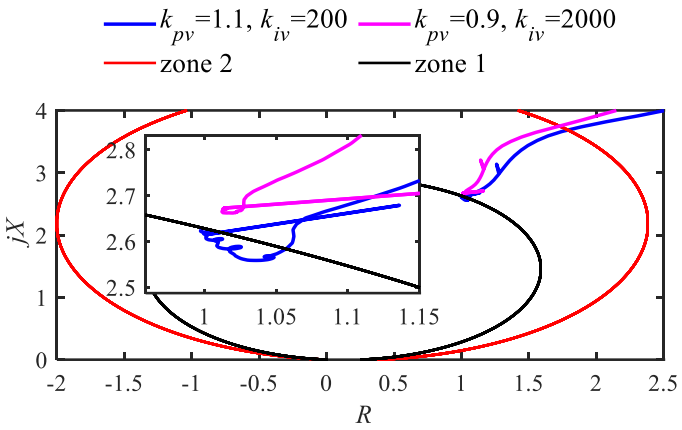

Fig. 5.7. Apparent impedance locus in the Phase A distance relay under different inner control parameters.

b) Performance under Different Current Limits

During AB faults with R_f =50 Ω, the apparent impedance is simulated under different current limits, as shown in Fig. 5.8. As the current limit increases, the apparent impedance reduces under steady state fault conditions, as elaborated in section 5.1.1. Fig. 5.9 identifies a maloperation issue of the distance protection caused by the current limit. During AB faults with R_f =5 Ω, the apparent impedance locus with a small current limit (1.15 pu) cannot enter the protection zone 1, causing the incorrect operation. Overall, the current limits alter the apparent impedance and then decrease the sensitivity of the distance protection.

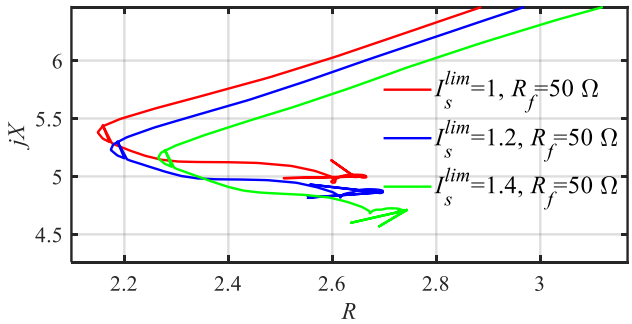

Fig. 5.8. Apparent impedance under different current limits.

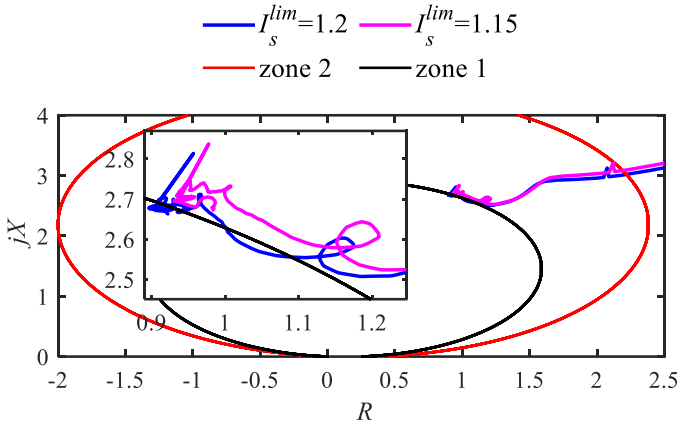

Fig. 5.9. Apparent impedance locus in the Phase AB distance relay under different current limits.

c) Performance under Different FRT Solutions

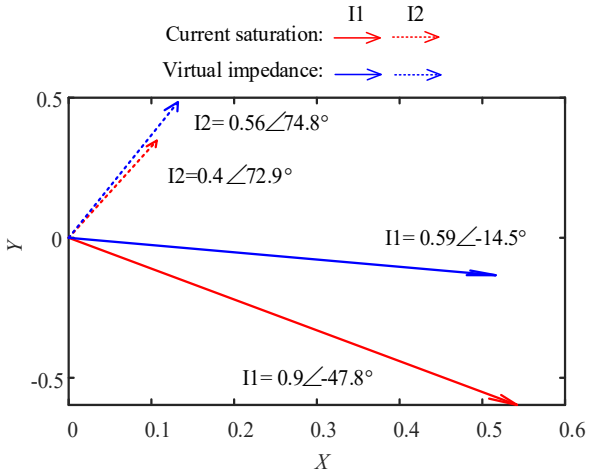

Fig. 5.10. Phasor representation of sequence currents under different FRT solutions.

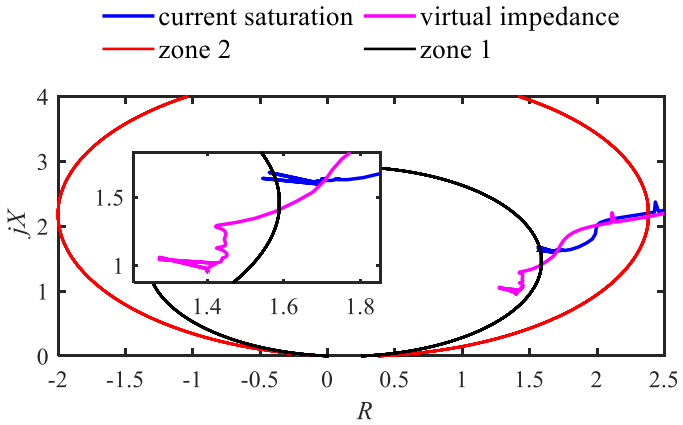

Fig. 5.11. Apparent impedance locus in Phase AB distance relay under different FRT solutions.

During AB faults with R_f =6 Ω, when k_{pv} =1 and k_{iv} =2000, the sequence currents regulated by the current saturation-based and virtual impedance-based methods are illustrated in Fig. 5.10. I1 and I2 denote positive and negative sequence currents, respectively. The magnitude and angle of the currents vary across different FRT solutions. This affects the trajectory of the apparent impedance, as shown in Fig. 5.11. The FRT solutions alter the current injection, ultimately causing different protection results.

d) Comparison with SGs and GFL converters

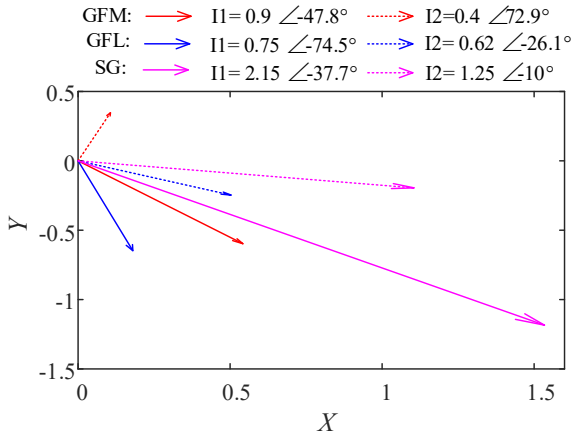

Fig. 5.12. Phasor representation of sequence currents under the GFM WP, GFL WP and SG.

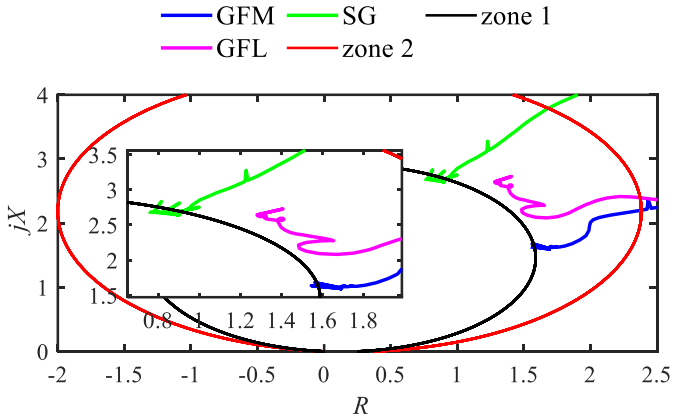

Fig. 5.13. Apparent impedance locus in Phase AB distance relay under the GFM WP, GFL WP and SG.

In this section, fault simulations are considered by replacing the GFM WP with the GFL WP and SG. During AB faults with R_f =5 Ω, the sequence currents and apparent impedances under different generators are shown in Fig. 5.12 and Fig. 5.13, respectively. The GFL WP employs negative sequence reactive current injection during faults. Hence, there is an I2 contribution of 0.62 pu. Since these sources yield varying current contributions, the resulting apparent impedances differ. The protection settings should be designed in accordance with the specific current contribution of GFM-IBRs.

5.1.3.2 Performance of Apparent Impedance Near IBRs with the Current Saturation-based CLM

To study the impacts of IEEE 2800 current injection requirements on distance protection, a modified IEEE PSRC D29 system integrated with Type-IV WTGs is used, as shown in Fig. 2.17. IBR1 on the left and IBR2 on the right. Distance relays are located at the point of interconnection (POI) of IBR1 and IBR2. IBR1 employs the specified current-limiting scheme that meets the IEEE 2800 standard, while IBR2 employs the conventional FRT scheme that meets German grid codes. The details of the conventional FRT scheme can be found in [135]. The manufacturer of distance relays is Generic Electric. The model is GE 60. The protection configuration and line parameters are listed in Table 5-1.

TABLE 5-1

Protection configuration and line parameters

Protection Functions and Settings		Value
Distance protection	direction	Forward
	shape	Quad
	RCA	85°
	range (zone 1/2/3)	80% / 135% / 200%
	delay (zone 1/2/3)	0 / 20 / 40 cycles
	VT ratio	115000:115
	CT ratio	500:5
Transmission line	R1/X1/B1	5.87/ 38.29/ 2.79e-4 Ω
	R0/X0/B0	33.3/ 115.9/ 1.79e-4 Ω

a) Performance under Varying Fault Proximity

For illustration, 10 Ω line-A-to-ground (AG) faults are applied at transmission lines L1 and L2 when t=2 s. The fault distance is set to 30 miles, 45 miles, and 55 miles, respectively. The fault duration is set to 1 s. Fig. 5.14−Fig. 5.16 show the phase A current angle and reactive current injection under the specified scheme (IBR1) and the conventional FRT scheme (IBR2). Longer fault distance causes a larger current angle and a smaller reactive current injection. Fig. 5.17 shows the apparent impedance locus under the specified scheme (IBR1) and the conventional FRT scheme (IBR2), where red and black lines denote the border of zone 1 and zone 2, respectively. The results show that IBR1 exhibits greater reactive current injection than IBR2 since the current capacity of IBR1 is fully utilized. Under the two FRT schemes, Zone 1 can correctly trip under the fault at 55 miles (78% total length) of transmission lines.

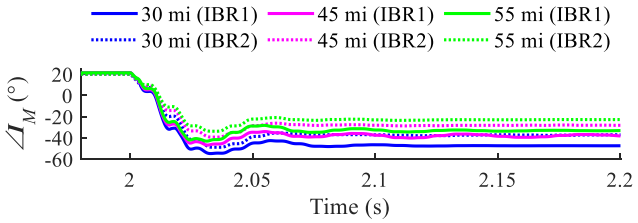

Fig. 5.14. Current angle $\angle \boldsymbol{I}_{Ma}$ under varying fault proximity

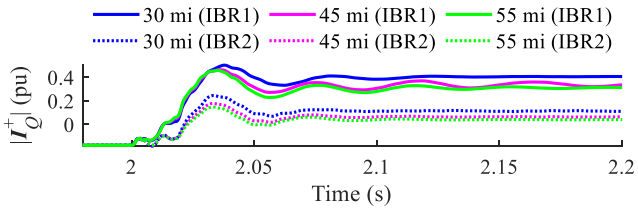

Fig. 5.15. I1R injection under varying fault proximity

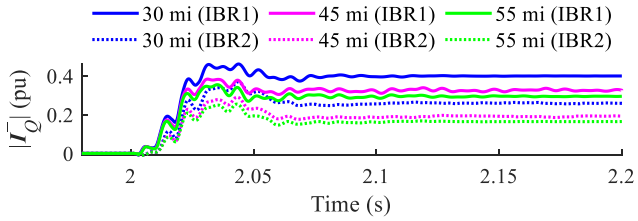

Fig. 5.16. I2R injection under varying fault proximity

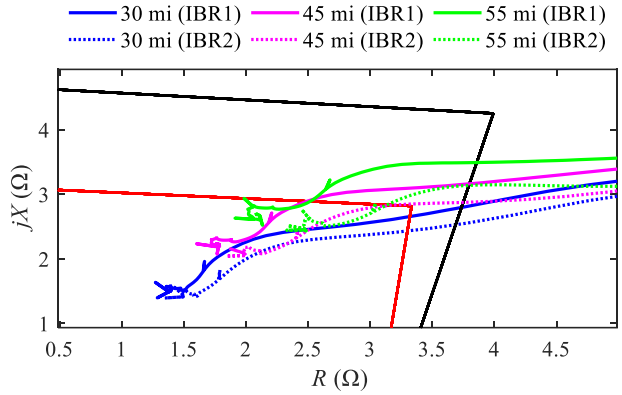

Fig. 5.17. Apparent impedance $\boldsymbol{Z}_M$ under varying fault proximity

b) Performance under Varying Fault Resistance

For illustration, AG faults are applied at 55 miles of L1 and L2 when t=2 s. The fault resistance is set to 10 Ω, 15 Ω, and 17 Ω, respectively. Fig. 5.18 and Fig. 5.19 show the ratio of $|\boldsymbol{I}_{Ga}|$ over $|\boldsymbol{I}_{Ma}|$ and the apparent impedance locus under the specified scheme (IBR1) and the conventional FRT scheme (IBR2).

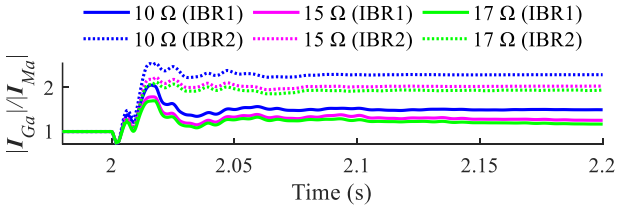

Fig. 5.18. Ratio of $|\boldsymbol{I}_{Ga}|$ over $|\boldsymbol{I}_{Ma}|$ under varying fault resistance

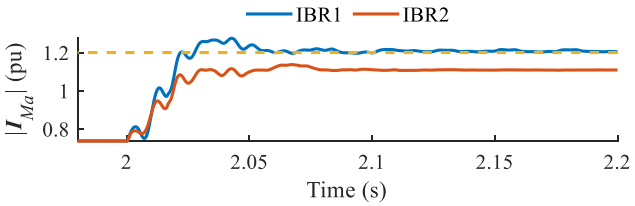

Fig. 5.19. Comparison of $|\boldsymbol{I}_{Ma}|$ under a 17 Ω fault resistance

From Fig. 5.18, the ratio of $|\boldsymbol{I}_{Ga}|$ over $|\boldsymbol{I}_{Ma}|$ under the conventional FRT scheme is higher than that under the specified scheme. The reason is that under fault steady state conditions, $|\boldsymbol{I}_{Ga}|$ can reach the maximum current limit by using the specified scheme, as shown in Fig. 5.19. Fig. 5.20 shows that with a 17 Ω fault resistance, the trajectory of apparent impedance under the conventional FRT scheme cannot enter zone 1, decreasing the sensitivity of distance protection. In contrast, the specified scheme enables zone 1 of protection to identify the fault correctly.

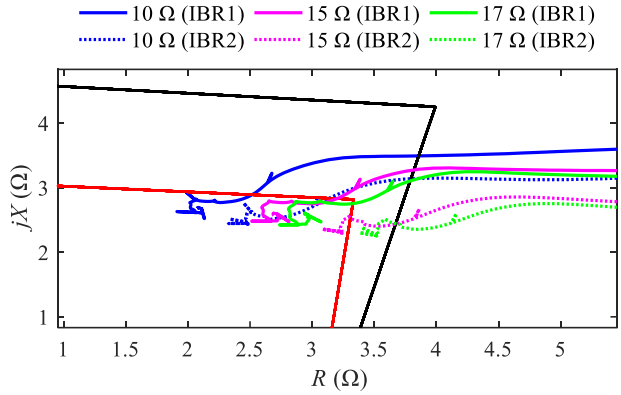

Fig. 5.20. Apparent impedance $\boldsymbol{Z}_M$ under varying fault resistance

c) Performance under Varying K factors

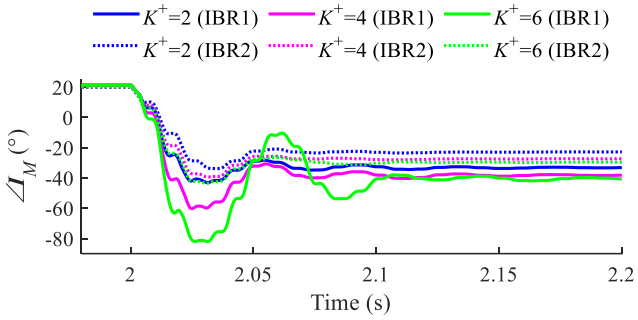

Fig. 5.21. Current angle $\measuredangle \boldsymbol{I}_{Ma}$ under varying K factor

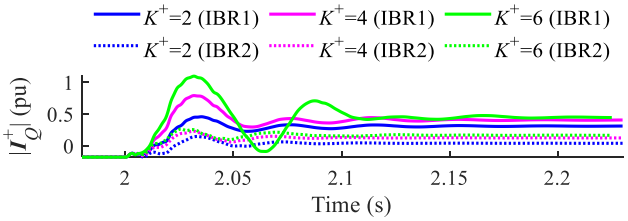

Fig. 5.22. I1R injection under varying K factor

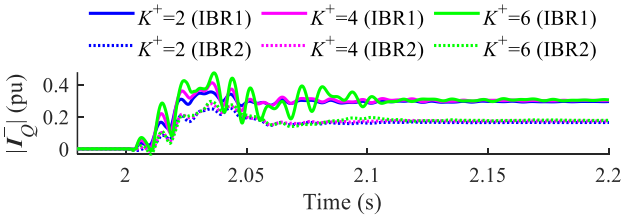

Fig. 5.23. I2R injection under varying K factor

For illustration, 10 Ω AG faults are applied at 55 miles of L1 and L2 when t=2 s. The K factor for I1R injection (K^+) is set to 2, 4, and 6, respectively. Fig. 5.21−Fig. 5.23 show the current angle, reactive current injection, and the apparent impedance locus under the IBR1 and IBR2. A larger K^+ results in a smaller current angle and a larger I1R injection. Moreover, since the specified scheme scales the phase current, there is a significant oscillation in waveforms when K^+=6, increasing the settling time, as shown in Fig. 5.24. The IEEE 2800 requires a step response time of less than 2.5 cycles and a settling time of less than 4 cycles for the injected fault current of a fully sized converter unit. Hence, although the fault

steady state current injection meets the IEEE 2800 when K^+=6, the dynamic performance fails to comply with IEEE 2800. Fig. 5.25 and Fig. 5.26 show that the trajectory of apparent impedance shifts up as K^+ increases, decreasing the speed of distance protection.

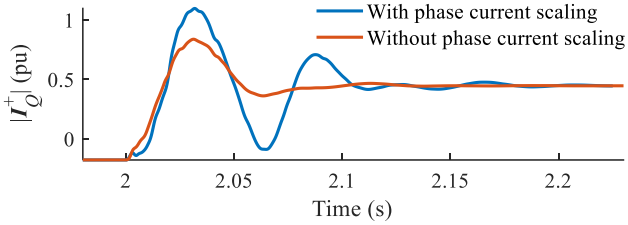

Fig. 5.24. Comparison of I1R injection of IBR1 when K^+=6

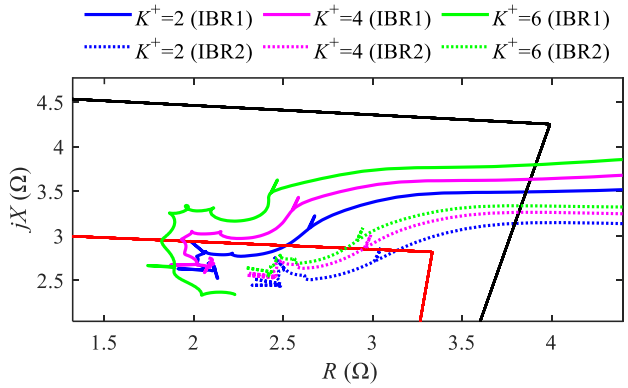

Fig. 5.25. Apparent impedance $\boldsymbol{Z}_M$ under varying K factor

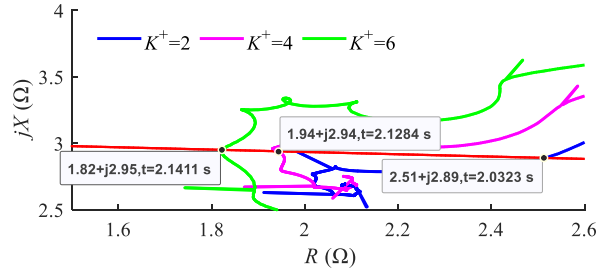

Fig. 5.26. Apparent impedance $\boldsymbol{Z}_M$ and crossover points of IBR1 under varying K factor

5.1.3.3 Performance of Apparent Impedance Near IBRs with the Virtual Impedance-based CLM

The current contribution under the VI-based CLM can be modified by the inner voltage control parameters and virtual impedance settings. In Scenario 2, 10 Ω AG faults are applied at 55 miles of L1 when t=2 s. The virtual impedance ratio ($\Delta_{X/R}$) is set to 1, 5, and 10, respectively. Fig. 5.27–Fig. 5.29 show the current angle, reactive current injection, and the apparent impedance locus under varying $\Delta_{X/R}$. A larger $\Delta_{X/R}$ results in a smaller current angle and a larger I1R injection. The settling time increases and exceeds 4 cycles, which fails to comply with the dynamic performance requirements in IEEE 2800. Fig. 5.29 shows that the trajectory of apparent impedance shifts up as $\Delta_{X/R}$ increases, decreasing the sensitivity of distance protection. When $\Delta_{X/R}$ is 5 and 10, the trajectory does not enter the zone 1 since the varying $\Delta_{X/R}$ alters the $\measuredangle \boldsymbol{I}_{Ma}$.

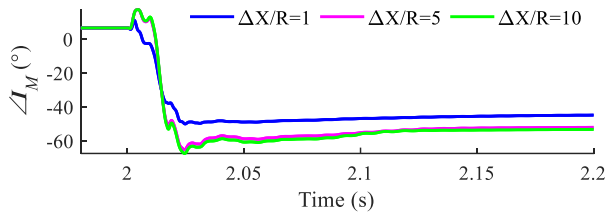

Fig. 5.27. Current angle $\measuredangle \boldsymbol{I}_{Ma}$ under varying $\Delta_{X/R}$

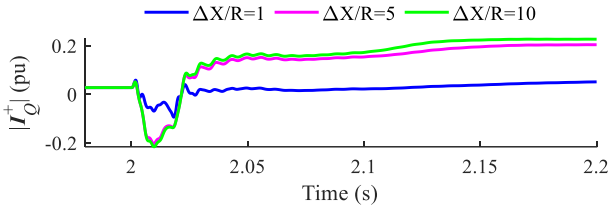

Fig. 5.28. I1R injection under varying $\Delta_{X/R}$

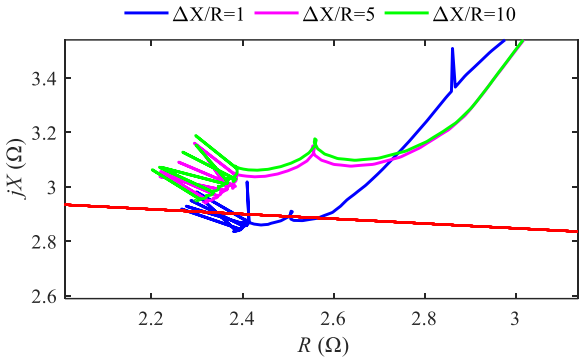

Fig. 5.29. Apparent impedance $\boldsymbol{Z}_M$ and crossover points of IBR1 under varying $\Delta_{X/R}$

The PI control parameters can also affect the current contribution of IBRs. In this paper, we use the integral coefficient for illustration. Fig. 5.30−Fig. 5.32 show the current angle, I1R injection, and apparent impedance locus under varying k_{iVI} (65, 200, 400). The results show that varying k_{iVI} affects the dynamic performance saliently. However, the modification to the fault steady-state value is minimal, resulting in little change to the trajectory of the apparent impedance. To achieve the dynamic performance requirements in IEEE 2800, the PI control tuning of VI-based limiters is essential.

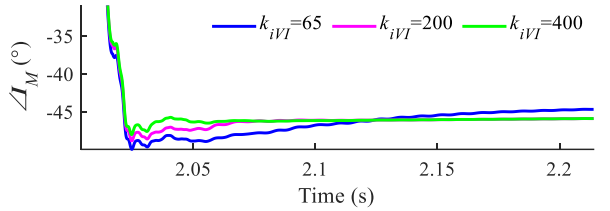

Fig. 5.30. Current angle $\measuredangle \boldsymbol{I}_{Ma}$ under varying k_{iVI}

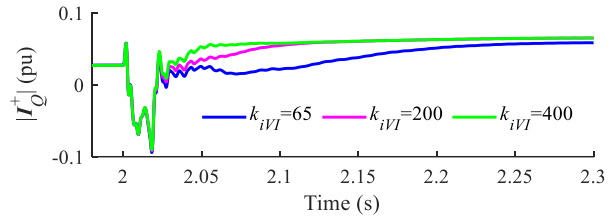

Fig. 5.31. I1R injection under varying k_{iVI}

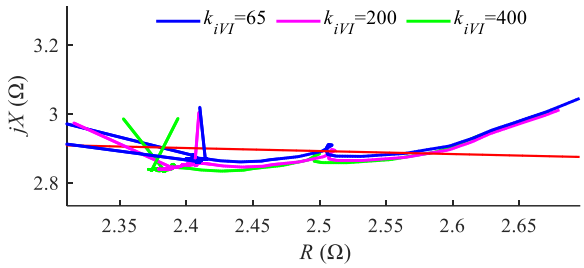

Fig. 5.32. Apparent impedance $\boldsymbol{Z}_M$ and crossover points of IBR1 under varying k_{iVI}

Fig. 5.33−Fig. 5.35 show the current angle, I1R injection, and the apparent impedance locus under varying k_{iV} (150, 200, 250). The results show that varying k_{iV} affects the dynamic performance and fault steady state value slightly, leading to a minor change to the trajectory of the apparent impedance.

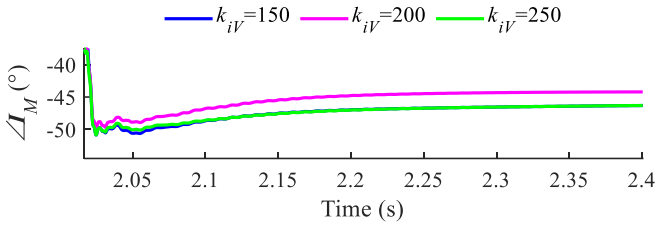

Fig. 5.33. Current angle $\angle \boldsymbol{I}_{Ma}$ under varying k_{iV}

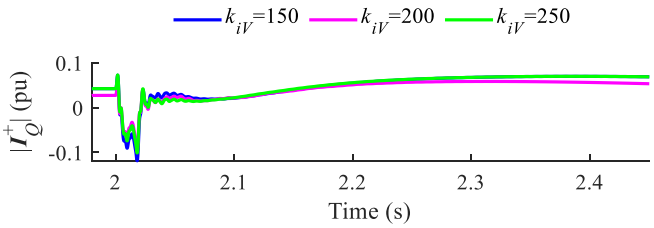

Fig. 5.34. I1R injection under varying k_{iV}

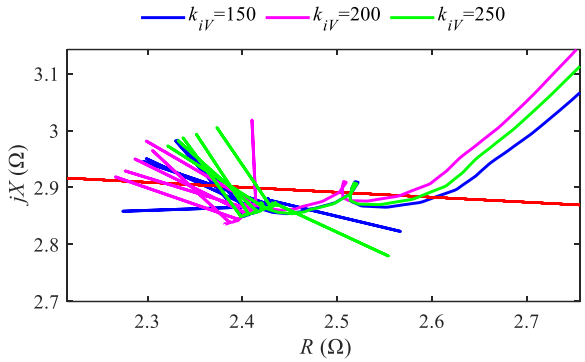

Fig. 5.35. Apparent impedance $\boldsymbol{Z}_M$ and crossover points of IBR1 under varying k_{iV}

Fig. 5.36−Fig. 5.40 show the current angle and magnitude, reactive current injection, and the apparent impedance locus under varying η_{12} (1, 2, 3). The results show that a larger η_{12} increases the current magnitude and I1R injection significantly. Due to the larger current contribution, the trajectory of the apparent impedance shifts downward, improving the sensitivity of protection.

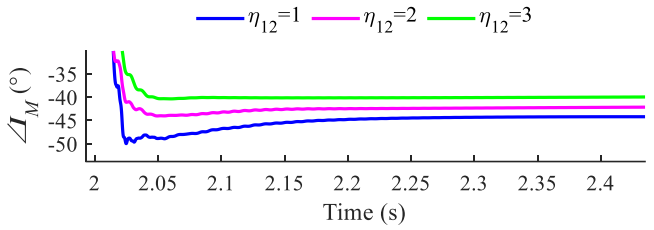

Fig. 5.36. Current angle $\measuredangle \boldsymbol{I}_{Ma}$ under varying η_{12}

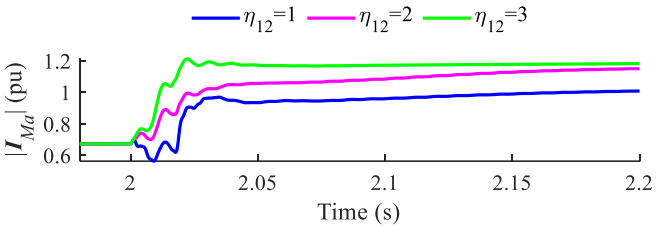

Fig. 5.37. Current magnitude $|\boldsymbol{I}_{Ma}|$ under varying η_{12}

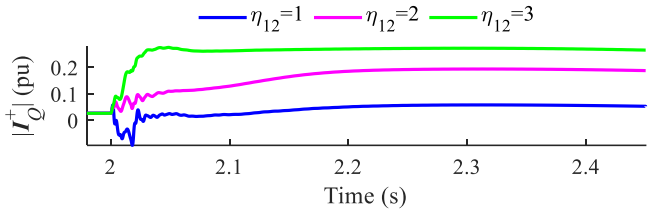

Fig. 5.38. I1R injection under varying η_{12}

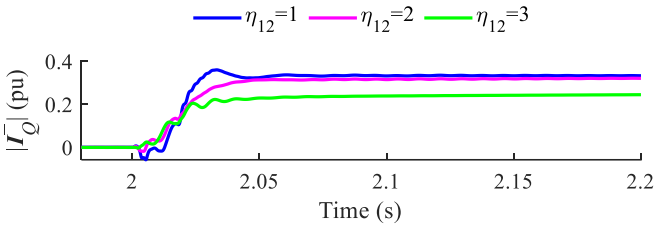

Fig. 5.39. I2R injection under varying η_{12}

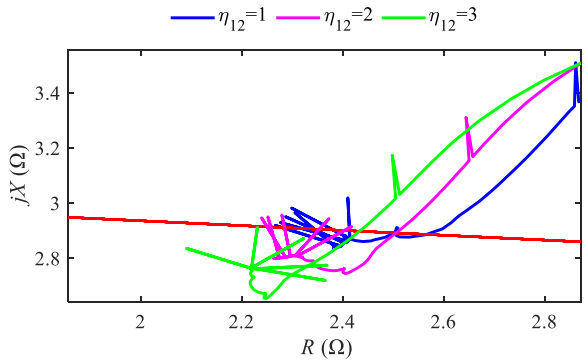

Fig. 5.40. Apparent impedance $\boldsymbol{Z}_M$ and crossover points of IBR1 under varying η_{12}

5.2 Impacts of GFM-IBR on Negative Sequence Components-based Protection

To validate the performance of the negative sequence components-based protection system, the instantaneous negative sequence overcurrent (50Q), directional negative sequence overcurrent (67Q), and fault-identification (FID) elements are tested under a 49-mile AG fault in a modified IEEE PSRC

D29 system (see Fig. 2.17). Although the impact of GFL-IBRs on the negative sequence-based protection elements have been studied before, the idea here is to provide the performance of GFM-IBRs with respect to GFL-IBRs. The protection settings are listed in Table 5-2.

TABLE 5-2
Settings of negative sequence components-based protection

Category	Physical meaning	Parameter
Relay measurement	VT ratio	115000:115
	CT ratio	500:5
50Q	I2 threshold	0.2 pu
67Q	Rated current	500 A
	Directional element characteristic angle	80°
	Forward and reverse limit angle	85°
	Overcurrent thresholds	0.1 A
FID	Characteristic angle	50°

The 50Q element activates when $\boldsymbol{I}^-$ surpasses a specified threshold, known as the pickup setting. From Fig. 5.41, the magnitude of $\boldsymbol{I}^-$ under GFM-BPSC, GFL-PNSC, and GFM-PNSC is 0.28 pu around, ensuring operation as expected. Whereas, as expected, under GFL-BPSC, this magnitude is around 0.05 pu which is smaller than the pickup setting of 0.2 pu, resulting in maloperation of the protection element 50Q.

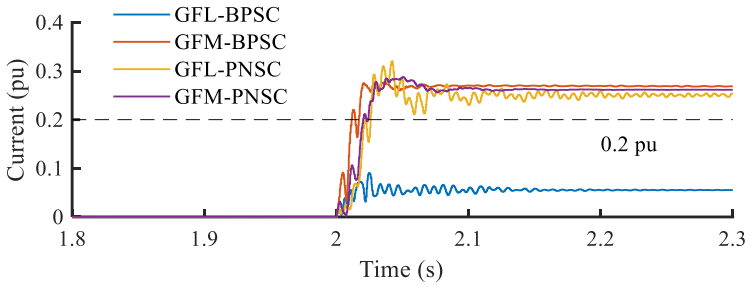

Fig. 5.41. The magnitude of $\boldsymbol{I}^-$ measured by a 50Q element during an AG fault.

The 67Q element [153] identifies the fault direction (forward or reverse relative to the relay) by measuring the phase angle difference between $\boldsymbol{V}^-$ and $\boldsymbol{I}^-$, i.e., the angle of $\boldsymbol{Z}^-$, as shown in Fig. 5.42(a). Under GFM-BPSC, GFL-PNSC, and GFM-PNSC, the angle of $\boldsymbol{Z}^-$ is −97.9°, −91.0°, and −91.3°, respectively. Thus, the $\boldsymbol{Z}^-$ vector falls within the forward zone (67QF), and the 67Q element successfully declares the fault direction as 67QF. In contrast, under GFL-BPSC, the angle becomes 138.2° which is mistakenly within the reverse zone (67QR), showing that the FRT control can alter the angle of $\boldsymbol{Z}^-$, thus affecting the fault direction detection by 67Q.

The FID element [63], [153], also known as phase selection, is utilized by protective relays to determine the type of fault, as shown in Fig. 5.42(b). $\boldsymbol{I}^0$ denotes the zero-sequence current. Under GFM-BPSC, GFL-PNSC, and GFM-PNSC, FID scheme sees a phase angle difference of about −10° between the $\boldsymbol{I}^-$ and $\boldsymbol{I}^0$, which is within the blue sector, and the scheme successfully declares the fault type as AG. However, under GFL-PNSC, the measured angle difference is about 115° which falls within the red sector, and the FID scheme mistakenly detects the fault type as CG.

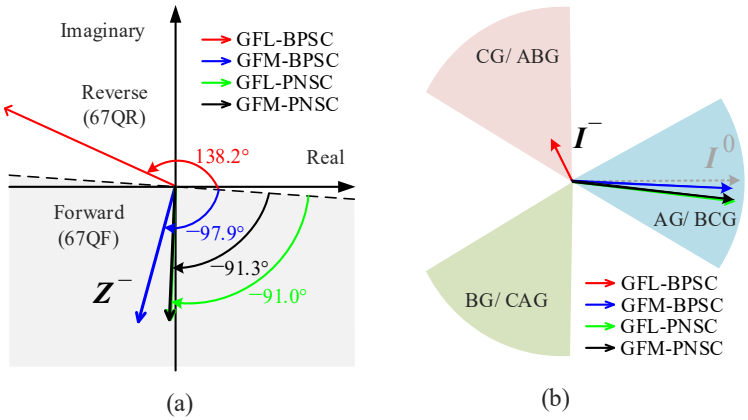

Fig. 5.42. Phasors measured by negative sequence component-based protection: (a) 67Q; (b) FID.

Overall, Fig. 5.43 shows the tripping results of 50Q, 67QF, and 67QR. The employed FRT control solutions in the GFM-BPSC, GFL-PNSC, and GFM-PNSC can address the negative sequence components-based protection issues for this case. However, GFM-BPSC exhibits a significant limitation as its current injection is highly sensitive to the inner control parameters and current limits. In practice, these parameters cannot be freely adjusted to meet current injection requirements. Depending on the proximity of the fault, the GFM-BPSC may not be able to address the asymmetrical FRT. Hence, GFM-PNSC and GFL-PNSC will be effective solutions to ensure the correct operation of negative-sequence component-based protection.

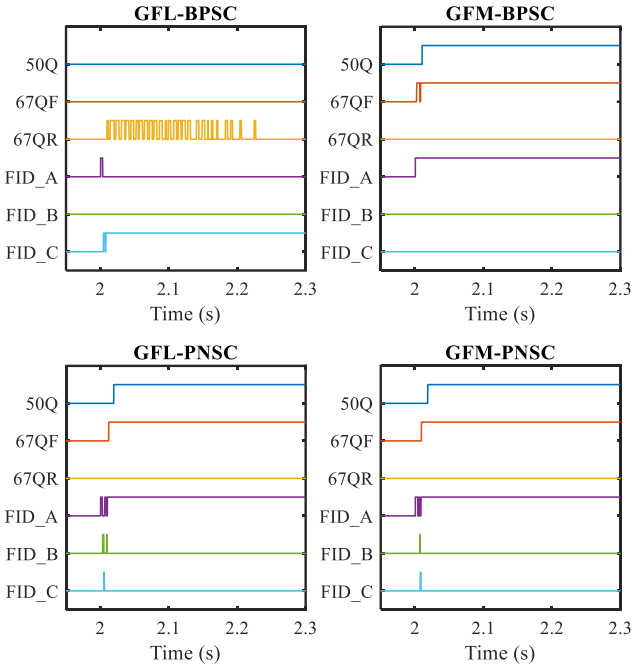

Fig. 5.43. Tripping results under different GFL and GFM control strategies

5.3 Conclusion

In this chapter, the apparent impedance measured by distance relay is elaborated mathematically in a two-bus system integrated by GFM-IBRs. The results indicate that, during unbalanced faults with

resistance, the inner control parameters, current limit, and FRT solutions can influence the impedance locus by providing different positive and negative sequence currents. Particularly, this section studies the impact of IEEE 2800 IBR FRT requirements on the performance of a line distance relay. The analysis in a simple system integrated with IBR indicates that the apparent impedance would be altered by the fault proximity, fault resistance, and K factors for reactive current injection. In a modified IEEE PSRC D29 system integrated with IBRs, the performance of distance protection and negative sequence components-based protection is explored under various FRT solutions. Main conclusions are drawn as follows:

(1) When the current capability is sufficient, during unbalanced faults, GFM-IBRs can mimic the positive sequence performance of SGs. However, the inner control parameters may adversely affect the negative sequence behaviour, thus reducing the protection's sensitivity. In the case studies, smaller k_{iv} leads to the decrease of apparent impedance. The impedance locus may not enter the correct protection zone under improper inner control parameters. When the current limit is reached, the current limit and FRT solutions determine the magnitude and angle of current references, which in turn changes the apparent impedance and ultimately impacts the protection outcomes. In the case studies, larger current limit leads to the decrease of apparent impedance. The impedance locus may not enter the correct protection zone when the current limit is small. The variation in current contributions from different sources (SGs and IBRs) leads to discrepancies in apparent impedances.

(2) Per IEEE 2800 standard, IBRs shall be capable of injecting current to the maximum current limit. Hence, the ratio of $|\boldsymbol{I}_{Ga}|$ over $|\boldsymbol{I}_{Ma}|$ under the IEEE 2800-conforming FRT scheme is lower than that under the conventional FRT scheme, weakening the impacts of fault resistance on apparent impedance trajectory. Therefore, compared to the conventional FRT scheme, the trajectory of apparent impedance under the IEEE 2800-conforming FRT scheme is less sensitive to fault resistance, improving the sensitivity of distance protection. The phase current scaling method in the IEEE 2800-conforming scheme FRT scheme causes an oscillation in waveforms when the K factor is large, increasing the settling time. Consequently, the trajectory of apparent impedance shifts up as the K factor increases, decreasing the speed of distance protection. Hence, the selection of K factors should be based on the converter current capacity to meet the dynamic performance requirement in IEEE 2800 and improve the speed of distance protection.

(3) In negative sequence components-based protection studies, maloperation issues of 50Q, 67QF, 67QR, and incorrect faulted phase selection are found under GFL-BPSC. The proposed FRT control solutions in GFM-BPSC, GFL-PNSC, and GFM-PNSC address these issues for the test case. Given the limitations of BPSC approaches, future work should focus on advancing PNSC strategies to ensure reliable IEEE 2800 compliance and asymmetrical FRT enhancement across varied operational conditions. The pickup settings of future protection schemes should consider both the limited current contribution of IBRs and the recommended adoption of PNSC strategies for more reliable protection coordination.

6 Conclusions

GFM controls are considered an avenue of solution to accommodate high-penetration IBRs. The thesis investigates the performance of GFM-IBRs under unbalanced grid conditions and proposes transient and FRT control solutions for enhancing system protection and stability.

To clarify the performance of IBRs in negative sequence systems, dynamic and static negative sequence models of GFM-IBRs are proposed for understanding and mitigating their negative-sequence behavior. Comparative studies on the negative sequence behavior of GFL- and GFM-IBRs with BPSC and PNSC are performed in a modified IEEE PSRC D29 system.

To enhance the FRT capability of GFM-IBRs, enhanced CS-based and VI-based CLMs are developed for grid code compliance. Asymmetrical FRT control solutions for GFM Type-IV and Type-III WTGs are proposed and validated using EPRI benchmark system.

For rapid and accurate short-circuit analysis in IBR-rich systems, phasor domain short circuit models of GFL- and GFM-IBRs are developed considering diverse FRT solutions. In an IEEE 39 bus system integrated with multi IBRs, the proposed short-circuit model accurately estimates the current contribution and voltage support capability under steady-state fault conditions by using Newton-based iterative solver.

To study the impacts of GFM-IBRs on protection elements, the performance of distance protection and negative sequence components-based protection is explored in systems with GFM-IBRs under various FRT solutions and fault scenarios.

Key conclusions of this thesis are summarized as follows:

I) For GFL-BPSC, the magnitude and angle of negative sequence impedance are primarily determined by the phase shift in measurement filters, leading to GFL inverter being an open circuit approximation in the negative sequence network. For GFM-BPSC, the magnitude and angle of negative sequence impedance are influenced by inner voltage control parameters. Consequently, GFM-BPSC exhibits significant limitations including current distortion and high sensitivity to inner control parameters, current limits, and fault proximity. The 2ω negative-sequence components induce undesirable oscillations across various frequencies, substantially degrading system dynamic performance. From internal oscillatory mode studies, the adoption of supplementary negative-sequence controls in GFM-IBRs to enhance control damping. Furthermore, FRT compliance cannot be guaranteed for all conditions with BPSC due to the constraints on inner controller tuning. PNSC strategies are strongly recommended as they enable independent control of sequence components and optimal utilization of converter capacity through current scaling, providing more reliable FRT compliance without compromising stability.

II) For full converter-based GFM-IBR, the CS-based CLM enables GFM-IBRs to provide optimal I1R and I2R injections, fully utilize current capacity by using current scaling methods, and emulate the negative sequence behavior of SGs during unbalanced faults. The adaptive VI-based CLM updates the positive sequence internal voltage vectors to retain inner voltage dynamics and achieves optimal utilization of current capacity via adaptive decoupled-sequence current limits. Voltages and currents can stabilize in less than two cycles after fault inception. For GFM Type-IV WTGs, the proposed

synchronization loop reduces the complexity of multiple parameter design and demonstrates robustness under asymmetrical grid conditions. In restricted mode, the VSL addresses imbalance between the wind turbine power output and the grid power demand, preventing the divergence of DC-link components. Compared with the GFL-WTG employing DDSRF-PLL, the proposed GFM synchronization control converges quickly without notable overshoot, enhancing frequency ride-through. During asymmetrical faults, the reactive current injection and the current scaling method maximize voltage support capabilities of WTGs, fulfilling overvoltage/undervoltage ride-through requirements. Following fault clearance, the VI-based CLM effectively eliminates current transients, preventing overcurrent issues during the transition process, thus improving the dynamic performance of WTG restoration and the safety of converter devices.

III) For GFM-DFIG, the internal voltage vectors are determined by the current reference generation. The CS-based and VI-based CLMs significantly influence the positive-sequence internal voltage vectors, while the negative-sequence internal voltage vectors are identical by using the same I2R injection method. The negative-sequence WTG current leads the negative-sequence stator voltage by 90-95 degrees, achieving the required negative-sequence behavior during asymmetrical faults. The proposed control scheme enables the GFM-DFIG to meet the LVRT requirements during the asymmetrical and symmetrical faults. In addition, the GFM-DFIG effectively meets the rotor current capacity, decreases transient components, and maintains the rotor line voltage lower than the DC voltage under steady state fault conditions, thus addressing the overcurrent and overmodulation issues. The CS-based CLM exhibits great capability in supporting the positive-sequence internal voltage vectors due to the I1R injection, while the I1R injection under the VI-based CLM cannot be guaranteed since it is regulated by adjusting the virtual voltage references. Compared to the CS-based CLM, the VI-based CLM exhibits better performance in reducing electromagnetic stress and rotor voltage demand and optimizing rotor current capacity.

IV) In large-scale IBR-rich power systems, with the CS-based CLM, the current contribution of IBRs is determined by their FRT strategies. With the VI-based CLM, the current injection of IBRs is determined by the equivalent voltage and impedance of IBRs and AC systems. From the comparative studies on these FRT strategies, the IEEE 2800 compliant limiter fully utilizes converter current capacity, and the VI-based limiter enhances the voltage support capability. The proposed short-circuit models enable protection engineers to efficiently analyze short-circuit behavior in IBR-integrated systems, support FRT strategy development, and conduct comprehensive protective relaying studies.

V) In distance protection studies, the variation in current contributions from different sources (SGs and IBRs) leads to discrepancies in apparent impedances. In actual GFM mode, the inner control parameters may adversely affect the negative sequence behaviour, thus reducing the protection's sensitivity. In restricted mode, the current limit and FRT solutions determine the magnitude and angle of current references, which in turn changes the apparent impedance and ultimately impacts the protection outcomes. The phase current scaling method in the IEEE 2800-conforming scheme FRT scheme weakens the impacts of fault resistance on apparent impedance trajectory, also causes an oscillation in waveforms when the K factor is large, increasing the settling time. Consequently, the trajectory of apparent impedance shifts up as the K factor increases, decreasing the speed of distance protection. Hence, the

selection of K factors should be based on the converter current capacity to meet the dynamic performance requirement in IEEE 2800 and improve the speed of distance protection.

VI) In negative sequence components-based protection studies, maloperation issues of 50Q, 67QF, 67QR, and incorrect faulted phase selection are found under GFL-BPSC. The proposed FRT control solutions in GFM-BPSC, GFL-PNSC, and GFM-PNSC address these issues for the test case. Given the limitations of BPSC approaches, future work should focus on advancing PNSC strategies to ensure reliable IEEE 2800 compliance and asymmetrical FRT enhancement across varied operational conditions. The pickup settings of future protection schemes should consider both the limited current contribution of IBRs and the recommended adoption of PNSC strategies for more reliable protection coordination.

Future works may include:

a) Small-signal stability analysis:

2ω oscillations are present in control systems due to voltage and current unbalance. Although control solutions (e.g. sequence decomposition methods and negative-sequence controls) were proposed to improve system dynamics (small-signal stability) of GFM-IBRs in unbalanced grids, the following topics are rarely discussed: System-level dynamics analysis of an unbalanced system with multiple GFM-IBRs, e.g., impacts of CS-based and VI-based CLMs and current coordination methods on IBR-rich system dynamics. Control solutions for IEEE 2800 dynamic performance compliance (e.g., step response time and settling time).

b) Enhanced protection scheme for IBR-rich systems:

To improve the performance of legacy protection systems, develop novel protection algorithms and control solutions near GFM-BPSC and GFM-PNSC for system-wide coordination. Investigate the impacts on system frequency and frequency protection in unbalanced grids, such as under-frequency load shedding and rate of change of frequency protection, ensuring compliance with primary frequency response (PFR) and fast frequency response (FFR) requirements

c) Transient stability analysis:

Solutions for enhancing transient stability focus on addressing the loss of synchronism in GFM-IBRs when operating in restricted modes. However, these solutions often overlook synchronization with the negative sequence system. There is a need for further development of robust PSL-PLL switching methods for GFM-IBRs with simple implementation to achieve effective synchronization in unbalanced grids. Additionally, the capability of GFM-IBRs to maintain the DC voltage level and eliminate DC-link oscillations during unbalanced faults has not been thoroughly investigated. To improve transient stability analysis, it is important to develop advanced unbalanced models of GFM-IBRs that strike a balance between accuracy and simplicity. This would help reduce the computational burden of transient stability analysis

7 Appendix

TABLE A1

IEEE PSRC D29 system parameters

Category	Physical meaning	Parameter
WTG	Aggregated number	100
	Rated power for a unit IBR	1 MVA
	DC voltage	2450 V
	DC capacitor	15 kJ/MVA
	Choke resistance/ inductance	0.01 pu/ 0.15 pu
	Filter reactive power	25 KVAR
	Active power commander	75 MW
WP transformer	Ratio	120 kV/ 35 kV
	Nominal power	210 MVA
	Impedance	0.0027+j0.08 pu
Relay Measurement	VT ratio,	115000:115
	CT ratio	500:5
50Q	I2 threshold	0.2 pu
67Q	Rated current	500 A
	Directional element characteristic angle	80°
	Forward and reverse limit angle	85°
	Overcurrent thresholds	0.1 A
FID	Characteristic angle	50°

TABLE A2

EPRI benchmark system parameters

Category	Physical meaning	Parameter
Transmission line	Positive/zero sequence resistance	0.028/0.1 Ω
	Positive/zero sequence inductance	0.325/1.0 Ω
	Positive/zero sequence capacitance	4.9575/2.8245 μS
WTG	Aggregated number	75
	Rated power for a unit IBR	1 MVA
	DC voltage	2450 V
	DC capacitor	15 kJ/MVA
	Choke resistance/ inductance	0.01 pu/ 0.15 pu
	Filter reactive power	25 kVAR
	Active power commander	75 MW
WTG control	VSM control (J / D_ω)	0.15/0.8038
	droop control (D_P)	0.0033
	dVOC (κ_1)	0.0033
	VSL (ξ_ω / $\xi_{\Delta\omega}$)	0.707 / 0.1
	PI parameters (DDSRF-PLL)	0.27, 1
	PI parameters (inner current)	1.02, 79.03
	PI parameters (inner voltage)	1, 200
	PI parameters (virtual impedance)	0.2, 65
	K factor	3
	Virtual impedance ratio	1
WP transformer	Ratio	120 kV/ 35 kV
	Nominal power	210 MVA
	Impedance	0.0027+j0.08 pu

8 References

[1] J. Zheng, J. Du, B. Wang, J. J. Klemeš, Q. Liao, and Y. Liang, "A hybrid framework for forecasting power generation of multiple renewable energy sources," *Renewable and Sustainable Energy Reviews,* vol. 172, p. 113046, 2023.

[2] Y. Lin, J.H. Eto, B.B. Johnson *et al*. "Research roadmap on grid-forming inverters,". National Renewable Energy Lab., Golden, CO (United States), NREL/TP-5D00-73476, 2020.

[3] J. Hou, C. Hu, S. Lei, L. Liang, and Y. Hou, "Security region of inverter-interfaced power systems: Existence, expansion, and application," *Renewable and Sustainable Energy Reviews,* vol. 192, p. 114222, 2024.

[4] R. Musca, A. Vasile, G. Zizzo, "Grid-forming converters. A critical review of pilot projects and demonstrators," *Renewable and Sustainable Energy Reviews*, Vol. 165, 2022.

[5] Y. Li, Y. Gu, and T. C. Green, "Revisiting Grid-Forming and Grid-Following Inverters: A Duality Theory," *IEEE Trans. Power Syst.,* vol. 37, no. 6, pp. 4541-4554, 2022.

[6] K. Strunz, K. Almunem, C. Wulkow, M. Kuschke, M. Valescudero, and X. Guillaud, "Enabling 100% Renewable Power Systems Through Power Electronic Grid-Forming Converter and Control: System Integration for Security, Stability, and Application to Europe," *Proceedings of the IEEE,* vol. 111, no. 7, pp. 891-915, 2023.

[7] R. H. Lasseter, Z. Chen, and D. Pattabiraman, "Grid-Forming Inverters: A Critical Asset for the Power Grid," *IEEE Trans. Emerg. Sel. Topics Power Electron.,* vol. 8, no. 2, pp. 925-935, 2020.

[8] Z. Pan, N. Jenkins, and J. Wu, "Black start from renewable energy resources: Review and a case study of Great Britain," *Renewable and Sustainable Energy Reviews,* vol. 209, p. 115143, 2025.

[9] A. Tayyebi, D. Groß, A. Anta *et al*. "Frequency Stability of Synchronous Machines and Grid-Forming Power Converters," *IEEE Journal of Emerging and Selected Topics in Power Electronics*, vol. 8, pp. 1004-1018, Jun. 2020.

[10] D. B. Rathnayake *et al.*, "Grid Forming Inverter Modeling, Control, and Applications," *IEEE Access,* vol. 9, pp. 114781-114807, 2021.

[11] V. Gevorgian, S. Shah, W. Yan, and G. Henderson, "Grid-Forming Wind: Getting ready for prime time, with or without inverters," *IEEE Electrification Magazine,* vol. 10, no. 1, pp. 52-64, 2022.

[12] H. Zhang, W. Xiang, W. Lin, and J. Wen, "Grid Forming Converters in Renewable Energy Sources Dominated Power Grid: Control Strategy, Stability, Application, and Challenges," *Journal of Modern Power Systems and Clean Energy,* vol. 9, no. 6, pp. 1239-1256, 2021.

[13] *IEEE Standard for Interconnection and Interoperability of Inverter-Based Resources (IBRs) Interconnecting with Associated Transmission Electric Power Systems*, IEEE Standard 2800-2022, Apr. 2022.

[14] Y. Chang, I. Kocar, J. Hu, U. Karaagac, K. Wing Chan, and a. Jean Mahseredjian, "Coordinated Control of DFIG Converters to Comply with Reactive Current Requirements in Emerging Grid Codes," *Journal of Modern Power Systems and Clean Energy,* vol. 10, no. 2, pp. 502-514, 2022.

[15] Y. Li, L. Fu, Q. Li *et al.*, "Small-signal modelling and stability analysis of grid-following and grid-forming inverters dominated power system," *Global Energy Interconnection*, vol. 6, no. 3, pp. 363-374, 2023.

[16] A. Singh, V. Debusschere, N. Hadjsaid *et al.*, "Slow-Interaction Converter-Driven Stability in the Distribution Grid: Small-Signal Stability Analysis With Grid-Following and Grid-Forming Inverters," *IEEE Trans. Power Syst.*, vol. 39, no. 2, pp. 4521-4536, 2024.

[17] R. Pan, D. Liu, S. Liu *et al.*, "Stability Comparison Between Grid-forming and Grid-following Based Wind Farms Integrated MMC-HVDC," *Journal of Modern Power Systems and Clean Energy*, vol. 11, no. 4, pp. 1341-1355, 2023.

[18] C. Yang, L. Huang, H. Xin *et al.*, "Placing Grid-Forming Converters to Enhance Small Signal Stability of PLL-Integrated Power Systems," *IEEE Trans. Power Syst.*, vol. 36, no. 4, pp. 3563-3573, 2021.

[19] U. Markovic, O. Stanojev, P. Aristidou *et al.*, "Understanding Small-Signal Stability of Low-Inertia Systems," *IEEE Trans. Power Syst.*, vol. 36, no. 5, pp. 3997-4017, 2021.

[20] H. Wu and X. Wang, "Small-Signal Modeling and Controller Parameters Tuning of Grid-Forming VSCs With Adaptive Virtual Impedance-Based Current Limitation," *IEEE Trans. Power Electron.*, vol. 37, no. 6, pp. 7185-7199, 2022.

[21] J. Yu, Y. Qi, H. Deng, X. Liu *et al.*, "Evaluating Small-Signal Synchronization Stability of Grid-Forming Converter: A Geometrical Approach," *IEEE Trans. Ind. Electron.*, vol. 69, no. 9, pp. 9087-9098, 2022.

[22] P. Liu, X. Xie, and J. Shair, "Adaptive Hybrid Grid-Forming and Grid-Following Control of IBRs with Enhanced Small-

Signal Stability under Varying SCRs," *IEEE Trans. Power Electron.*, pp. 1-5, 2024.

[23] F. Zhao, X. Wang, and T. Zhu, "Power Dynamic Decoupling Control of Grid-Forming Converter in Stiff Grid," *IEEE Trans. Power Electron.*, vol. 37, no. 8, pp. 9073-9088, 2022.

[24] L. Zhao, Z. Jin, and X. Wang, "Small-Signal Synchronization Stability of Grid-Forming Converters With Regulated DC-Link Dynamics," *IEEE Trans. Ind. Electron.*, vol. 70, no. 12, pp. 12399-12409, 2023.

[25] D. A. Aragon, E. Unamuno, S. Ceballos *et al.*, "Comparative small-signal evaluation of advanced grid-forming control techniques," *Electric Power Systems Research*, vol. 211, p. 108154, 2022.

[26] S. Eberlein and K. Rudion, "Impact of Inner Control Loops on Small-Signal Stability and Model-Order Reduction of Grid-Forming Converters," *IEEE Trans. Smart Grid*, vol. 14, no. 4, pp. 2812-2824, 2023.

[27] M. H. Ravanji, D. B. Rathnayake, M. Z. Mansour *et al.*, "Impact of Voltage-Loop Feedforward Terms on the Stability of Grid-Forming Inverters and Remedial Actions," *IEEE Trans. Energy Convers.*, vol. 38, no. 3, pp. 1554-1565, 2023.

[28] J. Liu, Y. Xia, W. Wei *et al.*, "Effect of Control Damping on Small-Signal Stability of Grid-Forming VSCs Considering Interaction Between Inner and Outer Loops," *IEEE Trans. Power Electron.*, pp. 1-10, 2024.

[29] J. Yu, S. Wang, Z. Liu *et al.*, "Accurate Small-Signal Terminal Characteristic Model and SISO Stability Analysis Approach for Parallel Grid-Forming Inverters in Islanded Microgrids," *IEEE Trans. Power Electron.*, vol. 38, no. 5, pp. 6597-6612, 2023.

[30] Z. Zhao *et al.*, "Decentralized Grid-Forming Control Strategy and Dynamic Characteristics Analysis of High-Penetration Wind Power Microgrids," *IEEE Trans. Sustain. Energy*, vol. 13, no. 4, pp. 2211-2225, 2022.

[31] Z. Yang, W. Liao, Q. Zhang *et al.* "Fault Coordination Control for Converter-Interfaced Sources Compatible With Distance Protection During Asymmetrical Faults," *IEEE Trans. Industrial Electronics*, vol. 70, pp. 6941-6952, Jul. 2023.

[32] B. Mahamedi and J. E. Fletcher, "The Equivalent Models of Grid-Forming Inverters in the Sequence Domain for the Steady-State Analysis of Power Systems," *IEEE Trans. Power Systems*, vol. 35, pp. 2876-2887, Jul. 2020.

[33] M. A. Awal, S. Cen, M. R. K. Rachi *et al.*, "Modeling, Analysis, and Design for Small-Signal Stability in Sequence-Decomposed Grid-Forming Control," *IEEE Trans. Ind. Appl.*, vol. 60, no. 1, pp. 865-875, 2024.

[34] S. J. Yague, A. Garcia-Cerrada, and P. Palacin Farre, "Comparison Between Modal Analysis and Impedance-based Methods for Analysing Stability of Unbalanced Microgrids with Grid-forming Electronic Power Converters," *Journal of Modern Power Systems and Clean Energy*, vol. 11, no. 4, pp. 1269-1281, 2023.

[35] P. J. Hart, J. Goldman, R. H. Lasseter, and T. M. Jahns, "Impact of Harmonics and Unbalance on the Dynamics of Grid-Forming, Frequency-Droop-Controlled Inverters," *IEEE Journal of Emerg. Sel. Topics Power Electron.,* vol. 8, no. 2, pp. 976-990, 2020.

[36] P. Sun, Z. Tian, M. Huang, *et al.*, "Additional Kinetic Energy Injection and Piecewise Damping Based Postfault Anti-Windup and Transient Stability Enhanced Control for Grid-Forming Inverter," *IEEE Trans. Power Electron.,* pp. 1-15, 2024.

[37] X. Wang, M. G. Taul, H. Wu, Y. Liao, F. Blaabjerg, and L. Harnefors, "Grid-Synchronization Stability of Converter-Based Resources—An Overview," *IEEE Open Journal of Industry Applications,* vol. 1, pp. 115-134, 2020.

[38] H. Xiao, H. He, L. Zhang, and T. Liu, "Adaptive Grid-Synchronization Based Grid-Forming Control for Voltage Source Converters," *IEEE Trans. Power Syst.*, vol. 39, no. 2, pp. 4763-4766, 2024.

[39] D. S. d. S. Andrade, Y. N. Batista, F. A. S. Neves, and H. E. P. d. Souza, "Fast Phase Angle Jump Estimation to Improve the Convergence Time of the GDSC-PLL," *IEEE Trans. Ind. Electron.,* vol. 67, no. 4, pp. 2852-2862, 2020.

[40] H. Wu, X. Wang, and L. Zhao, "Design Considerations of Current-Limiting Control for Grid-Forming Capability Enhancement of VSCs under Large Grid Disturbances," *IEEE Trans. Power Electron.*, pp. 1-5, 2024.

[41] L. Harnefors, J. Kukkola, M. Routimo, M. Hinkkanen, and X. Wang, "A Universal Controller for Grid-Connected Voltage-Source Converters," *IEEE Trans. Emerg. Sel. Topics Power Electron.*, vol. 9, no. 5, pp. 5761-5770, 2021.

[42] H. Xiao, H. He, L. Zhang, and T. Liu, "Adaptive Grid-Synchronization Based Grid-Forming Control for Voltage Source Converters," *IEEE Trans. Power Syst.*, vol. 39, no. 2, pp. 4763-4766, 2024.

[43] P. Liu, X. Xie, and J. Shair, "Adaptive Hybrid Grid-Forming and Grid-Following Control of IBRs with Enhanced Small-Signal Stability under Varying SCRs," *IEEE Trans. Power Electron.*, pp. 1-5, 2024.

[44] L. A. M. Lima and E. H. Watanabe, "Hybrid Control Scheme for VSC Presenting Both Grid-Forming and Grid-Following Capabilities," *IEEE Trans. Power Del.*, vol. 37, no. 6, pp. 4570-4581, 2022.

[45] M. Schweizer, S. Almer, S. Pettersson, A. Merkert, V. Bergemann, and L. Harnefors, "Grid-Forming Vector Current Control," *IEEE Trans. Power Electron.,* vol. 37, no. 11, pp. 13091-13106, 2022.

[46] L. Huang, C. Wu, D. Zhou, and F. Blaabjerg, “A Power-Angle-Based Adaptive Overcurrent Protection Scheme for Grid-Forming Inverter Under Large Grid Disturbances,” *IEEE Trans. Ind. Electron.*, vol. 70, no. 6, pp. 5927-5936, 2023.

[47] Y. Zhang, C. Zhang, M. Molinas, and X. Cai, “Control of Virtual Synchronous Generator with Improved Transient Angle Stability Under Symmetric and Asymmetric Short Circuit Fault,” *IEEE Trans. Energy Convers.*, pp. 1-18, 2024.

[48] S. P. Me et al., “Transient Stability Analysis of Virtual Synchronous Generator Equipped With Quadrature-Prioritized Current Limiter,” *IEEE Trans. Power Electron.*, vol. 38, no. 9, pp. 10547-10553, 2023.

[49] X. Zhao and D. Flynn, “Stability enhancement strategies for a 100% grid-forming and grid-following converter-based Irish power system,” *IET Renewable Power Generation*, vol. 16, no. 1, pp. 125-138, 2021.

[50] M. G. Taul, X. Wang, P. Davari, and F. Blaabjerg, “Current Limiting Control With Enhanced Dynamics of Grid-Forming Converters During Fault Conditions,” *IEEE Trans. Emerg. Sel. Topics Power Electron.*, vol. 8, no. 2, pp. 1062-1073, 2020.

[51] S. Jiang, Y. Zhu, T. Xu, and G. Konstantinou, “Current-Synchronization Control of Grid-Forming Converters for Fault Current Limiting and Enhanced Synchronization Stability,” *IEEE Trans. Power Electron.*, vol. 39, no. 5, pp. 5271-5285, 2024.

[52] L. Harnefors, M. Schweizer, J. Kukkola, M. Routimo, M. Hinkkanen, and X. Wang, "Generic PLL-Based Grid-Forming Control," *IEEE Trans. Power Electron.,* pp. 1-1, 2021.

[53] X. Tian, Y. Chi, P. Cheng, W. He, Y. Zhou, and J. Hu, "Dual-mode Switching Fault Ride-through Control Strategy for Self-synchronous Wind Turbines," *Journal of Modern Power Systems and Clean Energy*, vol. 11, no. 2, pp. 553-566, 2023.

[54] X. Yuan et al., "Two-Stage Coordinated Control of Type-4 Wind Turbine With Grid-Forming Ability for Active Damping Support," *IEEE Trans. Energy Convers.*, vol. 39, no. 2, pp. 817-830, 2024.

[55] S. Silwal, M. Karimi-Ghartemani, H. Karimi, M. Davari, and S. M. H. Zadeh, "A Multivariable Controller in Synchronous Frame Integrating Phase-Locked Loop to Enhance Performance of Three-Phase Grid-Connected Inverters in Weak Grids," *IEEE Trans. Power Electron.*, vol. 37, no. 9, pp. 10348-10359, 2022.

[56] G. Dupré, H. Karimi, M. Karimi-Ghartemani, L. Saydy, and S. M. Hoseinizadeh, "An Observer-Based Multivariable Controller for Improved Performance of Voltage Source Converters With LCL Filter Connected to Unbalanced Grid," *IEEE Trans. Ind. Appl.,* pp. 1-12, 2023.

[57] X. Lyu and D. Groß, "Grid Forming Fast Frequency Response for PMSG-Based Wind Turbines," *IEEE Trans. Sustain. Energy*, vol. 15, no. 1, pp. 23-38, 2024.

[58] A. Haddadi, I. Kocar, J. Mahseredjian *et al.*, "Negative sequence quantities-based protection under inverter-based resources Challenges and impact of the German grid code," *Electric Power Systems Research,* vol. 188, 2020.

[59] A. Azizi, A. Banaiemoqadam, A. Hooshyar *et al.*, "A Blind Spot in the LVRT Current Requirements of Modern Grid Codes for Inverter-Based Resources," *IEEE Trans. Power Del.,* vol. 38, no. 1, pp. 319-334, 2023.

[60] P. Rodriguez, J. Pou, J. Bergas *et al.*,"Decoupled Double Synchronous Reference Frame PLL for Power Converters Control," *IEEE Trans. Power Electron.,* vol. 22, no. 2, pp. 584-592, 2007.

[61] C. Fang, L. Mu, Z. Wang *et al.*, "Analysis of Grid-Forming IIDG’s Transient- and Steady-State Fault Model," *IEEE Trans. Smart Grid,* vol. 13, no. 2, pp. 1187-1199, 2022.

[62] A. Borrell, M. Velasco, M. Castilla *et al.*, "Collaborative Voltage Unbalance Compensation in Islanded AC Microgrids With Grid-Forming Inverters," *IEEE Trans. Power Electron.,* vol. 37, no. 9, pp. 10499-10513, 2022.

[63] A. Haddadi, M. Zhao, I. Kocar *et al.*, "Impact of Inverter-Based Resources on Negative Sequence Quantities-Based Protection Elements," *IEEE Trans. Power Del.,* vol. 36, no. 1, pp. 289-298, 2021.

[64] J. Andruszkiewicz, J. Lorenc, B. Staszak *et al.*, "Overcurrent protection against multi-phase faults in MV networks based on negative and zero sequence criteria," *International Journal of Electrical Power & Energy Systems,* vol. 134, 2022.

[65] Y. Chang, M. Zhao, and I. Kocar, "The impact of DFIG control schemes on the negative-sequence based differential protection," *Electric Power Systems Research,* vol. 211, 2022.

[66] Y. Liang, W. Li, and Z. Lu, "Effect of Inverter-Interfaced Renewable Energy Power Plants on Negative-Sequence Directional Relays and a Solution," *IEEE Trans. Power Del.,* vol. 36, no. 2, pp. 554-565, 2021.

[67] A. Jalilian, K. Muttaqi, D. Sutanto, and D. Robinson, "Distance Protection of Transmission Lines in Presence of Inverter-Based Resources: A New Earth Fault Detection Scheme During Asymmetrical Power Swings," *IEEE Trans. Ind. Appl.,* vol. 58, no. 2, pp. 1899-1909, 2022.

[68] B. Kasztenny and D. Finney, "Fundamentals of Distance Protection," presented at the 2008 61st Annual Conference for Protective Relay Engineers, 2008.

[69] S. F. Zarei, H. Mokhtari, M. A. Ghasemi, and F. Blaabjerg, "Reinforcing Fault Ride Through Capability of Grid Forming Voltage Source Converters Using an Enhanced Voltage Control Scheme," *IEEE Trans. Power Del.,* vol. 34, no. 5, pp. 1827-1842, 2019.

[70] D. Ríos-Castro, D. Pérez-Estévez, and J. Doval-Gandoy, "Grid-Connected Converter With Grid-Forming and Grid-Following Modes Presenting Symmetrical and Asymmetrical Fault Ride-Through Capability," *IEEE Trans. Emerg. Sel. Topics Power Electron.,* pp. 1-1, 2024.

[71] A. Banaiemoqadam, A. Azizi, A. Hooshyar, M. Kanabar, and E. F. El-Saadany, "Impact of Inverter-Based Resources on Different Implementation Methods for Distance Relays—Part I: Phase Comparators," *IEEE Trans. Power Del.,* vol. 38, no. 6, pp. 4090-4102, 2023.

[72] A. Banaiemoqadam, A. Azizi, A. Hooshyar, and E. F. El-Saadany, "Impact of Inverter-Based Resources on Different Implementation Methods for Distance Relays—Part II: Reactance Method," *IEEE Trans. Power Del.,* vol. 38, no. 6, pp. 4049-4060, 2023.

[73] A. Haddadi, I. Kocar, U. Karaagac, H. Gras, and E. Farantatos, "Impact of Wind Generation on Power Swing Protection," *IEEE Trans. Power Del.*, vol. 34, no. 3, pp. 1118-1128, 2019.

[74] A. Haddadi, M. Zhao, I. Kocar, E. Farantatos, and F. Martinez, "Impact of Inverter-Based Resources on Memory-Polarized Distance and Directional Protective Relay Elements," in 2020 52nd North American Power Symposium (NAPS), 11-13 April 2021 2021, pp. 1-6.

[75] A. Haddadi, I. Kocar, J. Mahseredjian, U. Karaagac, and E. Farantatos, "Performance of Phase Comparison Line Protection Under Inverter-Based Resources and Impact of the German Grid Code," in 2020 IEEE Power & Energy Society General Meeting (PESGM), 2-6 Aug. 2020 2020, pp. 1-5.

[76] C. Chao, X. Zheng, Y. Weng, Y. Liu, P. Gao, and N. Tai, "Adaptive Distance Protection Based on the Analytical Model of Additional Impedance for Inverter-Interfaced Renewable Power Plants During Asymmetrical Faults," *IEEE Trans. Power Del.,* vol. 37, no. 5, pp. 3823-3834, 2022.

[77] P. Mishra, A. K. Pradhan, and P. Bajpai, "Adaptive Distance Relaying for Distribution Lines Connecting Inverter-Interfaced Solar PV Plant," *IEEE Trans. Ind. Electron.,* vol. 68, no. 3, pp. 2300-2309, 2021.

[78] A. Banaiemoqadam, A. Hooshyar, and M. A. Azzouz, "A Control-Based Solution for Distance Protection of Lines Connected to Converter-Interfaced Sources During Asymmetrical Faults," *IEEE Trans. Power Del.,* vol. 35, no. 3, pp. 1455-1466, 2020.

[79] A. Banaiemoqadam, A. Hooshyar, and M. A. Azzouz, "A Comprehensive Dual Current Control Scheme for Inverter-Based Resources to Enable Correct Operation of Protective Relays," *IEEE Trans. Power Del.,* vol. 36, no. 5, pp. 2715-2729, 2021.

[80] N. Baeckeland, D. Venkatramanan, S. Dhople, and M. Kleemann, "On the Distance Protection of Power Grids dominated by Grid-forming Inverters," in *2022 IEEE PES Innovative Smart Grid Technologies Conference Europe (ISGT-Europe)*, 2022, pp. 1-6, doi: 10.1109/ISGT-Europe54678.2022.9960410.

[81] D. Liu, Q. Hong, Md. A. U. Khan, *et.al.*, "Evaluation of grid-forming converters impact on distance protection performance," in *16th International Conference on Developments in Power System Protection (DPSP 2022), Hybrid Conference*, Newcastle, UK, 2022, pp. 285-290.

[82] Y. Xiong, H. Wu, and X. Wang, "Efficacy analysis of legacy dual-blinder-based power swing detection scheme in grid-forming VSC-based power system," presented at the 22nd Wind and Solar Integration Workshop (WIW 2023), 2023.

[83] Technische Regeln den Anschluss von Kundenanlagen an das Hochspannungsnetz und Deren Betrieb (TAR Hochspannung), VDE-AR-N 4120 Anwendungsregel, Oct. 2018.

[84] K.-H. Kim, Y.-C. Jeung, D.-C. Lee, and H.-G. Kim, "LVRT Scheme of PMSG Wind Power Systems Based on Feedback Linearization," *IEEE Trans. Power Electron.*, vol. 27, no. 5, pp. 2376-2384, 2012.

[85] NERC Reliability Standard PRC-024-2 – Generator Frequency and Voltage Protective Relay Settings. [Online] Available: https://www.nerc.com/_layouts/15/PrintStandard.aspx?standardnumber=PRC-024-2&title=Generator%20Frequency%20and%20Voltage%2 0Protective%20Relay%20Settings&jurisdiction=United States

[86] "IEEE Standard for Interconnection and Interoperability of Distributed Energy Resources with Associated Electric Power Systems Interfaces," *IEEE Std 1547-2018 (Revision of IEEE Std 1547-2003),* pp. 1-138, 2018.

[87] E. Afshari, G. R. Moradi, R. Rahimi, B. Farhangi, Y. Yang, F. Blaabjerg, and S. Farhangi, "Control Strategy for Three-Phase Grid-Connected PV Inverters Enabling Current Limitation Under Unbalanced Faults," *IEEE Trans. Industrial Electronics*, vol. 64, no. 11, pp. 8908–8918, 2017.

[88] M. Ciobotaru, R. Teodorescu, and F. Blaabjerg, "A new single-phase PLL structure based on second order generalized

integrator," in 2006 37th IEEE Power Electronics Specialists Conference, 2006, pp. 1–6.

[89] D. Yazdani, A. Bakhshai, and P. K. Jain, "A Three-Phase Adaptive Notch Filter-Based Approach to Harmonic/Reactive Current Extraction and Harmonic Decomposition," *IEEE Trans. Power Electronics*, vol. 25, no. 4, pp. 914–923, 2010.

[90] S. Golestan, M. Ramezani, J. M. Guerrero, and M. Monfared, "dq-Frame Cascaded Delayed Signal Cancellation- Based PLL: Analysis, Design, and Comparison With Moving Average Filter-Based PLL," *IEEE Trans. Power Electronics*, vol. 30, no. 3, pp. 1618–1632, 2015.

[91] M. A. Awal, M. R. K. Rachi, H. Yu, S. Schroder, and I. Husain, "Symmetrical Components Extraction for Grid-Forming Voltage Source Converters," presented at the 2022 IEEE Energy Conversion Congress and Exposition (ECCE), 2022.

[92] B. Fan, T. Liu, F. Zhao, H. Wu, and X. Wang, "A Review of Current-Limiting Control of Grid-Forming Inverters Under Symmetrical Disturbances," *IEEE Open Journal of Power Electronics,* vol. 3, pp. 955-969, 2022.

[93] T. Liu, X. Wang, F. Liu, K. Xin, and Y. Liu, "A Current Limiting Method for Single-Loop Voltage-Magnitude Controlled Grid-Forming Converters During Symmetrical Faults," *IEEE Trans. Power Electron.,* vol. 37, no. 4, pp. 4751-4763, 2022.

[94] D. Ríos-Castro, D. Pérez-Estévez, and J. Doval-Gandoy, "Grid-Connected Converter With Grid-Forming and Grid-Following Modes Presenting Symmetrical and Asymmetrical Fault Ride-Through Capability," *IEEE Trans. Emerg. Sel. Topics Power Electron.,* pp. 1-1, 2024.

[95] B. Fan and X. Wang, "Fault Recovery Analysis of Grid-Forming Inverters With Priority-Based Current Limiters," *IEEE Trans. Power Syst.,* vol. 38, no. 6, pp. 5102-5112, 2023.

[96] N. Baeckeland, D. Chatterjee, M. Lu, B. Johnson, and G.-S. Seo, "Overcurrent Limiting in Grid-Forming Inverters: A Comprehensive Review and Discussion," *IEEE Trans. Power Electron.,* pp. 1-26, 2024.

[97] A. Ordono, A. Sanchez-Ruiz, M. Zubiaga, F. J. Asensio, and J. A. Cortajarena, "Current limiting strategies for grid forming inverters under low voltage ride through," *Renewable and Sustainable Energy Reviews,* vol. 202, 2024.

[98] A. Pal, D. Pal, and B. K. Panigrahi, "A Current Saturation Strategy for Enhancing the Low Voltage Ride-Through Capability of Grid-Forming Inverters," *IEEE Transactions on Circuits and Systems II: Express Briefs,* vol. 70, no. 3, pp. 1009-1013, 2023.

[99] B. Fan and X. Wang, "Equivalent Circuit Model of Grid-Forming Converters With Circular Current Limiter for Transient Stability Analysis," *IEEE Trans. Power Syst.*, vol. 37, no. 4, pp. 3141-3144, 2022

[100] E. Rokrok, T. Qoria, A. Bruyere, B. Francois, and X. Guillaud, "Transient Stability Assessment and Enhancement of Grid-Forming Converters Embedding Current Reference Saturation as Current Limiting Strategy," *IEEE Trans. Power Syst.*, vol. 37, no. 2, pp. 1519-1531, 2022.

[101] G. Wang, L. Fu, Q. Hu, C. Liu, and Y. Ma, "Transient Synchronization Stability of Grid-Forming Converter During Grid Fault Considering Transient Switched Operation Mode," *IEEE Trans. Sustain. Energy*, vol. 14, no. 3, pp. 1504-1515, 2023.

[102] M. A. Nasr and A. Hooshyar, "Controlling Grid-Forming Inverters to Meet the Negative-Sequence Current Requirements of the IEEE Standard 2800-2022," *IEEE Transactions on Power Delivery*, vol. 38, pp. 2541-2555, Aug. 2023.

[103] A. Azizi and A. Hooshyar, "Fault Current Limiting and Grid Code Compliance for Grid-Forming Inverters—Part II: Solution," *IEEE Trans. Sustain. Energy,* pp. 1-17, 2024.

[104] A. D. Paquette and D. M. Divan, "Virtual Impedance Current Limiting for Inverters in Microgrids With Synchronous Generators," in *IEEE Trans. Ind. Appl*., vol. 51, no. 2, pp. 1630-1638, March-April 2015.

[105] Y. Wang, Y. Kuang and Q. Xu, "A Current-Limiting Scheme for Voltage-Controlled Inverter Using Instantaneous Current to Generate Virtual Impedance," in *IEEE J. Em. Sel. Top. C. Syst.*, vol. 13, no. 2, pp. 524-535, June 2023.

[106] Y. Liu, J. Meng, Y. Wang, J. Wang, R. Liang and Z. Zhang, "Adaptive Virtual Impedance Current Limiting Strategy for Grid-Forming Converter," *2023 8th Asia Conference on Power and Electrical Engineering (ACPEE)*, Tianjin, China, 2023.

[107] A. H. Jafariazad, S. A. Taher, Z. D. Arani, M. H. Karimi and J. M. Guerrero, "Adaptive Supplementary Control of VSG Based on Virtual Impedance for Current Limiting in Grid-Connected and Islanded Microgrids," in *IEEE Trans. Smart Grid*, vol. 15, no. 1, pp. 89-98, Jan. 2024.

[108] T. Zheng, L. Chen, Y. Guo, and S. Mei, "Comprehensive control strategy of virtual synchronous generator under unbalanced voltage conditions," *IET Gener., Transmiss. Distrib.*, vol. 12, no. 7, pp. 1621–1630, Apr. 2018.

[109] T. Zheng, L. Chen, Y. Guo, and S. Mei, "Flexible unbalanced control with peak current limitation for virtual synchronous generator under voltage sags," *J. Modern Power Syst. Clean Energy*, vol. 6, no. 1, pp. 61–72, Jan. 2018.

[110] E. B. Avdiaj, S. D'Arco, L. Piegari, and J. A. Suul, "Negative Sequence Control for Virtual Synchronous Machines Under Unbalanced Conditions," *IEEE Trans. Emerg. Sel. Topics Power Electron.,* vol. 10, no. 5, pp. 5670-5685, 2022.

[111] W. Wes Baker, M. Patel, A. Haddadi, E. Farantatos, and J. C. Boemer, "Inverter Current Limit Logic based on the IEEE 2800-2022 Unbalanced Fault Response Requirements," presented at the 2023 IEEE Power & Energy Society General Meeting (PESGM), 2023.

[112] B. Mahamedi, M. Eskandari, J. E. Fletcher, and J. Zhu, "Sequence-Based Control Strategy With Current Limiting for the Fault Ride-Through of Inverter-Interfaced Distributed Generators," *IEEE Trans. Sustain. Energy,* vol. 11, no. 1, pp. 165-174, 2020.

[113] L. Huang, H. Xin, L. Zhang, Z. Wang, K. Wu, and H. Wang, "Synchronization and Frequency Regulation of DFIG-Based Wind Turbine Generators With Synchronized Control," *IEEE Trans. Energy Convers.*, vol. 32, no. 3, pp. 1251-1262, 2017.

[114] Z. Li, Z. Xie, S. Xu, and X. Zhang, "Improving Transient Stability of Grid-Forming DFIG Based on Enhanced Hybrid Synchronization Control," *IEEE Trans. Ind. Electron.*, pp. 1-14, 2024.

[115] S. Wang, J. Hu and X. Yuan, "Virtual Synchronous Control for Grid-Connected DFIG-Based Wind Turbines," in *IEEE Journal of Emerging and Selected Topics in Power Electronics*, vol. 3, no. 4, pp. 932-944, Dec. 2015.

[116] Y. Jiao and H. Nian, "Grid-Forming Control for DFIG Based Wind Farms to Enhance the Stability of LCC-HVDC," in *IEEE Access*, vol. 8, pp. 156752-156762, 2020.

[117] Z. Zhao et al., "Decentralized Grid-Forming Control Strategy and Dynamic Characteristics Analysis of High-Penetration Wind Power Microgrids," *IEEE Trans. Sustain. Energy*, vol. 13, no. 4, pp. 2211-2225, 2022.

[118] J. C. Martínez, J. L. Rodríguez Amenedo, S. Arnaltes Gómez, and J. Alonso-Martínez, "Grid-forming control of doubly-fed induction generators based on the rotor flux orientation," *Renewable Energy*, vol. 207, pp. 162-176, 2023.

[119] Z. Li, Z. Xie, and X. Zhang, "An Improved Strategy of Grid-Forming DFIG Based on Disturbance Rejection Stator Flux Control," *IEEE Trans. Ind. Electron.*, vol. 71, no. 3, pp. 2498-2509, 2024.

[120] X. Gao, Z. Xie, M. Li, S. Yang, and X. Zhang, "Analysis and Mitigation of Electromechanical Oscillations in Drivetrain for Hybrid Synchronization Control of DFIG-Based Wind Turbines," *IEEE Trans. Power Electron.*, vol. 39, no. 3, pp. 3002-3013, 2024.

[121] S. Wang and L. Shang, "Fault Ride Through Strategy of Virtual-Synchronous-Controlled DFIG-Based Wind Turbines Under Symmetrical Grid Faults," in *IEEE Transactions on Energy Conversion*, vol. 35, no. 3, pp. 1360-1371, Sept. 2020.

[122] H. Nian and Y. Jiao, "Improved Virtual Synchronous Generator Control of DFIG to Ride-Through Symmetrical Voltage Fault," in *IEEE Transactions on Energy Conversion*, vol. 35, no. 2, pp. 672-683, June 2020.

[123] R. Liu, J. Yao, P. Sun, J. Pei, H. Zhang, and Y. Zhao, "Complex Impedance-Based Frequency Coupling Characteristics Analysis of DFIG-Based WT During Asymmetric Grid Faults," *IEEE Trans. Ind. Electron.*, vol. 68, no. 9, pp. 8274-8288, 2021.

[124] L. Chen, B. Zhang, and X. Fan, "Asymmetrical Fault Ride-Through Control Strategy for Rotor-Side Converter of DFIG," *IEEE Trans. Energy Convers.,* vol. 35, no. 2, pp. 1046-1053, 2020.

[125] P. Verma, S. K, and B. Dwivedi, "A Cooperative Approach of Frequency Regulation Through Virtual Inertia Control and Enhancement of Low Voltage Ride-through in DFIG-based Wind Farm," *Journal of Modern Power Systems and Clean Energy*, vol. 10, no. 6, pp. 1519-1530, 2022.

[126] Z. Zheng, D. Song, K. Du, X. Xiao, J. Ren, and Q. Xie, "A Continuous Fault Ride-through Scheme for DFIGs Under Commutation Failures in LCC-HVDC Transmission Systems," *Journal of Modern Power Systems and Clean Energy*, vol. 11, no. 4, pp. 1126-1135, 2023.

[127] H. Mohammadpour, A. Banaiemoqadam, A. Hooshyar, and A. Al-Durra, "Eliminating the Need for a Less Strict Requirement for the Negative-Sequence LVRT Current of Type-III Wind Turbine Generators in the IEEE 2800 Standard," *IEEE Trans. Sustain. Energy*, vol. 14, no. 1, pp. 587-601, 2023.

[128] Z. Rafiee, R. Heydari, M. Rafiee, M. R. Aghamohammadi, and F. Blaabjerg, "Enhancement of the LVRT Capability for DFIG-Based Wind Farms Based on Short-Circuit Capacity," *IEEE Systems Journal*, vol. 16, no. 2, pp. 3237-3248, 2022.

[129] J. Gu et al., "Enhanced Excitation Converter With Parallel/Series DC-Link Based on TAB for DFIG to Improve the LVRT Capability Under Severe Grid Faults," *IEEE Trans. Power Electron.*, vol. 38, no. 10, pp. 12304-12308, 2023.

[130] H. Wu, H. Xu, Z. Li, R. Zhao, and J. Hu, "Reactive Current Distribution Strategy of DFIG's RSC and GSC Considering Electromagnetic Stress and Grid Codes Requirement," *IEEE Trans. Energy Convers.*, vol. 38, no. 1, pp. 273-283, 2023.

[131] L. Xu, "Enhanced Control and Operation of DFIG-Based Wind Farms During Network Unbalance," *IEEE Trans. Energy Convers.,* vol. 23, no. 4, pp. 1073-1081, 2008.

[132] Y. Chang, I. Kocar, J. Hu and M. Berger, “Comparison of Internal Voltage Vectors of DFIG-based Wind Turbine Generator

and Synchronous Generator during Asymmetrical Fault," Electric Power Systems Research, vol. 223, 2023.

[133] S. Ouni, S. M. A. Emran, S. M. Hoseinizadeh, and H. Karimi, "A New Robust Control Strategy for Grid-Forming Voltage Source Converters," presented at the 2023 IEEE Power & Energy Society General Meeting (PESGM), 2023.

[134] H. Karimi, Y. Seyedi, and M. Karimi-Ghartemani, "A Robust and Simple Phase-Locked Loop for Unbalanced Power Grid Applications," in 2019 IEEE 28th International Symposium on Industrial Electronics (ISIE), 12-14 June 2019, pp. 29-34.

[135] U. Karaagac *et al.*, "A Generic EMT-Type Model for Wind Parks With Permanent Magnet Synchronous Generator Full Size Converter Wind Turbines," *IEEE Power and Energy Technology Systems Journal,* vol. 6, no. 3, pp. 131-141, 2019.

[136] M. Nasiri and R. Mohammadi, "Peak Current Limitation for Grid Side Inverter by Limited Active Power in PMSG-Based Wind Turbines During Different Grid Faults," *IEEE Trans. Sustain. Energy,* vol. 8, no. 1, pp. 3-12, 2017.

[137] W. Yi and X. Lie, "Coordinated Control of DFIG and FSIG-Based Wind Farms Under Unbalanced Grid Conditions," *IEEE Trans. Power Del.,* vol. 25, no. 1, pp. 367-377, 2010.

[138] MathWorks Simscape Team (2024). Renewable Energy Integration Design with Simscape (https://github.com/simscape/Renewable-Energy-Integration-Simscape/releases/tag/23.2.1.20), GitHub.

[139] T. Kauffmann, U. Karaagac, I. Kocar, S. Jensen, J. Mahseredjian, and E. Farantatos, "An Accurate Type III Wind Turbine Generator Short Circuit Model for Protection Applications," *IEEE Trans. Power Del.,* vol. 32, no. 6, pp. 2370-2379, 2017.

[140] Y. Chang, I. Kocar, E. Farantatos, A. Haddadi, and M. Patel, "Short-Circuit Modeling of DFIG-Based WTG in Sequence Domain Considering Various Fault- Ride-Through Requirements and Solutions," *IEEE Trans. Power Del.,* vol. 38, no. 3, pp. 2088-2100, 2023.

[141] T. Kauffmann *et al.*, "Short-Circuit Model for Type-IV Wind Turbine Generators With Decoupled Sequence Control," *IEEE Trans. Power Del.,* vol. 34, no. 5, pp. 1998-2007, 2019.

[142] J.-S. Lacroix, "Multiphase short-circuit analysis solver in phase domain using a modified-augmented-nodal analysis approach," Ph.D. dissertation, PolyPublie, École Polytechnique de Montréal, Montreal, QC, Canada, 2012.

[143] I. Kocar, J. Mahseredjian, U. Karaagac, G. Soykan and O. Saad, "Multiphase Load-Flow Solution for Large-Scale Distribution Systems Using MANA," *IEEE Trans. Power Del.,* vol. 29, no. 2, pp. 908-915, Apr. 2014.

[144] A. Haddadi, E. Farantatos, and I. Kocar, "A Robust Solver for Phasor-Domain Short-Circuit Analysis with Inverter-Based Resources," arXiv:2411.12006, Nov. 2024.

[145] *Inverter Based Resource Short-Circuit Modeling — 2024 Research Summary*. EPRI, Palo Alto, CA: 2024. 3002030170.

[146] S. Favuzza, R. Musca, G. Zizzo, and J. A. Sa'ed, "Comparative Modeling and Analysis of EMT and Phasor RMS Grid-Forming Converters Under Different Power System Dynamics," *IEEE Trans. Ind. Appl.,* vol. 60, no. 2, pp. 3613-3624, 2024.

[147] C. Fang, L. Mu, Z. Wang, and G. Chen, "Analysis of Grid-Forming IIDG's Transient- and Steady-State Fault Model," *IEEE Trans. Smart Grid,* vol. 13, no. 2, pp. 1187-1199, 2022.

[148] V. C. Cunha *et al.*, "Generalized Formulation of Steady-State Equivalent Circuit Models of Grid-Forming Inverters," *IEEE Open Access Journal of Power and Energy,* vol. 8, pp. 352-364, 2021.

[149] R. C. Dugan and T. E. McDermott, "An open source platform for collaborating on smart grid research," in *Proc. IEEE Power Energy Soc. Gen. Meeting*, Jul. 2011, pp. 1–7.

[150] W. Du *et al*., "Positive-Sequence Modeling of Droop-Controlled Grid-Forming Inverters for Transient Stability Simulation of Transmission Systems," *IEEE Trans. Power Del.*, vol. 39, no. 3, pp. 1736-1748, June 2024.

[151] Z. Chen, H. Liu, P. J. Hart, W. Du, F. Tuffner and U. C. Nwaneto, "Per-phase Phasor Modeling of GFL and GFM Inverters for Distribution System Dynamic Studies," *2024 IEEE Power & Energy Society Innovative Smart Grid Technologies Conference (ISGT)*, Washington, DC, USA, 2024.

[152] I. Kocar, J. -S. Lacroix and F. Therrien, "General and simplified computation of fault flow and contribution of distributed sources in unbalanced distribution networks," *2012 IEEE Power and Energy Society General Meeting*, San Diego, CA, USA, 2012, pp. 1-8.

[153] A. Haddadi, I. Kocar, and E. Farantatos. "Impact of inverter-based resources on protection schemes based on negative sequence components." *EPRI: Palo Alto, CA, USA*, vol. 36, no. 1, pp. 289-98, 2019.